PROJEKTNR. 13845

Självläkande betong med miljövänliga bindemedel - 2

Slutrapport

Magdalena Rajczakowska

2023-02-22

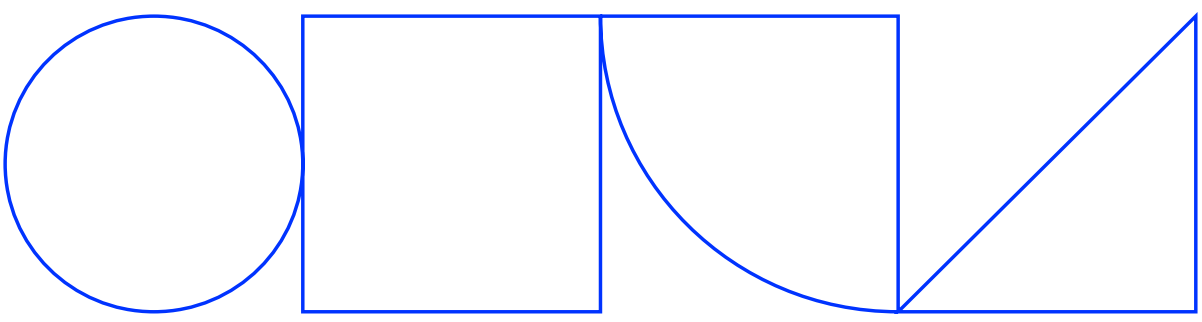

DOCTORAL THESIS

Stimulated autogenous self-healing of mechanically and thermally cracked cementitious materials

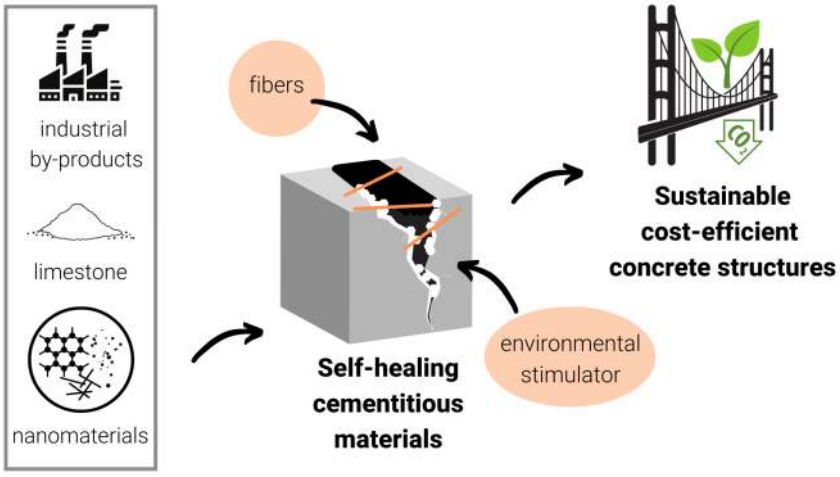

Magdalena Rajczakowska

Building Materials

LULEÅ UNIVERSITY OF TECHNOLOGY

DOCTORAL THESIS

Stimulated autogenous self-healing of mechanically and thermally cracked cementitious materials

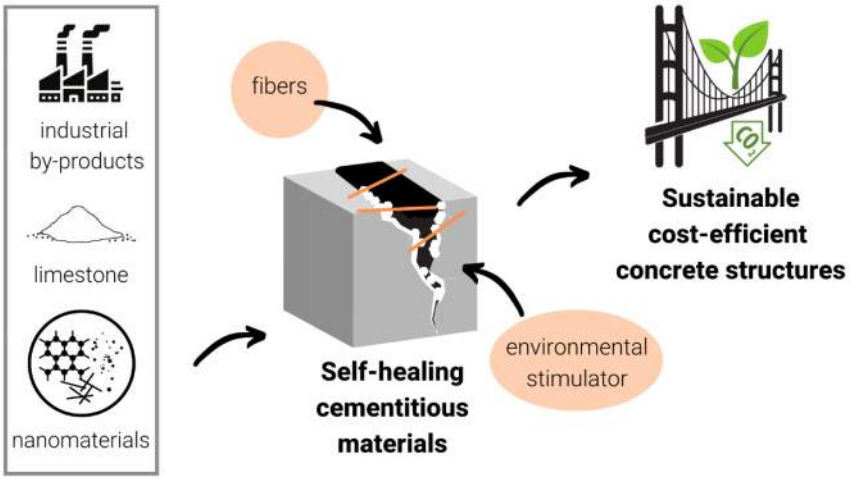

Magdalena Rajczakowska

Luleå, February 2023

Building Materials

Department of Civil, Environmental and Natural Resources Engineering

Luleå University of Technology
SE-97187 Luleå, Sweden

The cover image shows a schematic overview of the research project approach

Printed by Luleå University of Technology, 2023

ISSN 1402-1544
ISBN: 978-91-8048-227-1 (print)
ISBN: 978-91-8048-228-8 (electronic)

Luleå 2023

www.ltu.se

ACADEMIC THESIS

For the Degree of Doctor of Philosophy (Ph.D.) in Building Materials, which by due permission of the Technical Faculty Board at Luleå University of Technology will be publicly defended on:

Tuesday, February 21st, 2023, 10:00 am

Room C305, Luleå University of Technology

Opponent Examiner:

Prof. **Erik SCHLANGEN**, Delft University of Technology, the Netherlands

Examining committee:

Prof. Kim **VAN TITTELBOOM**, Ghent University, Belgium

Assoc. Prof. **Fiberato FERRARA**, Polytechnic of Milan, Italy

Prof. **Andrzej GARBACZ**, Warsaw University of Technology, Poland

Principal supervisor:

Prof. **Andrzej CWIRZEN**, Luleå University of Technology, Sweden

Assistant supervisors:

Assoc. Prof. **Karin HABERMEHL-CWIRZEN**, Luleå University of Technology, Sweden

Adj. Prof. **Hans HEDLUND**, Luleå University of Technology, Sweden

"It is good to have an end to journey toward;
but it is the journey that matters, in the end."

Ursula K. Le Guin,

"The Left Hand of Darkness"

ACKNOWLEDGEMENTS

This research project was conducted in the Building Materials group of Luleå University of Technology. This dissertation would not have been possible without the sponsors: Trafikverket (Swedish Transport Administration), Svenska Byggbranschens Utvecklingsfond (Development Fund of the Swedish Construction Industry) and Skanska.

> "Do random events ever lead to concrete results? Seems unlikely – after all, they are random."
>
> (Burger and Starbird, 2005)

Well, in fact, they do. A series of (seemingly) random events brought me to Luleå, a place in dangerous proximity to the polar circle, a couple of years ago. Events that transformed me as a scientist and, most importantly, as a person. Apart from their randomness, these events had one thing in common: they involved extraordinary and kind people—to these people, I would like to express my sincere gratitude:

To my supervisor, Prof. Andrzej Cwirzen, for believing that I am the right person to do the job, for sharing his immense knowledge and experience with me, and for always having time to discuss my problems and ideas.

To my co-supervisors, Prof. Karin Habermehl-Cwirzen and Prof. Hans Hedlund, for their continuous support during my Ph.D. studies, insightful comments, and suggestions.

To Prof. Mats Emborg and Carina Hannu, for encouraging words, invaluable advice, and assistance along the way.

To Prof. Dariusz Łydżba, for scientific inspiration and sparking research "obsession" in me.

To Damian Stefaniuk, for helping me make one of the best decisions in my life.

To Ilda Tole, for our endless discussions, support interventions, exciting plans, crazy initiatives, and never-ending fun in "deadline mode".

To Ankit Kothari, for our friendship, listening to me in difficult times, and for your selfless help.

To people from the Building Materials Group: Ploy, Klaudja, Marcin, Yaser, Vasiola, Ece, for creating a warm working environment where one can feel safe to be who they are.

To my best friends in Poland who always believe in me and deal with my delayed replies and disappearance from the radar.

Last but not least, to my family. I would like to thank my Parents, who never stopped encouraging me to pursue my dreams. *Dziękuję, Mamo i Tato!* And special thanks to my Husband and Children who were always there for me, every step of the way, in success and failure, without questioning and hesitation. Words cannot express my gratitude.

Magdalena Rajczakowska

Luleå, February 2023

SUMMARY

It is estimated that each year, approximately 8 billion cubic meters of concrete are produced worldwide, a vast number comparable to 1 m^3 per person, making the construction industry a major contributor to overall global CO_2 emissions. Throughout the manufacturing process of the most common cement binder, ordinary Portland cement (OPC), CO_2 emissions reach 842 kg per ton of clinker produced. Besides production-related emissions, concrete is a brittle material prone to cracking, wherein the mechanical performance and durability of the material degrade. In addition, maintenance and repairs of concrete structures require material resources, adversely affecting the concrete's overall environmental impact.

At the same time, concrete is a very popular building material, primarily due to its low price, accessibility, and multifunctionality, enabling it to be used in most construction environments. Given its versatility and widespread use, decreasing its carbon footprint is essential. It can be achieved through different methods, such as partially replacing OPC with industrial by-products or activating waste materials, using low-carbon cement, or reusing and recycling. Another area of interest in achieving increased service life for concrete is developing and utilizing cementitious materials with self-healing properties.

Cementitious materials have an inherent ability to self-repair cracks up to widths of 150 µm. However, wider cracks can be healed by employing various "stimulators" to boost the self-healing process, such as adding specific types of fibers, crystalline admixtures, or particular exposure conditions. Partial healing can also be achieved in extreme conditions. For example, structures that sustained high-temperature damage can be partially healed by executing post-fire curing. The recovery mechanism involves rehydration and self-healing of high-temperature cracks. Several variables define the process efficiency, such as the curing conditions, binder type, loading temperature, and post-fire cooling. The goal of this Ph.D. research project was to investigate the physicochemical processes and mechanisms behind the autogenous self-healing of cementitious materials. Two types of damage were evaluated: mechanical Cracking and high-temperature damaged binders. Furthermore, identifying potentially novel stimulators for enhanced self-healing properties was one of the project objectives. The application of low-carbon cementitious materials was of primary interest.

A comprehensive exploratory and experimental program was devised and implemented to evaluate factors affecting autogenous self-healing, including the age of the material, exposure conditions, amount of unhydrated cement, and self-healing duration. Environmentally friendly binders were primarily used for the different mix compositions. Observations were made at the crack mouth and deep inside the crack by analyzing the crack closure and chemical composition of the newly formed self-healing products. In addition, the strength recovery and durability of the specimens were investigated. Quantitative analysis and correlations were examined between microstructural features, geometrical crack characteristics, and self-healing efficiency parameters. Physicochemical mechanisms for thermally and mechanically cracked cementitious materials were studied. Machine Learning techniques were used to predict the compressive strength recovery after high-temperature exposure numerically. Four algorithms were deployed and trained on a database of results collected from the literature review, and corresponding hyperparameters were tuned for optimized model results. Individual Conditional Expectation and Partial Dependency plots were used to visualize and interpret the results.

It was observed that high cement content in the concrete mix does not guarantee an efficient autogenous self-healing of cracks. A dense, impermeable binder microstructure constrained the transport of silicon and calcium ions to the crack and reduced the precipitation of the healing products. With the addition of fly ash, the crack closure ratio close to the crack mouth increased, but recovery of flexural strength was not supported, presumably due to the small number of load-bearing phases inside the crack. All SCM-limestone cementitious materials have shown superior self-healing efficiency compared to pure OPC or OPC/limestone binders, presumably due to a synergistic effect between the limestone and the mineral additions. The binder composition affected the self-healing mechanism, leading to varying levels of performance recovery. Calcium carbonate

was detected mainly at the crack mouth, whereas ettringite and calcium silicate hydrate (C-S-H) were found deeper inside the crack. Flexural and compressive strength was regained, presumably because of C-S-H and ettringite formation.

On the other hand, after calcite crystals sealed the crack at the surface, the concentration of the ions inside the crack presumably increased, leading to better self-healing performance. Healing based on pure water exposure had limited efficiency despite applying various water volumes and temperature cycles. The highest crack closure was observed with the addition of a retarding admixture in the curing water. The admixture supposedly blocked the formation of a dense hydration shell on the surface of the unhydrated cement grains. Phosphorus and calcium were detected in the self-healing phases within the crack. Recovery of flexural strength by forming C-S-H in the crack was recorded when using water mixed with micro silica particles.

Using lime water with a small dosage of carbon nanomaterials displayed marginally improved high-temperature crack closure and mechanical performance compared with ordinary cement paste and tap water curing. Two distinct processes were identified for the recovery process of a thermally cracked cementitious material, i.e., rehydration and self-healing of the cracks. Phase assemblage and the cement paste porosity were exposed to changes with increasing loading temperature. These changes were presumably partially reversed upon application of a water re-curing process after cooling, i.e., the unhydrated cement grains further hydrate, forming new hydrates, pores are filled with new hydration products, and existing phases react to form new ones, e.g., CaO reacted with water to form $Ca(OH)_2$. It can be hypothesized that the mechanism of the crack healing is the same as in the mechanically cracked concrete, i.e., based on diffusion-dissolution-precipitation processes. The developed machine learning model interpretation indicated that strength recovery depends on the temperature range that caused the damage, re-curing conditions, and the amount of fine and coarse aggregate.

Keywords: cementitious materials, self-healing, exposure, fly ash, calcite, C-S-H, cracking

SAMMANFATTNING

Uppskattningsvis produceras, cirka 8 miljarder kubikmeter betong över hela världen varje år. En stor mängd som är jämförbar med 1 m^3 per person, vilket gör byggindustrin till en stor bidragsgivare till de totala globala CO_2-utsläppen. Under hela tillverkningsprocessen av det vanligaste cementbindemedlet, vanlig Portlandcement (OPC), når CO_2-utsläppen 842 kg per ton producerad klinker. Förutom produktionsrelaterade utsläpp är betong ett sprött material som är benäget att spricka, varvid materialets mekaniska prestanda och hållbarhet försämras. Underhåll och reparationer av betongkonstruktioner kräver materialresurser, vilket negativt påverkar betongens totala miljöpåverkan.

Samtidigt är betong ett mycket populärt byggmaterial, främst på grund av lågt pris, tillgänglighet och multifunktionalitet, vilket gör att det kan användas i de flesta byggmiljöer. Med tanke på dess mångsidighet och utbredda användning är det viktigt att minska dess koldioxidavtryck. Det kan uppnås genom olika metoder, såsom partiell ersättning av OPC med industriella biprodukter eller aktiverande avfallsmaterial, användning av cement med låg kolhalt eller återanvändning och återvinning. Ett annat intresseområde för att uppnå ökad livslängd för betong är att utveckla och utnyttja cementbaserade material med självläkande egenskaper.

Cementbaserade material har en inneboende förmåga att självreparera sprickor upp till bredder på 150 µm. Men även bredare sprickor kan läkas genom att använda olika "stimulatorer" för att öka självläkningsprocessen, såsom att lägga till specifika typer av fibrer, kristallina tillsatser eller särskilda exponeringsförhållanden. Partiell läkning kan också uppnås under extrema förhållanden. Till exempel kan strukturer som fått skador vid höga temperaturer delvis läkas genom att utföra härdning efter brand. Återhämtningsmekanismen involverar rehydrering och självläkning av högtemperatursprickor. Flera variabler definierar processeffektiviteten, såsom härdningsförhållanden, bindemedelstyp, laddningstemperatur och kylning efter brand. Målet med detta forskningsprojekt var att undersöka de fysikalisk-kemiska processerna och mekanismerna bakom den autogena självläkningen av cementbaserade material. Två typer av skador utvärderades: mekanisk sprickbildning och högtemperaturskadade bindemedel. Dessutom var ett av projektets mål att identifiera potentiellt nya stimulantorer för förbättrade självläkande egenskaper. Användningen av cementbaserade material med låg kolhalt var av primärt intresse.

Ett omfattande utforskande och experimentellt program utarbetades och implementerades för att utvärdera faktorer som påverkar autogen självläkning, inkluderande materialets ålder, exponeringsförhållanden, mängd ohydratiserat cement och självläkningslängd. Miljövänliga bindemedel användes i första hand för de olika blandningssammansättningarna. Observationer gjordes vid sprickmynningen och djupt inne i sprickan, genom att analysera sprickförslutningen och den kemiska sammansättningen av de nybildade självläkande produkterna. Dessutom undersöktes hållfastheten och hållbarheten hos proverna. Kvantitativ analys och korrelationer undersöktes mellan mikrostrukturella egenskaper, geometriska sprickegenskaper och självläkande effektivitetsparametrar. Fysikalisk-kemiska mekanismer för termiskt och mekaniskt spruckna cementbaserade material studerades. Maskininlärningsalgoritmer användes för att förutsäga återhämtningen av tryckhållfastheten efter exponering vid hög temperatur numeriskt. Fyra algoritmer distribuerades och tränades på en databas med resultat som samlats in från litteraturöversikten, och motsvarande hyperparametrar justerades för optimerade modellresultat. Individuella villkorliga förväntningar och partiellt beroende användes för att visualisera och tolka resultaten.

Det observerades att hög cementhalt i betongblandningen inte garanterar en effektiv autogen självläkning av sprickor. En tät, ogenomtränglig bindemedelsmikrostruktur begränsade transporten av kisel- och kalciumjoner till sprickan och minskade utfällningen av läkningsprodukterna. Med tillsats av flygaska ökade sprickförslutningsförhållandet nära sprickmynningen, men återhämtningen av böjhållfastheten stöddes inte, förmodligen på grund av det ringa antalet bärande faser inuti sprickan. Alla cementbaserade SCM-kalkstensmaterial har visat överlägsen självläkande

effektivitet jämfört med rena OPC- eller OPC/kalkstensbindemedel, förmodligen beroende på en synergistisk effekt mellan kalkstenen och mineraltillsatserna. Bindemedelskompositionen påverkade den självläkande mekanismen, vilket ledde till varierande nivåer av prestandaåterhämtning. Kalciumkarbonat detekterades huvudsakligen vid sprickmynningen, medan ettringit och kalciumsilikathydrat (C-S-H) hittades djupare inuti sprickan. Böj- och tryckhållfasthet återvanns, förmodligen på grund av C-S-H och ettringitbildning.

Å andra sidan, efter att kalcitkristaller förseglat sprickan vid ytan, antas koncentrationen av joner inuti sprickan öka, vilket leder till bättre självläkande prestanda. Läkning baserad på exponering av rent vatten hade begränsad effektivitet trots olika vattenvolymer och temperaturcykler. Den högsta sprickförslutningen observerades med tillsats av en retarderande blandning i härdningsvattnet. Blandningen antas ha blockerat bildandet av ett tätt hydratiseringsskal på ytan av de ohydratiserade cementkornen. Fosfor och kalcium upptäcktes i de självläkande faserna i sprickan. Återhämtning av böjhållfasthet genom att bilda C-S-H i sprickan registrerades vid användning av vatten blandat med mikrokiseldioxidpartiklar.

Användning av kalkvatten med en liten dos av kolnanomaterial visade marginellt förbättrad sprickförslutning vid hög temperatur och mekanisk prestanda jämfört med vanlig cementpasta och kranvattenhärdning. Två distinkta processer identifierades för återhämtningsprocessen av ett termiskt sprucket cementartat material, det vill säga rehydrering och självläkning av sprickorna. Fasmontering och cementpastans porositet utsattes för förändringar med ökande belastningstemperatur. Dessa förändringar reverserades förmodligen delvis vid applicering av en vattenåterhärdningsprocess efter kylning, det vill säga. de ohydratiserade cementkornen hydratiseras ytterligare, bildar nya hydrater, porerna fylls med nya hydratiseringsprodukter och befintliga faser reagerar för att bilda nya, till exempel reagerade CaO med vatten för att bilda $Ca(OH)_2$. Det kan antas att mekanismen för sprickläkningen är densamma som i den mekaniskt spruckna betongen, det vill säga baserad på diffusions-upplösning-fällningsprocesser. Den utvecklade tolkningen av maskininlärningsmodellen indikerade att hållfasthetsåterhämtningen beror på temperaturområdet som orsakade skadan, återhärdningsförhållanden och mängden fin och grov ballast.

Nyckelord: cementbaserade material, självläkande, exponering, flygaska, kalcit, C-S-H, sprickbildning

STRESZCZENIE

Szacuje się, że każdego roku na całym świecie produkuje się około 8 miliardów metrów sześciennych betonu, czyli około 1 m^3 betonu na osobę, co czyni przemysł budowlany jednym z największych producentów CO_2 w całkowitej globalnej emisji gazów cieplarnianych. W procesie produkcji najpowszechniejszego spoiwa cementowego, cementu portlandzkiego, emisja CO_2 sięga nawet 842 kg na tonę wyprodukowanego cementu. Poza emisjami związanymi z produkcją, beton jest materiałem wrażliwym na warunki atmosferyczne, kruchym i podatnym na pękanie, co powoduje pogorszenie jego właściwości mechanicznych oraz ogranicza trwałość. Naprawa konstrukcji betonowych wymaga wykorzystania dużej ilości betonu w celu regeneracji powstałych uszkodzeń, co także niekorzystnie wpływa na środowisko.

Z drugiej strony, beton jest bardzo popularnym materiałem budowlanym, przede wszystkim ze względu na niską cenę, dostępność i wielofunkcyjność, pozwalającą na zastosowanie tego materiału w większości warunków środowiskowych. Biorąc pod uwagę wszechstronność i szerokie zastosowanie betonu, niezbędne jest zmniejszenie jego śladu węglowego. Można to osiągnąć różnymi metodami, takimi jak częściowe zastąpienie cementu portlandzkiego produktami ubocznymi z przemysłu, zastosowanie pucolanów cementu niskoemisyjnego lub ponowne użycie i recykling wykorzystanego betonu. Innym obszarem zainteresowania, jest opracowywanie i wykorzystywanie materiałów cementowych o właściwościach samonaprawiających się w celu wydłużenia czasu użytkowania betonu.

Materiały na bazie cementu mają naturalną zdolność do samoleczenia pęknięć o szerokości do 150 μm. Natomiast szersze pęknięcia można naprawić, stosując różne „stymulantory" w celu przyspieszenia procesu samoregeneracji, poprzez dodanie określonych rodzajów włókien, domieszek krystalicznych lub stworzenie określonych warunków ekspozycji. Częściową regenerację beton potrafi również osiągnąć w ekstremalnych warunkach. Na przykład materiały, które uległy uszkodzeniu w wysokiej temperaturze, potrafią częściowo dokonać samoleczenia powstałych spękań. Mechanizm regeneracji w tym przypadku obejmuje ponowną „pielęgnację" materiału, która ułatwia samoleczenie pęknięć wysokotemperaturowych. Wydajność tego procesu zależy od kilku zmiennych, takich jak temperatura, w której materiał został uszkodzony, rodzaj spoiwa cementowego, czy też sposób pielęgnacji.

Celem niniejszej pracy doktorskiej było zbadanie procesów i mechanizmów fizykochemicznych leżących u podstaw autogenicznej samonaprawy materiałów na bazie cementu, z naciskiem na zastosowanie spoiw niskoemisyjnych. Przeanalizowano dwa źródła powstawania uszkodzeń: spękania mechaniczne oraz spowodowane wpływem wysokiej temperatury. Ponadto, celem projektu było zidentyfikowanie nowych stymulatorów, które mogą ułatwiać lub przyspieszać proces samoleczenia materiału.

W ramach realizacji projektu opracowano i wdrożono kompleksowy program eksploracyjny i eksperymentalny w celu oceny czynników wpływających na autogeniczną samonaprawę betonu, w tym: wieku materiału, warunków ekspozycji, ilości nieuwodnionego cementu i czasu trwania samonaprawy. Projektując skład mieszanek zastosowano przede wszystkim spoiwa przyjazne dla środowiska. Obserwacje prowadzono u wylotu pęknięcia oraz głęboko wewnątrz rys, analizując proces uszczelniania, a także skład chemiczny związków chemicznych powstałych w trakcie samoleczenia. Ponadto zbadano wytrzymałość i trwałość próbek. Praca badawcza obejmowała analizę ilościową wyników oraz poszukiwanie związków pomiędzy cechami mikrostruktury materiału, geometrią rysy i efektywnością samoleczenia. Na podstawie uzyskanych wyników przeanalizowano mechanizmy fizykochemiczne samoregeneracji materiału w zależności od źródła uszkodzeń, biorąc pod uwagę zniszczenie pod wpływem czynników termicznych i mechanicznych. W celu zbudowania modelu matematycznego regeneracji wytrzymałości na ściskanie w procesie samoleczenia, wykorzystano różne algorytmy uczenia maszynowego (Machine Learning). Model został wyszkolony na dużym zbiorze danych uzyskanych z przeglądu literatury. Przetestowano i zoptymalizowano cztery rożne algorytmy, na których podstawie wybrano model z najbardziej

trafną prognozą. Do wizualizacji i interpretacji wyników wykorzystano wykresy częściowej zależności (Partial Dependence) oraz indywidualnych oczekiwań warunkowych (Individual Conditional Expectation).

Zaobserwowano, że duża zawartość cementu w mieszance betonowej nie gwarantuje skutecznego procesu samonaprawy spękań. Gęsta, nieprzepuszczalna mikrostruktura spoiwa ograniczała transport jonów do pęknięcia blokując wytrącanie się produktów naprawy. Po dodaniu popiołu lotnego współczynnik zamknięcia pęknięć w pobliżu ujścia pęknięcia zwiększył się, ale wytrzymałość na zginanie nie została dostatecznie odzyskana, prawdopodobnie z powodu małej liczby faz nośnych wewnątrz pęknięcia. Spoiwa cementowe na bazie wapnia i materiałów niskoemisyjnych (pucolan) wykazały lepszą skuteczność samonaprawy w porównaniu z cementem portlandzkim, prawdopodobnie dzięki efektowi synergii pomiędzy składnikami spoiwa. Skład spoiwa wpływał na mechanizm samonaprawy, prowadząc do różnych poziomów odzyskiwania właściwości mechanicznych. U wylotu szczeliny wykryto głównie węglan wapnia, natomiast ettringit i uwodniony krzemian wapnia (C-S-H) stwierdzono w głębi szczeliny. Pierwotne parametry mechaniczne tj. wytrzymałość na zginanie i ściskanie, zostały odzyskane prawdopodobnie z powodu tworzenia się hydratu krzemianu wapnia (C-S-H) i ettringitu.

Z drugiej strony, po tym, jak kryształy kalcytu uszczelniły pęknięcie na powierzchni, stężenie jonów wewnątrz pęknięcia prawdopodobnie wzrosło, prowadząc do lepszej wydajności samonaprawy. Naprawa szczelin w wyniku ekspozycji na czystą wodę miała ograniczoną skuteczność pomimo zastosowania różnych objętości wody i cykli temperaturowych. Największe zamknięcie rys zaobserwowano po dodaniu do wody domieszki opóźniającej. Domieszka miała blokować tworzenie się gęstej powłoki hydratacyjnej na powierzchni nieuwodnionych ziaren cementu. W fazach powstałych w obrębie pęknięcia wykryto fosfor i wapń. Użycie wody zmieszanej z mikrocząstkami krzemionki umożliwiło odzyskanie wytrzymałości na zginanie poprzez tworzenie C-S-H w pęknięciu.

W przypadku obciążenia termicznego, materiał z niewielkim dodatkiem nanorurek węglowych, który był pielęgnowany wodą wapienną, wykazywał nieznacznie lepszą skuteczność samoleczenia w porównaniu ze zwykłym zaczynem cementowym pielęgnowanym wodą. Zidentyfikowano dwa odrębne procesy regeneracji spękanego termicznie materiału cementowego, tj. rehydratację i samonaprawę pęknięć. Skład fazowy i porowatość materiału zmieniały się znacznie wraz ze wzrostem temperatury obciążenia. Zmiany te zostały prawdopodobnie częściowo odwrócone po zastosowaniu pielęgnacji wodą po obniżeniu temperatury materiału, tj. nieuwodnione ziarna cementu uległy dalszej hydratacji, tworząc nowe fazy, pory wypełniły się nowymi produktami hydratacji, a istniejące fazy przereagowały tworząc nowe, np. CaO przereagował z wodą tworząc $Ca(OH)_2$.

Można postawić hipotezę, że mechanizm samonaprawy pęknięć jest taki sam jak w betonie zarysowanym mechanicznie, tj. oparty na procesach dyfuzja-rozpuszczanie-wytrącanie. Ponadto, interpretacja modelu matematycznego procesu regeneracji wytrzymałości na ściskanie wykazała, że najważniejszymi czynnikami warunkującymi odzyskanie właściwości mechanicznych betonu na bazie cementu portlandzkiego jest maksymalna temperatura obciążenia termicznego, warunki ekspozycji (pielęgnacja) oraz ilości drobnego i grubego kruszywa.

Słowa kluczowe: materiały na bazie cementu, samoleczenie, ekspozycja, popiół lotny, kalcyt, C-S-H, zarysowanie

TABLE OF CONTENTS

TERMS AND ABBREVIATIONS

Self-healing	The in-built ability of the material to automatically sense and repair the damage, including sealing of cracks, recovery of mechanical performance, and durability.
Stimulators	A substance that enhances the autogenous self-healing performance of the cementitious material, i.e., the recovery of durability and/or mechanical properties. It can be related to inner conditions, e.g., mix composition or environmental exposure.
Mechanically induced cracks	Cracks formed when the material is subjected to mechanical loading, e.g., by compression, tension, or bending.
Thermally induced cracks	Cracks formed when the material is subjected to high temperatures.
Crack closure at depth	The healing of the crack deeper inside the specimen, in this thesis sometimes referred to as "internal crack closure."
Surface crack closure	The healing of the crack at the crack mouth/opening, at the surface, in this thesis, also referred to as "external crack closure" or "surface crack closure."
Environmental exposure	Self-healing stimulator applied externally on the material, e.g., by immersion of the specimen in a solution. In this thesis, also referred to as "exposure," "exposure conditions," and "healing treatment."

ACW	Average crack width
ANN	Artificial neural networks
BE	Backscatter electrons
Calcite	Calcium carbonate / $CaCO_3$
CC/SCC	Surface crack closure ratio, defined by Eq. (3.2)
CH	$Ca(OH)_2$ / Portlandite
CH0	Portlandite change with respect to the intact state, defined by Eq. (4.13)
CHt	Portlandite change with respect to the damaged state, defined by Eq. (4.14)
C-S-H	calcium silicate hydrate
CSR0	Compressive strength recovery with respect to the intact specimen before temperature loading, defined by Eq. (4.10)
CSR100	Compressive strength recovery of 100% damage, defined by Eq. (3.7)
CSR80	Compressive strength recovery of 80% damage, defined by Eq. (3.7)
CSRt	Compressive strength recovery with respect to the damaged specimen after temperature loading, defined by Eq. (4.11)

ECC	Engineered Cementitious Composites
EDS/EDX	Energy-dispersive X-ray spectroscope
ET	Ensemble of trees
FA	Fly ash
FD	Fractal dimension, defined by Eq. (3.11)
FRCC	Fiber Reinforced Cementitious Composites
FSR0	Compressive strength recovery with respect to the intact specimen before temperature loading, defined by Eq. (4.8)
FSRt	Compressive strength recovery with respect to the damaged specimen after temperature loading, defined by Eq. (4.9)
I	The cumulative rate of water absorption, defined by Eq. (3.3)
ICA	Initial crack area
IP	Inner product
IP0	Change in Si/Ca ratio of the inner product of C-S-H with respect to the intact state, defined by Eq. (4.13)
IPt	Change in Si/Ca ratio of the inner product of C-S-H with respect to the damaged state, defined by Eq. (4.14)
IR180	Recovery / changes of the cumulative water absorption at 180 min for healed and undamaged specimens, defined by Eq. (3.5)
IR25	Recovery / changes of the cumulative water absorption at 25 min for healed and undamaged specimens, defined by Eq. (3.4)
L	Exposure to lime water with a cycle length of 3 days wet and 3 day dry
LM	Limestone
MAE	Mean Absolute Error, defined by Eq. (4.4)
MCW	Maximum crack width
MSE	Mean Squared Error, defined by Eq. (4.2)
MWCNT	Multi-wall carbon nanotubes
NRMSE	Normalized Root Mean Squared Error, defined by Eq. (4.6)
OP	Outer product
OP0	Change in Si/Ca ratio of the outer product of C-S-H with respect to the intact state, defined by Eq. (4.13)
OPC	Ordinary Portland cement
OPt	Change in Si/Ca ratio of the outer product of C-S-H with respect to the damaged state, defined by Eq. (4.14)
P0	Porosity change with respect to the intact state, defined by Eq. (4.13)
PP	polypropylene

Pt	Porosity change with respect to the damaged state, defined by Eq. (4.14)
PVA	polyvinyl alcohol
R	Exposure to water mixed with retarding admixture with a cycle length of 3 days wet and 3 day dry
R^2	coefficient of determination, defined by Eq. (4.5)
Retarder	Phosphate-based retarding admixture
RMSE	Root Mean Squared Error, defined by Eq. (4.3)
RT	Regression tree
R_t	The transmission time recovery ratio, defined by Eq. (3.1)
S	Flexural strength recovery after mechanical damage healing with respect to the intact state, defined by Eq. (3.9)
S/GGBS	Ground granulated blast furnace slag
SCM	Supplementary Cementitious Materials
SE	Secondary electrons
SEM	Scanning Electron Microscope
SF	Silica fume
SP	Superplasticizer
S_p	Flexural strength recovery after mechanical damage healing with respect to the damaged state defined by Eq. (3.8)
SR25	Recovery / changes of the coefficient of sorptivity for healed and undamaged specimens coefficient of sorptivity, defined by Eq. (3.6)
SVM	Support Vector Machines
T	Tortuosity, defined by Eq. (3.10)
UC0	Unhydrated cement change with respect to the intact state, defined by Eq. (4.13)
UCt	Unhydrated cement change with respect to the damaged state, defined by Eq. (4.14)
UHPC	Ultra-High-Performance Concrete
UHPFRC	Ultra-high-performance fiber-reinforced concrete
W	Exposure to water with cycle length of 3 days wet and 3 day dry
W0	Exposure to water with cycle length of 5 days wet and 1 day dry
wt%	weight of the binder
XRD	X-ray Powder Diffraction

LIST OF FIGURES AND TABLES

FIGURES:

TABLES:

1

Introduction

"Our planet which gets smaller every year, with its fantastic proliferation of mass media, is witnessing a process that escapes definition, characterized by a refusal to remember."

Czesław Miłosz
1980 Literature Nobel Prize winner

1. INTRODUCTION

United Nations Sustainable Development Goals (SDG) cannot be fulfilled without a radical transformation of the concrete industry. By 2050, the world population is predicted to increase from 7.6 billion to 10 billion (United Nations, 2019). Meanwhile, twice as many people will live in metropolitan areas. Therefore, environmentally friendly, robust, and functional building materials with long service life are necessary for a sustainable built environment. Concerning quantity, concrete is the most important building material, second after water most used substance in the world (UN Environment et al. 2018). Each year, concrete production reaches over 8 billion cubic meters, equal to 1 m^3 per person per year (Salet and Wolfs, 2016). In 2020, approximately 4.17 billion tons of ordinary Portland cement (OPC) were produced, an increase of over 30 since the 1950s (CEMBUREAU, 2022). The calcination and grinding connected to the OPC production lead to the emission of around 800 kg of CO_2 per ton of clinker (di Summa et al. 2022), contributing to 6-10% of the total anthropogenic greenhouse gas emissions (IEA, 2009). The price of carbon dioxide is increasing due to rigorous emission targets, which is described as the so-called "Time Value of Carbon" (Karimpour et al. 2014). This process will potentially result in a doubling of cement prices by 2030 (Imbabi et al. 2012). The high demand for urban living places, the exponential growth of the construction industry, and its colossal environmental impact call for substantial technological intervention.

On the other hand, concrete is also a cheap, robust, and versatile building material made with local ingredients, which can be applied in almost any environmental conditions. There are no alternatives to concrete, as replacing it with other building materials, e.g., steel or timber would lead to an even higher carbon footprint (Ferrara, 2019). Therefore, efforts are needed to reduce the carbon emissions of concrete by, e.g., partial replacement of OPC with industrial by-products, activated waste materials, application of low carbon types of cement, or reusing and recycling concrete (Environment, U. N. et al.).

In addition, due to their brittle nature, cementitious materials are prone to cracking. Interconnected cracks form discontinuities in the hydrated binder matrix, which facilitate aggressive substances' transport path into the material (Borg et al. 2018). This affects concrete's durability, causes corrosion of steel reinforcement, and decreases the service life of concrete structures. In 2016, the Association for Materials Protection and Performance (former NACE International), in their report titled "International Measures of Prevention, Application, and Economics of Corrosion Technology (IMPACT)," estimated that the global costs of corrosion reached 2.5 trillion USD, equal to 3.4% of the global GDP (Gross domestic product). Approximately 10% of this cost is connected to the construction industry. Furthermore, the repair and maintenance of concrete structures is a reoccurring necessity since at least half of the repaired structures fail again, 75% of those in the first 10 years of service (Borg et al. 2018). This situation is inconvenient not only from the economic point of view but also brings societal and environmental issues. The current post-COVID unstable economy and a lingering climate disaster demand that society shifts to

durable long-lasting building materials, which do not require extensive repairs or material-costly replacements. Therefore, one can ask an important question:

> What can be done to increase the durability of cementitious materials?

Biomimicry is the concept of designing functional materials following nature (Jamei and Vrcelj, 2021). Biological organisms possess extraordinary properties, e.g., they can survive in extreme environments and have unprecedented energy absorption capabilities and mechanical performance. (Ahamed et al. 2022). Cementitious materials exhibit unique similarities with biological organisms, i.e., they are capable of self-repair (Figure 1.1).

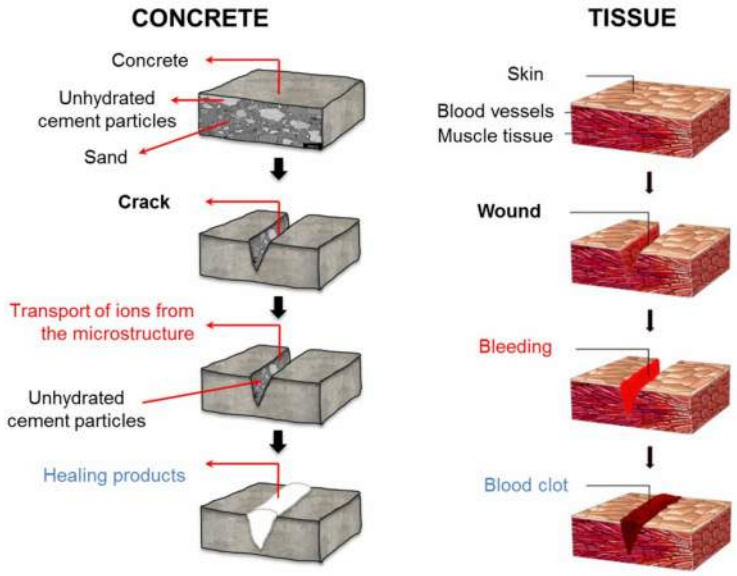

Figure 1.1. Self-healing of concrete by mimicking tissue healing; modified from (Tavangarian & Li, 2015)[1]

Self-healing materials can be described as "*materials which have a negative rate of damage formation at one or more stages in their lifetime*" (De Rooij et al. 2013). Skin, a composite built of several components such as blood vessels and muscle tissues, is an example of a self-healing material. Throughout its "service life", skin is subjected to damage, i.e., wounds and cuts, which, with little human intervention, is self-repaired owing to the physicochemical processes occurring in the material (Figure 1.1). Similarly, concrete has an intrinsic ability to heal cracks in the presence of moisture, called autogenous self-healing (Rajczakowska et al. 2019a). The International Union of Laboratories and Experts

[1] Reproduced from (Tavangarian & Li, 2015) with permission from Elsevier

in Construction Materials, Systems, and Structures (RILEM) defines autogenous self-healing as a mechanism of material recovery that involves only its original components, i.e., hydrated binder, aggregates, and potential additives (De Rooij et al., 2013). This phenomenon was empirically observed already in the XIXth century by the French Academy of Science (Wu et al., 2012). The presence of white precipitates was noticed in the cracks of water-retaining structures and pipes. The autogenous self-healing is quite efficient in narrow cracks, having a width of up to 150 μm. It depends on numerous variables, i.e., concrete mix composition, healing time, concrete age, environmental exposure, crack width, and temperature. Because of crack healing, the durability and/or mechanical performance of concrete can be partially recovered.

Following the skin analogy, mechanical injury, such as a cut is only one type of relatively straightforward damage that can affect the tissues. What about other problems such as burns, acne, dermatitis, carcinomas…? These skin conditions often change the surrounding tissues, alternating the healing mechanism. A cancerogenic process spreading into other body parts also requires more extensive treatment or stimulus than a shallow wound. Similarly, cementitious materials can self-heal damages that occurred due to different kinds of deterioration processes, e.g., alkali-aggregate reaction, sulfate, and chloride attack as well as a high-temperature exposure. However, the initial conditions, i.e., the hydrated cement paste microstructure, change because of physical and chemical processes resulting from the non-mechanical loading imposed (Figure 1.2). This leads to a more complex self-healing mechanism.

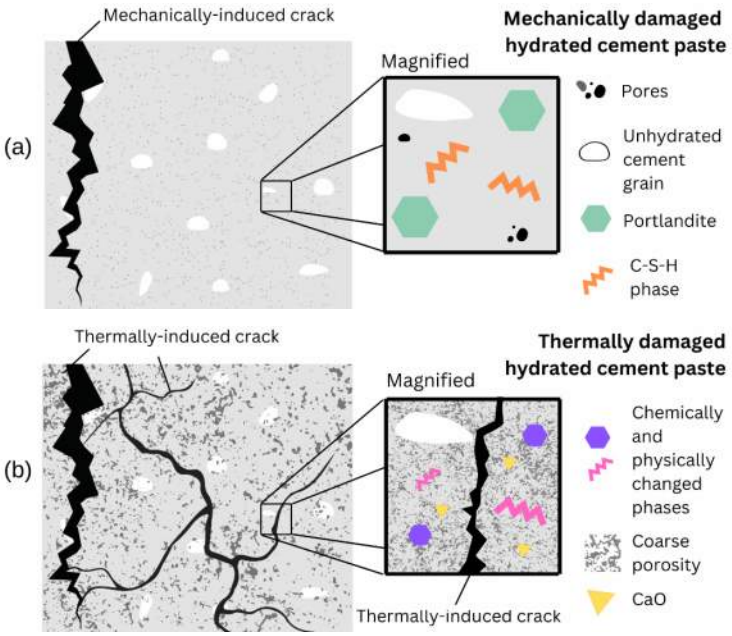

Figure 1.2. Comparison of mechanical (a) and thermally induced (b) damage in hydrated cement paste; modified from (Rajczakowska et al. 2023c).

The autogenous self-healing process can be improved by applying certain *stimulators*, i.e., substances that enhance the recovery of durability and mechanical properties.

> "As our knowledge expands, we recognize the vastness of our ignorance"
>
> Stanisław Lem, "Short Circuits", 2004

The self-healing of cementitious materials has been of interest to the scientific community, construction companies, and engineers for decades. The potential that lies in this solution is immense. It could become a "quick fix" to the durability issues, resulting in decreased costs of repairs and maintenance of structures. Consequently, the carbon emissions connected to the rehabilitation of buildings would be drastically reduced. Recently performed Life Cycle Assessment (LCA) analysis shows that the environmental impact of concrete can be reduced by 56%–75% thanks to self-healing properties (Van Belleghem, 2019).

Nevertheless, despite continuous scientific efforts, there are still knowledge gaps that hinder large-scale applications of this technology. Due to the multi-variability of the self-healing process, the mechanism is still not fully understood. This limits full control over the recovery. There are still few studies dealing with self-healing of durability-related deterioration processes. Continuous development of novel cementitious binders with different chemical compositions leads to changes in the intact hydrated material microstructure. This affects, to a great extent, the healing process. Finally, the up-scaling of modern production technologies, i.e., 3D printing, creates new challenges for developing efficient self-healing materials.

1.1. AIM AND OBJECTIVES

The **aim** of this study was to investigate the governing factors of the autogenous self-healing mechanism for the mechanically and thermally induced cracks in cementitious materials.

The following **objectives** were defined:

1. Compare different self-healing methodologies with respect to the fresh and hardened properties of concrete, their cost, safety, and full-scale applications.
2. Adapt and/or modify a testing methodology for the experimental evaluation of the autogenous self-healing
3. Apply interpretable artificial intelligence modeling for a data-driven analysis of the self-healing process
4. Investigate/develop novel stimulators of the autogenous self-healing process, with a focus on environmentally friendly binders

5. Study effects of different variables on the self-healing mechanism of mechanically and thermally cracked cementitious materials
6. Propose a self-healing model(s) based on physicochemical processes for mechanically and thermally cracked cementitious materials

1.2. RESEARCH QUESTIONS

The following **research questions** were defined.

1. What is a more reliable self-healing approach for concrete considering the efficiency, impact on fresh and hardened properties, cost, safety, and full-scale applications? **(Paper I)**
2. How do the mix composition and age affect the efficiency of the autogenous self-healing process of mechanically induced cracks? **(Papers II and IV)**
3. What are the driving factors of the self-healing of thermally induced cracks? **(Paper V)**
4. What is the effect of environmental exposure on the self-healing of mechanically and thermally cracked cementitious materials? **(Paper III, VII and VIII)**
5. Which geometrical parameters of the crack impact the self-healing of mechanically induced cracks? **(Paper IV)**
6. What are the differences in self-healing mechanisms of mechanically and thermally induced cracks? **(Papers II-VIII)**

1.3. SCIENTIFIC APPROACH

This research was initiated with the literature review on the self-healing of cementitious materials. Firstly, the autogenous and autonomous approaches were compared with respect to their effect on the initial concrete properties in the fresh and hardened state as well as functionality. Based on the analysis, autogenous self-healing was selected as more practical and compatible with concrete properties at a present technological level. Further literature studies included an investigation of the physicochemical principles of self-healing and critical factors affecting its efficiency. Furthermore, different types of auto-repaired damage were included in the analysis, i.e., related to mechanical loading and deterioration processes. Identified knowledge gaps indicated two research paths: the self-healing of mechanically and thermally induced cracks.

Two approaches were selected to obtain an initial understanding of the self-healing mechanism. For mechanically induced cracks, initial experiments were performed to scan for significant factors potentially affecting the self-healing efficiency, i.e., high amount of cement, age, time of healing, and presence of fly ash. The analysis results pointed out that a dense microstructure is a factor potentially preventing efficient healing, whereas fly ash facilitated calcite precipitation on the surface. A simplified healing mechanism was

proposed, and several research questions were formulated. The further experimental analysis consisted of the effect of exposure conditions, binder composition, and microstructure.

A large database was created based on the literature review for thermally induced cracks. The data were analyzed using machine learning modeling. The performed feature importance analysis revealed a strong dependence between the compressive strength recovery and the healing exposure conditions, i.e., re-curing regime. The obtained results enable the formulation of research questions and the planning of further experiments. Furthermore, the effect of exposure on the healing of high-temperature cracks was included. Finally, the results were analyzed and discussed. The main physicochemical processes controlling the self-healing of the mechanically- and thermally- induced cracks were identified.

An overview of the scientific approach is presented in Figure 1.3.

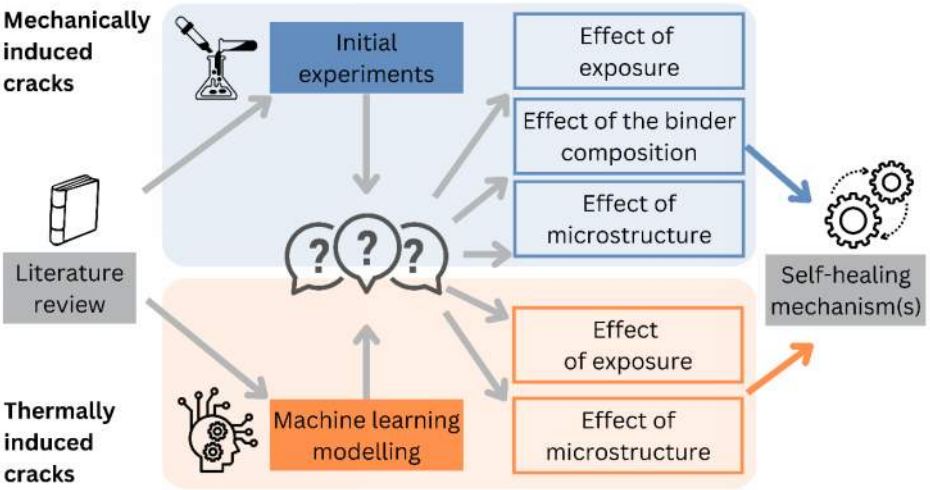

Figure 1.3. Scientific approach.

1.4. LIMITATIONS

The performed research had the following limitations:

- There are several chemical and physical triggers of concrete deterioration processes, i.e., high temperature, alkali-aggregate reaction, chloride penetration, sulfate attack, and carbonation. Each of these processes leads to damage that can be potentially auto-repaired by cementitious materials. However, in this study, only high-temperature exposure was considered, i.e., thermally induced cracks, as a representation of the deterioration processes.

- The focus of this doctoral thesis was on experimental research. Experiments were performed on a small-scale. The up-scaled tests are still in progress while preparing this manuscript, and results are excluded from this Ph.D. thesis.
- The number of specimens corresponding to each analyzed case in the initial studies (Paper II and III) was small. Therefore, the results should be treated as qualitative rather than quantitative. In the case of Paper II, it stems from the fact that it was planned as a preliminary "scanning" of several factors influencing the self-healing efficiency. In Paper III, the investigation is based on microscopic studies, i.e., Scanning Electron Microscope (SEM) and optical microscope. The procedure involved polishing the specimens several times to achieve different cross-sections of the crack. Due to time restrictions, the number of specimens was limited.
- The chemical analysis of the self-healing material formed inside the cracks was performed using (SEM) with Energy Dispersive Spectroscopy (EDS). The Author is aware of other methods which could be employed, e.g., X-ray powder diffraction (XRD) or thermogravimetry (TGA). Nevertheless, these methods usually require powder-like material for analysis. Initial trials revealed that the extraction of formed material from cracks is unreliable. Therefore, experimental procedures for preparing the cross-sections of the crack for the SEM analysis were developed and applied. It should be noted that it does not give quantitative information which can be generalized to all specimens.
- Differences in sizes and types of specimens could influence the obtained results. Two types of specimens were used in the case of mechanically cracked specimens, i.e., standard 40 mm x 40 mm x 160 mm beams and small 12 mm x 12 mm x 60 mm beams. The reason for the small size of the beams was to prevent unnecessary contamination/alteration of the healing material during the cutting of the specimens for SEM analysis. Mechanically cracked specimens were made of mortars, whereas cement paste was used for the high-temperature cracking. The choice was based on the initial trials performed and the possibility of acquiring comparable surface cracking patterns.

1.5. STRUCTURE OF THE THESIS

This doctoral thesis is a compilation of seven research papers (Papers I – VII) and one conference contribution (Paper VIII). The thesis consists of six chapters, which are briefly outlined below:

		Key papers
Chapter 1	**Introduction** It is an overview of the study. It describes the aim and scope of the research, and the research questions, together with study limitations.	

Chapter 2	**Literature review** Presents a literature review on the self-healing of mechanically and thermally cracked cementitious materials.	*Paper I*
Chapter 3	**Mechanically induced cracks** Focuses on the self-healing of cementitious materials with mechanically induced cracks. Materials and methods, as well as research results, are included.	*Papers II-IV* *Paper VIII*
Chapter 4	**Thermally induced cracks** Presents details regarding the self-healing of cementitious materials subjected to high-temperature loading. Machine learning modeling, materials and methods, and research results are included.	*Papers V-VII*
Chapter 5	**Discussion and outlook** Combines all results with a discussion and analysis of the physicochemical processes related to self-healing; Ongoing research and perspectives for further studies are considered	*Papers II-VIII*
Chapter 6	**Conclusions** Formulates conclusions; an approach to answering the research questions is made;	*Papers I -VIII*

1.6. LIST OF APPENDED PUBLICATIONS

The following publications formed the basis for this research and were appended in the end of the thesis.

PAPER I **Rajczakowska, M.**, Habermehl-Cwirzen, K., Hedlund, H., & Cwirzen, A. (2019). Autogenous self-healing: a better solution for concrete. *Journal of Materials in Civil Engineering*, 31(9), 03119001.

https://doi.org/10.1061/(ASCE)MT.1943-5533.0002764

Contributions: Conceptualization – A. Cwirzen; Methodology, literature studies, and their analysis, writing of the original draft of the paper – **M. Rajczakowska**; Draft reviewing and editing – K. Habermehl-

Cwirzen and A. Cwirzen; Supervision and project administration – H. Hedlund

Main findings: The paper presents a state-of-the-art review of self-healing concrete approaches. A comparison of autogenous and autonomous self-healing is done concerning their influence on intact concrete performance. Fresh as well as mechanical properties were studied. In addition, self-healing efficiency and price are analyzed. Analysis indicated that autogenous self-healing is the most compatible and efficient methodology thus far.

PAPER II

Rajczakowska, M., Nilsson, L., Habermehl-Cwirzen, K., Hedlund, H., & Cwirzen, A. (2019). Does a High Amount of Unhydrated Portland Cement Ensure an Effective Autogenous Self-Healing of Mortar?. *Materials*, 12(20), 3298.

https://doi.org/10.3390/ma12203298

Contributions: Conceptualization, methodology, validation, investigation, formal analysis, software, data curation, visualization, writing—original draft preparation – **M. Rajczakowska**; Methodology, validation, investigation – L. Nilsson; Conceptualization, writing—review and editing, resources, supervision, project administration, and funding – A. Cwirzen; Resources, supervision, project administration, and funding – K. Habermehl-Cwirzen and H. Hedlund.

Main findings: In this paper, the first experimental results are presented. The autogenous self-healing of Ultra-High-Performance Concrete (UHPC) subjected to water immersion is investigated. The influence of several variables is studied, i.e., cement amount, the addition of fly ash, concrete age, and healing time. Results suggested that the amount of unhydrated cement is not the driving factor in the healing efficiency. The dense microstructure presumably prevented the transport of ions from the binder matrix to the crack. A simplified model of the self-healing process is proposed.

PAPER III

Rajczakowska, M., Habermehl-Cwirzen, K., Hedlund, H., & Cwirzen, A. (2019). The effect of exposure on the autogenous self-healing of ordinary Portland cement mortars. *Materials*, 12(23), 3926.

https://doi.org/10.3390/ma12233926

Contributions: Conceptualization, methodology, validation, investigation, formal analysis, software, data curation, visualization, writing—original draft preparation – **M. Rajczakowska**; Conceptualization, methodology, writing – review and editing, resources, supervision, project administration, and funding – A. Cwirzen; Resources, supervision, project administration, and funding – K. Habermehl-Cwirzen and H. Hedlund.

Main findings: In this paper, self-healing of cement mortar under different environmental conditions was investigated. Different groups of healing treatments were proposed, i.e., different water immersion regimes, temperatures, application of chemical admixtures and application of solutions containing micro-particles. Water exposure led to relatively small crack closure. Phosphate-based retarding admixture- and micro-silica-water mixtures were found to be the most efficient environmental stimulators.

PAPER IV **Rajczakowska, M.**, Tole, I. Habermehl-Cwirzen, K., Hedlund, H., & Cwirzen, A. (2023). Autogenous self-healing of low embodied energy cementitious materials: effect of multi-component binder and crack geometry

Under review in *Construction and Building Materials,* November 2022

Contributions: Conceptualization, methodology, validation, investigation, formal analysis, software, data curation, visualization, writing—original draft preparation – **M. Rajczakowska**; investigation, software, data curation – I. Tole; writing – review and editing, resources, supervision, project administration, and funding – A. Cwirzen; Resources, supervision, writing – review and editing – K. Habermehl-Cwirzen; supervision – H. Hedlund.

Main findings: This study studied the self-healing of multicomponent binders with a high amount of limestone. Several factors were analyzed, i.e., binder-related parameters such as phase composition and porosity, as well as crack geometry. The self-healing efficiency was described using sorptivity change, compressive strength recovery, and crack closure. Quantitative analysis was performed, and correlations between different variables and self-healing efficiency were studied.

PAPER V

Rajczakowska, M., Szeląg, M. Habermehl-Cwirzen, K., Hedlund, H., & Cwirzen, A. (2023). Interpretable machine learning for prediction of concrete post-fire self-healing

Under review in *Materials,* January 2023

Contributions: Conceptualization, methodology, validation, investigation, formal analysis, software, data curation, visualization, writing—original draft preparation – **M. Rajczakowska**; methodology, validation, writing – review, and editing – M. Szeląg; writing – review and editing, resources, supervision, project administration, and funding – A. Cwirzen; project administration, supervision – K. Habermehl-Cwirzen; supervision – H. Hedlund.

Main findings: This paper used machine learning (ML) methods to predict the compressive strength recovery of high-temperature damaged cementitious materials. Exhaustive literature studies were performed to prepare a large database for the modeling. Twelve input variables were selected, i.e., w/c, age of concrete, amount of cement, fine aggregate, coarse aggregate, peak loading temperature, duration of peak loading temperature, cooling regime, duration of cooling, curing regime, duration of curing, and specimen volume. A model was selected among four ML methods, i.e., Support Vector Machines (SVM), Regression Trees (RT), Artificial Neural Networks (ANN), and Ensemble of Regression Trees (ET). Monte Carlo analysis was performed to assess the robustness of the selected model. Partial Dependency and Individual Conditional Expectation Plots were used to interpret the model. In addition, feature importance analysis was performed.

PAPER VI

Rajczakowska, M., Szeląg, M., Habermehl-Cwirzen, K., Hedlund, H., & Cwirzen, A. Is Cement Paste Modified with Carbon Nanomaterials Capable of Self-Repair after a Fire?. Nordic Concrete Research, 67(2), 79-97.

Contributions: Conceptualization, methodology, validation, investigation, formal analysis, software, data curation, visualization, writing—original draft preparation – **M. Rajczakowska**; methodology, validation, writing – review, and editing – M. Szeląg; writing – review and editing, resources, supervision, project administration, and funding – A. Cwirzen; project administration, supervision – K. Habermehl-Cwirzen; supervision – H. Hedlund.

Main findings: In this paper, the self-healing of the cement paste with multi-wall carbon nanotubes (MWCNTs) exposed to water immersion was studied. Two loading temperatures were applied, i.e., 200ºC and 400ºC. Compressive and flexural strength recovery was evaluated. Cracking patterns, before and after healing, were assessed with the use of image processing methodology. Microscopic studies using SEM and an optical microscope were performed to assess crack closure deeper inside the specimens.

PAPER VII **Rajczakowska, M.**, Szeląg, M. Habermehl-Cwirzen, K., Hedlund, H., & Cwirzen, A. (2023). Autogenous self-healing of thermally damaged cement paste with carbon nanomaterials subjected to different environmental stimulators

Submitted to *Case Studies in Construction Materials,* January 2023

Contributions: Conceptualization, methodology, validation, investigation, formal analysis, software, data curation, visualization, writing—original draft preparation – **M. Rajczakowska**; Conceptualization, methodology, validation, writing – review, and editing – M. Szeląg; writing – review and editing, resources, supervision, project administration, and funding – A. Cwirzen; project administration, supervision – K. Habermehl-Cwirzen; supervision – H. Hedlund.

Main findings: In this paper, self-healing of thermally induced cracks was studied under different re-curing regimes, i.e., environmental exposures. Three types of cyclic treatments were used: water immersion, retarding admixture mixed with water, and limewater. In addition, cement pastes with and without MWCNTs were analyzed. Self-healing efficiency was evaluated based on strength recovery and crack closure. SEM studies of the crack closure deeper inside the specimen were performed together with a chemical analysis of the composition of the filling material. In addition, changes in microstructural parameters after the healing process were analyzed, i.e., porosity and C—S—H composition.

PAPER VIII **Rajczakowska, M.**, Habermehl-Cwirzen, K., Law, D., Gunasekara, C., Hedlund, H., & Cwirzen, A. (2020). Improved self-healing of mortars with partial cement replacement. *In 74th RILEM Annual Week and 40th Cement and Concrete Science Conference*, 31

August-4 September 2020. Hosted online by The University of Sheffield.

Conference abstract, poster, and presentation

Contributions: Conceptualization, methodology, validation, investigation, formal analysis, software, data curation, visualization, writing—original draft preparation – **M. Rajczakowska**; writing – review and editing – D. Law and C. Gunasekara; writing – review and editing, resources, supervision, project administration, and funding – A. Cwirzen; project administration, supervision – K. Habermehl-Cwirzen; supervision – H. Hedlund.

1.7. ADDITIONAL PAPERS/CONFERENCES

The Author of this thesis was happy to collaborate with other scientists on research directly and indirectly linked to the work presented in this dissertation. Below, there are conference and journal papers listed being the outcome of these cooperations. However, these works were excluded from the scope of this doctoral thesis.

Journal papers:

Kothari, A., **Rajczakowska, M.**, Buasiri, T., Habermehl-Cwirzen, K., & Cwirzen, A. (2020). Eco-UHPC as Repair Material—Bond Strength, Interfacial Transition Zone and Effects of Formwork Type. Materials, 13(24), 5778.

Tole, I., **Rajczakowska, M.**, Humad, A., Kothari, A., & Cwirzen, A. (2020). Geopolymer based on mechanically activated air-cooled blast furnace slag. Materials, 13(5), 1134.

Tole, I., Habermehl-Cwirzen, K., **Rajczakowska, M.**, & Cwirzen, A. (2018). Activation of a raw clay by Mechanochemical process—effects of various parameters on the process efficiency and cementitious properties. Materials, 11(10), 1860.

Humad, A. M., Provis, J. L., Habermehl-Cwirzen, K., **Rajczakowska, M.**, & Cwirzen, A. (2021). Creep and long-term properties of alkali-activated swedish-slag concrete. Journal of Materials in Civil Engineering, 33(2).

Ghasemi, Y., **Rajczakowska, M.**, Emborg, M., & Cwirzen, A. (2020). Shape-dependent calculation of specific surface area of aggregates versus X-ray microtomography. Magazine of Concrete Research, 72(2), 88-96.

Conference abstracts:

Rajczakowska, M., Habermehl-Cwirzen, K., Hedlund, H., & Cwirzen, A. (2019). Self-Healing Potential of Geopolymer Concrete. Multidisciplinary Digital Publishing Institute Proceedings, 34(1), 6.

Kothari, A., **Rajczakowska, M**., & Cwirzen, A. (2022). UHPC overlay as sustainable solution to preserve old concrete structures. *In International Conference on Concrete Repair, Rehabilitation and Retrofitting (ICCRRR 2022)*, Cape Town, South Africa, October 3-5, 2022. EDP Sciences.

Special publications:

Rajczakowska, M. (2019). Self-healing concrete (Licentiate thesis, Luleå tekniska universitet).

Cwirzen, A., **Rajczakowska, M.** (2022). Självläkning av betong – en dröm eller verklighet?. *Bygg & teknik*. nr 6-2022.

Rajczakowska, M., (2021). Kapitel 22.7:1 Självläkning av sprickor, *Betonghandbok Material del 2*, p. 614-618.

2

Literature review

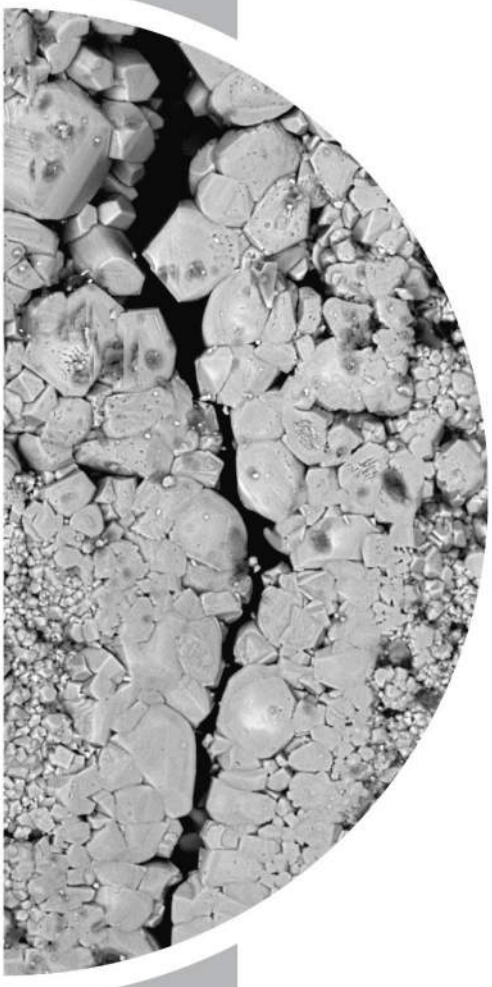

"I was taught that the way of progress was neither swift nor easy."

Maria Skłodowska
1903 Physics and 1911 Chemistry
Noble Prize Winner

2. LITERATURE REVIEW

In Chapter 2, the literature review on self-healing cementitious materials is performed. First, the basic definitions and principles are discussed. Then, self-healing approaches for cementitious materials are presented and compared, including autonomous methods (bacteria and capsule-based) and autogenous self-healing. Since this doctoral thesis focuses on the autogenous approach, a detailed analysis of factors influencing recovery efficiency is carried out based on the selected publications. Furthermore, the self-healing of thermally damaged concrete is described as an example of non-mechanical damage. Finally, the modeling progress in this field is evaluated.

2.1. SELF-HEALING PRINCIPLES

Healing injuries is critical for biological organisms and governs their longevity (Yang et al. 2015). Analogously, for synthetic materials, auto-repair of damage allows them to extend their service life without costly repairs and maintenance interventions. Self-healing materials "*exhibit the ability to repair themselves and to recover functionality using the resources inherently available to them*" (Blaiszik et al. 2010). Performance recovery is possible owing to the stimuli-responsive attributes of the materials (Yang and Urban, 2015). The sequence of self-healing starts with the trigger, e.g., mechanical damage. Afterward, similarly to biological organisms, the transport of healing substances toward the damage site occurs, and chemical/physical repair takes place (Blaiszik et al. 2010, Rajczakowska et al. 2019d). Up to now, self-healing properties have been designed for different materials, e.g., polymers (White, 2001; Li and Zuo, 2020; Sun et al., 2021), ceramics (Greil et al., 2020), metals (Ferguson et al., 2014), and concrete (De Belie et al. 2018).

The concept of self-healing was first introduced in polymer science in 1970 (Malinskii et al., 1970; Van Tittelboom & De Belie, 2013). Over the past decades, several different approaches have been explored, including capsule-based healing (Figure 2.1a), vascular networks (Figure 2.1b), and intrinsic healing (Blaiszik et al. 2010).

Capsules are small containers filled with a monomer released into the crack upon damage (Figure 2.1a). Subsequently, the substance polymerizes inside the crack after reaction with the catalyst, leading to the crack mending (White et al., 2001; Hager et al., 2010). The capsules provide a one-time use solution, i.e., once broken, the healing agent is consumed and cannot be refilled.

Vascular networks (Figure 2.1b) are interconnected hollow channels embedded in the material through which the healing material is transported. When a crack hits the wall of the channel, it breaks and releases the self-healing agent. Afterward, the network can be externally refilled with the healing substance, allowing for multiple healing, contrary to the capsules-based approach (Blaiszik et al. 2010)

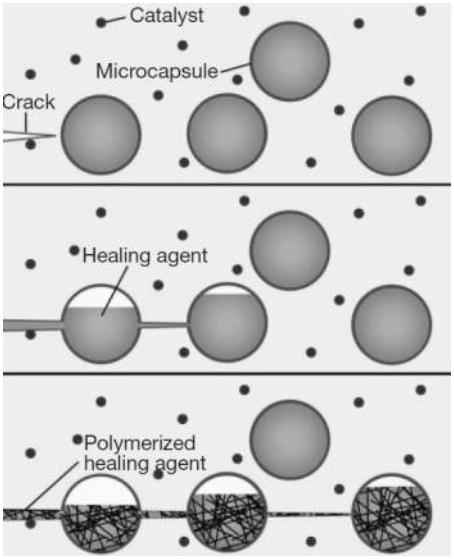

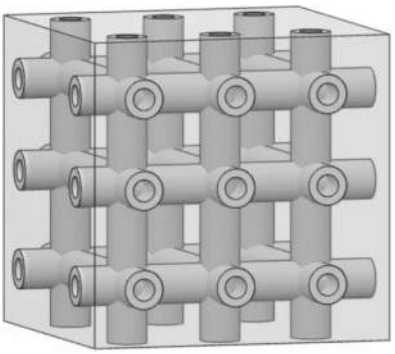

Figure 2.1. (a) The capsule-based approach of crack healing in polymers (White et al., 2001)[2]. (b) A schematic of the microvascular healing concept (Islam and Bhat, 2021).[3]

Capsule and vascular networks are autonomic self-healing methods requiring sequestered self-healing agents. On the other hand, intrinsic, i.e., autogenous, self-healing, requires only external triggers to succeed (Blaiszik et al. 2010). In addition, external and internal stimulators can increase the efficiency of the process.

2.2. SELF-HEALING CEMENTITIOUS MATERIALS

Concrete is a building material with high compressive strength but weak in tension. This behavior results in cracking, i.e., the formation of discontinuities in the hydrated binder matrix, which facilitates the ingress of aggressive substances into the material. As a result, concrete deteriorates, leading to durability issues and reinforcement corrosion, consequently hindering its structural performance. Several processes contribute to the deterioration, e.g., carbonation, alkali-aggregate reaction, sulfate attack, freezing, and thawing (Tang et al. 2015).

The maintenance and repairs related to concrete cracking are costly and time-consuming. Therefore, the development of cementitious materials capable of self-repair is of paramount importance. There are two major self-healing approaches for the self-healing concrete: autonomous (Figure 2.2bc) and autogenous self-healing (Figure 2.2a).

In the autonomous auto-repair, the self-healing components are specially designed external substances which are purposefully embedded in the concrete mix during casting, e.g., microcapsules or bacteria. On the other hand, the autogenous method assumes that the self-healing property stems directly from the standard concrete ingredients, i.e., hydrated

[2] Reproduced from (White et al., 2001) with permission from Nature Publishing Group.
[3] Reproduced from (Islam and Bhat, 2021), Creative Commons Attribution-Non Commercial 3.0 License

cement binder. Therefore, its efficiency can be improved by optimizing, e.g., mix composition and alternating environmental exposure.

During the past decade, many studies on autonomous self-healing have been published focusing on impressive self-healing efficiency obtained, primarily at the laboratory scale. Nevertheless, since concrete is a crude material with a harsh internal environment and high pH, self-healing methods designed initially for other types of materials, e.g., microcapsules, demonstrated considerable difficulties concerning concrete properties in the fresh and hardened state.

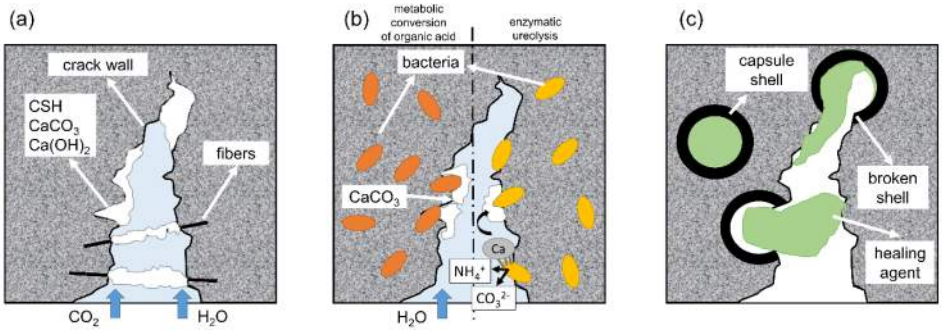

Figure 2.2. Approaches used for the self-healing of concrete: (a) autogenous self-healing, (b) bacteria-based autonomous self-healing (left – metabolic conversion mechanism, right – enzymatic ureolysis), (c) capsule-based autonomous self-healing (Rajczakowska et al. 2019a)[4]

The next subchapters discuss the principles of the concrete self-healing approaches, i.e., autonomous and autogenous self-healing. Bacteria and capsule-based healing is analyzed as autonomous methods. Vascular networks and shape memory polymers are excluded from this review. Finally, the limitations of both methods are compared concerning the original properties of concrete, upscaling, complexity, and price.

2.3. AUTONOMOUS SELF-HEALING

2.3.1. Bacteria-based approach

Sealing of cracks facilitated by bacteria was observed already in 1995 (Gollapudi et al. 1995). External application of bacteria-modified mortars for concrete repair was also studied (Orial et al., 2002; De Muynck et al., 2008; Van Tittelboom et al., 2010; Ramakrishnan et al., 2013). In the past decades, autonomous bacteria-based self-healing of concrete was explored (Jonkers and Schlangen, 2007; Jonkers et al., 2010; Tziviloglou et al., 2016).

[4] Reproduced from (Rajczakowska et al. 2019a) with permission from ASCE

Two mechanisms of bacterial auto-repair of cementitious materials were studied: metabolic conversion of organic acid (Figure 2.2b left) and enzymatic ureolysis (Figure 2.2b right). The former involves the transformation of a precursor compound, e.g., calcium lactate, into calcium carbonate according to the following reaction:

$$Ca(C_3H_5O_2)_2 + 7O_2 \rightarrow CaCO_3 + 5CO_2 + 5H_2O$$

Bacteria are the catalysts of this reaction, facilitating the cracks filling with the produced calcite (Jonkers, 2011). The superior effectiveness of the process, six times higher than autogenous self-healing, relies on the additional reaction of the produced carbon dioxide with the Portlandite inside the crack, resulting in the growth of calcium carbonate (Jonkers, 2007).

On the other hand, the principle of enzymatic ureolysis is the production of urease by bacteria following the reactions below (e.g., Van Tittelboom et al. 2010):

$$CO(NH_2)_2 + H_2O \rightarrow NH_2COOH + NH_3$$

$$NH_2COOH + H_2O \rightarrow NH_3 + H_2CO_3$$

$$H_2CO_3 \leftrightarrow HCO_3^- + H^+$$

$$2NH_3 + 2H_2O \leftrightarrow 2NH_4^+ + 2OH^-$$

$$HCO_3^- + H^+ + 2NH_4^+ + 2OH^- \leftrightarrow CO_3^{2-} + 2NH_4^+ + 2H_2O$$

In addition, the calcium ions from inside the crack are deposited on the surface of bacteria which act as nucleation sites (Figure 2.2 right). Calcium ions react with carbonates, resulting in the calcite precipitation as follows:

$$Ca^{2+} + Cell \rightarrow Cell - Ca^{2+}$$

$$Cell - Ca^{2+} + CO_3^{2-} \rightarrow Cell - CaCO_3 \downarrow$$

As in the case of metabolic conversion of organic acid, the self-healing phases sealing the crack are calcium carbonate compounds.

Bacteria can be placed in concrete directly or encapsulated in different materials, e.g., ceramsite (Chen et al. 2016) and lightweight aggregate (Tziviloglou et al. 2016), following the capsule-based approach (Section 2.3.2).

More up-to-date information regarding bacteria-based self-healing can be found in the comprehensive reviews, e.g. (Roy et al. 2020; Nodehi et al. 2022; Bagga et al. 2022).

2.3.2. Capsule-based approach

Autonomous self-healing of cementitious materials based on capsules involves embedding the healing agent into a small container to protect it from premature release before the damage occurs. The healing agent is discharged when the crack propagates through the capsule (Figure 2.2c). This process leads to sealing and blocking the crack propagation, resulting in permeability and strength recovery (Wang et al., 2017).

Three components play a significant role in the mechanism of capsule-based self-healing. First, the encapsulated chemical compound is the healing agent released to the crack. The most studied healing agents include epoxy resins (Han & Xing, 2016; Perez et al., 2015; Wang et al., 2017) and sodium silicate (Giannaros et al., 2016; Alghamri et al., 2016; Tan et al., 2016; Kanellopoulos et al., 2015,2016; Mostavi et al., 2015) or two-component polyurethane foam (Van Tittelboom et al., 2011; Hilloulin et al., 2015). Second, the capsule shell material, i.e., the protective coating, is designed to restrict the healing agent inside the capsule. Compatibility of different shell materials for concrete applications was tested, e.g., glass (Van Tittelboom et al., 2011; Qureshi et al., 2016), ceramic (Van Tittelboom et al., 2011), polymers (Kanellopoulos et al., 2016; Lv et al., 2016; Hilloulin et al., 2015) or lightweight aggregate (Sisomphon et al., 2011; Alghamri et al., 2016). Finally, the critical feature of the capsule-based approach is the release mechanism, i.e., the trigger, which leads to the damage of the capsule walls and the subsequent release of the healing agent. In cementitious materials, the cracks act as mechanical triggers. However, other release mechanisms were also proposed, e.g., sunlight (Zhu et al. 2023) and ultrasound (Song et al. 2022).

The current state of the art of capsule-based self-healing can be found in comprehensive reviews, e.g. (Huang et al. 2022).

2.4. AUTOGENOUS SELF-HEALING

Autogenous self-healing of cementitious materials involves solely the components typically used as concrete ingredients, e.g., hydrated binder or fibers (Figure 2.2a). It requires favorable environmental conditions for the process to be activated. The discovery of autogenous self-healing dates back to 1836 when white precipitates were noticed in the cracks of structures, such as retaining structures, culverts, and pipes, by researchers from the French Academy of Science (Wu et al., 2012). In the past decades, many studies focused on this phenomenon's efficiency and physicochemical background. Several processes were linked to the self-healing activity, e.g., dissolution of specific ions inside the crack, continuous hydration, deposition, and crystallization of healing phases (Hearn and Morley, 1997).

Since concrete constantly evolves concerning its mix composition and is applied under various environmental conditions, the physicochemical mechanism of autogenous self-healing is still under investigation. However, three major groups of self-healing processes were suggested, i.e., mechanical, physical, and chemical (De Rooij et al., 2013). Mechanical processes include blocking the crack with fine particles originating, e.g., from the crack surface. Physical processes are associated with the swelling of the hydrated binder inside the crack. On the other hand, the chemical mechanism involves ongoing hydration of unhydrated cement grains and calcite precipitation. The latter depends on several factors, such as temperature, the pH value, and the concentration of Ca^{2+} and CO_3^{2-} ions in the crack solution, and it can be described with the following chemical reactions (Edvardsen, 1999):

$$Ca^{2+} + CO_3^{2-} \leftrightarrow CaCO_3 \qquad (pH_{water} > 8)$$

$$Ca^{2+} + HCO_3^- \leftrightarrow CaCO_3 + H^+ \qquad (7.5 < pH_{water} < 8)$$

The sealing of the cracks is caused by the formation of different phases on the walls of the crack, i.e., crystal-like, consisting of mainly $CaCO_3$ and gel-like products, including calcium silicate hydrate (C-S-H) (Huang et al., 2013).

Autogenous self-healing is a time-dependent process (Huang et al., 2013) governed by many factors related to environmental conditions, mix composition, type of damage, or crack geometry (Figure 2.3), which makes it complex and somewhat unpredictable. For instance, the spatial distribution of the self-healing phases presumably depends on the distance from the surface; however, its mechanism and kinetics are not entirely explained (Gagné & Argouges, 2012; Sisomphon et al., 2012).

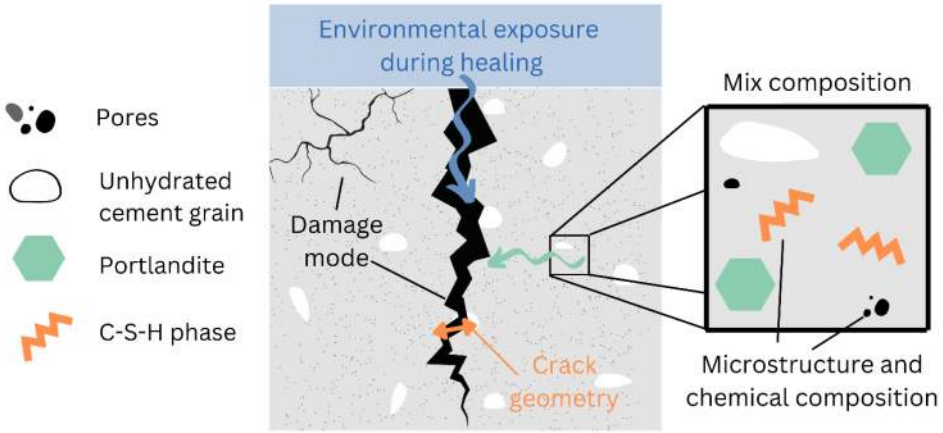

Figure 2.3. Factors affecting autogenous self-healing of concrete.

In the following sections, the influence of the main factors on autogenous self-healing is discussed.

2.4.1. Effect of crack geometry

Geometrical characteristics of the crack influence the crack sealing, consequently affecting the durability and strength recovery. Cracks widths above 200 µm were observed to heal faster because there was more space for the growth of the healing phases, and the transport of CO_2 and water was facilitated (Gagné & Argouges, 2012). However, the crack closure ratio was smaller for wider cracks than for the narrow ones, with the opening below 50 µm (Gagné & Argouges, 2012). In contrast, permeability tests demonstrated that the healing rate is higher for narrower cracks (Reinhardt and Jooss, 2003; Van Tittelboom et al., 2012). A similar observation was made for high-strength cementitious composites in case of a wider crack range, up to 600 µm (Tomczak and Jakubowski, 2018). The healing efficiency of the crack's widths above 300 µm in water exposure was below 20% (Gagné & Argouges, 2012). Maximum crack width of approximately 80 µm was closed entirely in the case of Engineered Cementitious Composites (ECC) with slag cured in wet/dry cycles. Crack width reduction ratio (Qiu et al., 2016; Tomczak and Jakubowski, 2018) and strength

regain (Hilloulin et al., 2016) negatively correlated with the initial maximum crack width. The calcite formation rate depended on crack width (Edvardsen, 1999).

Other crack geometry descriptors were used to describe the self-healing efficiency. The crack area demonstrated better responsiveness to the change of healing than the crack width parameter (Ahn et al. 2021). The average surface crack area correlated with the decrease in flow rate due to healing; however, a significant variation of results was obtained, possibly due to self-healing occurring deeper inside the crack but not on the surface (Roig-Flores et al. 2015). Limitation in the healable crack depth was noticed, suggesting that the self-healing takes place primality at the surface (Suleiman and Nehdi, 2018; Tomczak and Jakubowski, 2018). Crack tortuosity increased due to healing because of the formation of obstacles inside the crack (Hou et al., 2022).

Despite the proven effect of crack density and complexity parameters, e.g., tortuosity or surface roughness, on the transport properties of cementitious composites (Zhou and Pang, 2012; Akhavan and Rajabipour, 2012), there is little evidence linking these parameters to the healing efficiency.

2.4.2. Effect of mix composition

The mix composition of cementitious materials affects the self-healing efficiency and recovery mechanism. Therefore, the addition of Supplementary Cementitious Materials (SCMs) and mineral additives as potential self-healing stimulators was extensively studied (Table 2.1).

Table 2.1. Supplementary Cementitious Materials and mineral additives used for autogenous self-healing (Rajczakowska et al. 2019a)[5].

SCM/additions	References
Slag	(Alyousif et al. 2015; Darquennes et al. 2016; Huang et al. 2014; Hung et al. 2018; Jiang et al. 2015; Mehdipour et al. 2018; Olivier et al. 2016; Qian et al. 2009; Qiu et al. 2016; Ryou et al. 2015; Sahmaran et al. 2013; Sahmaran et al. 2015; Schlangen et al. 2006; Van Tittelboom et al. 2012)
Fly ash	(Alyousif et al. 2015; Herbert and Li 2013; Herbert and Li 2012; Hung and Su 2016; Hung et al. 2018; Kan and Shi 2012; Liu et al. 2017; Liu et al. 2017b; Ma et al. 2014b; Mehdipour et al. 2018; Na et al. 2012; Özbay et al. 2013; Qian et al. 2009; Ryou et al. 2015; Sahmaran et al. 2013; Sahmaran et al. 2015; Şahmaran et al. 2008; Sherir et al. 2016; Sherir et al. 2017a; Sherir et al. 2017b; Siad et al. 2015; Siad et al. 2017; Suryanto et al. 2016; Termkhajornkit et al. 2009; Van Tittelboom et al. 2012; Yildirim et al. 2014; Zhang and Zhang 2017; Zhu et al. 2012)
Lime	(Jo et al. 2015; Siad et al. 2015; Yildirim et al. 2014)
Silica	(Jiang et al. 2015; Nishiwaki et al. 2015; Ryou et al. 2015)
Metakaolin	(Ryou et al. 2015)

[5] Reproduced from (Rajczakowska et al. 2019a) with permission from ASCE

Crystalline admixtures	(Ahn and Kishi 2010; Ferrara et al. 2014a; Ferrara et al. 2016a; Jiang et al. 2014; Jiang et al. 2015; Jo et al. 2015; Qureshi and Al-Tabbaa 2016; Roig-Flores, M. et al. 2015; Roig-Flores, M. et al. 2016; Sherir et al. 2016; Sherir et al. 2017a; Sherir et al. 2017b; Siad et al. 2017; Sisomphon et al. 2012; Sisomphon et al. 2013)
Fibers	(Alyousif et al. 2015; Ferrara et al. 2016b; Ferrara et al. 2017; Herbert and Li 2013; Herbert and Li 2012; Homma et al. 2009; Hung and Su 2016; Kan et al. 2010; Kan and Shi 2012; Kim, D. J. et al. 2014; Liu et al. 2017; Liu et al. 2017; Ma et al. 2014; Mehdipour et al. 2018; Nishiwaki et al. 2012; Nishiwaki et al. 2014; Nishiwaki et al. 2015; Özbay et al. 2013; Roig-Flores et al. 2015; Sherir et al. 2017; Sherir et al. 2017; Siad et al. 2015; Sisomphon et al. 2013; Snoeck and De Belie 2012; Suryanto et al. 2016; Yang et al. 2011; Yildirim et al. 2014; Yu et al. 2010; Zhang and Zhang 2017; Zhu et al. 2012; Zhu et al. 2016)

The effect of basic mix parameters on self-healing was vague, suggesting high dependence of the self-healing process on other variables, such as the type and extent of damage, crack width, or environmental conditions. For the water-to-cement ratio range between 0.35 and 0.60, no clear relation was found between w/c and self-healing efficiency (Gagné & Argouges, 2012). In contrast, an increase in water to cement ratio from 0.4 to 0.5 negatively affected self-healing, presumably due to a smaller amount of unhydrated cement (Tittelboom et al., 2012). On the other hand, the effect of the amount of cement on the self-healing efficiency was inconclusive in the case of high-strength concrete (Tomczak and Jakubowski, 2018). Low w/c and high cement amount were potentially the causes of the successful strength recovery of Ultra-High-Performance Concrete (UHPC) (Hilloulin et al. 2016; Granger et al. 2007). The aggregate presence presumably negatively affected the calcite precipitation conditions (Edvardsen, 1999). On the other hand, the recycled aggregate seemed to affect autogenous self-healing positively, but the underlying mechanism was not known (Medjigbodo et al., 2018).

Replacement of cement with alternative binders was found to enhance the self-healing properties in most cases. The addition of fly ash or slag positively affected the self-healing of UHPC, with the most pronounced effect at an early age (7 days), presumably due to a pozzolanic reaction (Beglarigale et al. 2021). Alternative binders improved the self-healing due to ongoing hydration for smaller cracks; however, the strength recovery was minimal (Van Tittelboom et al. 2012). The positive effect of slag on self-healing appeared in several studies (Huang et al., 2014; Darquennes et al., 2016; Olivier et al., 2016). The ongoing hydration mechanism was suggested due to a slower hydration rate and a high amount of unhydrated binder. Cementitious materials with a high slag volume (66 wt%) demonstrated enhanced recovery; however, saturated calcium hydroxide solution was used as environmental exposure activating the process (Huang et al. 2014). A higher amount of fly ash replacement (27 wt%) increased the self-healing rate, possibly due to ongoing hydration (Amos Esteves et al. 2021). Ongoing hydration and pozzolanic action were suggested as the presumable explanation for the enhanced self-healing of mortars modified with 10 wt% silica fume, 30 wt% fly ash, and 50 wt% slag. A recent investigation of ternary cementitious materials, including slag and metakaolin, concluded that enhanced stiffness recovery could be achieved due to ongoing hydration and the formation of large quantities of healing

products (Namnoum et al. 2021). Nevertheless, the information on the self-healing of ternary and quaternary environmentally friendly binders is scarce since primary OPC and binary mixes were studied.

Crystalline admixtures (CA) and expansive additives added directly to the concrete mix enhanced the self-healing efficiency. The crack closure and water permeability change were evident, with the increased maximum healable crack width from 150 μm to 400 μm. (Sisomphon et al., 2012). The mechanism presumably involved increasing pH, which optimized the conditions for calcite precipitation (Sisomphon et al., 2012). A higher rate and efficiency of healing were achieved by adding CA to concrete (Ferrara et al. 2014; Roig-Flores et al. 2015). In addition, the reliability of the healing process was higher, with a lower variation of results (Roig-Flores et al. 2016). Recent metanalysis on the effect of crystalline admixtures (de Souza Oliveira et al. 2021) suggested that the self-healing boosting by CA depends on their type and the optimum mix composition; a dosage of up to 2% was efficient (de Souza Oliveira et al. 2021). Water was required for the self-healing to occur both with and without CA (Roig-Flores et al. 2015). Recently, steel fiber reinforced UHPC with slag and CA showed high mechanical performance recovery compared to the reference mix, despite the same crack closure (Cuenca et al. 2021). The possible synergistic effect between fibers and CA was hypothesized.

2.4.3. Effect of environmental conditions

Despite a high dependency of the healing process on environmental conditions, few studies considered exposure's effect on recovery efficiency and mechanism (Table 2.2).

Table 2.2. Previous studies on the effects of exposure on the efficiency of the autogenous self-healing of Portland cement-based materials (Rajczakowska, 2019d).[6]

Exposure type	Reference
Constant water immersion	(Qian et al. 2009; Qian et al. 2010; Yang et al. 2011; Şahmaran et al. 2013; Jiang et al. 2014, 2015; Suleiman and Nehdi, 2018)
Wet/dry cycles	(Qian et al. 2010; Yang et al. 2009; Yang et al. 2011; Kan and Shi, 2012; Qiu et al. 2016)
Temperature	(Reinhardt & Jooss, 2003; Suleiman and Nehdi, 2018).
Relative humidity	(Suleiman and Nehdi, 2018).
Freeze-thaw cycles	(Zhu et al. 2012; Şahmaran et al. 2013)
Sea water	(Palin et al. 2015; Danner et al. 2019)
Air/CO_2	(Qian et al. 2009; Qian et al. 2010; Şahmaran et al. 2013)
NaOH/dry cycles	(Qiu et al. 2016)
Saturated $Ca(OH)_2$ solution	(Huang et al. 2014; Huang & Ye, 2015)

For example, constant water immersion was found efficient exclusively for narrow cracks; however, only surface crack closure was evaluated (Qian et al. 2009; Qian et al. 2010; Yang et al. 2011; Şahmaran et al. 2013; Jiang et al. 2014, 2015). The flow of water negatively affected the healing, presumably decreasing the ion concentration inside the

[6] Reproduced from (Rajczakowska, 2019d), Creative Commons 3.0 License

crack (Jiang et al., 2015). Furthermore, an X-ray microtomography investigation concluded that there were no healing phases inside the cracks of cementitious exposed to water (Suleiman and Nehdi, 2018). No improvement was obtained by applying different temperatures and relative humidity cycles (Suleiman and Nehdi, 2018). In contrast, higher temperatures accelerated the self-healing reactions (Roig-Flores et al., 2016). On the other hand, in the case of Engineered Cementitious Composites (ECC), for crack width below 50 μm, cyclic water immersion enabled self-healing (Yang et al. 2009). Furthermore, dual kinetics of the recovery process was observed, i.e., fast during the first five curing cycles and then slowing down (Yang et al., 2009; Yang et al., 2011; Kan and Shi, 2012; Qian et al., 2010; Huang et al. 2014). Air exposure and freeze/thaw cycles did not promote self-healing (Şahmaran et al. 2013, Zhu et al. 2012; Qian et al. 2009, Qian et al. 2010). The presence of the additional ions in the water, e.g., seawater exposure, facilitated the healing process, with successful crack closure of crack widths up to 0.5 mm. Nevertheless, the strength was affected negatively (Palin et al. 2015).

The types of phases formed inside the healed cracks were generally independent of exposure conditions, consisting mainly of C-S-H (Kan and Shi, 2012; Şahmaran et al., 2013; Zhu et al., 2012), calcium carbonate and calcium hydroxide (Qian et al., 2009; Jiang et al. 2015; Kan and Shi, 2012; Şahmaran et al. 2013; Zhu et al. 2012). In cementitious materials with slag binder, various self-healing exposures governed the phase growth suggesting different mechanisms of action. For instance, water led to calcite formation due to carbonation, sodium hydroxide formed C-S-H by the alkali activation process (Qiu et al. 2016), while calcium hydroxide solution resulted in the growth of C-S-H, ettringite, hydrogarnet and OH–hydrotalcite inside the crack (Huang et al. 2014).

2.4.4. Effect of fiber addition

The potential positive effect of fibers on self-healing in water was already suggested in 1984. The formation of healing products of the interface between steel fibers and cement matrix was observed (Gray, 1984). Recent years brought impressive development in understanding the role of fibers in the self-healing process. Cementitious materials with fiber addition demonstrated enhanced self-healing behavior, e.g., ECC (Yang et al. 2009), Fiber Reinforced Cementitious Composites (FRCC) (Nishiwaki et al., 2012), and, lately, ultra-high-performance fiber-reinforced concrete (UHPFRC) (Moreira et al. 2022). Types of fiber material for self-healing concrete are summarized in Table 2.3.

Generally, the volume fraction of fibers added to concrete depends on the required effect. For instance, low and moderate amounts, between 0.2% and 1%, are added to control the plastic shrinkage cracking (Cuenca & Ferrara, 2017). On the other hand, fracture toughness and fatigue resistance can be boosted by using higher volumes of fibers, between 1% and 2%, as secondary reinforcement. The success of ECC is associated with their optimized design to achieve strain-hardening behavior, i.e., the ability to endure increasing loading and deformation after first cracking, thanks to the addition of fibers (Li, 1998). This bridging effect of fibers enables crack width control, forming many narrow cracks with widths below 100 μm.

Table 2.3. Types of fiber material for self-healing concrete (Rajczakowska et al. 2019a)[7].

Healing agent	Reference
Polyvinyl alcohol (PVA)	(Keskin et al., 2016) (Yang et al., 2009) (Sahmaran et al., 2013) (Yang et al., 2011) (Liu et al., 2017) (Siad et al., 2017) (Nishiwaki et al., 2012) (Nishiwaki et al., 2014) (Nishiwaki et al., 2015) (Snoeck et al., 2014) (Kan & Shi, 2012)
Ethylene vinyl alcohol (EVOH)	(Nishiwaki et al., 2012) (Nishiwaki et al., 2014)
Polyacetal (POM)	(Nishiwaki et al., 2012)
Polypropylene (PP)	(Sanjuan et al., 1997) (Nishiwaki et al., 2012)
Polyethylene (PE)	(Nishiwaki et al., 2014) (Homma et al., 2009)
Natural fibers	(Snoeck & de Belie, 2012) (Snoeck et al., 2015)
Steel	(Kim et al., 2014) (Nishiwaki et al., 2014) (Ferrara et al., 2016) (Homma et al., 2009)

The effect of fibers on the autogenous self-healing of cementitious materials is based on two mechanisms, i.e., crack width control and potential polarity of fiber material.

The former was observed for ECC under different environmental exposures (Yang et al., 2005; Zhang and Zhang, 2017) and mix compositions (Zhang et al., 2014). Furthermore, considering the high dependence of the self-healing efficiency on the initial crack width (Section 2.4.1), crack width reduction to values below 100 μm (Nishiwaki et al., 2014) or even 50-80 μm (Yang et al., 2009; Liu et al., 2017; Siad et al., 2017; Kan & Shi, 2012) significantly facilitates the strength and durability recovery.

On the other hand, a boosting effect related to the polarity of the fibers was observed in some cases. Such fibers, the polyvinyl alcohol (PVA), exposed inside the crack become nucleation sites for calcium ions and promote the formation of the self-healing phases (Nishiwaki et al., 2012). Higher self-healing efficiency was obtained for the specimens containing PVA fibers compared to the polypropylene (PP) fibers, which did not demonstrate polarity (Nishiwaki et al., 2012; Choi et al., 2016). Due to their hydrophilic character, natural fibers also boosted the recovery of cementitious materials, assisting the formation of calcium carbonate crystals (Snoeck, 2015). C-S-H and calcium carbonate were found inside the cracks of fiber-reinforced cementitious materials (Keskin et al., 2016;

[7] Reproduced from (Rajczakowska et al. 2019a) with permission from ASCE

Yang et al., 2009; Sahmaran et al., 2013; Yang et al., 2011; Liu et al., 2017; Kan & Shi, 2012).

2.4.5. Effect of non-mechanical damage

Cementitious materials exhibit autogenous self-healing properties when subjected to both mechanical and non-mechanical types of deterioration. The former occurs when the structure is subjected to, e.g., compression, tension, or bending, and cracks occur upon reaching the material's strength limit (Yao et al., 2012). In this case, the chemical composition of the material is stable, with cracking being an "inhomogeneity" introduced into its microstructure. The self-healing mechanism of the mechanically induced cracks depends on several variables, e.g., binder composition (Rajczakowska et al., 2019; Sahmaran et al., 2013), age and healing time (Tomczak & Jakubowski 2018), initial crack width (Reinhardt & Jooss, 2003), environmental exposure (Rajczakowska et al., 2019c; Suleiman & Nehdi, 2021), or the presence of fibers (Nishiwaki et al., 2012). Two major processes contribute to the sealing of the cracks, i.e., continued hydration of the unhydrated cementitious binder and calcium carbonate formation (de Rooij et al., 2013; Huang et al., 2021). Partial strength and durability recovery can be achieved as a result of cracks being filled with self-healing products, i.e., a mixture of calcium silicate hydrate (C—S—H), calcium carbonate, and calcium hydroxide (CH) (Zhang et al., 2020).

On the other hand, the non-mechanical type of loading includes durability-related damage such as chemical attacks, e.g., carbonation, chloride ingress, sulfate attack, alkali-aggregate reaction (AAR), or physical actions, e.g., freeze and thaw and high-temperature exposure (Yao et al., 2012). These processes cause cracking and chemical alterations of the cementitious binder, potentially leading to a more complex self-healing mechanism. However, there is limited data on the relation between the non-mechanical loading and the self-healing process.

Concrete exposed to a marine environment, i.e., a mixture of chloride and sulfate ions, partially sealed the cracks below 200 μm (Tian et al., 2022). The impurities from the seawater blocked the crack, obstructing the self-healing process. Brucite, dolomite, and calcite were found in these cracks (Tian et al., 2022). Chloride exposure did not alter the self-healing mechanism for ordinary Portland cement and 50 wt% of slag mortars unless magnesium sulfate was present in the solution (Maes et al., 2016). Compared to water treatment, exposure to sulfates and chlorides enhanced the self-healing activity of the ECC (Liu et al., 2017). Major self-healing products were ettringite and gypsum. Nevertheless, due to its microstructure with a narrow crack width of approximately 50 μm, the material was only moderately affected by the chemical attack with slight deterioration (Liu et al., 2017). ECC with slag and fly ash also demonstrated good strength recovery under chloride and marine tidal exposures (Shumuye et al., 2022). Healing of the cracks caused by the AAR and refined porosity was observed for mortars subjected to cyclic water immersion (Munhoz et al., 2021). Freeze and thaw cycles, with water as the freezing medium, enhanced the self-healing more than when de-icing salts were used (Zhu et al., 2012).

2.5. AUTOGENOUS VS. AUTONOMOUS SELF-HEALING

Autogenous and autonomous methods were compared concerning their effect on fresh and young concrete properties, hardened concrete properties, efficiency, price, and full-scale applicability. The critical analysis based on the available literature was presented in detail in Paper I (Rajczakowska et al. 2019a). In this doctoral thesis, only a summary of this investigation is shown. It should be mentioned that the scope of the review was based on the literature available until 2019. The limitations of each self-healing method have been listed in Table 2.4 (Rajczakowska et al. 2019a).

Table 2.4. Summary of the limitations of autonomous and autogenous self-healing strategies (Rajczakowska et al. 2019a).[8]

Area	Autonomous self-healing methods	Autogenous self-healing methods
Fresh and young concrete	• Low survival rate of capsules and bacteria during the mixing process, • Loss of workability with increased number of capsules • Bacteria nutrients slow down or even completely hinder hydration of Portland cement leading to lower strength values	• Loss of workability due to fibers • Higher amount of cement resulting in an increased hydration heat, higher shrinkage, an increased crack risk • Problems with proper fiber dispersion and sensitivity to the mixing process • Insufficient fiber-matrix bond
Hardened concrete	• Glass capsules increase the risk of alkali-silica reaction • Material incompatibility between the capsule shell and the binder matrix results in a negative alteration of the microstructure and chemical composition of the surrounding binder matrix • The increase in the volume fraction of capsules, decreases the compressive strength and the fracture toughness of the matrix • Reduction of the Young's Modulus of elasticity of the binder matrix due to a lower Young's Modulus of the capsule material as well as the presence of voids left by ruptured capsules • Higher volume fraction of bacteria leads to a strength loss • SAP application greatly decreases the strength of concrete	• The hydrophilic nature of PVA fibers causes their premature rupture under tension, • The use of fly ash decreases the compressive strength
Efficiency	• Too low stresses created by the forming crack are not able to break the capsule shell • Capsules with switchable properties of the shell are often not brittle enough to be broken by the forming crack • Premature polymerization of the healing agent inside the capsule due to contact with moisture lowers the probability and effectiveness of the healing process • Lack of water and oxygen hinders the healing process in the case of bacteria-based systems	• Age of the specimen at cracking has a great influence on the healing efficiency • The healing process might take several days/weeks • Exposure conditions might be a limitation for the healing to occur • Only limited crack widths can be fully healed

[8] Reproduced from (Rajczakowska et al. 2019a) with permission from ASCE

	• Capsules might be debonded from the surrounding matrix causing crack formation around it instead of breaking the capsule • The high viscosity of the healing agent can cause problems with efficient penetration of the crack • The total maximum volume fraction of capsules is limited due to workability issues and loss of strength which leads to a lower healing efficiency • Chemical interaction between epoxy and hardener or bacteria with nutrient can hinder the healing process	
Price and full scale	• Very high price in comparison to the methods used for autogenous healing • Difficult to apply on the full scale	• Higher CO_2 footprint due to higher amount of binder

2.6. SELF-HEALING OF THERMALLY INDUCED CRACKS

One example of non-mechanical loading which affects the potential self-healing of cementitious materials is exposure to high temperature, e.g., a fire. Concrete subjected to a high temperature undergoes drastic physical and chemical changes, including a gradual disintegration of all the major phases (Li et al., 2020). Ettringite decomposes at approximately 90ºC, followed by the disappearance of C-S-H gel between 200ºC and 450ºC and the transformation of Portlandite into lime at approximately 530 – 560ºC (Castellote et al., 2004). After cooling, the moisture from the air is absorbed, leading to the reaction of CaO to form calcium hydroxide and larnite (Ca_2SiO_4) (Castellote et al., 2004). Water evaporation causes cracking and coarsening of porosity, which leads to strength and durability deterioration (Poon et al., 2001; Rajczakowska et al., 2022).

Properties of concrete subjected to high-temperature loading can be partially self-healed by exposure to re-curing treatments, i.e., environmental stimulators. Several processes are speculated to contribute to this auto-repair, e.g., rehydration of disintegrated phases and sealing microcracks with self-healing products. However, the effect of different variables on the recovery process is still not fully understood. For instance, the effect of basic material properties was found inconclusive. Some studies reported a lack of dependence of the self-healing on the binder-related parameters, such as cement amount (Li et al. 2017) or mix composition (Lin et al. 2011). On the other hand, adding SCMs was important, however, with varied results (Poon et al., 2001; Mendes et al., 2011; Ming et al., 2020). FA enhanced the recovery, whereas slag (S) had a negative effect (Mendes et al., 2011). The synergy between calcium carbonate whisker (CW) and FA was identified (Ming et al., 2020). High-strength concrete was found to be more efficient, and the dense microstructure was indicated as one of the causes (Henry et al., 2011; Poon et al., 2001). A combination of cooling and the re-curing process was found to be necessary for the self-healing activation. In general, water re-curing together with air cooling led to better self-healing performance than air alone (Akca & Özyurt, 2018; Henry et al., 2011; Lin et al., 2011; Poon et al., 2001). On the other hand, water cooling resulted in rapid deterioration due to expansion presumably caused by the reaction of lime with water (Mendes et al.,

2011; Poon et al., 2001). Despite the significant dependency of the thermally cracked concrete self-healing on the re-curing conditions, only two major types of treatments were studied, i.e., involving exposure to air or water (Rajczakowska et al. 2023a). A summary of different studies on the recovery of high-temperature damage is presented in Table 2.5.

Table 2.5. Examples of self-healing performance of different fire-exposed cementitious materials (FA – fly ash, GGBFS – granulated ground blast furnace slag, OPC – ordinary Portland cement, MK – metakaolin, SF – silica fume) (Rajczakowska et al. 2022)[9].

Reference	Loading temperature (ºC)	Binder type	Additives/ fibers	Type of cooling and re-curing	Self-healing performance
(Poon et al. 2001)	600, 800	OPC, SF, F-type FA, GGBFS, MK; concrete	-	Air cooling and water re-curing Air cooling and air re-curing (with 2h water pre-soaking)	Blended binders have better mechanical and durability recovery than pure OPC Water re-curing and lower loading temperature lead to efficient self-healing High-strength concrete had a better recovery than normal-strength concrete
(Henry et al. 2011)	550	OPC; normal and high-strength mortars	-	Air-cooling and re-curing Water cooling and re-curing	Water re-curing exposure gave the highest strength and durability recovery
(Karahan, 2011)	400, 600, 800, 1000	OPC; mortar	-	Furnace cooling and air re-curing Room cooling and air re-curing Water cooling and air re-curing	Air (furnace/room) cooling and air-recuring caused further compressive strength reduction Water cooling and air-recuring lead to strength recovery
(Lin et al. 2011)	400, 500, 600, 800, 1000	OPC; concrete	-	Air cooling and water re-curing Air cooling and air re-curing	Higher strength recovery for water re-curing. Mix proportions did not have a significant effect on the healing performance
(Mendes et al. 2011)	400, 800	OPC, GGBFS, concrete	-	Furnace cooling and room re-cuing Water cooling and room re-curing	For 800ºC one week of furnace-air and water-air treatment resulted in no healing Water cooling caused additional damage GGBFS showed worse performance after 800 ºC
(Li et al. 2017)	800	OPC + F-type FA; concrete	-	Air-cooling in the furnace and	Better recovery for furnace-cooled specimens

[9] Reproduced from (Rajczakowska et al. 2022), Creative Commons Attribution-NonCommercial-NoDerivatives 3.0 License

				water/ RH of 95% re-curing Air-cooling in room conditions and water/ RH of 95% re-curing	The amount of cement did not affect the healing
(Akca and Özyurt, 2018)	1000	OPC, GGBFS, F-type FA; concrete	Steel fibers, polypropylene fibers	Air cooling and re-curing Air cooling and water re-curing	Cracks healed with $CaCO_3$ and increased mechanical properties in water re-cured samples Air re-curing gave negative results
(Ming et al. 2020)	200, 400, 800	OPC, FA	calcium carbonate whisker (CW)	Furnace cooling and water re-curing	CW improved the mechanical performance recovery at 400 and FA at 800ºC The synergistic effect of CW and FA on self-healing was observed

2.7. MODELING OF AUTOGENOUS SELF-HEALING

The research on cementitious materials, as in other areas of material science, evolves according to four paradigms of science (Figure 2.4), i.e., empirical, theoretical, computational, and data-driven science (Agrawala and Choudhary, 2016; Li et al., 2022). Many studies on autogenous self-healing of cementitious materials use trial-and-error experiments (De Rooij et al., 2013), following the first paradigm (Figure 2.4). Even though the self-healing concept has been around for decades, it is still relatively new. Concrete is a heterogeneous composite with high complexity arising from infinite mix combinations, novel binder chemistry, and variation of physical properties (Li et al. 2022, Van Damme 2018; Scrivener et al. 2008). Considering the multi-variability of the self-healing process, there is limited experimental data available that covers all aspects of autogenous self-healing. Nevertheless, developing an accurate self-healing model would not only facilitate understanding of the self-healing mechanism but also lead to savings on the expensive experimental campaigns.

There were few attempts to explain the relationship between the concrete microstructure vs. the self-healing properties with the application of theoretical science, e.g., the hydration, morphology, and structural development model (HYMOSTRUC) (Huang and Ye, 2012; Huang et al., 2013), following the second paradigm of science (Figure 2.4). With the increasing availability of computational power, the models were expanded using numerical simulations (Figure 2.4, third paradigm), e.g. (Di Luzio and Cusatis, 2013) (Chen and Ye, 2019). In recent years, as an auxiliary direction, machine learning (ML) predictions (Figure 2.4, fourth paradigm) emerged. This type of modeling can identify trends and patterns on large datasets, considering multiple variables and nonlinear relations while maintaining high accuracy. The following sections present a brief overview of autogenous self-healing models, including mechanically and thermally damaged concrete.

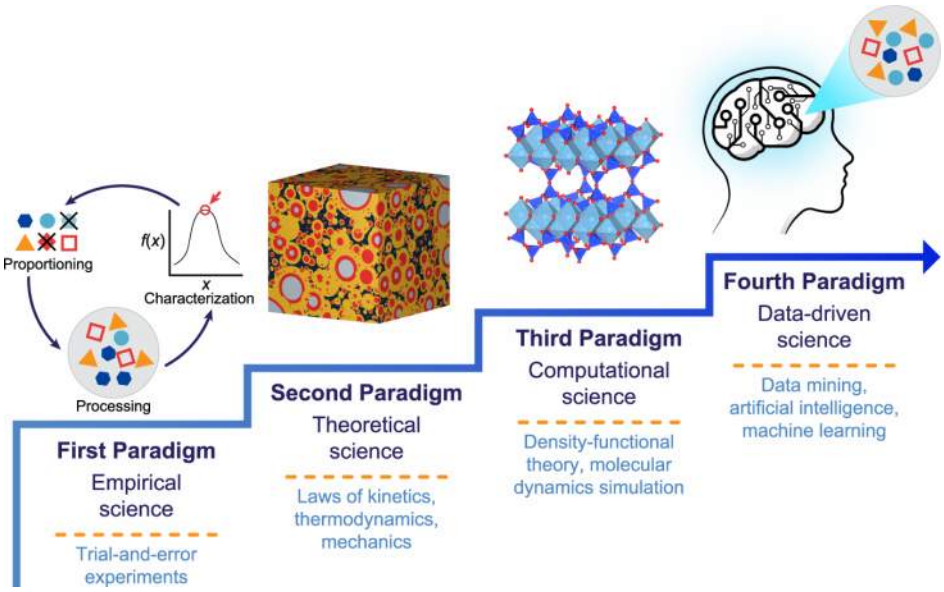

Figure 2.4. The four paradigms of concrete science, i.e., empirical, theoretical, computational, and data-driven (Li et al. 2022); modified from (Agrawala and Choudhary, 2016)[10]

2.7.1. Theoretical models

A 2D reactive transport model based on thermodynamics theory as well as water transport and ion diffusion theory, were used to model self-healing by ongoing hydration (Huang and Ye, 2012; Huang et al., 2013). The simulation was done by HYMOSTRUC software. First, the amount of self-healing products was calculated using thermodynamics modeling (Figure 2.5). Then, the amount of extra water necessary for efficient self-healing was also calculated (Huang and Ye, 2012). Later the model was also extended to 66wt% slag cement (Huang et al. 2014) Effect of carbonation on self-healing was studied using thermodynamic modeling. Finally, the crack-filling kinetics analysis was performed. Mechanical recovery of the material was not considered.

An analytical model linking the macro-scale cracking pattern with the mesoscale stiffness recovery of a single crack was developed for ECC (Ma et al. 2019). The predicted macro-scale stiffness recovery was compared with the experimental values of the composite stiffness. The model successfully predicted the self-healing of ECC at any strain (Ma et al. 2019).

[10] Reproduced from (Li et al. 2022; modified from (Agrawala and Choudhary, 2016), Creative Commons license Attribution 4.0 International (CC BY 4.0)

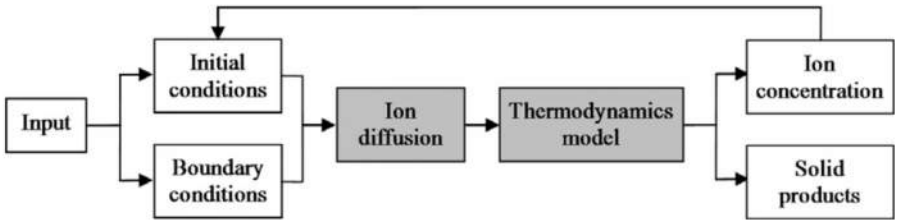

Figure 2.5. Further hydration model scheme by (Huang and Ye, 2012)[11]

There is scarcely any data on concrete's high-temperature damage recovery modeling. Mechanical properties recovery was predicted with a theoretical model based on the stress-strain curves fitting (Neto et al. 2022). The model was applied for cement-lime masonry mortars, and a good agreement with experimental results was observed. A complex multi-scale modeling framework was proposed considering carbonation, de-carbonation, and re-carbonation processes (Iwama and Maekawa, 2022). The model could predict the compressive and tensile strength after high-temperature loading and subsequent healing by exposure to different relative humidity levels. It is worth noting that presently American Concrete Institute (ACI, 2007) and Eurocode codes (2004) consider the performance of concrete after a fire. Unfortunately, the models do not include the cooling and curing conditions (Alhamad et al., 2022).

2.7.2. Computational simulations

A simulation of the mechanism of self-healing by ongoing hydration of unhydrated cement nuclei (UCN) was proposed by He et al. (2007, 2009). A concurrent algorithm-based computer simulation system called SPACE (Software Package for the Assessment of Compositional Evolution) was used. The random spatial distributions of different numbers of UCNs were generated, and cracks with different widths were simulated. The area fraction of the UCNs "crossing" the propagating crack suggested the healing capacity. The maximum healable crack was calculated and correlated with cement properties, e.g., fineness. Power's hydration model was applied for the prediction (He et al., 2009; Jensen and Hansen, 2001).

Similarly, models were formulated which allowed for the calculation of the self-healing efficiency based on the ongoing hydration mechanism, applying different cracking modes: the splitting crack mode (Lv and Chen, 2012, Figure 2.6) and dome-like crack mode (Lv and Chen, 2013). The same assumptions were made in the case of another study by (He et al. 2009). The amount of unhydrated cement and UCN particle size distribution were the most influential factors.

[11] Reproduced from (Huang and Ye, 2012) with permission from Elsevier

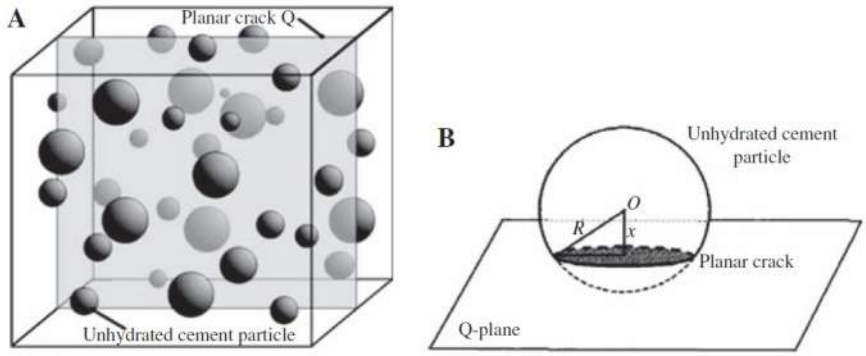

Figure 2.6. The scheme of a splitting crack mode: (A) UCN intersected by crack plane; (B) single UCN split by the crack plane. (Lv and Chen, 2012)[12].

Water penetration in cement paste was predicted using the moisture transport numerical model based on the finite difference method (Huang et al. 2010). It was observed that the penetration increases with the presence of cracks. The model did not explicitly address the self-healing process; however, it gave bases for the analysis of crack water penetration.

A hydro-chemo-mechanical model for predicting mechanical recovery was developed for UHPC using the finite element method (Hilloulin et al. 2014). It was concluded that a significant mechanical performance recovery could be attributed to a relatively small crack closure if the filling material exhibits mechanical properties close to the intact specimen.

Self-healing by calcite precipitation in ECC was studied with chemical-diffusive modeling (Aliko-Benítez et al. 2015) and the finite element method. A simulation of the self-healing of a water-immersed large-scale concrete structure was successfully performed.

The SMM (Solidification-Microprestress-Microplane) model M4 (Di Luzio and Cusatis, 2013) numerical model was used to predict mechanical property recovery (Di Luzio et al. 2018) Ongoing hydration mechanism was studied with a high prediction accuracy; however, the model had some limitations, e.g., it neglected the effects of calcium leaching and dissolution.

Both crack closure and geometrical changes were simulated using the Lattice Boltzmann single-component model supported by thermodynamics (Chen and Ye, 2019). An ongoing hydration mechanism was considered; however, no mechanical recovery was considered, only with respect to the crack closure. It was demonstrated that full crack closure could occur in some places inside the crack without affecting the overall crack closure in a significant way.

[12] Reproduced from (Lv and Chen, 2012), copyright 2012 by Walter de Gruyter, Creative Commons 3.0

2.7.3. Data-driven modeling

There were few attempts to address the autogenous self-healing of cementitious materials using machine learning and artificial intelligence.

An artificial neural network (ANN) with a hybrid genetic algorithm was used to predict crack closure due to autogenous self-healing (Suleiman and Nehdi, 2017). Eleven input variables were considered: cement content, water-to-cement ratio, type and dosage of supplementary cementitious materials, bio-healing materials, and expansive and crystalline additives. As a result, the high accuracy of the model was achieved, with a coefficient of determination R^2 equal to 0.99762 (Suleiman and Nehdi, 2017).

Another approach compared six different ML algorithms to predict healing performance measured by crack width and resonance frequency changes (Huang et al. 2021). The following methods were used: ANN, a k-nearest neighbor, a decision tree regression, a support vector regression, and ensemble models: a gradient boosting regression and a random forest. An extensive database of 1417 measurements was built based on a literature study. Sixteen features were considered, such as type and dosage of healing material, fiber diameter, length, and tensile strength, the initial cracking data and initial cracking width, the time for healing, the healing condition (environmental exposure), the amount and type of cement, the amount of superplasticizer, fine aggregates, fly ash, slag, and the water-binder ratio. The highest accuracy (R^2=0.958) was obtained for the ensemble GBR model (Huang et al. 2021).

The ensemble methods, i.e., AdaBoost, bagging, and stacking, were used to increase the prediction accuracy of ML algorithms for the modeling of self-healing of ECC based on the final crack width (Chen et al. 2022). As a result, all algorithms demonstrated low error and reasonable accuracy (R^2 above 0.85). Nevertheless, only four input variables were selected, i.e., initial crack width, fly ash, silica fume, and hydrated lime powder (Chen et al., 2022).

An interesting combination of meta-analysis and ANN modeling was proposed by (Gupta et al. 2021). Six input variables were studied, i.e., cement and SCM amounts, fiber content, w/c ratio, crack width, and healing time. Contrary to the other studies which focused on crack closure, here, the self-healing index was considered the model's response, considering both durability and mechanical performance recovery. In addition, the self-healing mix optimization graphs were suggested. Nevertheless, a relatively low R^2 value was achieved, approximately 0.77, for the validation and testing set.

Despite a relatively large amount of data on recovery of high-temperature damage, no attempts have been made to apply data-driven modeling for this type of self-healing.

2.8. MACHINE LEARNING ALGORITHMS

Understanding and designing synthetic materials relies on four major components: processing, structure, properties, and performance (PSPP) (Olson, 1997). Science follows the "forward" cause-and-effect path, from processing to performance, whereas engineering – the "inverse" goals and means flow. Scientific observations and results of experiments, e.g., measurement of properties based on material composition, can be used to build forward models to predict material performance. On the other hand, the inverse models can maximize the material's performance by finding the most optimal composition/structure (Agrawala and Choudhary, 2016). The inverse models can also be used for materials discovery, e.g., implementation into the experimental workflow (Figure 2.7).

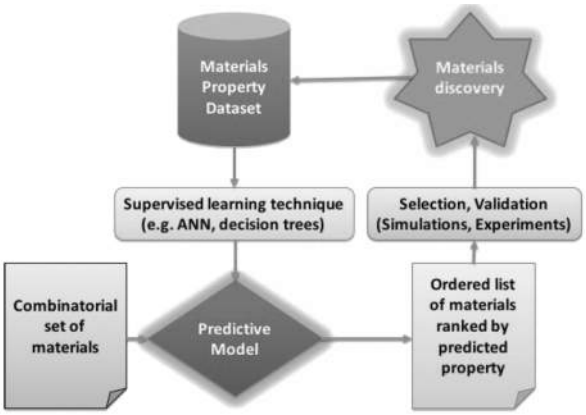

Figure 2.7. An example of an inverse model following the PSPP approach (Agrawala and Choudhary, 2016)[13]

The forward prediction, based on a large material dataset obtained, e.g., from the available literature, can be used as an inverse model to find possible nonlinear dependencies or identify factors having a significant effect on the performance. Based on the analysis, new experiments can be designed to confirm the hypothesis. Those newly generated results can then be added to the database to develop a revised version of the forward predictive model (Figure 2.7).

Machine learning tools are often applied to create a data-driven forward PSPP model as they allow for regression analysis and high-accuracy predictions on large datasets with multiple input variables. In the following subsections, several ML algorithms applied within the scope of this study are shortly described. This section was redrafted from (Rajczakowska et al., 2023a).

[13] Reproduced from (Agrawala and Choudhary, 2016), Creative Commons license Attribution 4.0 International (CC BY 4.0)

2.8.1. Artificial neural networks

Artificial Neural Networks are computing systems inspired by and strive to mimic the working of a human brain - a subset of machine learning and the main field of study for deep learning (Paruelo & Tomasel, 1997). It is a supervised learning technique commonly used for a wide range of problems for classification and regression. A basic network, called the feedforward net, consists of several fully connected layers. These are the input layer (with input variables), one or more hidden layers, and the output layer, interconnected by axons representing weights for each input connection together with the so-called biases, i.e., the deviation between weights (Strieth-Kalthoff et al., 2020).

2.8.2. Regression tree and an ensemble of trees

A decision tree is a non-parametric supervised learning algorithm used to generate a predictive model for classification and regression tasks. As the name suggests, it has a hierarchical, tree-like structure consisting of a starting root node, which may branch out to multiple nodes. Eventually, each branch ends up in a terminal node, referred to as the leaf node. It is very popular due to its ease of use and interpretability (Yang et al., 2017).

An ensemble regression tree is a combination of several individual regression trees. The objective is to increase the model's predictive performance, compared to individual trees, by using the "wisdom of crowds" principle (Strieth-Kalthoff et al., 2020). Regression analysis achieves better prediction accuracy by taking the average vote from multiple decision trees. As a result, it performs very well in classification and regression tasks; however, it is characterized by computational complexity.

There are two general ensemble algorithms, i.e., bagging and gradient boosting. The former is constructed tree-by-tree, whereas the latter is iteratively (Strieth-Kalthoff et al., 2020).

2.8.3. Support Vector Machines

Support Vector Machines, developed by Vapnik on statistical learning theory (Vapnik, 1999), are supervised learning models that can be applied to classification and regression tasks. This technique aims to find the most optimal hyperplane that offers the greatest margin between the support vectors – the data points at the edge of the different classes (Asteris et al. 2021). Data are compared using Kernel functions, usually nonlinear (Strieth-Kalthoff et al., 2020). The algorithm offers high accuracy and low generalization error. SVM for regression problems uses an alternative ε-insensitive loss function. Details regarding this method can be found in (Vapnik, 1999; Vapnik, 1999).

2.9. SUMMARY

In Chapter 2, a literature review was performed to describe briefly the concepts related to the self-healing of cementitious materials and determine the research gaps.

The following main conclusions/research gaps were established based on Chapter 2 and Paper I:

- Autogenous self-healing, based on usual concrete ingredients, seemed cheaper, easier, and safer than autonomous methods when analyzing typical requirements of current concrete technology. Therefore, concerning the actual structural applications, autogenous self-healing is a better solution for concrete.
- There are elements of the autogenous self-healing mechanism which are not fully understood. For instance, the effect of basic mix parameters, e.g., cement amount, is still inconclusive. Therefore, the underlying physicochemical processes should be studied in search of relations between microstructural parameters/chemical composition and self-healing efficiency.
- With the continuous evolution of environmentally friendly binders, there is a need to verify the effect of multiple SCMs on self-healing properties.
- Majority of research on autogenous self-healing deals with mechanical loading. However, durability-related issues are an important cause of damage in concrete. In addition, there is scarce data on the relationship between self-healing and non-mechanical loading, including high-temperature exposure.
- The efficiency of the autogenous self-healing is limited to a narrow crack range and does not assure the healing of the crack at depth or mechanical strength recovery. The potential commercial success of this method requires further studies of novel stimulators.
- Data-driven modeling appears to be a promising direction for accurately predicting self-healing properties. However, despite a relatively large amount of data on the recovery of high-temperature damage, no attempts have been made to apply machine learning for this type of self-healing.

3

Mechanically induced cracks

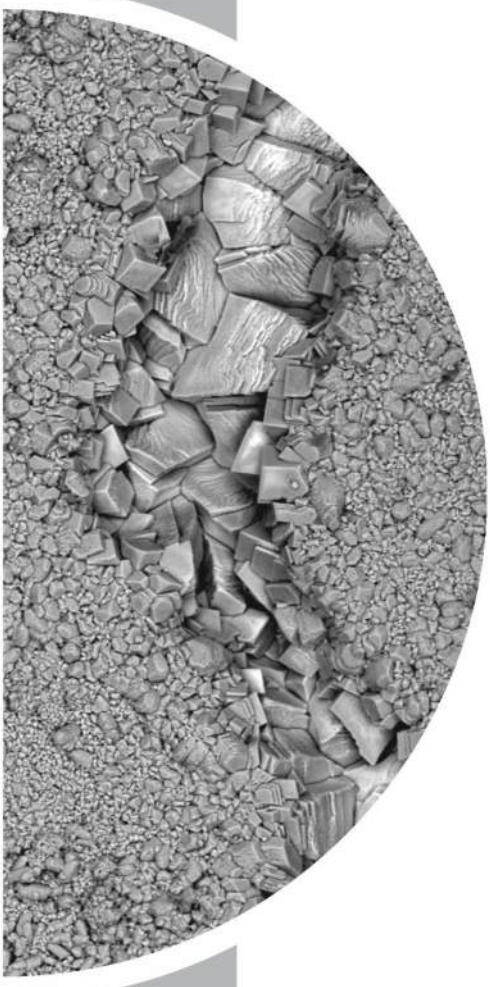

"A dream will always triumph over reality, once it is given the chance."

Stanisław Lem
Polish writer

3. MECHANICALLY INDUCED CRACKS

In Chapter 3, the autogenous self-healing of mechanically induced cracks is studied. The methodology is presented in Figure 3.1. The goal of the initial studies (*Study A*) was to confirm the self-healing efficiency dependence on the amount of unhydrated cement particles. Therefore, the UHPC was investigated, due to its high amount of cement and low water-to-cement ratio, resulting in a large amount of unhydrated binder. In addition, several elementary variables possibly affecting the healing process were studied: type of cement, healing duration, and age at cracking. Based on the preliminary evaluation and within the context of literature, the self-healing mechanism was suggested, and features possibly hindering the efficiency of the process were identified (Obstacles 1 and 2, Figure 3.1). These elements determined further experimental setup, including *Studies B* and *C*. In *Study B*, the effect of exposure conditions on the self-healing of cement mortars was investigated, focusing on overcoming Obstacle 1. On the other hand, *Study C* investigated the effect of mix composition-related parameters on the auto-recovery process to address Obstacle 2.

Chapter 3 describes the materials and methods (Section 3.1) and analysis of the obtained results (Section 3.2.). The results are divided into subchapters (Sections 3.2.1-3.2.6) representing the factors related to the self-healing mechanism, i.e., healing time, cracking age, exposure conditions, mix composition, crack geometry, and initial microstructure of the material. A thorough discussion of the results and their implications regarding the proposed mechanism is presented in Chapter 5.

Chapter 3 was redrafted based on (Rajczakowska et al. 2019bc) and (Rajczakowska et al. 2023b).

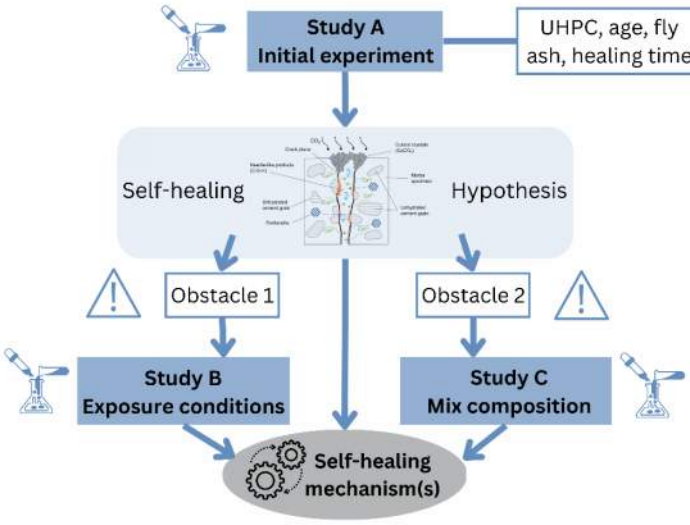

Figure 3.1. The overview of the methodology used in Chapter 3.

3.1. EXPERIMENTAL SETUP

3.1.1. Materials

Mortars and pastes were prepared using ordinary Portland cement (OPC) produced by Cementa (Skövde, Sweden). In *Study A*, two types of cement were used, i.e., CEM I 42.5 N and CEM II/A-V 52.5 N commercial blend with approximately 20% of fly ash included. In *Studies B* and *C,* only CEM I 42.5 N was applied. The chemical composition of the types of cement is listed in Table 3.1.

Table 3.1. Chemical composition of the applied types of cement (Rajczakowska et al. 2019b), fly ash (FA), and blast furnace slag (S) (Rajczakowska et al. 2023b).

	Study A, B, C	*Study A*	*Study C*	
Chemical analysis	**CEM I 42.5 N**	**CEM II/A-V 52.5 N**	**FA**	**S**
	Mean value (%)			
CaO	63.30	57.1	1.37	38.5
SiO_2	21.20	22.2	60.2	37.9
Al_2O_3	3.40	6.20	17.7	13.2
Fe_2O_3	4.10	3.40	2.78	0.37
MgO	2.20	2.90	0.43	7.78
Na_2O	0.18	0.31	0.60	0.45
K_2O	0.56	1.20	0.58	0.64

In *Study C*, partial cement replacement was done by a mixture of limestone (LM), fly ash (FA), ground granulated blast furnace slag (S), and silica fume (SF). Australian low-calcium (Type F) FA and slag provided by Thomas Cement from Bremen, Germany, were used, with chemical composition presented in Table 3.1. The choice of binder materials is argued in the discussion part of the thesis (Chapter 5) since it connects to the conclusions from *Study A*.

In addition, quartz and silica fume were used to prepare Ultra-High-Performance Concrete (UHPC) in *Study A*. Elkem Microsilica (Oslo, Norway) Grade 920D (SF), limestone powder Nordkalk Limus 40 from Nordkalk AB and quartz Norquartz 45 were used. The grading of the SCMs is shown in Figure 3.2a.

Two types of fine aggregate provided by Baskarpsand AB (Habo, Sweden) with particles smaller than 1 mm were used (Figure 3.2b). A fine aggregate of type B15 was used in *Study A, B, C,* and B35 only in *Study A*. No coarse aggregate was applied.

To enable a low w/c ratio of the UHPC, a water-reducing admixture was used, i.e., polycarboxyl ether superplasticizer (SP), type BASF (Gothenburg, Sweden) MasterGlenium SKY 600.

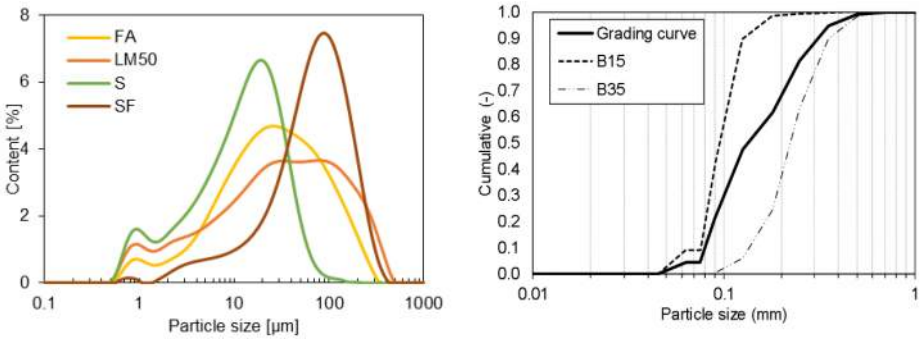

(a) (b)

Figure 3.2. (a) Grading of SCMs and limestone *(Study C)* (Rajczakowska et al. 2023b). (b) grading curves of fine aggregates B15 *(Study A, B, C)* and B35 *(Study A)* as well as UHPC mix grading curve *(Study A)* (Rajczakowska et al. 2019b).

Two types of polymer fibers were used, i.e., polyvinyl alcohol (PVA) and polypropylene (PP), with an approximate diameter of 0.025 mm and length of around 5 mm, in varied amounts. The primary purpose of the fibers was to enable crack width control during the cracking procedure. However, a potential boosting effect was also taken into consideration, as reported by others (Nishiwaki et al. 2012). Therefore, in *Study A*, a relatively high amount,1.5%vol of PVA fibers, was used, and in Study B, 1.0%wt (of cement) PVA fibers. The difference in dosing is connected to the different sizes of mortar specimens used, and it was determined based on a trial-and-error approach. On the other hand, in *Study C*, the PP fibers were applied in a relatively low amount, 0.5%wt of binder, to decrease the "boosting" effect, however, maintain the crack control properties. PP fibers were found to perform worse than PVA, considering self-healing efficiency, due to lack of polarity (Nishiwaki et al. 2012).

Mix compositions of the mortars and pastes produced are shown in Table 3.2 (*Study A and B*) and Table 3.3 (*Study C*). The justification for the choice of mortar ingredients is discussed in Chapter 5.

Two types of molds were used to prepare the specimens, i.e., steel molds with dimensions 4 cm x 4 cm x 16 cm and Teflon molds with dimensions 1.2 cm x 1.2 cm x 6 cm. The former is a standard-size mold used for mortars. The latter was designed to facilitate microstructural analysis while enabling mechanical properties testing. It was anticipated that excessive preprocessing, e.g., using water, could affect the phases formed due to healing and alter the microstructure. Therefore, small specimen sizes did not require extensive cutting to prepare the samples for the impregnation necessary for Scanning Electron Microscope (SEM) analysis. Furthermore, Teflon was used as a mold material to omit the necessity for oil application on the mold walls. For larger quantities of mortar, 4 cm x 4 cm x 16 cm beams, a Hobart mixer was used, whereas for 1.2 cm x 1.2 cm x 6 cm specimens – a small vacuum mixer type Bredent was used.

The paste in *Study C* was prepared by mixing the binder components with water in a vacuum mixer, type Bredent, at 390 rpm for 2 min. The pastes were cast into cylindrical

polypropylene molds with a diameter of 33 mm, which were then sealed for 7 days (Rajczakowska et al. 2023b).

Table 3.2. Mortar mix composition for Study A and B (modified from Rajczakowska et al. 2019ab)

	Study A			*Study B*		
Ingredient	**U (kg/m³)**	**A (kg/m³)**	**B (kg/m³)**	**C (kg/m³)**	**CFA (kg/m³)**	**CS (kg/m³)**
Cement type	CEM I	CEM I	CEM II, fly ash 20%	CEM I	CEM I	CEM I
w/c	0.22	0.45	0.45	0.35	0.35	0.35
Cement	1000	675	675	960	768	768
FA	0	0	Included in cement	0	192	0
S	0	0		0	0	192
Water	220	303.7	303.7	336	336	336
Quartz	300	0	0	0	0	0
B15	350	1196	1196	960	960	960
B35	350	0	0	0	0	0
SF	200	0	0	0	0	0
SP	22.5	0	0	7.7	7.7	7.7
PVA fibers	1.5%vol	1.5%vol	1.5%vol	1.0%wt	1.0%wt	1.0%wt
28-day compressive strength [MPa]	143 ± 11	39.5 ± 2.5	36.5 ± 2.0	Not measured		

Table 3.3. Mortar and paste mix composition for Study C (limestone (LM), fly ash (FA), blast furnace slag (S), and silica fume (SF)) (Rajczakowska et al. 2023b).

	Study C							
Mix	**OPC (CEM I) (g)**	**LM (g)**	**FA (g)**	**S (g)**	**SF (g)**	**w/b (-)**	**B15* (g)**	**PP fiber* (g)**
REF	1000	0	0	0	0	0.4	1000	5
LM50	500	500	0	0	0	0.4	1000	5
FA12.5	500	437.5	62.5	0	0	0.4	1000	5
FA25	500	375.0	125.0	0	0	0.4	1000	5
FA50	500	250.0	250.0	0	0	0.4	1000	5
S12.5	500	437.5	0	62.5	0	0.4	1000	5
S25	500	375.0	0	125.0	0	0.4	1000	5
S50	500	250.0	0	250.0	0	0.4	1000	5
SF12.5	500	437.5	0	0	62.5	0.4	1000	5
SF25	500	375.0	0	0	125.0	0.4	1000	5
SF50	500	250.0	0	0	250.0	0.4	1000	5
FA S	500	250.0	125.0	125.0	0	0.4	1000	5
FA SF	500	250.0	125.0	0	125.0	0.4	1000	5
S SF	500	250.0	0	125.0	125.0	0.4	1000	5
FA S SF	500	125.0	125.0	125.0	125.0	0.4	1000	5

***B15 and PP were not used in the case of paste preparation**

Mortars were removed from the molds after 24 hours and cured in plastic containers underwater at 20°C. The curing time was 1 day (mix U1, A1, and B1), and approximately 12 months (mix U12) in *Study A*, and 7 days in *Studies B* and *C*. In *Study A*, the effect of the material's age on the self-healing process was under investigation. On the other hand, in *Study B* and *C*, the material's early age was anticipated to improve the healing efficiency due to the larger amount of unhydrated binder.

3.1.2. Mechanical crack induction

Two types of mechanical crack induction methods were used, i.e., the three-point bending test (*Study A, B,* and *C*) and the compression test (Study C).

The three-point bending test was conducted as a modified flexural strength test based on EN 1015-11:2019 (2019). Both specimen sizes were used, i.e., 1.2 cm x 1.2 cm x 6 cm and 4 cm x 4 cm x 16 cm beams. A universal loading machine with displacement control, type Wykeham Farrance, with a 50 kN loading cell combined with the QuantumX MX440B universal measuring amplifier (HBM, Darmstadt, Germany) was used. A constant loading rate of 0.5 mm/min was applied. Since, as mentioned in Section 2.4.1, the effect of crack width on self-healing is significant, in this research, crack widths below 300 μm, an accepted service state limit were maintained in anticipation of a reasonable crack closure (Roig-Flores et al. 2015). Several research studies dealt with this crack range, e.g., (Edvardsen 1999), (Roig-Flores et al. 2015), (Gagné & Argouges 2012), and (Ahn et al. 2021). The maximum crack opening was controlled by observation with a digital optical microscope, type Dino-Lite Pro AM-413T (Dino-Lite Europe, Naarden, The Netherlands) with a 1.3 MP camera and a field of view of 1280×1024 pixels.

The compression test was performed with the uniaxial compression machine, type Instron, model 1342 (Instron, Norwood, United States). Non-standard specimen size was used, i.e., 4 cm x 4 cm x 4 cm, prepared by cutting the 4 cm x 4 cm x 16 cm beams. Since the damage degree was observed to affect the recovery of mechanical performance due to autogenous self-healing (Zhong and Yao, 2008), two damage degrees were applied in this study, determined by trial tests. First, at 7 days the specimens were loaded until failure (100% damage) to determine the compressive strength and induce larger cracks and higher degree damage. Then, additional samples were loaded up to 80% of the maximum load they could withstand (80% damage) to achieve less apparent damage and possibly smaller crack widths within the material.

3.1.3. Self-healing exposure

After crack induction, the specimens were kept under specific environmental conditions, i.e., exposure conditions, for the healing duration, which varied between the experiments. Below a description of each setup is presented with a brief justification.

In *Study A*, continuous complete immersion in tap water at 20 °C for 21 days was applied without renewal or movement of water. The exposure was expected to maximize the effects of the self-healing due to ongoing hydration process for the mortars with a high

amount of unhydrated cement. The specimens were kept together in a plastic container, which could have affected the ion concentration in the solution. Nevertheless, the conditions were kept the same for all the samples.

On the other hand, the goal of *Study B* was to verify the effect of different environmental conditions on the self-healing process. Therefore, the exposures were chosen based on the conclusions from *Study A*, which served as a preliminary exploratory investigation (Figure 3.1). A detailed discussion of the results and connections between the studies is presented in Chapter 5. The applied treatments and their scientific justification are summarized in Table 3.4.

Table 3.4. Exposure conditions applied in this study with justification – *Study B* (Rajczakowska et al., 2019c).

Exposure	Abbreviation	Justification
Air	**EXP 0**	Non-healed samples
Deionized water mixed with Accelerator in proportions 3:1 (immersion)	**EXP 1**	Increasing the rate of hydration process inside the crack; possibly faster healing; different composition of hydrates (Elkhadiri et al. 2009; Escalante-Garcia & Sharp, 1998; Matschei & Glasser, 2010)
Deionized water mixed with Retarder in proportions 3:1 (immersion)	**EXP 2**	Slowing down the hydration – more hydrates can precipitate on the surface of unhydrated cement grains (Escalante-Garcia & Sharp, 1998; Kjellsen et al., 1991)
Saturated lime water immersion	**EXP 3**	The more Ca^{2+} ions in the solution, the higher the pH
Coca-Cola immersion	**EXP 4**	Introducing phosphate anions into the self-healing solution; possibly beneficial retarding effect of sugar on the hydration of self-healing products
Deionized water immersion	**EXP 5**	Reference exposure
Deionized water immersion with cyclic evaporation (72 h cycle)	**EXP 6**	Changing the water regime by introducing the cycles of evaporation as well as different water volumes to modify the concentration of ions inside the crack
Dry/wet (deionized water) cycles 24 h/24 h	**EXP 7**	
Deionized water immersion up to 1 mm height of the sample	**EXP 8**	
Deionized water immersion up to 5 mm height of the sample	**EXP 9**	
Water immersion temperature cycle 24 h/ 20°C and 24 h/ 40°C	**EXP 10**	Increasing/decreasing the rate of the hydration process as well as changing the hydration product composition. Possible ettringite formation leads to a higher strength regain in case of lower temperature (Liu et al., 2017; Xu et al., 2012)
Water immersion temperature cycle 24 h/ 20°C and 24 h/ 5°C	**EXP 11**	
Deionized immersion with micro-silica particles 1.25%w	**EXP 12**	Providing the nucleation sites inside the crack for the self-healing products

In the case of Exposure 1, a commercial SIKA accelerator contained 40%–60% nitrate salts and 40%–60% water. The retarding admixture applied in Exposure 2 was SIKA Retarder, described by the producer as modified phosphates containing sodium metaphosphate (20%–30%), sodium gluconate $C_6H_{11}NaO_7$ (2%–5%), and water (70%–

80%) (Rajczakowska et al., 2019c). Treatment with the commercially available drink Coca-Cola was also applied. This substance includes water, high fructose corn syrup, white sugar, carbonic-acid gas, phosphoric acid (approximately 530 mg/L) (Bello et al., 1996), and caffeine (Choi et al., 2019). However, the detailed chemical composition is unknown (Rajczakowska, 2019d). The healing process was maintained for 28 days for each exposure. Each specimen was kept in an independent cylindrical plastic container, and deionized water was used to ascertain control over the ion concentration of the solution.

In *Study C*, four cycles of 3 days wet and 3 days dry phases were applied to simulate a more realistic, considering field conditions and self-healing exposure. The length of the cycles was determined by trial and error on the small specimens (1.2 cm x 1.2 cm x 6 cm beams) by visual observations of the crack closure. Each set of specimens belonging to the same binder composition was immersed in tap water in the same plastic container and sealed during the wetting phase. A similar water level was maintained for all containers. During the drying phase, the specimens were removed from the water and kept in the same room with a crack opening facing up at approximately 20°C and 40% RH. The water was exchanged after each cycle to facilitate the possible calcium-leaching process. The purpose was to impose higher ion concentration gradients and potentially increase the ion transfer into the crack. In previous studies, the calcium leaching caused corrosion by renewed deionized water was studied in relation to the radioactive waste disposal facilities; however, the rate of the reactions was slow (Adenot and Buil, 1992).

3.1.4. Self-healing efficiency measurements

The self-healing efficiency was assessed based on several parameters, i.e., ultrasound transmission time, crack closure, strength recovery, and water absorption rate changes. In addition, the effect of the material's microstructure at the moment of cracking was considered (e.g., porosity, unhydrated cement amount) and crack geometry. The experimental setup differed in each study depending on the research questions and logistics. The list of measured parameters in each Study is presented in Table 3.5.

Table 3.5. List of parameters measured in *Study A*, *B*, and *C*.

Study A	***Study B***	***Study C***
Ultrasound transmission time	Crack closure – crack mouth	Crack closure – crack mouth
Crack closure – crack mouth	Crack closure – at depth	Compressive strength recovery, two damage degrees
Chemical composition and morphology of healing products	Chemical composition and morphology of healing products	Water absorption rate
Unhydrated cement amount	The pH of the healing solution	Crack geometry parameters (tortuosity, fractal dimension, crack width)
Flexural strength recovery	Flexural strength recovery	Initial microstructure of the hydrated binder (porosity, Si/Ca ratio, portlandite, and calcite amounts)

Below, the methods used to characterize the self-healing in this research are briefly summarized.

The transmission time was measured using the Pundit Lab instrument with exponential transducers and a frequency of 54 kHz following EN 12504-4:2004 (2004) standard. The readings were performed before cracking ($t_{t,0}$), after cracking ($t_{t,1}$) as well as, after 14 ($t_{t,14}$) and 21($t_{t,21}$) days of healing. The transmission time recovery ratio R_t was defined as (Rajczakowska 2019d, Rajczakowska 2019b):

$$R_{t,i} = \frac{t_{t,0} - t_{t,i}}{t_{t,0}} \quad [-] \tag{3.1}$$

where i is the moment in time of healing, $t_{t,0}$ is the transmission time before cracking, and $t_{t,i}$ is the transmission time at the moment i of healing.

The crack closure at the crack mouth was calculated based on the images obtained with a digital light microscope, type Dino-Lite Pro AM-413T with a 1.3 MP camera and a field of view of 1280 × 1024 pixels (Rajczakowska et al. 2019b). A special stand was designed to acquire the images in the same position before and after healing (Figure 3.3a). The analyzed crack length was approximately 32 mm in *Study A* and *C* (4 cm x 4 cm x 16 cm beams) and 10 mm in *Study B* (1.2 cm x 1.2 cm x 6 cm beams). In *Study B*, two surfaces were analyzed, Surface 1 at the side of the specimen and Surface 2 at the crack opening (Figure 3.43b). In addition, four specific image positions were selected in *Study C* to facilitate crack geometry analysis (Figure 3.3c).

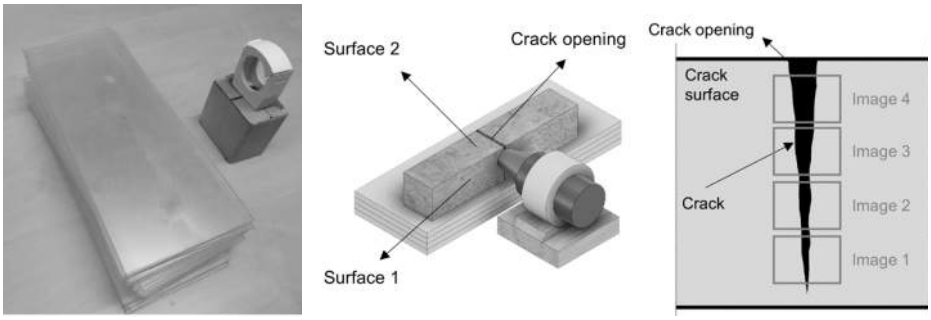

(a) (b) (c)

Figure 3.3. (a) Picture of the optical microscope setup, (b) the scheme for taking a picture of the crack, (c) four image positions used in *Study C*; modified from (Rajczakowska et al., 2019c) and (Rajczakowska et al. 2023b).

The images were converted to 8-bit grayscale, and the crack was segmented from the image by applying thresholding algorithms. Details can be found in papers II, III, and IV (Rajczakowska et al. 2019bc and Rajczakowska et al. 2023b). The Fiji image processing package (Schindelin et al. 2012) was used for image processing and analysis. The calculation was performed on the binarised images of cracks, where white pixels (of value

1) depicted the crack area and black pixels (of value 0) the hydrated binder matrix (Rajczakowska et al. 2019b). The crack closure ratio *CC* was calculated as follows:

$$CC = \frac{A_b - A_h}{A_b} \ [-] \tag{3.2}$$

where A_b and A_h are the area (sum of white pixels) of the crack before and after healing, respectively.

In addition, the cracks were studied at depth to verify the self-healing phases formed deeper inside the specimen, using two methods. Method 1 involved splitting the mortar specimen into two parts and assessing the crack plane (Figure 3.4). The morphology and chemical composition of the formed self-healing products were evaluated using SEM with Energy Dispersive Spectroscopy (EDS).

On the other hand, Method 2 was based on the SEM and EDS analysis of the specimen cross-sections (Figure 3.5). The middle part of the beam was cut to fit a sample fragment in the resin impregnation mold. The specimens were then impregnated in epoxy resin under vacuum using Struers CitoVac and Labosystem (Struers, Ballerup, Denmark). Struers MD Largo discs and DP-Spray M diamond suspensions with decreasing particle sizes were applied to polish the surface of the sample. Polishing was done twice to obtain two cross-sections, i.e., Cross-section 1 just below the surface (approximately 1 mm below the surface) and Cross-section 2, in the middle of the sample height (6 mm below the surface).

The analysis was conducted using Jeol JSM-IT100 SEM (JEOL Ltd., Tokyo, Japan) with Bruker EDS (Bruker Corporation, Billerica, MA, USA). To avoid charging, the imaging was done in secondary electron (SE) and backscatter electron (BE) modes under a low vacuum. At least three points were analyzed for each self-healing product. Details of the procedures are described in Papers II and III (Rajczakowska et al. 2019bc).

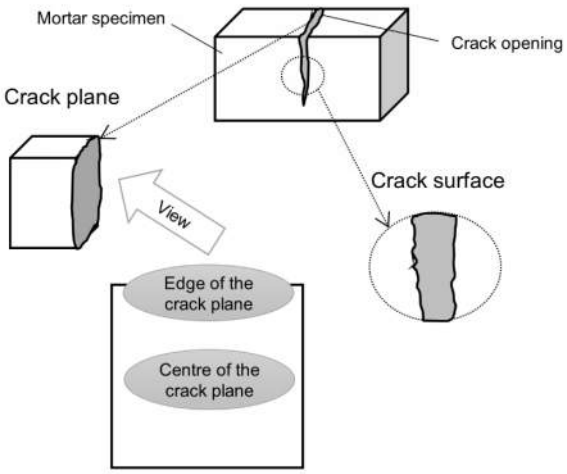

Figure 3.4. Crack studies deeper inside the specimen – Method 1 (Rajczakowska et al. 2019d).

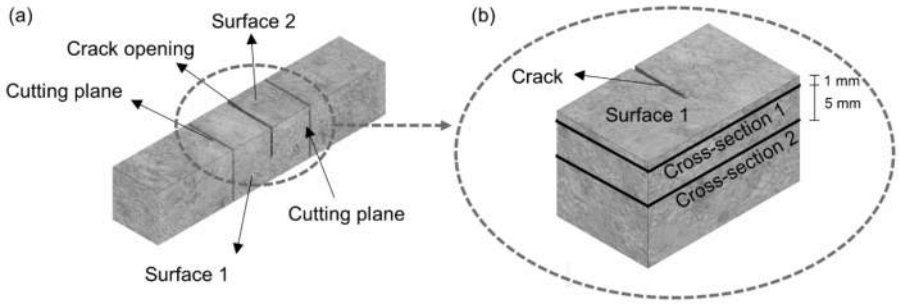

Figure 3.5. Crack studies deeper inside the specimen – Method 2 (Rajczakowska et al. 2019c).

The water absorption rate test was conducted using a similar procedure to ASTM C1585 standard (2020). Non-standard specimens were used, i.e., 4 cm x 4 cm x 16 cm beams. Firstly, the samples were oven-dried at 55°C until the weight change was less than 0.2%. Afterward, the beam's surface was covered with a silicone layer on four sides to establish a quasi-one-directional water movement (Zhang et al. 2014). Covered beams were situated in a plastic container filled with water up to a level of approximately 4 mm above the bottom surface of the specimen (Figure 3.6). Sample mass changes were measured in specific time intervals, i.e., 0, 5, 15, 25, 45, 60, 120, and 180 min, after the removal of surplus water with a cotton cloth. Between the measurements, the specimens were kept in water (Gupta et al. 2018). The cumulative rate of water absorption I in each moment t was calculated according to the following formula:

$$I(t) = \frac{\Delta m}{A \cdot \rho} \quad [\text{mm}] \tag{3.3}$$

where Δm is the change in mass of the sample (g), A is the area of the bottom surface (mm^2) and ρ is the density of water (g/mm^3) (Rajczakowska et al. 2023b).

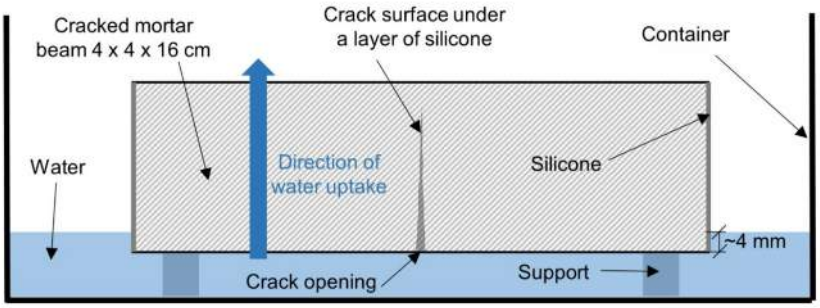

Figure 3.6. Water absorption rate test setup (Rajczakowska et al. 2023b).

The test was performed on the healed specimens after four dry/wet cycles. As a reference, the water absorption rate of intact specimens was measured on the same day, i.e., 7+24 days. The performance of the damaged specimens before healing was not included in

the analysis. Initially, the test was performed on the specimens after cracking for selected binders; however, the results were inconclusive. Comparison with the intact mortars gave a better indication of the healing performance in relation to the initial properties of the material. This study uses a similar approach for compressive strength recovery evaluation. Comparison with undamaged state, excluding the cracked (non-healed) mortars, was also studied by other researchers, e.g. (Feng et al. 2019) or (Gupta et al. 2018). Since the damage variation might alter the results, a thorough evaluation of the crack mouth's geometry was performed, demonstrating a low scatter of the crack characteristics (Section 3.2.5). In addition, an average value of three specimens was analyzed to decrease the error.

The following self-healing efficiency parameters were defined based on the water absorption rate measurement:

$$IR25 = I_{25,h} - I_{25,uh} \quad [\text{mm}] \tag{3.4}$$

$$IR180 = I_{180,h} - I_{180,uh} \quad [\text{mm}] \tag{3.5}$$

$$SR25 = \frac{S_{25,h}}{S_{25,un}} \quad [-] \tag{3.6}$$

where $I_{25,h}$ and $I_{25,uh}$ are the values of cumulative water absorption at 25 min for healed and undamaged specimens, respectively, and $I_{180,h}$ and $I_{180,uh}$ are the values of cumulative water absorption at 180 min for healed and undamaged samples, respectively. On the other hand, S_{25} denotes the coefficient of sorptivity, and $S_{25,h}$ and $S_{25,un}$ are the slopes of the initial 25 min of the water absorption curves for healed and undamaged specimens, respectively. Smaller values of *IR2, IR180,* and *SR25* correspond to more successful healing (Rajczakowska et al., 2023b).

Compressive strength recovery was measured on 4 cm x 4 cm x 4 cm specimens for two damage degrees, 80% (CSR80) and 100% (CSR100), as described in Section 3.1.2. The values of healed specimens were compared with the intact specimens measured on the same day, i.e., at 7+24 days, to avoid bias concerning the possible ongoing hydration/pozzolanic activity in the material during the healing period. The compressive strength recovery parameter CSR_{PL} was calculated according to the equation below:

$$CSR_{PL} = \frac{S_{PL}}{S_{un}} \quad [-] \tag{3.7}$$

where PL is the preloading peak load (80 or 100%), S_{PL} is the compressive strength after healing of a specimen subjected to a given preloading peak load and S_{un} is the reference compressive strength of undamaged cubes. The efficiency of the healing process is greater for higher values of the CSR parameter (Rajczakowska et al., 2023b).

Flexural strength recovery was tested on the 1.2 x 1.2 x 6 cm specimens using the three-point bending setup described in Section 3.1.2. Two recovery definitions were used, S_p and S, formulated as follows (Rajczakowska et al. 2019bc):

$$S_p = \frac{S_H - S_{\mathrm{bH}}}{S_{\mathrm{bH}}} \tag{3.8}$$

$$S = \frac{S_H - S_0}{S_0} \tag{3.9}$$

where S_{bH} represents the flexural strength of the pre-cracked samples stored in the air and tested at the same time as healed specimens, S_H depicts the flexural strength of the healed specimens, S_0 denotes the flexural strength of the intact specimens. A higher value of the flexural strength recovery indicates more efficient self-healing (Rajczakowska et al. 2019bc).

The geometry of the cracks before healing was described using various parameters, i.e., initial crack area (ICA), maximum crack width (MCW), average crack width (ACW), tortuosity (T), and fractal dimension (FD). Calculation of the parameters was done based on the optical images of the crack taken in four positions on the 4 cm x 4 cm x 16 cm beams (Figure 3.3). Image analysis was performed using the Fiji image processing package (Schindelin et al. 2012). The main steps in the calculation procedure are presented in Figure 3.7. (Rajczakowska et al., 2023b).

The local thickness algorithm (Hildebrand & Rüegsegger, 1997) was applied to calculate the width of the crack (MCW and ACW) using the Local Thickness plugin in the Fiji package (Saito & Toriwaki, 1994). After image binarization, 32-bit local thickness maps were produced (Figure 3.7a1), with pixel values associated with the crack width in each point (Rajczakowska et al. 2023b). Afterward, local thickness histograms were generated (Figure 3.7a2). The MCW was assumed as the maximum value from the histogram, whereas the ACW was computed as a weighted average based on the number of counts per each crack width (Rajczakowska et al., 2023b).

The crack tortuosity (T) characterizes how the crack shape differs from the straight line and it can be calculated according to the following equation (San Wu et al. 2006):

$$\mathrm{T} = \frac{L_{actual}}{L_{Euclidean}} \quad [-] \tag{3.10}$$

where L_{actual} is the actual length of the crack and $L_{Euclidean}$ is the shortest distance between beginning and the end of the crack in Euclidean space (San Wu et al. 2006; Rajczakowska et al. 2023b). The higher the T parameter, the "windier" the crack, with T equal to 1 corresponding to a straight line. To calculate the tortuosity of the cracks, the binarized images were preprocessed (Figure 3.7b1-b3). First, dilation was applied to consolidate scattered parts of the crack together (Figure 3.7b1), followed by a "skeletonization" procedure (Arganda-Carreras et al. 2010; Lee et al. 1994) with the use of the Skeletonize(2D/3D) plugin available in the Fiji package. Obtained skeleton (Figure 3.7b2) was cleaned from artifacts below 70 pixels (Figure 3.7b3). The obtained crack outline was measured using Analyze Skeleton(2D/3D) Fiji plugin to determine L_{actual} and $L_{Euclidean}$ distances (Rajczakowska et al., 2023b).

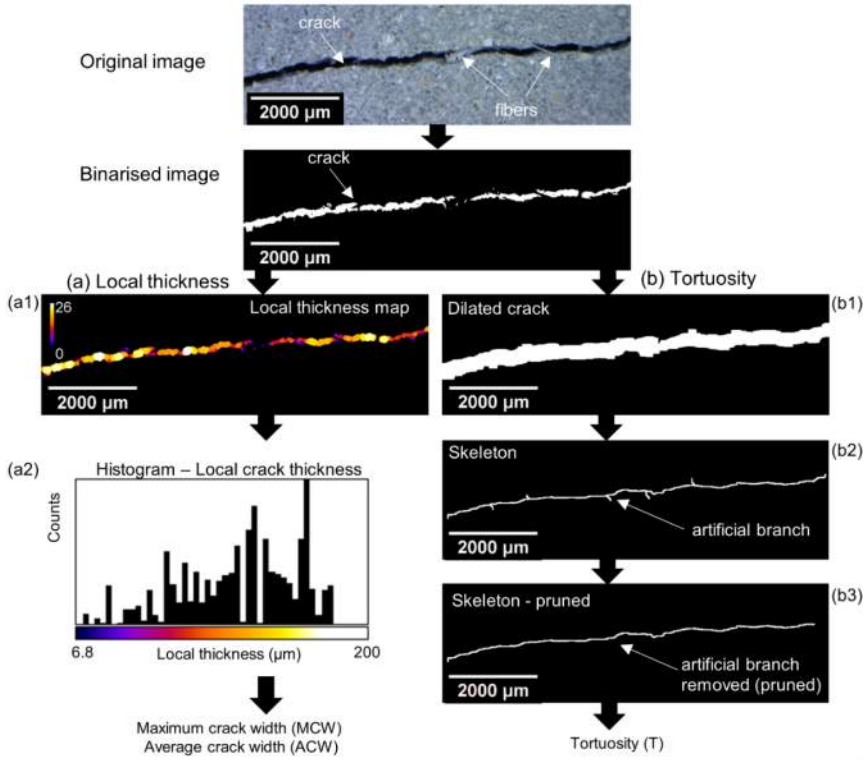

Figure 3.7. The image processing procedure for the (a1-a2) calculation of maximum crack width (MCW), average crack width (ACW), and (b1-b3) tortuosity (T) (Rajczakowska et al. 2023b).

The complexity of the crack was represented by the fractal dimension (FD), which indicates the arrangement change with the change in scale. Fractal dimension "*given as an integer number gives information about the degree of filling a given metric space with the object being analyzed"* (Szeląg, 2020). For instance, for a curve, the range of fractal dimension can be equal between 1 and 2 (Szeląg, 2020). FD can be calculated using several methods; however, in this study, the box-counting algorithm was used due to its uncomplicated character. This method includes placing a series of boxes of decreasing dimensions over the image of the crack. Then, the number of boxes that contain the crack for each box size is determined (Foroutan-pour et al. 1999). The definition of the FD for the box-counting method is presented below (Szeląg, 2020):

$$\mathrm{FD} = \lim_{\varepsilon \to \infty} \frac{\log N_\varepsilon}{\log \varepsilon} \tag{3.11}$$

where N_ε denotes the number of boxes intersecting the crack in the image, and ε represents the scale, that is, the box size in relation to the image size. This limit is calculated in practice as a slope of the regression line of the log-log plot of the data (Szeląg, 2020; Rajczakowska

et al. 2023b). In this research, FracLac for ImageJ (Karperien, 2013) software was used to compute the FD of the cracks. The largest box was limited to 45% length of the shorter edge of the image. A linear grid sampling size with twelve different grid orientations was used (Rajczakowska et al. 2023b).

Parameters and chemical composition of the hydrated binder microstructure were determined using SEM and XRD techniques. The inner C-A-S-H phase's porosity and Si/Ca ratio were calculated based on SEM imaging, whereas Portlandite and calcite phases were estimated by semi-quantitative analysis of peaks from the XRD measurements. Below a short description of the sample preparation and measurement procedures is presented.

Preparing SEM specimens included cutting approximately 3 mm thick slices from the middle of the sample. The procedure roughly followed the one in the study of Georget et al. (2021). The solvent exchange method was used for hydration stoppage with isopropanol for 7 days. Specimens were dried in a desiccator for 48 hours before resin impregnation and polishing were done using Struers CitoVac and Labosystem. Polished sections were prepared with Struers MD Largo discs and DP-Spray M diamond suspensions with 9 μm, 3 μm, and 1 μm particles for subsequent polishing steps. The first step of polishing lasted 30 min and 20 N pressure was used; the second step – 2 h and 25 N, and finally, 3 h and 25 N for the thirst step. Lubrication and cooling were done with paraffin-based lamp oil instead of water to preserve the specimen microstructure. Ultrasonic bath cleaning in isopropanol was applied between each step. Before the analysis, the impregnated and polished specimens were stored again in a desiccator for 48 hours for drying (Rajczakowska et al., 2023b).

Microstructural analysis was performed using Jeol JSM-IT100 SEM with Bruker EDX in BE mode under a low vacuum with 30 Pa pressure, an accelerating voltage of 15 kV, and a working distance of 12±1 mm.

The porosity of the hardened binder was calculated as an average value from 30 SEM BE images taken at 400 x magnification (Figure 3.8a), following the overflow method (Wong et al. 2006). Image processing was done using Fiji image processing package (Schindelin et al. 2012) with ImageJ2 software (Schindelin et al. 2015; Rueden et al. 2017), whereas OriginPro (v 2020) software was used to estimate the final threshold, i.e., the so-called critical overflow point (Figure 3.8b). The porosity was calculated as the number of black pixels in relation to the total number of pixels corresponding to the image, based on the images binarised with the determined earlier threshold. The average porosity value from 30 images was considered (Rajczakowska et al., 2023b).

On the other hand, the Si/Ca ratio of the inner product (IP) C–A–S–H was calculated following the guidelines from the publication of Rossen and Scrivener (2017). Images at 4000x magnification were analyzed in 10 different locations of the specimen. Point analysis was used for the elemental analysis by selecting 10 points manually within the boundaries of IP C–A–S–H (Figure 3.9a). The number of X-rays per acquisition was equal to 50,000 counts per analysis (approximately 7 min per location), and it was kept constant for all

measurements. The so-called Edge of the Cloud of Points method (Rossen & Scrivener, 2017) was used to estimate the average atomic ratio Si/Ca of IP C–A–S–H (Figure 3.9b).

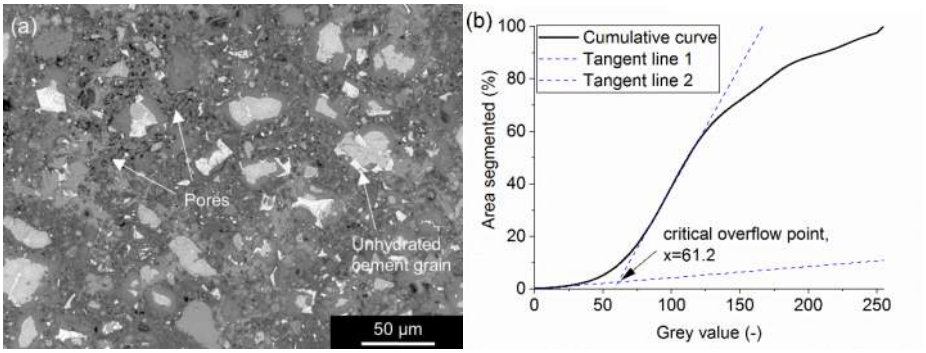

Figure 3.8. (a) example of SEM image (BE 400x) for porosity analysis; (b) Porosity threshold estimation from cumulative curve (Rajczakowska et al. 2023b).

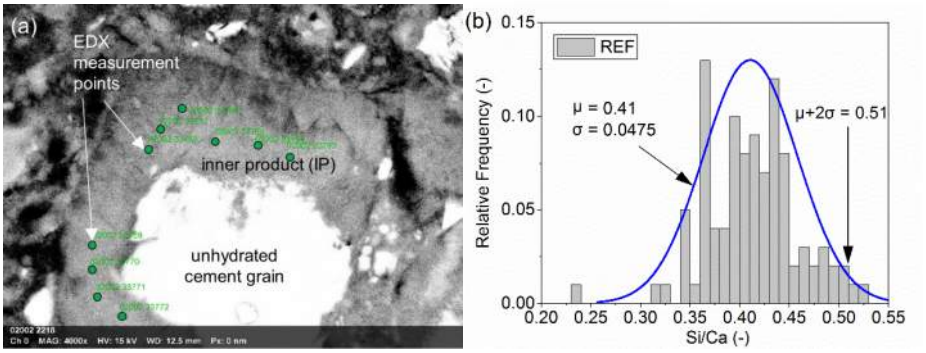

Figure 3.9. (a) 4000x BSE-SEM image of a polished section with marked 10 EDX measurement points in the inner product (IP) C–A–S–H in one location; (b) fitting procedure for IP C–A–S–H Si/Ca ratio based on (Rossen and Scrivener, 2017) (Rajczakowska et al. 2023b).

The specimens for XRD analysis were prepared following a procedure similar to the RILEM TC-238 recommendation (Snellings et al. 2018). First, a 3 g of paste, crushed with mortar and pestle into a fine powder, was immersed in 100 ml of isopropanol for 15 min to stop hydration. Then, the material was vacuum filtered on the Büchner filter and oven-dried at 40°C for around 8 min.

An XRD, type Empyrean from PANalytical with PIXcel 3D detector (Malvern Panalytical Ltd., Royston, UK) was used with Cu-K radiation and a wavelength of 1.54060 Å, generated at 45 kV and 40 mA. Each measurement lasted approximately 15 min following a step size of 0.0260, and the angle range of 2θ was from 5° to 65°. Identification of Portlandite and calcite phases was made using Panalytical's Highscore Plus software, equipped with a COD database. The semiquantitative calculation was performed with

OriginPro's Quick Peak tool to estimate the first peak area and half-maximum height (FWHM) for each phase after the baseline subtraction (Rajczakowska et al., 2023b).

3.2. RESULTS AND ANALYSIS

3.2.1. Effect of material's age at cracking

The age effect was evaluated for the UHPC specimens cracked at one day (mix U1) and approximately 12 months (mix U12) after casting. Since the mix composition for UHPC contains a large amount of cement, a relatively high amount of unhydrated cement particles would be expected, even at a mature age. Therefore, based on the ongoing hydration mechanism, similar healing efficiency was expected for both materials. Nevertheless, based on the obtained results, the age effect on self-healing was inconclusive.

The crack closure ratio was higher for the early-age specimen U1, reaching approximately 0.65 compared to 0.45 for U12 (Figure 3.10c). Nevertheless, the variation of the results was high, possibly due to local crack width differences. Visually no significant differences were observed (Figure 3.10a). Large amounts of white cuboid crystals were observed on the surface of the PVA fibers, bridging the crack for both specimens (Figure 3.10de).

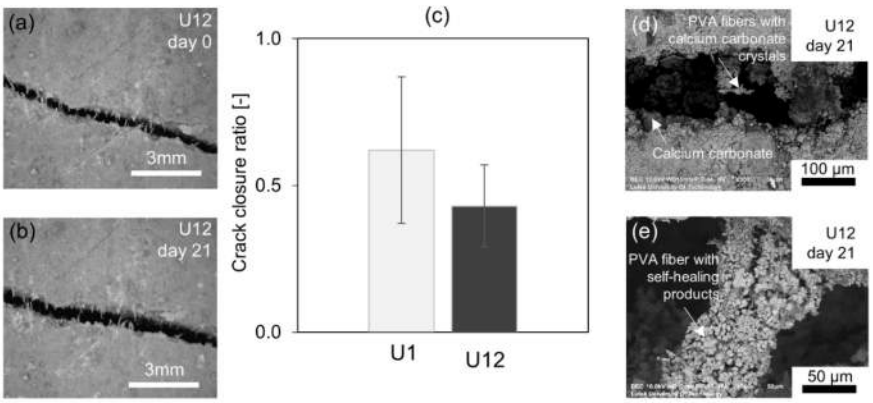

Figure 3.10. Light microscope image of the crack: (a) before healing for sample U12; (b) after 21 days of healing for sample U12; (c) crack closure ratio for samples U1 and U12; (d) SEM BSE image (300x) of the crack at the surface for the sample U12; (e) SEM BSE image (300x) of the self-healing products deposited on the PVA fiber in the specimen U12 (Rajczakowska et al. 2019b).

In terms of flexural strength recovery, the U1 specimen demonstrated better performance despite relatively low surface crack closure, which could presumably suggest the formation of the C-S-H phases forming deeper inside the crack due to the ongoing hydration of unhydrated cement (Figure 3.11). It should be noted that the SEM analysis of

the polished section did not show significant differences between the two mixes in terms of the amount of unhydrated cement, with 17.02 % for mix U1 and 17.34 % for mix U12.

Nevertheless, evaluation of the internal crack planes (Figures 3.12 and 3.13) revealed a higher amount of C-S-H phases for the early-age specimens U1. In addition, ettringite was observed in the case of U1, presumably contributing to the higher strength regain (Gonzalez et al., 1997). Cracks of both mixes were filled with calcite crystals to some extent.

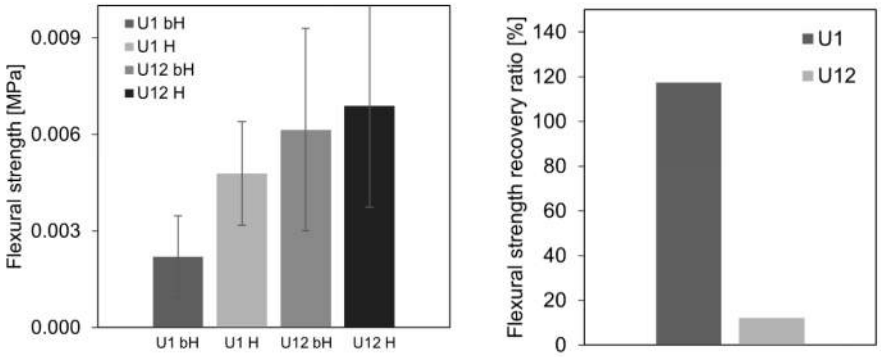

(a) (b)

Figure 3.11. (a) The mean flexural strength measured before healing but after cracking (bH) and after healing of the initially cracked samples (h) (b) flexural strength recovery ratio for mixes U1 and U12. (Rajczakowska et al. 2019b).

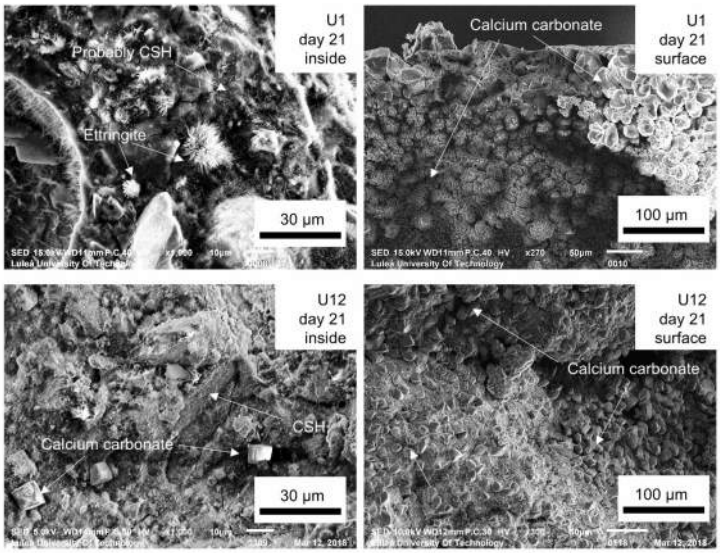

Figure 3.12. SEM SE images (1000x and ~300x) of the crack plane for U1 and U12 (Rajczakowska et al. 2019b).

Furthermore, the spatial distribution of the healing products was studied, i.e., at the crack mouth (Area A, Figure 3.13) and inside, approximately in the middle of the crack (Area B, Figure 3.13). The morphology and chemical composition of the observed two distinct phases was evaluated (Table 3.6).

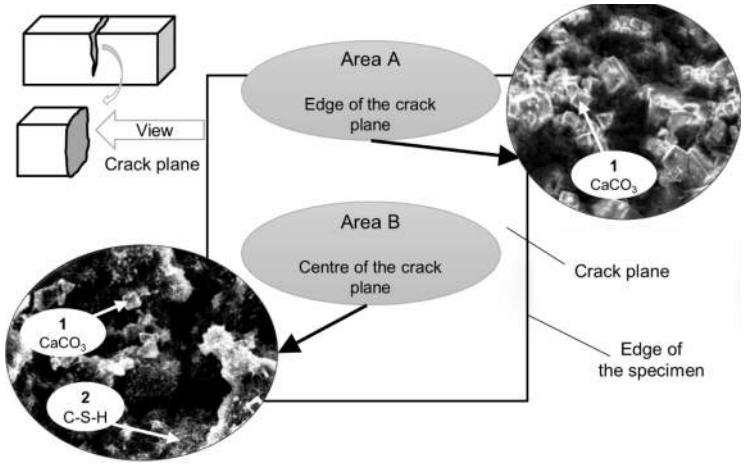

Figure 3.13. Spatial distribution of the self-healing products inside the specimens after 21 days (BE images, 1500x) (Rajczakowska et al. 2019b).

Table 3.6. Results of the SEM-EDS analysis (Rajczakowska et al. 2019b).

Elements	Atomic Norm. %	
	Product Type 1	**Product Type 2**
C	18.48	18.45
Ca	19.08	8.39
Si	0.00	7.36
Al	0.00	0.95
O	62.44	63.85
K	0.00	1.00
Ca/Si	0.00	1.14

The results of elemental point analysis with SEM-EDS suggested that the cubic-like morphology corresponded to calcium carbonate, with no silicon present (Product 1, Table 3.6). This healing phase was observed primarily in Area A, at the edge of the crack plane. On the other hand, needle-like morphology, dominating in Area B, was labeled as C-S-H, with Ca/Si ratio close to 1 (Product 2, Table 3.6).

The self-healing performance of UHPC was less pronounced than anticipated considering a high amount of unhydrated cement particles. The recovery further diminished

with the age of the material. Since both materials had a similar amount of unhydrated cement particles based on the SEM analysis, another factor influenced the materials' performance. It can be hypothesized that a dense binder matrix microstructure with a low water-to-cement ratio and a high amount of silica fume hindered the transport of ions from the hydrated binder into the crack (Figure 3.1, Obstacle 2)

3.2.2. Effect of healing duration

Ultrasound transmission time measurements were used to estimate the changes in healing with time for mixes A1, B1, U1, and U12. It was observed that after an initial substantial increase caused by the crack induction, transmission time gradually decreased, possibly due to the formation of healing phases (Figure 3.14a). Transmission time recovery (Figure 3.14b) was reached approximately after 14 days of healing in water for all mortar mixes, which agrees with other studies (Kan & Shi, 2012; Ma et al., 2014).

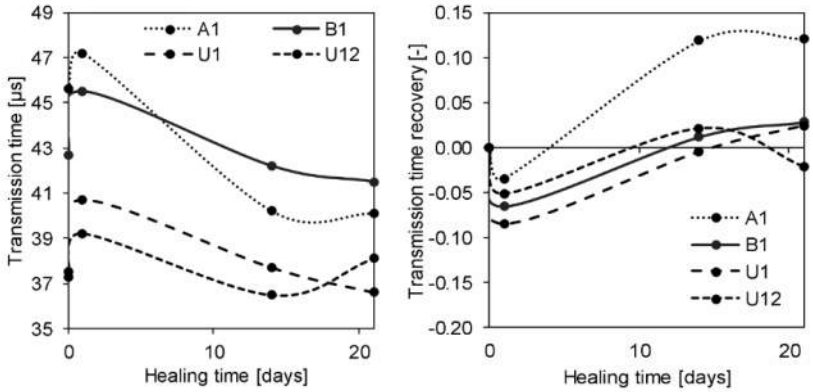

Figure 3.14. (a) Transmission time evolution for samples A1, B1, U1, and U12, (b) transmission time recovery ratio evolution for samples A1, B1, U1, and U12 (Rajczakowska et al. 2019b).

It can be hypothesized that at the beginning of the self-healing process, the local water-to-cement ratio inside the crack is high due to a small number of unhydrated particles uncovered, which can likely cause accelerated hydration leading to a high initial growth rate of healing phases (Huang et al., 2013). Furthermore, formed healing products could block the dissolution of the calcium ions into the crack by creating a dense shell on the cement grain surface, consequently slowing down the self-healing process (Obstacle 1, Figure 3.1) (Huang et al., 2013).

3.2.3. Effect of environmental exposure

Four environmental exposure groups were studied, i.e., different water immersion regimes, temperature cycles, water containing accelerating/retarding chemical admixtures, and water containing additional ions or particles (Table 3.4). Each specimen was kept in a

separate container, and the treatment lasted 28 days. In addition, mortar specimens based on OPC were tested with w/c equal to 0.35 and cement to sand ratio equal to 1 (Table 3.2).

Water immersion

Optical microscope and SEM images before and after 28 days of healing of Surface 1, Cross-section 1, and Cross-section 2 are shown in Figure 3.15 for Exposures 5, 6, 7, 8, and 9 (water immersion, water evaporation, dry/wet cycles, water/1 mm and water/ 5 mm). No significant healing at the crack mouth or internally was observed for the applied water immersion regimes (Rajczakowska et al., 2019c).

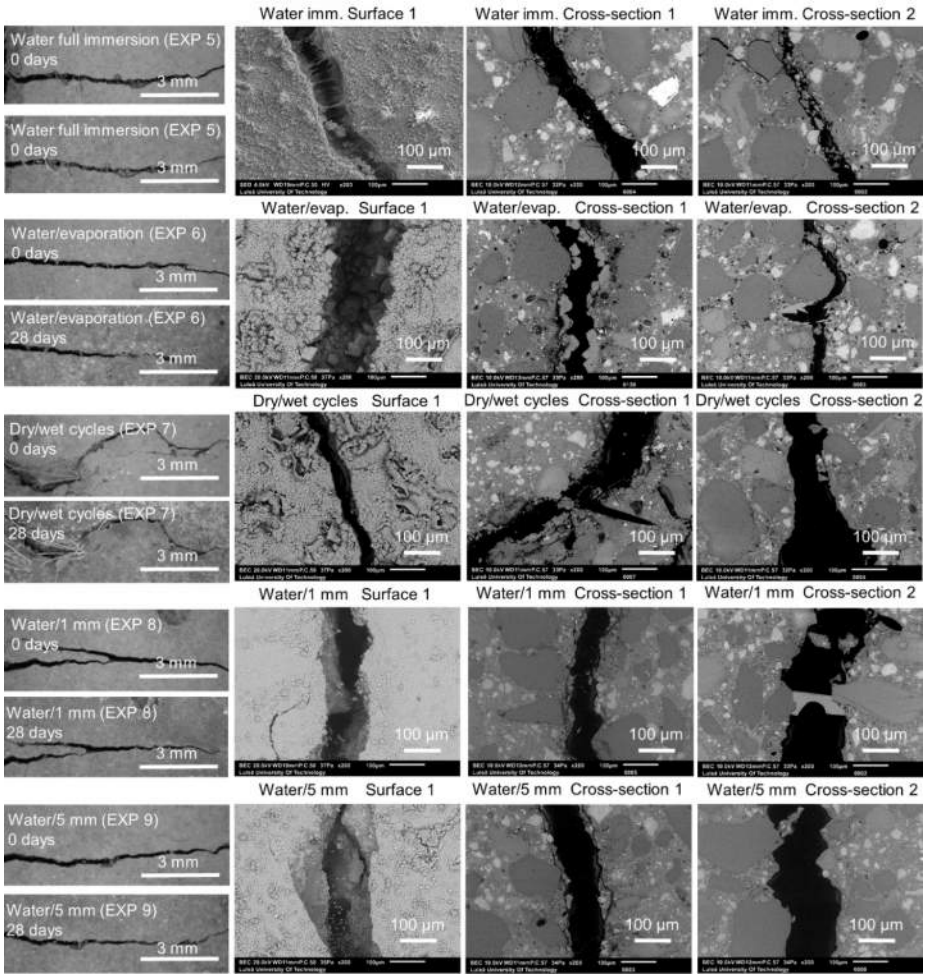

Figure 3.15. Example images of Surface 1 observed with the optical microscope before (0 days) and after healing (28 days) and the SEM (BSE, 200x) and cross-sections (SEM BSE, 200x) of the specimens healed for 28 days in Exposures 5-9 (water immersion, water evaporation, dry/wet cycles, water/1 mm, water/ 5 mm) (Rajczakowska et al., 2019c).

Measurement of the pH of the healing solution suggested that high pH was obtained after the initial 12 hours for all water exposures (Figure 3.16a). Subsequently, the pH value stabilized for Exposures 5, 8, and 9, whereas a continuous decrease was observed for Exposures 6 and 7, reaching approximately 9-10 after 28 days.

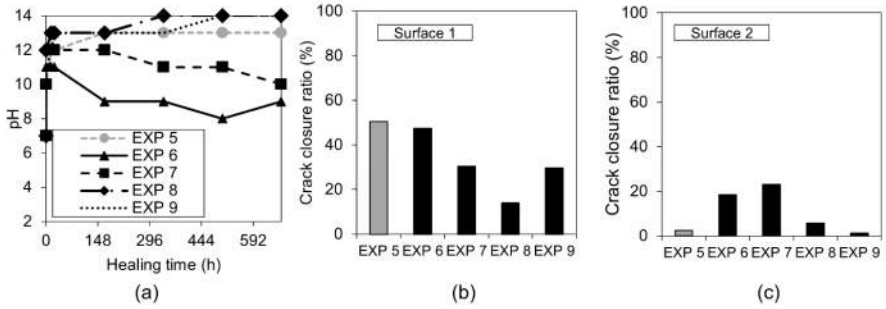

Figure 3.16. (a) pH changes vs. time for Exposures 5-9; Crack closure ratio for Exposures 5-9: (b) Surface 1, (c) Surface 2. (Rajczakowska et al. 2019c).

Self-healing at crack opening (Surface 2) was below 20% for all environmental conditions (Figure 3.176c). Exposure 8, with the smallest volume of water, exhibited the lowest crack closure at Surface 1 (Figure 3.16b). The best crack closure performance at Surface 1 was demonstrated by Exposures 5 and 6, associated with continuous water immersion and evaporation, respectively. Calcite precipitates with a Si/Ca ratio of 0.18 were noticed both at the surface and deeper inside the crack (Figure 3.17ac), leading to the complete sealing of crack widths up to 50 μm.

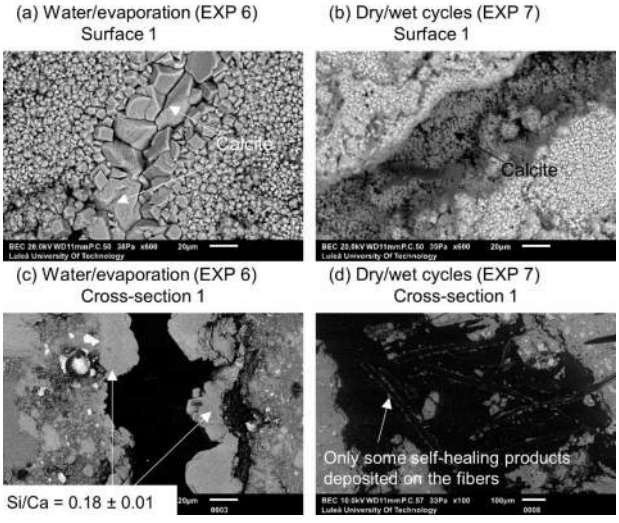

Figure 3.17. (a) Surface 1 Exposure 6 (SEM BSE 600x); (b) Surface 1 Exposure 7 (SEM BSE 600x); (c) Cross-section 1 Exposure 6 (SEM BSE 600x); (d) Cross-section 1 Exposure 7 (SEM BSE 100x) (Rajczakowska et al., 2019c).

In the case of Exposure 7 (cyclic water immersion), only minimal self-healing was observed with calcium carbonate present at the crack mouth (Figure 3.17b) and inside, on the surface of PVA fibers (Figure 3.17d). A short wetting phase (1 day) could be the possible reason for the failure of this healing treatment, i.e., there was not enough time for the calcium ions to transfer to the crack.

In addition, water exposure possibly led to the release of sulfates from the unhydrated cement grains, which facilitated the formation of ettringite inside the cracks (Figure 3.18). This healing phase was observed for Exposures 5, 8, and 9.

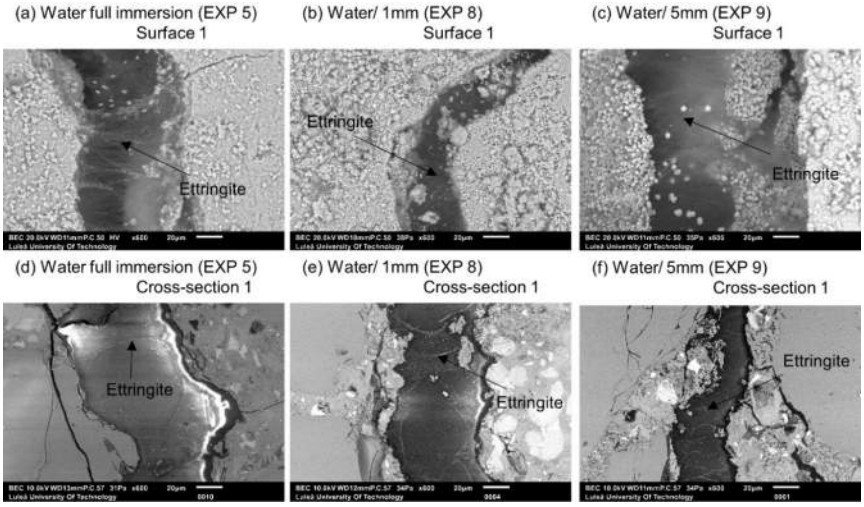

Figure 3.18. (a) Surface 1 Exposure 5 (SEM BE 600x), (b) Surface 1 Exposure 8 (SEM BSE 600x), (c) Surface 1 Exposure 9 (SEM BSE 600x), (d) Cross-section 1 Exposure 5 (SEM BSE 600x), (e) Cross-section 1 Exposure 8 (SEM BSE 600x), (f) Cross-section 1 Exposure 9 (SEM BSE 600x) (Rajczakowska et al., 2019c).

Temperature cycles

Two exposures involving complete water immersion with cyclic temperature changes were evaluated, i.e., Exposure 10 with 24h at 20°C followed by 24h at 40°C and Exposure 11 with 24h at 20°C followed by storage at 5°C.

Similar crack closure of approximately 60% was achieved on Surface 1 and 2 for both Exposures 10 and 11 (Figure 3.19bc). In comparison, reference Exposure 5, cured continuously in water at 20°C, obtained a negligible crack closure on Surface 2 (Figure 3.19c). Representative images of the crack mouth and specimens' cross-sections are shown in Figure 3.20. Over time, pH changes were observed for Exposures 10 and 11 (Figure 3.19a). A significant decrease was observed after 148 h as opposed to the reference Exposure 5, which maintained the constant pH of the solution.

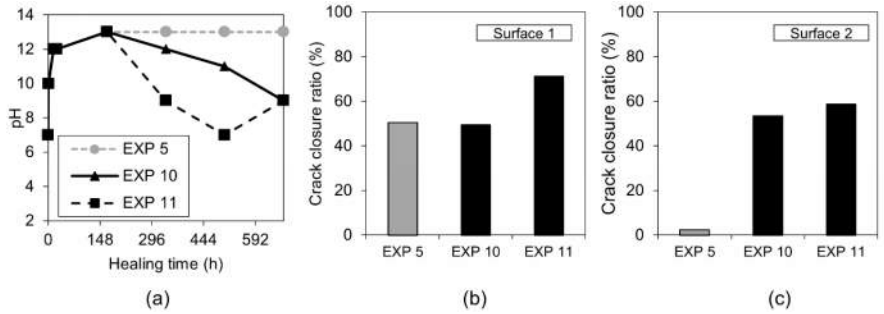

Figure 3.19. (a) pH changes in time for Exposures 5, 10, and 11; Crack closure ratio for different temperature exposures: (b) on Surface 1, (c) on Surface 2 (Rajczakowska et al., 2019c).

Calcite precipitation was the main healing phase for Exposure 10 (Figure 3.212ab), where higher temperatures possibly accelerated the reaction (Roig-Flores et al., 2016). On the other hand, calcite and ettringite were observed in the low-temperature cycle (Exposure 11, Figure 3.21cd), which agrees with other studies (Liu et al. 2017). Furthermore, analysis of the cross-sections of the specimens revealed limited quantities of self-healing products deeper inside the cracks for both temperatures. Nevertheless, based on the crack closure results, it can be concluded that temperature cycles have a presumably positive effect on crack healing; however, the healing is limited, possibly due to the short cycle. A similar observation was made by other researchers (e.g., Suleiman and Nehdi, 2018).

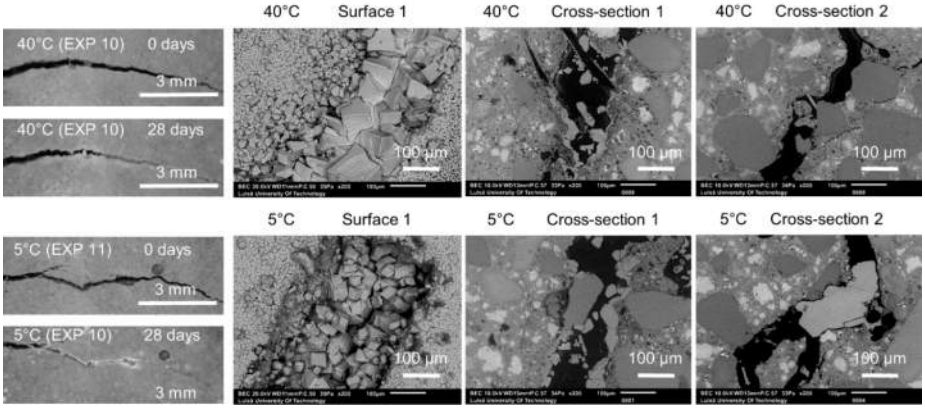

Figure 3.20. Representative images of surfaces and cross-sections of specimens healed at various temperature variation cycles (Exposure 10 and 11) (Rajczakowska et al., 2019c).

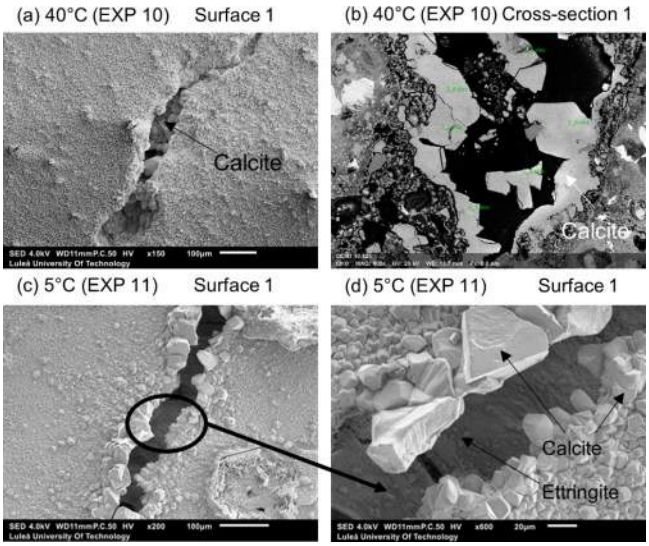

Figure 3.21. (a) Calcite on the surface of the crack healed at 40°C (EXP 10, SEM SE image 150x), (b) Calcite inside the crack (Cross-section 1) healed at 40°C (EXP 10, SEM BSE image 800x), (c) Ettringite on the surface of the crack healed in 5°C (EXP 11, SEM SE image 200x), (d) Ettringite on the surface of the crack healed in 5°C (EXP 11, SEM SE image 200x) (Rajczakowska et al., 2019c).

Accelerating and retarding admixtures

An attempt to modify the reaction rate inside the crack was made by adding accelerating (Exposure 1) and retarding admixtures (Exposure 2) into the water exposure. Representative images of Surface 1 and specimens' cross-sections for Exposure 1 and 2 are demonstrated in Figure 3.22.

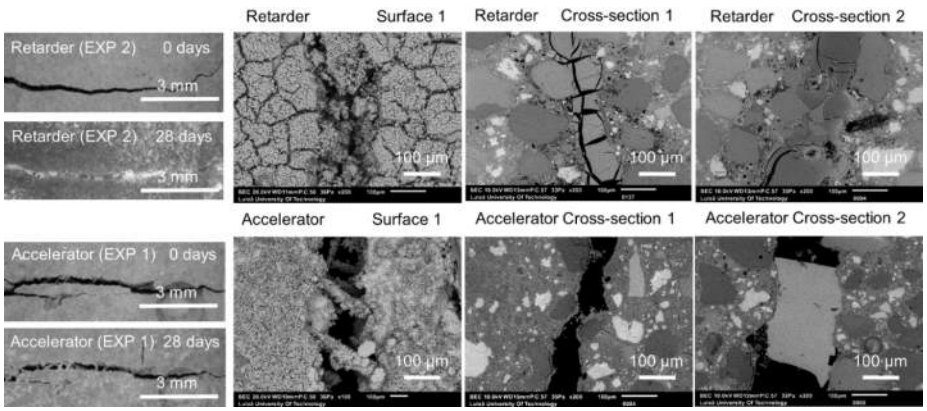

Figure 3.22. Representative images of the surface and cross-sections of the specimens healed in Exposures 2 (Retarder) and 1 (Accelerator) (Rajczakowska et al., 2019c).

It is visible that the retarding admixture addition facilitated the crack closure both at the crack mouth and deeper inside the crack, as detected on SEM images of the cross-sections (Figure 3.22 top). The crack closure ratio was close to 1 for both Surface 1 and 2 (Figure 3.23bc), indicating almost complete crack sealing. On the other hand, the efficiency of healing in accelerating admixture did not show a substantial increase in comparison to reference Exposure 5, where tap water was used (Figure 3.23bc)

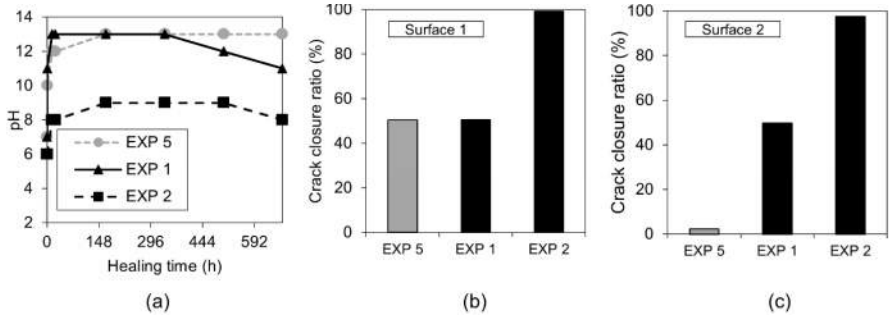

Figure 3.23. (a) pH changes in time for Exposures 5, 1, and 2; Crack closure ratio for Exposures 5, 1, and 2: (b) on Surface 1, (c) on Surface 2 (Rajczakowska et al., 2019c).

Analysis of the pH changes indicated that accelerator exposure did not affect the pH of the solution, as it followed the pattern of the reference Exposure 5 (Figure 3.23a). In contrast, a nearly constant pH equal to approximately 9 was obtained in the case of Exposure 2 (retarding admixture) throughout the healing process (Figure 3.23a).

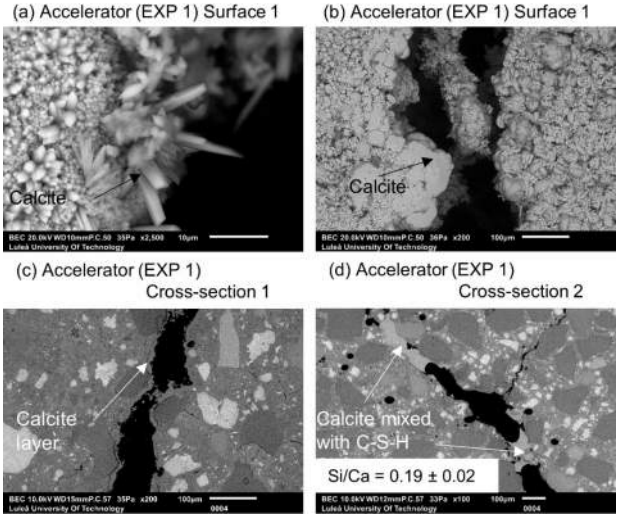

Figure 3.24. Different forms of calcite on the Surface 1 of EXP 1 specimen: (a) SEM BE 2500x, (b) SEM BE 200x, (c) EXP 1 Cross-section 1 – visible calcite layer (SEM BE 200x), (d) EXP 1 Cross-section 2 healing products (SEM BE 100x) (Rajczakowska et al., 2019c).

In addition, the morphology and chemical composition of the healing phases at the crack mouth and inside the crack was performed using SEM with EDS. In the accelerator (Exposure 1) case, calcium carbonate dominated as a healing product with various morphologies (Figure 3.24ab). The formation of different types of $CaCO_3$ could be presumably linked to the different concentrations of ions CO_3^{2-} and Ca^{2+} in the healing solution (Kirov et al., 1972; Choi et al., 2017) compared to the pure water immersion (Exposure 5). Nevertheless, the healing process was restricted almost entirely to the crack mouth, with only a limited amount of calcite presumably mixed with C-S-H, with a Si/Ca ratio of 0.19, visible at the cross-sections (Figure 3.24cd).

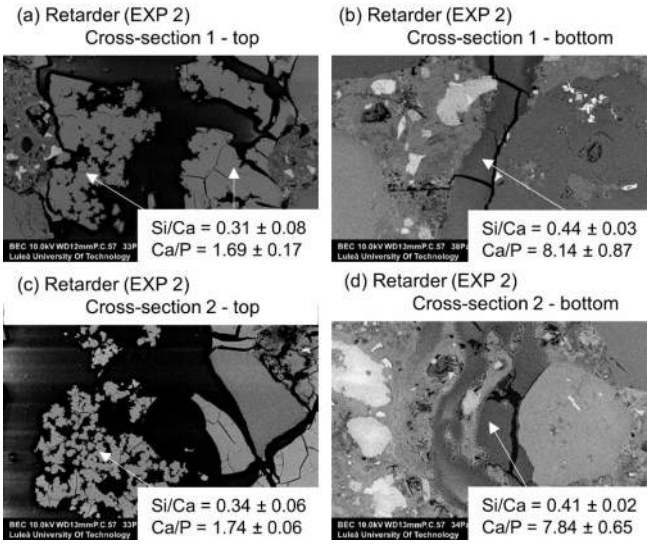

Figure 3.25. (a) Self-healing products at Cross-section 1 at the top of the crack – close to the crack opening (EXP 2, SEM BSE image 600x), (b) Self-healing products at Cross-section 1 at the bottom of the crack (EXP 2, SEM BSE image 100x), (c) Self-healing products at Cross-section 2 at the top of the crack (EXP 2, SEM BSE image 600x), (d) Self-healing products at Cross-section 2 at the bottom of the crack (EXP 2, SEM BSE image 600x) (Rajczakowska et al., 2019c).

On the other hand, in the case of retarding admixture (Exposure 2), distinct chemical composition and morphology of the self-healing products were observed (Figure 3.25). SEM analysis detected the formation of phases containing calcium and phosphorus with traces of silicon and aluminum. In addition, a pattern was noted concerning the Si/Ca and Ca/P, which presumably increased with the distance from the surface (crack mouth) at both cross sections 1 and 2 (Figure 3.25a-d, Figure 3.26ab), suggesting a higher concentration of ions deeper inside the crack.

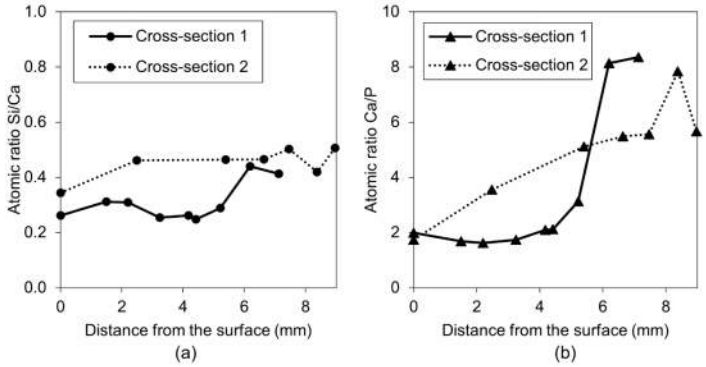

Figure 3.26. (a) Si/Ca atomic ratio of the self-healing products vs. the crack length measured at Cross-sections 1 and 2 for Exposure 2 (Retarder), (b) Ca/P atomic ratio of self-healing products vs. crack the length measured at Cross-sections 1 and 2 for the Exposure 2 (Retarder) (Rajczakowska et al., 2019c).

The presence of phosphorus in the elemental analysis of the self-healing materials inside the crack is associated with the chemical composition of the retarding admixture containing sodium metaphosphate. It can be speculated that chemical reactions occur inside the crack, including ions from the dissolved admixture in water, with the ions transported into the crack from the unhydrated cement grains and binder matrix, e.g., calcium from Portlandite. The phosphate-based admixture retarding action is associated with the forming of an adsorption layer on the anhydrous clinker grains, isolating them from contact with water and preventing the release of ions into the crack (Tan et al. 2017). It can be hypothesized that the phosphate anions bond with calcium ions to form unstable compounds (Kalina et al. 2016). However, later the phosphate compounds likely dissolve into the crack, forming less soluble phases, such as C-S-H and, with high enough phosphate concentration, calcium hydroxyapatite (HAP) (Kalina et al. 2016; Bénard et al. 2005). The growth of calcium-phosphate compounds could explain the low pH of the crack solution (Mekmene et al., 2009). The visible cracking of the healing products inside the crack (Figure 2.25b) might be related to shrinkage caused by other chemical reactions (Bénard et al., 2008). It should be noted that the cracking could result in a durability decrease; therefore, further testing of this approach, e.g., water permeability tests, should be conducted.

Additional ions/particles in the self-healing solution

Environmental exposures, including water mixed with additional ions and particles, were studied as a possible stimulator of the healing process, i.e., additional phosphate ions (Exposure 4, Coca-Cola), calcium ions (Exposure 3, lime water), and micro-silica particles (Exposure 12). Exemplary images of the crack mouth and specimen cross-sections are demonstrated in Figure 3.27. It is visible that each of the exposures had a significant effect on the crack closure.

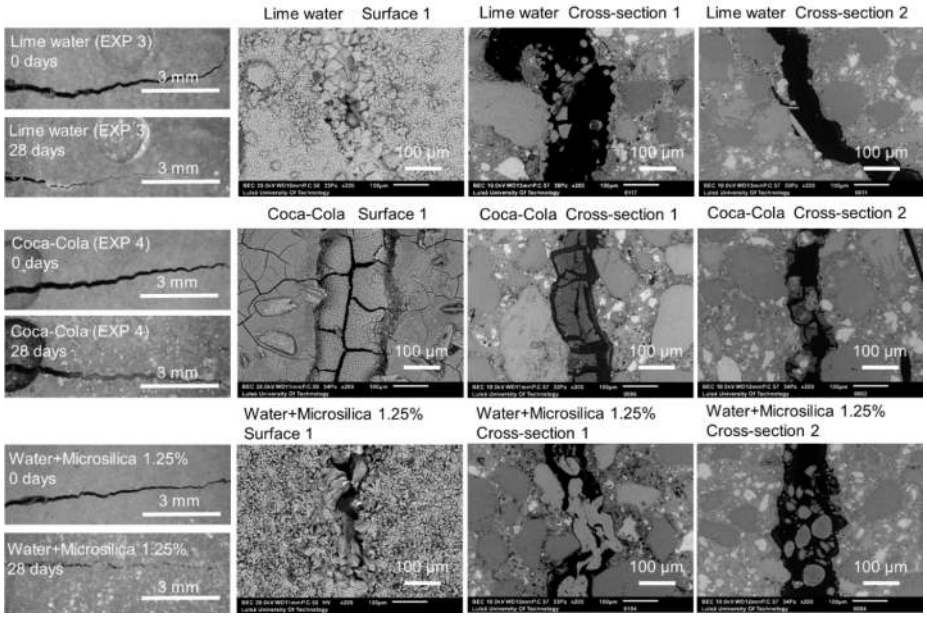

Figure 3.27. Representative images of surfaces and cross-sections of specimens healed in Exposures 3 (lime water), 4 (Coca-Cola), and 12 (water and 1.25%w micro-silica particles) (modified from Rajczakowska et al., 2019c).

On Surfaces 1 and 2, the crack closure of the analyzed Exposures 3, 4, and 12, reaching between 60% and 80%, was considerably higher than that of the reference Exposure 5 (Figure 3.28bc). The crack mouth was almost entirely closed (crack closure equal to 80%) for the micro-silica mixture (Exposure 12); however, Exposure 2 (retarding admixture) presented better performance, reaching almost 100% (Figure 3.28bc). The pH of the healing solutions increased at the beginning, followed by a substantial decrease and stabilization at approximately 9, after 14 days (Figure 3.28a).

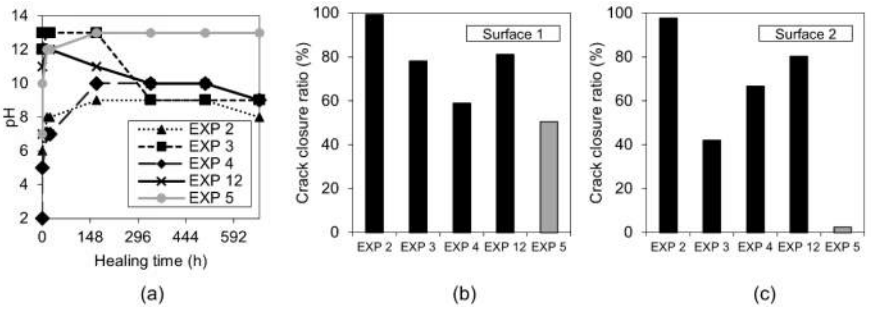

Figure 3.28. (a) pH changes in time for Exposures 5, 3, 3, 4, and 12; Crack closure ratio for Exposures 5, 3, 3, 4, and 12: (b) on Surface 1, (c) on Surface 2 (Rajczakowska et al., 2019c).

Analysis with SEM and EDS suggested that in the case of limewater exposure (Exposure 3), a mixture of calcite and C-S-H was formed externally and, to some extent, deeper inside the crack (Figure 3.30cd). The chemical composition of the formed phases was relatively constant with the distance from the crack mouth, with a Si/Ca ratio of around 0.3 (Figure 3.29b). On the other hand, in the micro-silica water mixture (Exposure 12), a dense layer of calcium carbonate mixed with C-S-H was observed at the surface and slightly below it at Cross-section 1 (Figure 3.30ab). Deeper inside the crack, the Si/Ca of the crack filling increased (Figure 3.29c). Investigation of the morphology of the found material indicated that, presumably, micro-silica particles sedimented inside the crack and blocked it at higher depths (Figure 3.30b). Those particles possibly served as nucleation sites for the self-healing products, i.e., calcite, closer to the crack mouth, where the ion concentration was optimal (Figures 3.28 and 3.30a).

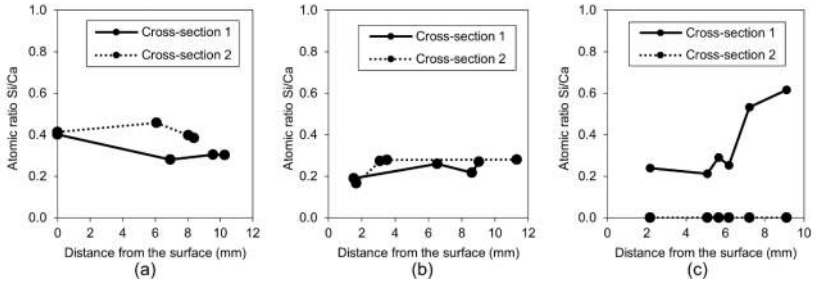

Figure 3.29. Si/Ca atomic ratios: (a) Exposure 4 (Coca-Cola); (b) Exposure 3 (Lime water), (c) Exposure 12 (micro-silica) (Rajczakowska et al., 2019c).

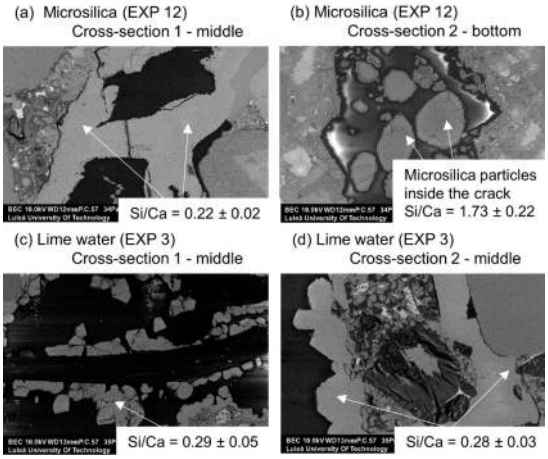

Figure 3.30. (a) Self-healing products in Cross-section 1 in the middle of the crack (EXP 12, SEM BSE image 400x), (b) Self-healing products at Cross-section 2 at the bottom of the crack (EXP 12, SEM BSE image 400x), (c) Self-healing products at the Cross-section 1 in the middle of the crack (EXP 3, SEM BSE image 500x), (d) Self-healing products at the Cross-section 2 in the middle of the crack (EXP 3, SEM BSE image 1000x) (Rajczakowska et al., 2019c).

In contrast, Exposure 4 followed a similar behavior as Exposure 2, possibly due to the presence of phosphate ions and sucrose (Zhang et al. 2010). Calcium-phosphate-like compounds were observed in the crack, with Ca/P between 3 and 9 and some silicone (Figure 3.31). The Si/Ca ratio of the healing products at a distance from the crack mouth did not show significant changes. Nevertheless, the unknown chemical composition of the Coca-Cola solution prevents a complete understanding of the possible self-healing mechanism.

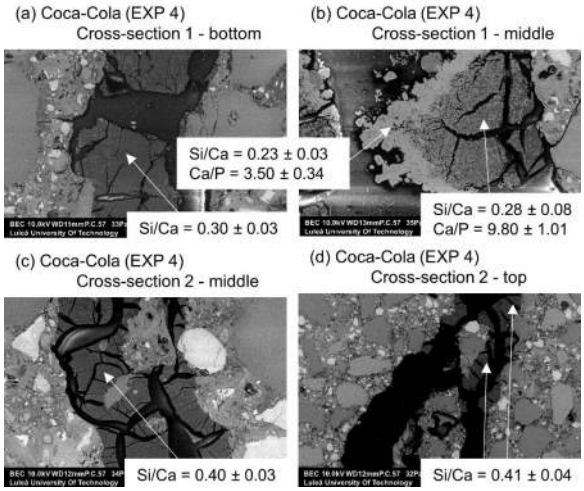

Figure 3.31. Exposure 4, Self-healing products in Cross-section 1 (a) at the bottom of the crack (SEM BSE image 400x), (b) in the middle of the crack (SEM BSE image 600x); Self-healing products at Cross-section 2 (c) in the middle of the crack (SEM BSE image 600x), (d) at the top of the crack (SEM BSE image 100x) (Rajczakowska et al. 2019c).

Exposure conditions vs. Strength recovery

Further analysis included verification of flexural strength recovery (Figure 3.32c) for selected environmental conditions which demonstrated relatively efficient crack healing, i.e., Exposure 2 (Retarder), Exposure 3 (limewater), Exposure 4 (Coca-Cola), Exposure 5 (reference, water immersion), Exposure 6 (water evaporation), Exposure 12 (water with micro-silica) and Exposure 0 (cured in the air) as control. In addition, to verify the influence of the changes in healing mixture concentration, two new amounts of Retarder and micro-silica were used, i.e., 7 wt% and 2.5 wt%, as Exposures 2a (retarding admixture) and 12a (micro-silica), respectively. Furthermore, the crack closure ratio for Surface 1 (Figure 3.32a) and Surface 2 (Figure 3.32a) was calculated based on the optical microscope images for the same specimens on which the strength was measured.

The crack closure ratio for analyzed specimens was relatively high in the case of Surface 1 for all exposure conditions (Figure 3.32a). On the other hand, Surface 2 demonstrated a lower value with higher variation, possibly because the large width of the

crack at the opening was relatively constant (Figure 3.33b). In general, the best performance was obtained for Exposure 2 (retarding admixture)

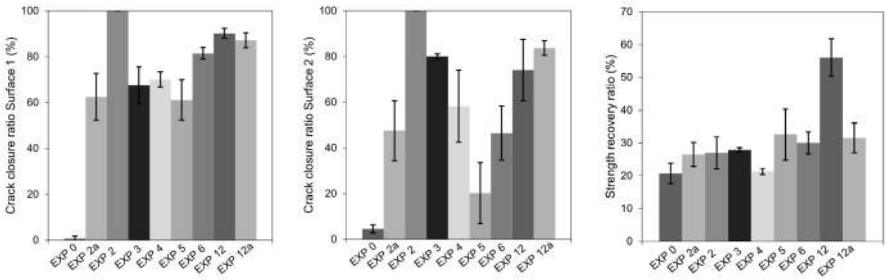

(a) (b) (c)

Figure 3.32. (a) Crack closure of selected exposures for Surface 1; (b) Crack closure of selected exposures for Surface 2; (c) Strength recovery for selected exposures (modified from Rajczakowska et al., 2019c) (Rajczakowska et al. 2019c).

Nevertheless, the flexural strength recovery was not impressive, with values similar to air exposure, which had no crack closure (Exposure 0, Figure 3.32ab). A more pronounced recovery was only visible for Exposure 12 (water with micro-silica particles). On the other hand, the sealed cracks of Exposure 2 (retarding admixture) did not lead to strength regain. A more thorough discussion of the results with possible mechanisms behind self-healing is presented in Chapter 5 of this thesis.

Exposure conditions vs. Mix composition

In addition, selected healing exposures were applied for mortars with partial cement replacement. Samples were prepared with Portland cement CEM I 42.5 N and 20wt% (by binder) replacement with blast furnace slag (mix CS) and fly ash (mix CFA). The water-to-binder ratio was 0.35, and binder to sand ratio was 1 (Table 3.2).

All the specimens exhibited visible self-healing at the crack mouth, except for the reference ones cured in air. Images of the side of the crack (Surface 1) for selected exposures (water cycle, lime water, and Retarder 30%), obtained before (0 days) and after healing (28 days) are shown in Figure 3.33 for slag samples and Figure 3.34 for fly ash samples.

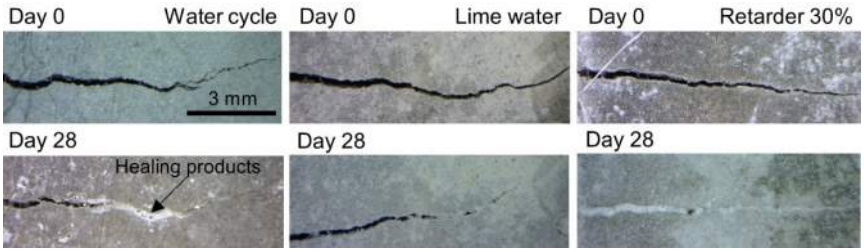

Figure 3.33. Optical microscope images before (day 0) and after healing (day 28) of slag samples for selected exposures (Rajczakowska et al. 2020).

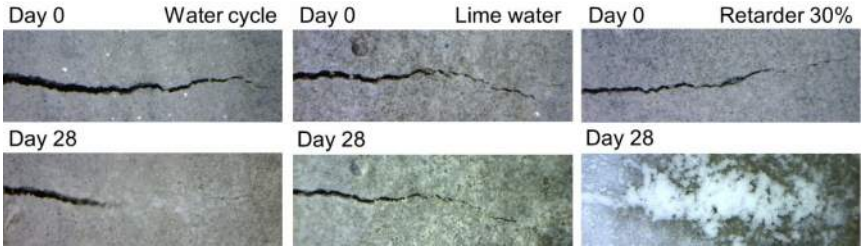

Figure 3.34. Optical microscope images before (day 0) and after healing (day 28) of fly ash samples for selected exposures (Rajczakowska et al. 2020).

The calculation based on the digital optical microscope images confirmed that the crack closure above 50% was achieved for almost all the exposures (Figures 3.35a and 3.36a). The most effective healing was achieved for a 30% retarder mixture for slag and fly ash mixes. Very good crack closure was also observed in the 7% retarder and micro-silica mixture exposures. Water cycles were more effective than constant water immersion. Lime water did not significantly improve the crack closure compared with deionized water conditions.

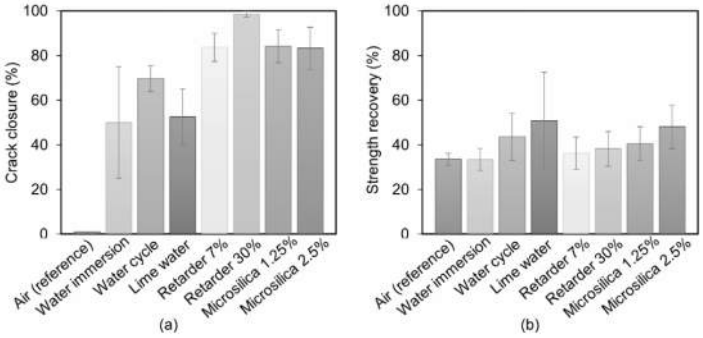

Figure 3.35. Self-healing results of slag samples for different exposures: (a) crack closure, (b) strength recovery (Rajczakowska et al. 2020).

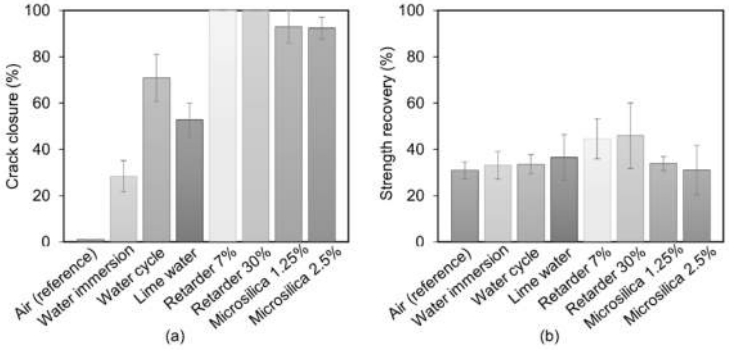

Figure 3.36. Self-healing results of fly ash samples for different exposures: (a) crack closure, (b) strength recovery (Rajczakowska et al. 2020).

None of the exposures resulted in significant flexural strength recovery. However, the highest strength regain was found in lime water specimens for slag samples and retarder mixtures for fly ash mortars (Figures 3.35b and 3.36b).

The pH measurements showed significant differences for water cycles, lime water, and retarding admixture (Figure 3.37). It suggests different kinetics and mechanisms behind the self-healing processes inside the crack. The observed characteristics of the pH changes are consistent with previous findings for cement mortars (Rajczakowska et al. 2019c).

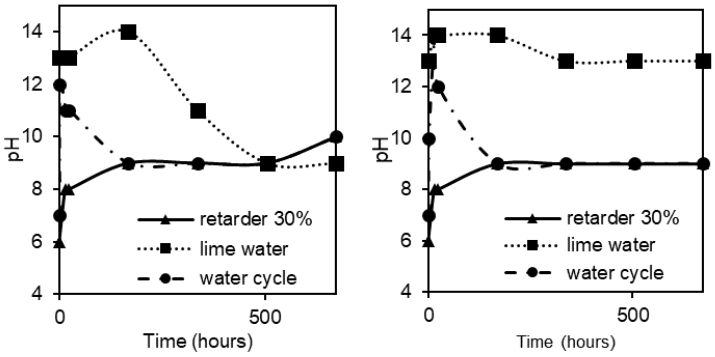

Figure 3.37. Registered pH changes for selected exposures for: (left) slag and (right) fly ash specimens (Rajczakowska et al. 2020).

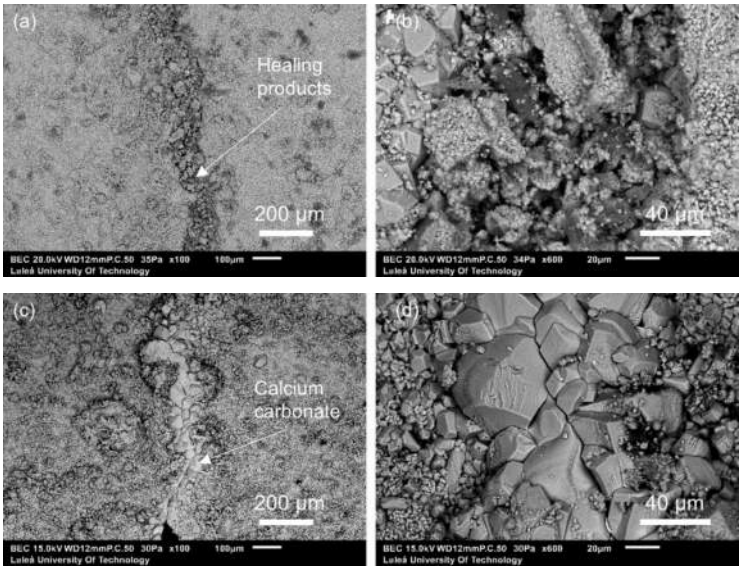

Figure 3.38. Scanning Electron Microscope images of the self-healing products inside the crack of the specimens exposed to water cycles: (a) slag (SEM BSE 100x), (b) slag (SEM BSE 600x), (c) fly ash (SEM BSE 100x), (d) fly ash (SEM BSE 600x) (Rajczakowska et al. 2020).

Scanning Electron Microscope analysis demonstrated that most self-healing products inside the cracks healed in water and limewater corresponded to calcium carbonate crystals (Figures 3.38abcd and 3.39abcd). A similar pattern was identified earlier (e.g., Huang et al. 2014).

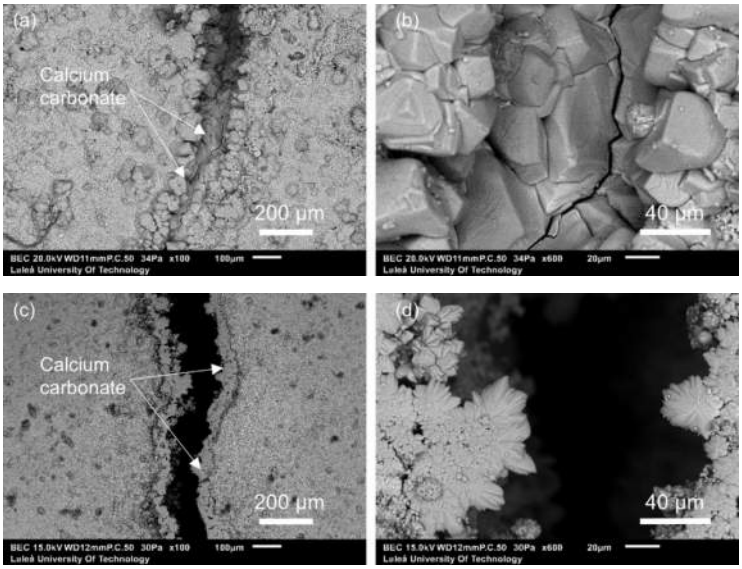

Figure 3.39. Scanning Electron Microscope images of the self-healing products inside the crack of the specimens exposed to lime water: (a) slag (SEM BSE 100x), (b) slag (SEM BSE 600x), (c) fly ash (SEM BSE 100x), (d) fly ash (SEM BSE 600x) (Rajczakowska et al. 2020).

The morphology of the self-healing products of the samples exposed to retarding admixture, which exhibited the most effective crack closure, was visibly different (Figure 3.40ab). Further chemical analysis using EDS indicated a mixture of C-S-H and calcium phosphate compounds.

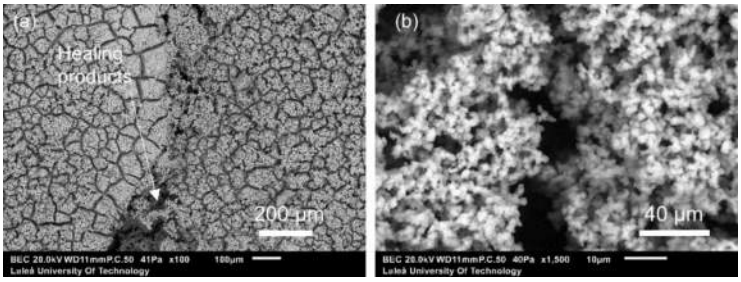

Figure 3.40. Scanning Electron Microscope images of the self-healing products inside the crack of the specimens exposed to retarding admixture: (a) slag (SEM BSE 100x), (b) slag (SEM BSE 600x), (c) fly ash (SEM BSE 100x), (d) fly ash (SEM BSE 600x) (Rajczakowska et al. 2020).

The further potential of the retarding admixture was demonstrated based on the images of the cross-section of the slag specimen (Figure 3.41). It was visible that the crack was filled with self-healing products on the surface and inside the sample. On the other hand, the specimen exposed to water cycles did not show a similar trend, despite relatively successful external crack closure. Unfortunately, internal healing did not contribute to flexural strength recovery (Figures 3.35b and 3.36b).

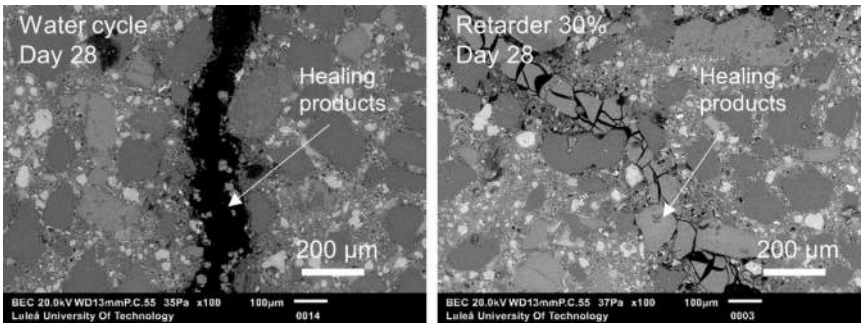

Figure 3.41. Cross-section of the crack for the slag specimen exposed to (a) water cycle, (b) retarding admixture (Rajczakowska et al. 2020).

3.2.4. Effect of mix composition

Initial study – high strength mortars and UHPC

Preliminary studies (*Study A*, Figure 3.1) focused on evaluating the self-healing of UHPC mixes (U1) compared to high-strength mortars, with 20%wt fly ash (B1) and without fly ash (A1). All specimens were cracked at one day and contained PVA fibers.

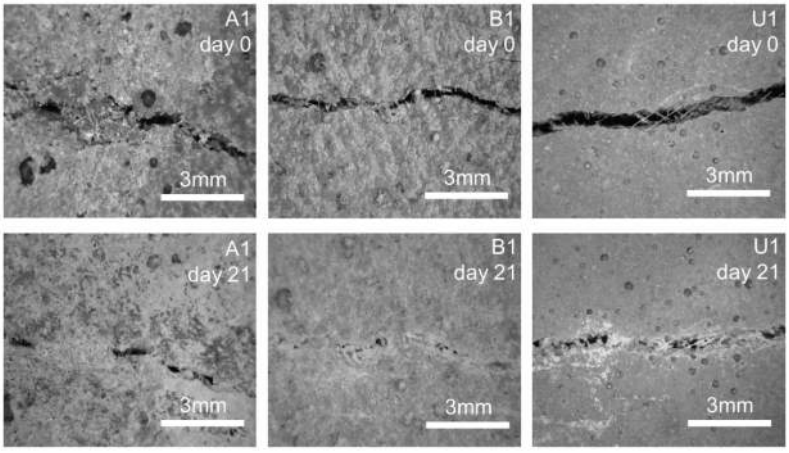

Figure 3.42. Example of light microscope images of the crack before healing. Four images were taken for each sample: (a) A1, (b) B1, (c) U1, and after 21 days of storage in water: (d) A1, (e) B1, (f) U1. (Rajczakowska et al. 2019b)

Representative images before and after healing for each mix are shown in Figure 3.42. All mixes demonstrated visible partial crack sealing, with the highest crack closure ratio of approximately 0.8 for mix B1 containing 20%wt of fly ash (Figure 3.43a). In addition, white precipitates were visible on the surface of the PVA fibers suggesting that they facilitated the self-healing process by serving as nucleation sites (Kan et al., 2010). At the crack mouth, calcium carbonate precipitation was observed with cuboid-like crystals visible on SEM images (Figure 3.43bc)

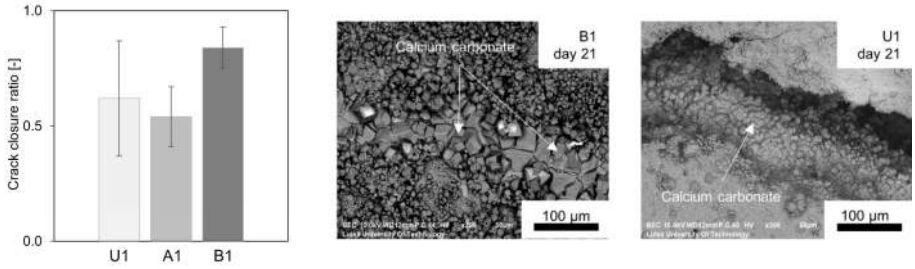

(a) (b) (c)

Figure 3.43. (a) Crack closure ratio; and SEM BE images (300x) of the crack at the surface for (b) B1, (c) U1. (Modified from Rajczakowska et al. 2019b)

Specimens A1 and U1, based on OPC, demonstrated strength recovery (Figure 3.44ab); however, a noticeable scatter of the results could be observed, possibly due to the impact of crack characteristics, such as crack depth and tortuosity. In addition, it should be noted that the values of healed specimens (stored in water) were here compared with those of pre-cracked specimens kept in the air, justifying a high calculated recovery ratio (Figure 3.44a). Nevertheless, a significant difference was observed between the OPC mixes and mix B1 with fly ash, which did not achieve any strength regain (Figure 3.44b). As mentioned earlier, mix B1 exhibited high crack closure; however, the primary healing phase was calcite. On the other hand, as pointed out in Section 3.2.1, C-S-H phases were found deeper inside the crack of the U1 specimen, indicating that this load-bearing phase possibly contributed to the strength regain.

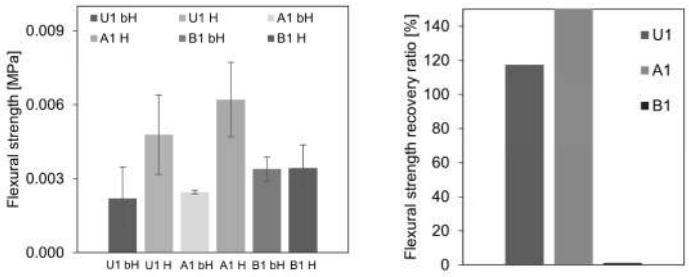

(a) (b)

Figure 3.44. (a) Flexural strength of cracked samples measured before healing (bH) and after healing (H), (b) flexural strength recovery ratio S for each type of mix. (Rajczakowska et al. 2019b)

Supplementary Cementitious Materials and limestone

Mortars with 50% cement replacement with limestone and SCMs (Table 3.3) were studied in the next stage of the research (*Study C,* Figure 3.1). Crack closure, mechanical performance regains, and water absorption rate was investigated as self-healing efficiency parameters.

Figure 3.45 shows the optical microscope images of the crack fragments for each mix before and after healing. Again, a white filling is noticeable in the cracks after healing, presumably corresponding to the calcium carbonate phases formed due to the calcite precipitation process.

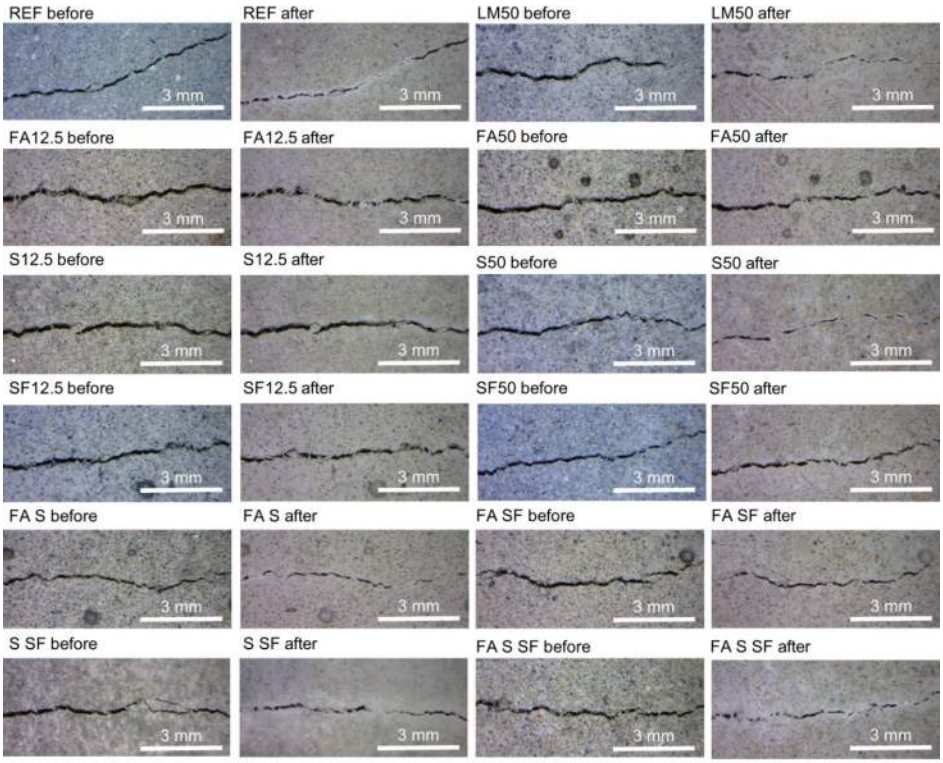

Figure 3.45. Images of the cracks before and after self-healing for selected mix compositions (Rajczakowska et al. 2023b)

Based on the optical microscope images, the calculated crack closure at the crack mouth is demonstrated in Figure 3.46. The crack closure parameters were divided based on the average crack width (Figure 3.46). The results suggested that the crack healing was more distinct for crack widths below 130 μm; however, the efficiency of crack closure was relatively low, with values below 60%, which can be possibly associated with the cyclic healing exposure (Suleiman and Nehdi, 2018). Therefore, increasing the wetting phase's

length or the total healing time could presumably promote more pronounced crack healing (Luo et al. 2021).

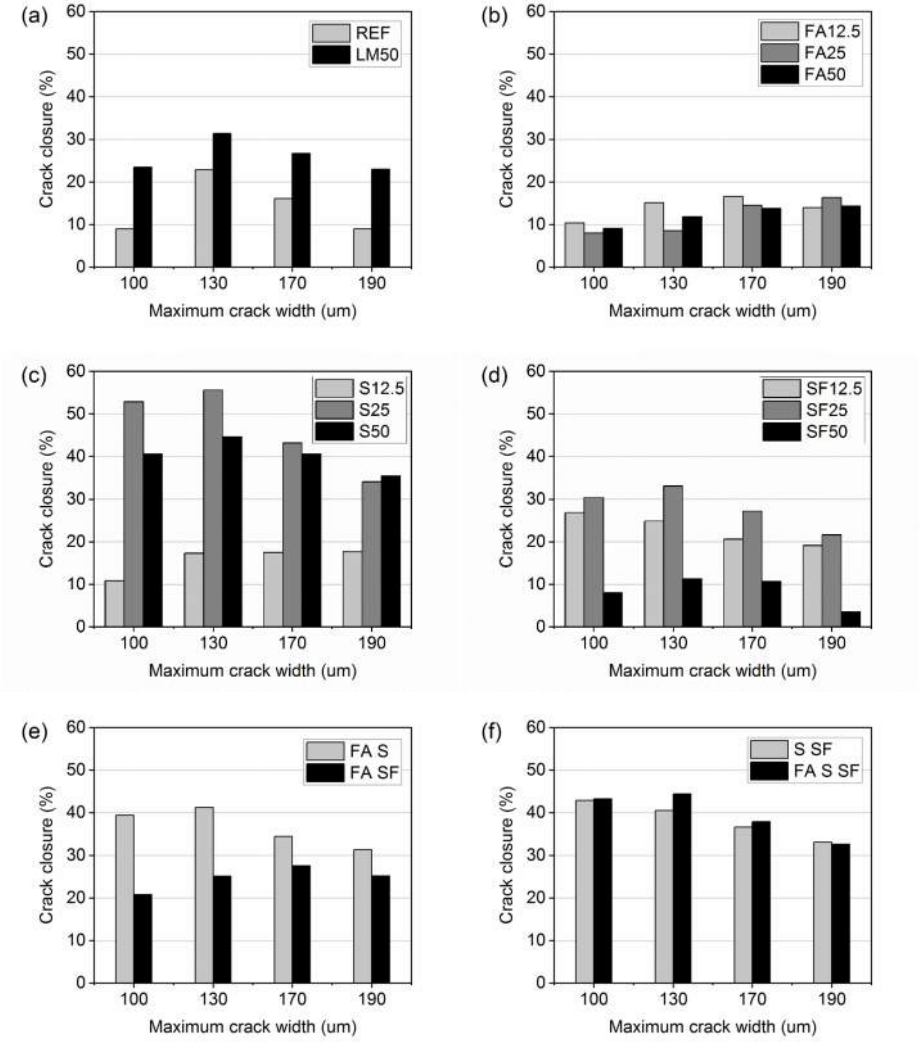

Figure 3.46. Crack closure (CC) for mixes: (a) REF and LM50, (b) FA12.5/25/50, (c) S12.5/25/50, (d) SF12.5/25/50, (e) FA S and FA SF, (f) S SF and FA S SF (Rajczakowska et al. 2023b)

The addition of limestone (LM50) improved the crack closure compared to the OPC mix (REF) (Figure 3.46a). Mortars with a high amount of slag, S25, and S50, demonstrated the highest crack closure reaching around 60% (Figure 3.46c). Other slag-based binders, i.e., ternary and quaternary binders FA S, S SF, and FA S SF, also performed better than the reference mix with pure OPC (Figure 3.46ef). On the other hand, the addition of fly ash

(mixes FA12.5, FA25, and FA50) seemed to hinder crack closure, possibly due to the low amount of CaO and decreased reactivity in Type F fly ash used (Namnoum et al. 2021).

Adding up to 25% of silica fume had no visible effect on the crack closure compared to the limestone mix (LM50). In contrast, a negative influence of silica fume was observed for the SF50 mix (Figure 3.46d).

Compressive strength recovery parameters, CSR80 and CSR100, are presented in Figures 3.47 and 3.48. In addition, the compressive strength results, mean value, and standard deviation, after 28 days and after the healing process of each damage extent (80% and 100%) are included in Annex A, Table A.1.

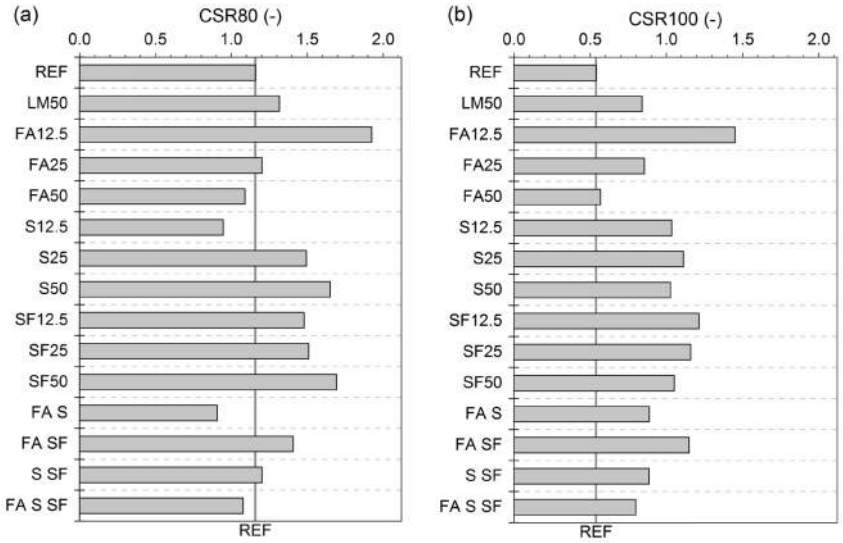

Figure 3.47. Compressive strength regains for all the mixes after self-healing: (a) after 80% damage, (b) after 100% damage (Rajczakowska et al. 2023b).

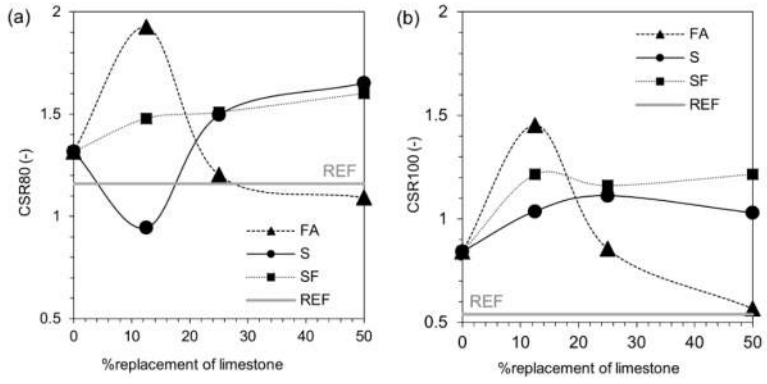

Figure 3.48. Changes of compressive strength regain with the wt% limestone replacement with FA, S, and SF: (a) after 80% damage, (b) after 100% damage (Rajczakowska et al. 2023b).

A low amount of fly ash (mix FA12.5) led to the most distinct strength recovery, both for 80% and 100% induced damage; however, higher amounts of fly ash (mixes FA25 and FA50) were less efficient (Figure 3.47ab, Figure 3.48ab). On the other hand, the relation was inverse for slag, i.e., increasing the slag content resulted in better strength recovery, which is primarily visible for lower damage extent (parameter CSR80, Figure 3.47a). Finally, no noticeable differences in CSR were obtained for varying the silica content; however, the overall effect of silica fume addition was favorable compared to the OPC mix (REF).

Nevertheless, several matters related to the proposed methodology should be discussed, which presumably had a high impact on the CSR results. First, it can be seen that the CSR values, especially for CSR80, are higher than 1. The definition of the CSR parameter used in this study compares the "healed" compressive strength with the strength of the intact specimens on the day of testing, i.e., 7 + 24 days. The approach was aimed to eliminate the bias resulting from the early age of cracking (7 days), which would occur if healed strength was compared to the strength before healing (at cracking, 7 days), ignoring the hydration and pozzolanic reaction taking place during the healing period, i.e., 24 days (Beglarigale et al. 2021). Therefore, this element cannot justify the high values of healed strength.

However, it should be noted that binders applied in this study contain large amounts of low-reactivity materials. For instance, F-type fly ash has very low reactivity, and even up to 90 days are required to reach the equivalent of 28-day strength (Gopalan, 1993). The higher fly ash replacement is used, the greater part of reactions occur at a later age (Gopalan, 1993). The cracked specimens had low hydration degrees, so many unhydrated particles were still present. Cracking was induced by compression, resulting in microcracks forming in the whole volume of the material. Damaged and intact specimens were subjected to water immersion for the healing period. Since the hydration and pozzolanic reaction were still ongoing, it can be speculated that water from the healing solution could reach the unhydrated grains via the microcrack network better than in the case of intact samples, possibly accelerating the hydration. For higher amounts of fly ash, there might not have been enough $Ca(OH)_2$ for the pozzolanic reaction, hence lower mechanical performance. In addition, other studies found dry and wet cycles to positively affect the compressive strength of SCM binders with fly ash, slag, and over 8% silica fume compared with the OPC mix (Toutanji et al. 2004). Even though seawater was used (Toutanji et al. 2004), the mechanism's similarities cannot be ruled out.

In addition, the cracks at 80% maximum load damage were likely finer than at 100%. Therefore, there is a higher probability of a complete crack sealing with self-healing products, in contrast to the cracks that occurred for a higher degree of damage. This effect is visible when comparing parameters CSR80 (Figure 3.47a) and CSR100 (Figure 3.47b). The strength recovery decreased for each mix with increasing damage amount. Other studies found the extent of damage significant for self-healing strength recovery. For example, it was observed that there is a specific "threshold" damage for the self-healing process efficiency (Zhong and Yao, 2008). Below the threshold, the self-healing efficiency increases with the greater extent of damage, whereas an opposite relation occurs above the

threshold. For certain loading degrees, materials' compressive strength after healing was observed to be slightly higher than before, even in the case of the OPC mixes cracked at 28 days (Zhong and Yao, 2008). These literature findings agree with the results of this research, i.e., CSR80 for REF was equal to 1.16. Therefore, it can be concluded that the strength recovery parameter possibly combines the reactions inside the binder matrix and the crack self-healing.

Finally, possibly due to immature microstructure and varied damage within the specimen's volume, the scatter of the results of the "healed" compressive strength is rather high, on average between ±5 and ±7 MPa (Annex A, Table A.1), which, for generally low strength of the SCM-modified specimens (20-40 MPa), contributes to a noticeable error. Nevertheless, the strength regains differences are relatively significant between the OPC mix and the SCM-limestone binders; thus, the conducted analysis can be considered valid.

A water absorption rate test was used to compare the transport properties recovery of the mortars. Figure 3.49 demonstrates the absorption curves versus the square root of time for each mix composition, whereas Figure 3.50 shows water absorption recovery parameters at 25 and 180 min (IR25 and IR180) and sorptivity recovery during 25 min (SR25). In addition, in Annex A, Table A.2, cumulative values of water absorption at 25 min (I25) and 180 min (I180, end of experiment) are listed together with the calculated sorption coefficient for the first 25 min S25 (mean values and standard deviations). It should be mentioned that only the results of the water absorption rate tests were acquired for the healed and intact specimens. The methodology is described in Section 3.1.

Mixes with large amounts of slag and silica fume (S50 and SF50) demonstrated healing efficiency almost two times better than the REF mix, both in terms of IR25 and IR180 (Figure 3.50a). In addition, slag binder S50 obtained results of SR25 close to 1 (Figure 3.50b), indicating that the recovery of material reached almost the value of the intact state, which is also visible in Figure 3.49c. The increase in fly ash from 12.5% to 50% hindered the self-healing process, whereas the opposite was visible for slag and silica fume binders. These results are consistent with the compressive strength results.

Higher strength and water absorption recovery parameters were observed compared to crack closure, measured at the crack mouth. It could indicate that the healing products formed deeper inside the crack, which would not be detectable by the optical microscope measurement. There can be several explanations for healing products growing inside the specimen. For instance, the crack geometry in depth might be different, e.g., uniform, convex and concave, and the sealing would occur in the narrowest points of the crack (Roig-Flores et al. 2015). On the other hand, the concentration of ions changes with crack depth, presumably controlled by the calcite layer formed at the crack mouth (Rajczakowska et al. 2019b). Therefore, different ion concentrations might facilitate the formation of load-bearing phases deeper inside the crack, e.g., C-S-H, which could enable strength recovery. In addition, healing products precipitation at depth but not at the crack mouth was found to be more pronounced for the wet/dry water immersion cycles (Luo et al. 2021).

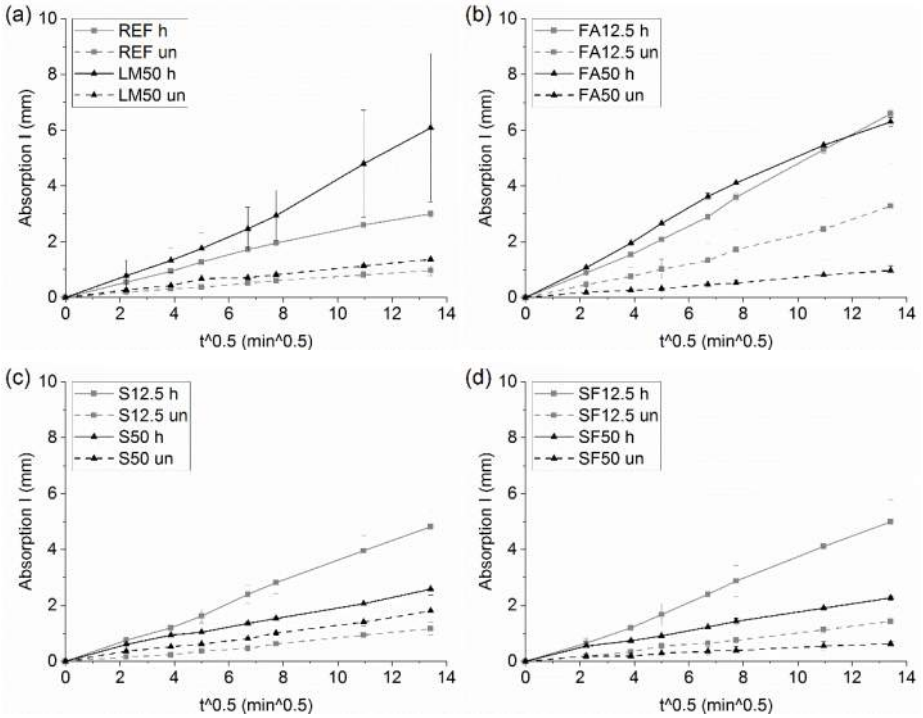

Figure 3.49. Measured water absorption curves (h – healed, un – undamaged specimen) for (a) REF and LM50, (b) FA12.5 and FA50, (c) S12.5 and S50, (d) SF12.5 and SF50 (Rajczakowska et al. 2023b).

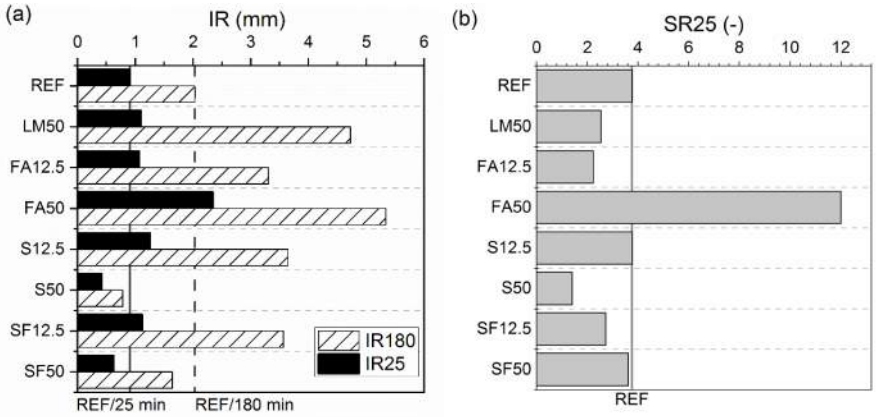

Figure 3.50. (a) Water absorption recovery at 25 and 180 min (IR25 and IR180), (b) Sorptivity recovery during 25 min (SR25) (the lower the value, the better the healing) (Rajczakowska et al. 2023b).

3.2.5. Effect of crack geometry

Crack tortuosity and fractal dimension were calculated based on the images of the crack taken in four positions (Section 3.1, Figure 3.5). In addition, the average and maximum crack widths were calculated using the local thickness algorithm (Section 3.1).

In Figure 3.51, the tortuosity (Figure 3.51a) and fractal dimension (Figure 3.51b) of the crack are presented, belonging to each average crack width group, i.e., 100, 130, 170, and 190 μm. No significant relation between the crack width changes and tortuosity was observed. On the other hand, the complexity of the crack presumably increased with the increased crack width (Figure 3.51b)

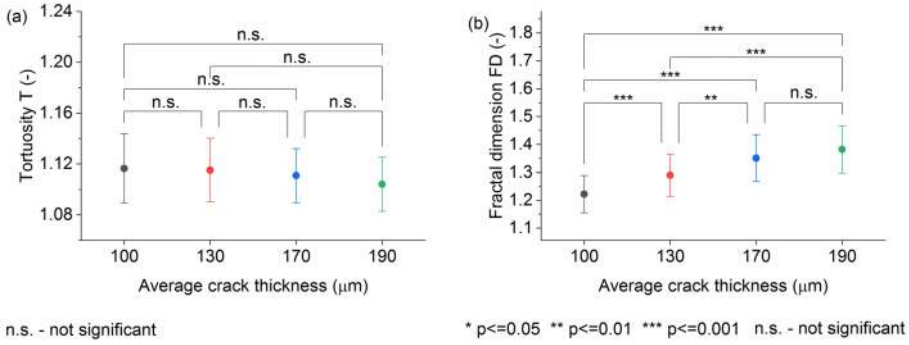

Figure 3.51. Relation between crack complexity parameters and average crack width: (a) tortuosity (T), (b) fractal dimension (FD) (Rajczakowska et al. 2023b).

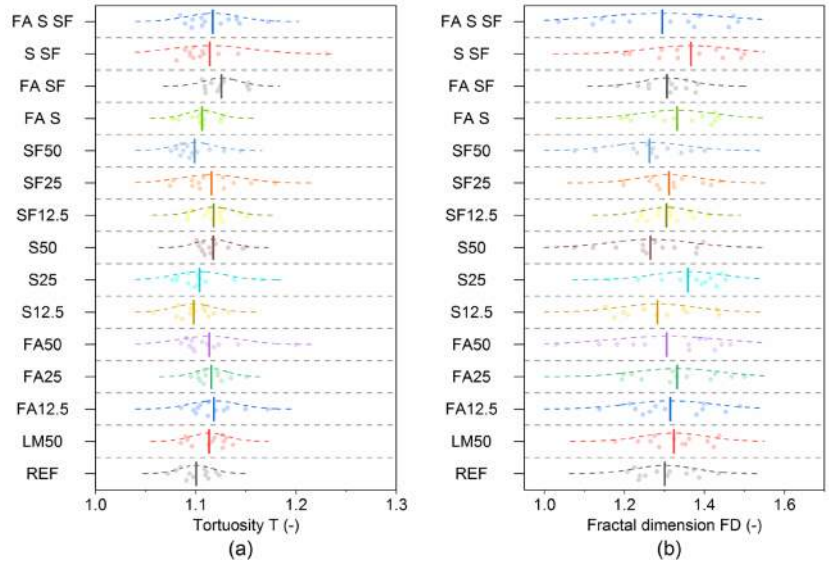

Figure 3.52. Complexity parameters of the cracks for each mix (scatter with mean line and normal distribution): (a) tortuosity (T), (b) fractal dimension (FD) (Rajczakowska et al. 2023b).

Analysis of the crack complexity parameters for each mortar mix indicated that only minor differences occurred. Despite a significant spread of the results, average tortuosity was between 1.1 and 1.13 (Figure 3.52a), whereas the fractal dimension (FD) for all the cementitious materials was between 1.26 and 1.37 (Figure 3.52b). These findings could suggest that, on average, the induced cracks did not vary significantly between the mix compositions, which validates to some extent the results of the water absorption rate test, relying on the similarity of damage. Minor differences could be attributed to the three-point bending test used to produce cracks and lack of coarse aggregate, leading to relatively linear cracks with limited complexity.

Pearson's linear correlation coefficients were calculated to examine the relations between initial crack geometry (ICA, T, FD, MCW, ACW) and self-healing efficiency (CSR80, CSR100, IR25, IR180, SR25, CC). Depending on the number of observation pairs, the statistical significance of the correlation coefficients were calculated at the significance level $\alpha = 0.05$. The coefficient values are presented in Figures 3.53ab and 3.54a, with marked statistically significant intervals.

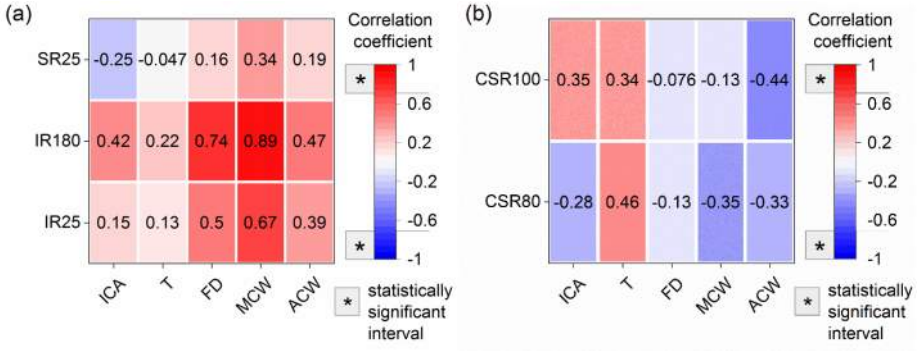

Figure 3.53. Pearson's linear correlation coefficients between initial crack geometrical parameters and (a) water absorption rate recovery, (b) compressive strength recovery parameters (Rajczakowska et al. 2023b).

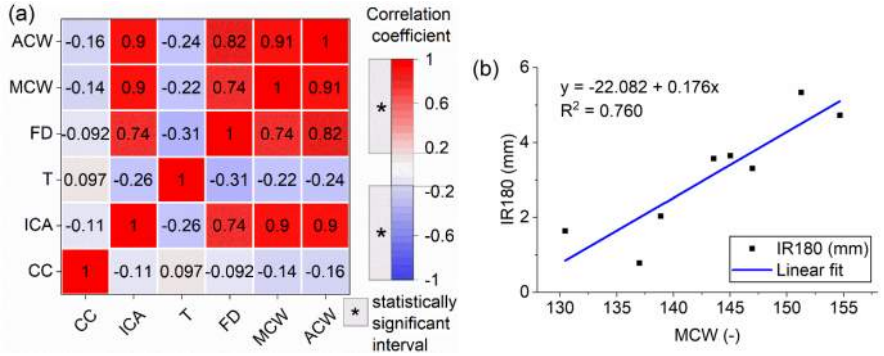

Figure 3.54. (a) Pearson's linear correlation coefficients between initial crack geometrical parameters and crack closure (b) relation between MCW vs. IR180 (Rajczakowska et al. 2023b).

Based on the acquired results, it is visible that the crack geometry had a limited effect on the crack closure at the crack mouth (CC) (Figure 3.54a) as well the strength recovery (Figure 3.53b). Nevertheless, a more particular relation could be observed between the fractal dimension (FD), maximum crack width (MCW), and recovery of transport properties (IR180). The correlation coefficient equals 0.74 for FD – IR180 and 0.89 for MCW – IR180, indicating a relatively strong correlation between these parameters (Figure 3.53a, Figure 3.54b). It could indicate that the more complex and wider the crack, the lower the self-healing performance of the material.

A very low correlation between crack closure and maximum and average crack width was surprising; however, they might be connected to the narrow range of values within the parameters. Therefore, future studies should focus on verifying the crack geometry effect on self-healing by investigating more extreme cracking cases without varying other potentially influential factors, such as binder composition.

3.2.6. Effect of initial microstructure

The effect of initial microstructural parameters related to the binder composition was investigated to facilitate the understanding and discussion of the self-healing mechanism.

First, the XRD studies were conducted on the initial intact microstructure of the hydrated binder paste for each composition at 7 days (Figure 3.55a-d). Particular attention was given to the amount of $Ca(OH)_2$ and $CaCO_3$ as presumable sources of calcium ions. These phases were marked with P and C in Figure 3.55a-d, corresponding to Portlandite and calcite.

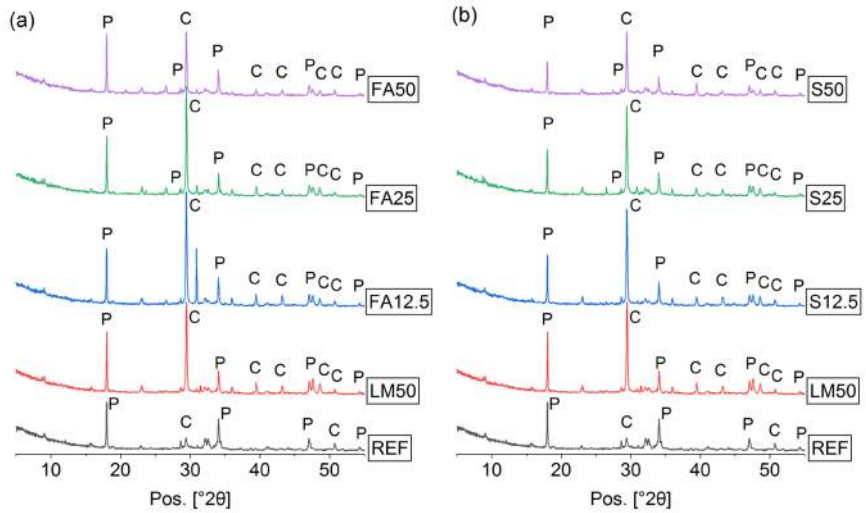

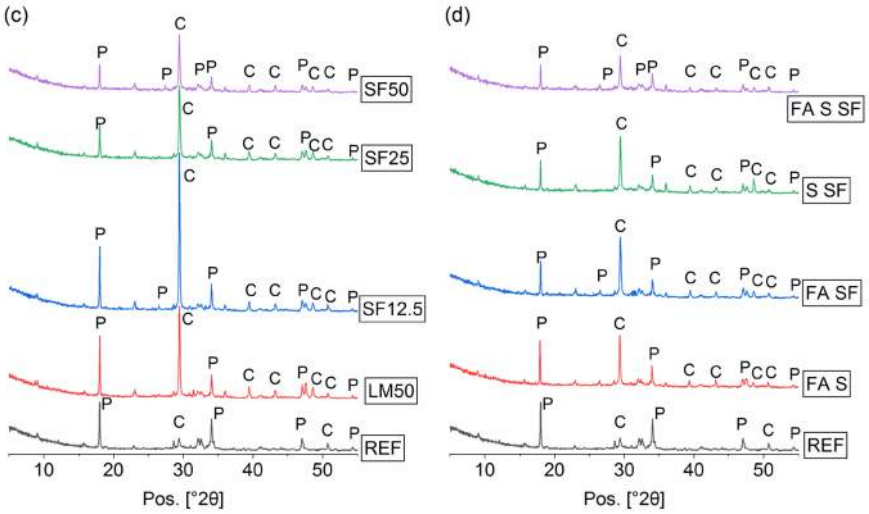

Figure 3.55. XRD patterns with marked Portlandite (P) and calcium carbonate (C) phases (Rajczakowska et al. 2023b).

The results revealed that, as expected, different binder formulations had different C and P peak intensities due to varied chemical compositions and chemical reactions occurring in the hydrated binder matrix. Therefore, a semi-quantitative comparison was performed by calculating the area under the first peak of each phase for Portlandite and calcite (Table 3.7).

Table 3.7. Calculated peak areas for Portlandite and calcium carbonate (Rajczakowska et al. 2023b).

Mix	**Portlandite At approx. 2θ=18°**		**Calcium carbonate At approx. 2θ=29°**	
	Peak Area (-)	FWHM (-)	Peak Area (-)	FWHM (-)
REF	78.001	0.123	22.806	0.199
LM50	82.546	0.103	230.526	0.188
FA12.5	86.041	0.113	285.189	0.182
FA25	87.740	0.108	251.088	0.177
FA50	88.863	0.111	153.797	0.185
S12.5	75.843	0.115	241.069	0.187
S25	68.424	0.107	196.889	0.168
S50	51.268	0.116	137.819	0.159
SF12.5	93.414	0.106	370.029	0.173
SF25	55.699	0.113	201.401	0.206
SF50	37.819	0.115	137.511	0.175
FA S	73.534	0.124	124.986	0.190
FA SF	52.063	0.119	164.117	0.214
S SF	45.042	0.104	153.214	0.194
FA S SF	35.681	0.109	81.325	0.183

Minimal changes in the amount of Portlandite were observed for different amounts of FA replacement (Table 3.7). A decreased amount of $Ca(OH)_2$ for S and SF presumably indicated that it was consumed in the pozzolanic reaction at 7 days since these binders are more reactive than FA. The lower consumption of Portlandite for FA binder can also be linked to low porosity (Figure 3.58), limiting the transport within the dense matrix and restricting the reactions (Durdziński 2016). On the other hand, the calcium carbonate phases decrease with the increasing ratio of SCMs, with the smallest values for ternary and quaternary binders - FA SF, S SF, and FA S SF, which can possibly be associated with the calcite consumption (Durdziński, 2016).

In addition, the Si/Ca ratio of the inner, high-density product of C–A–S–H gel was studied based on the SEM with EDS procedure presented in Section 3.1. Values between 0.4 and 0.6 were obtained depending on the mix composition (Figure 3.56). More significant amounts of silica fume replacement (mix SF50) resulted in a higher Si/Ca ratio equal to approximately 0.62, which was significantly higher than the OPC mix (REF) with a Si/Ca value of 0.42.

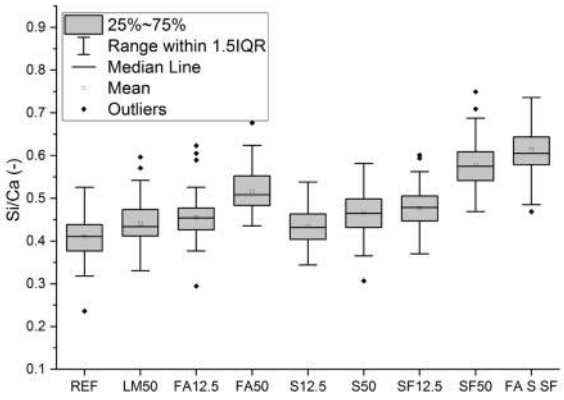

Figure 3.56. Effect of the mix composition on the IP C–A–S–H Si/Ca ratio (Rajczakowska et al. 2023b).

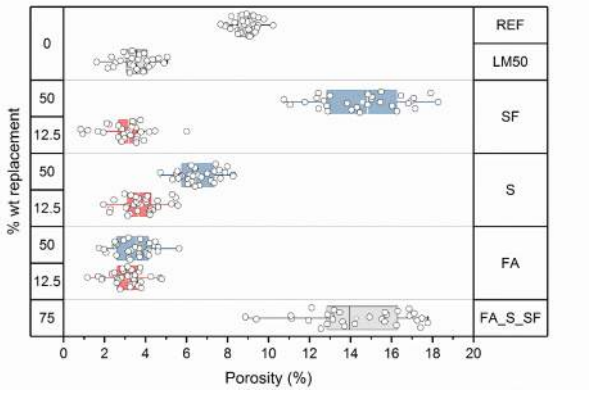

Figure 3.57. Effect of the mix composition on the porosity of the paste (Rajczakowska et al. 2023b).

In addition, the porosity calculation based on the SEM images (Section 3.1) showed apparent differences between different mix formulations (Figure 3.57, Table A.3. Annex A). For example, fly ash (FA12.5 and FA50), low slag (S12.5), silica fume (SF12.5), and limestone (LM50) mix exhibited relatively low porosity values between 3 and 5%. On the other hand, the OPC mix (REF), high slag (S50) and silica fume (SF50) replacement, and quaternary mix FA S SF were characterized by high porosity, reaching values of approximately 15%.

Pearson's linear correlation coefficient was calculated to examine the relations between phase composition (calcite, Portlandite, Si/Ca), microstructure (porosity), and self-healing efficiency (CSR, CC, IR25, IR180, SR25). The coefficient values are shown in Figure 3.58, with marked significant intervals calculated depending on the number of observation pairs at the statistical significance level $\alpha = 0.05$.

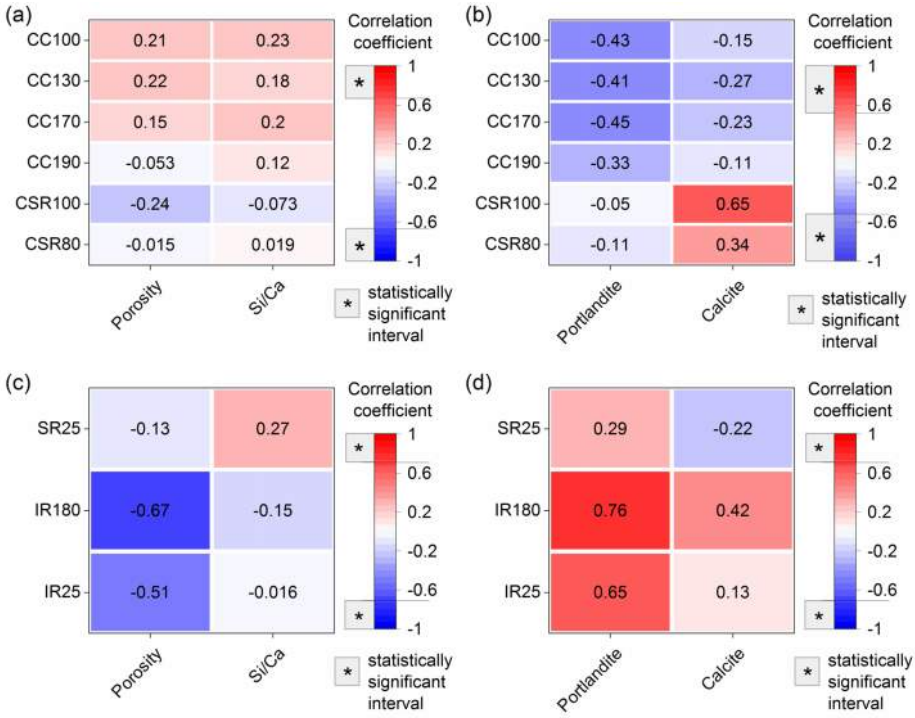

Figure 3.58. Pearson's linear correlation coefficients (r) between microstructure parameters/chemical composition and self-healing efficiency (Rajczakowska et al. 2023b).

A moderate negative correlation (correlation coefficient above 0.5) was obtained between the porosity of the hardened paste and water absorption recovery parameters (IR180 and IR25) (Figure 3.58c). In other words, a more porous binder matrix presumably leads to more efficient healing, which agrees with previous results in *Study A* (Initial studies). In addition, a more permeable matrix possibly enables the transfer of ions from the binder to the crack. However, no correlation was observed between the porosity and compressive strength recovery (Figure 3.58a). Therefore, it indicated that other variables,

such as the phase assemblage of the hardened binder, possibly drove the strength recovery. On the other hand, a moderate positive correlation was noticed between the amount of calcite and strength recovery, especially for the higher degree of damage (CSR100) (Figures 3.58b and 3.29a).

It should be mentioned that the porosity calculation was restricted by the two-dimensional character of the analysis, i.e., based on polished cross-sections of the specimen. As a result, it does not adequately describe the three-dimensional interconnectivity of the pores, critical from the point of view of the substance transport to the crack, which could be visualized using other techniques such as X-ray microtomography. In addition, the effect of pore size distribution and tortuosity of the transport path could be relevant (Durdziński, 2016).

The crack closure parameter (CC) showed a limited correlation with the amount of Portlandite. It could indicate that a smaller amount of Portlandite initially in the matrix leads to a higher degree of crack sealing at the crack mouth (Figure 3.58b). Correspondingly, a moderate positive correlation was observed between the Portlandite and water absorption recovery parameters, IR180 and IR25 (Figures 3.58d and 3.59b). In other words, less pronounced healing can be possibly expected when there is a high amount of Portlandite initially. Again, it could signify that more critical features govern the self-healing process.

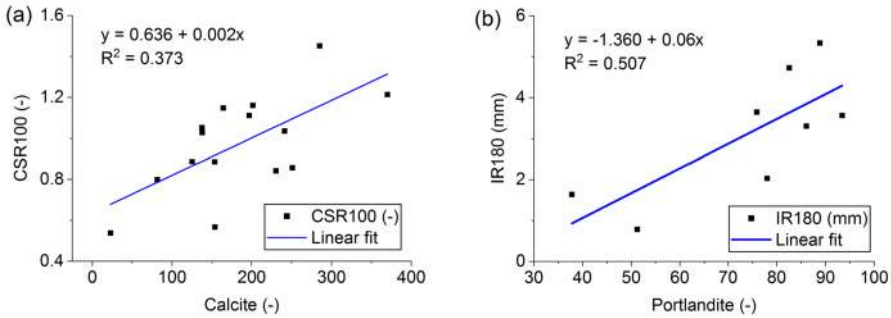

Figure 3.59. Most significant correlations with linear fit: (a) Calcite vs. CSR100, (b) Portlandite vs. IR180 (Rajczakowska et al. 2023b).

Since Portlandite is necessary for the pozzolanic reaction of SCMs, the analysis of the relation between $Ca(OH)_2$ and self-healing efficiency is affected by the reactivity of the binder components used in this study. For instance, a relatively low Portlandite amount at 7 days for silica fume (Table 3.7) could be caused by the fact that the pozzolanic reaction has already consumed most of the available CH. Therefore the remaining $Ca(OH)_2$ could serve as a calcium supply for the self-healing process. In contrast, low reactivity characteristics of fly ash result in more CH accessible at cracking age, which could be required for pozzolanic reaction later instead of supporting the self-healing of the cracks.

A more thorough discussion of the combined results from *Studies A, B,* and *C*, is presented in Chapter 5.

3.3. SUMMARY

In Chapter 3, the self-healing of mechanically cracked cementitious materials was studied, considering the environmental exposure, mix composition, cracking age, healing time, initial crack geometry, and microstructure.

The following main conclusions were established based on Chapter 3:

- A high amount of cement alone does not guarantee a successful self-healing performance
- Transport of ions from hydrated binder into the crack is crucial, and in the case of materials with dense binder matrix, such as UHPC, it can hinder their recovery performance
- Under constant water immersion, fly ash supported crack closure by calcite precipitation, but did not exhibit strength recovery, due to a limited amount of C-S-H at depth
- A pattern was observed regarding the spatial distribution of self-healing phases, i.e., calcium carbonate at the crack mouth and C-S-H and ettringite deeper inside the crack. Calcium carbonate did not support strength recovery but presumably controlled the ion concentration inside the crack
- All SCMs-limestone cementitious materials have shown better self-healing efficiency than pure OPC or OPC/limestone binders. Binder composition affected the self-healing mechanism leading to different levels of performance recovery
- The portlandite amount demonstrated higher correlation with the crack closure than the strength regains, contrary to the calcite amount. A higher amount of calcium carbonate in the hardened binder matrix results in a significantly higher strength regain due to the self-healing process
- Water absorption rate changes were found to be dependent on the geometrical complexity of the crack measured externally at the crack mouth
- Exposure to water alone enabled self-healing but only to a limited extent. Adding phosphate-based retarding admixture into the water resulted in a pronounced crack closure. On the other hand, mixing water with micro-silica promoted the recovery of strength

4

Thermally induced cracks

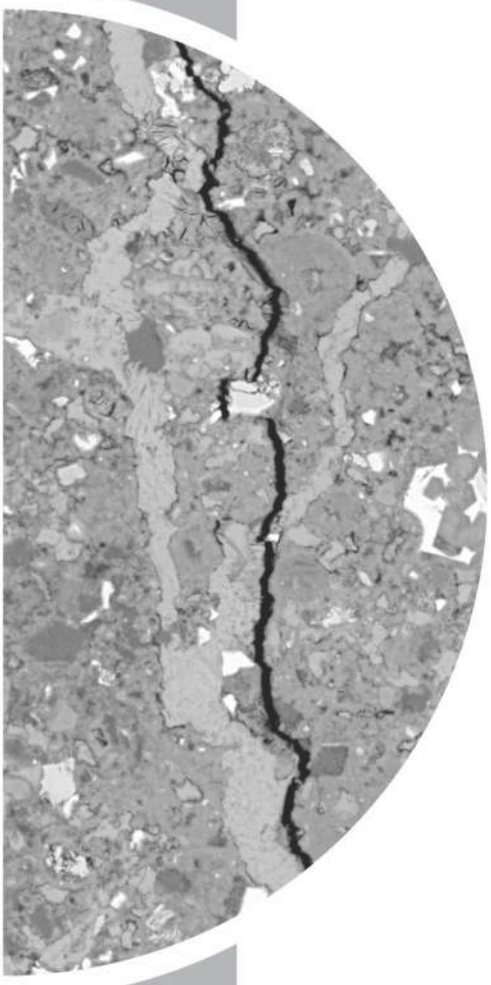

"All my life through, the new sights of Nature made me rejoice like a child"

Maria Skłodowska
1903 Physics and 1911 Chemistry
Noble Prize Winner

4. THERMALLY INDUCED CRACKS

Chapter 4 deals with the autogenous self-healing of high-temperature damage in cementitious materials. The methodology is presented in Figure 4.1. The goal of *Study A* was to construct an accurate prediction (mathematical model) of the compressive strength recovery due to the self-healing process based on an extensive database of experimental results from the literature. The obtained regression model was then analyzed, and the results of the interpretation pointed out the most critical variables affecting self-healing (Variables 1 and 2, Figure 4.1). In addition, after the literature review, Variable 3 was selected as a potential stimulator of the self-healing process (Figure 4.1). These elements determined further experimental plan, executed within *Study B* (Figure 4.1). In *Study B*, research was conducted to assess the self-healing efficiency of the high-temperature damage considering the influence of Variables 1, 2, and 3.

Chapter 4 describes the machine learning modeling (Section 4.1) and experimental part (Section 4.2.). Section 4.1 presents the modeling process and modeling results analysis together with the model interpretation. On the other hand, Section 4.2 includes information about the materials and methods used (Section 4.2.1) and an analysis of the obtained results (Section 4.2.2). Similarly to Chapter 3, the results are divided into subsections representing the factors related to the self-healing mechanism, i.e., environmental conditions, loading temperature, microstructural changes, and nanomaterials. A thorough discussion of the results and their implications regarding the proposed mechanism is presented in Chapter 5.

Chapter 4 was redrafted after (Rajczakowska et al. 2022), (Rajczakowska et al. 2023a), and (Rajczakowska et al. 2023c).

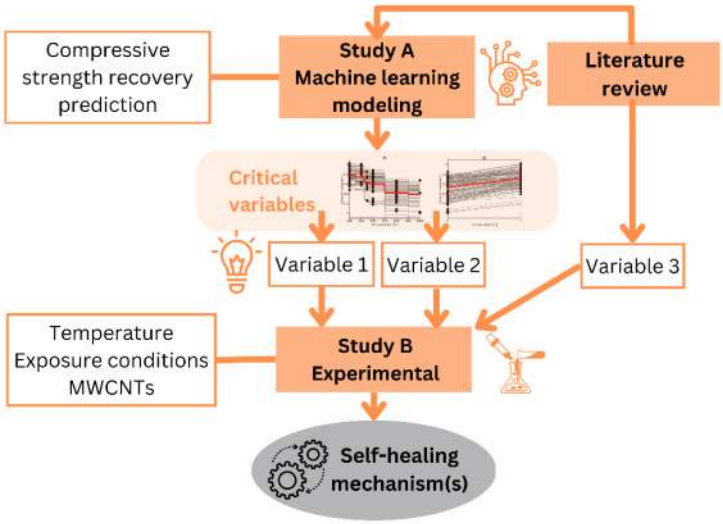

Figure 4.1. The methodology used in Chapter 4 – thermally induced cracks.

4.1. MACHINE LEARNING MODELING

4.1.1. Data source

Machine learning predictions are based on a large number of data, with the required number of observations at least one order higher than the number of variables (Li et al., 2022). Considering that the experiments are costly and time-consuming in cement and concrete science, adopting results from other studies is a pragmatic, generally accepted method (e.g., Chou et al. 2014, Naseri et al. 2020, Young et al. 2019, Feng et al. 2020). Consequently, in this study, a database was constructed containing 197 records from twelve independent experimental studies found in the literature (Table 4.1). The database details are presented in Table B.1. of Annex B.

Table 4.1. Sources used for the database construction (Rajczakowska et al. 2023a).

No.	Reference	Samples in dataset
1	(Akca & Özyurt, 2018)	2
2	(Endait & Wagh, 2020)	56
3	(Hamad, 2017)	3
4	(Henry et al., 2008)	4
5	(Henry et al., 2011)	8
6	(Horiguchi & Suhaendi, 2010)	4
7	(Karahan, 2011)	11
8	(Lin et al., 2011)	48
9	(Mendes et al., 2011)	5
10	(Poon & Azhar, 2003)	24
11	(Suresh et al., 2022)	4
12	(Yaragal et al., 2015)	28
	Total	**197**

Certain limitations of using different studies in the database should be acknowledged. First, the characteristics of raw ingredients used for cementitious materials preparation, e.g., fineness of cement, and grading of the aggregates, may differ between the studies; hence their effect on the healing process will be difficult to verify. Similarly, other parameters, such as the casting procedures and conditions, types of molds, and curing applied, may diverge, affecting the developed model's generalization ability.

The following input variables of the model were selected: w/c, age of concrete, amount of cement, fine aggregate, coarse aggregate, peak loading temperature, duration of peak loading temperature, cooling regime, duration of cooling, curing regime, duration of curing, and specimen volume. The choice of variables was made based on two factors. First, the potential influence on the high-temperature damage self-healing was considered; state of the art on self-healing of thermally induced cracks was studied in Chapter 2, Section 2.6 of this thesis. Secondly, the data availability was decisive concerning the selection of inputs. Therefore, parameters that were found in many studies were given priority.

A few assumptions and delimitations were chosen considering the input variables. First, cooling (I8) and curing regime (I10) were taken into account as binary categorical variables, with values “0” and “1” corresponding to air and water exposure, respectively. This simplification was caused by the lack of detailed cooling and curing conditions, e.g., relative humidity or temperature, reported in the literature. Specimen size effect (I12) was considered indirectly by calculating the sample volume used for compressive strength testing. The cooling time was assumed to be 120 min based on the data reported in several studies, even when it was not specified directly. Some data points were removed from the database in case of missing information, e.g., when no compressive strength was reported or when exclusively cooling was applied with no curing regime. Finally, the effect of fibers and Supplementary Cementitious Materials was disregarded due to limited data, i.e., records containing these materials were removed from the database.

The model's output was described by the compressive strength recovery (CSR) of the high-temperature damaged concrete due to the self-healing process. Compressive strength test is standardized; therefore, it can be expected that the results of this measurement are associated with less bias than, e.g., an in-house developed crack closure experimental method. In addition, it was the most reported property in the analyzed studies. The *CSR* parameter can be defined as follows (Rajczakowska et a. 2023a):

$$CSR = \frac{\sigma_h}{\sigma_0} \quad [-] \tag{4.1}$$

where σ_h depicts the compressive strength after the self-healing process, and σ_0 is the compressive strength of the intact specimens before the temperature loading.

Statistical descriptors of each variable, including minimum (Min) and maximum (Max) values, median, mean, standard deviation (Std), and skewness (Sk), are listed in Table 4.2. In addition, the histograms and relation of each input to the output are presented in Annex B, Figure B.1.

Table 4.2. Statistical descriptors of the inputs and output (Rajczakowska et al., 2023a).

Input/ Output	Name	Unit	Min	Max	Median	Mean	Std	Sk
I1	w/c	-	0.3	0.68	0.5	0.51	0.11	0.37
I2	Age	days	3	90	28	43.65	30.70	0.45
I3	Cement	kg/m3	300	767	392	422.80	84.87	2.24
I4	Fine aggregate	kg/m3	638.04	1620	768	896.20	257.66	1.42
I5	Coarse aggregate	kg/m3	0	1201.59	914	818.98	329.04	-1.56
I6	Peak loading temperature	°C	400	1000	600	569.04	148.65	0.70
I7	Duration of peak loading temperature	min	60	200	120	92.49	33.51	0.44
I8	Cooling regime	-	0	1	-	-	-	-
I9	Duration of cooling	min	10	4320	120	1146.50	1816.16	1.17
I10	Curing regime	-	0	1	-	-	-	-
I11	Duration of curing	days	1	180	27	34.33	45.72	2.22
I12	Specimen volume	cm^3	64	21205.8	1000.0	2823.5	3616.9	2.8
O	Compressive strength recovery	-	0.018	1.03	0.66	0.65	0.22	0.74

Since one of the assumptions of regression analysis, e.g., ordinary least squares regression models, is the independence of variables, the correlation analysis of the chosen input was performed (Sage et al., 2022). As a result, strong correlations ($R \geq 0.7$) between several input variables were observed (Figure 4.2). For instance, concrete mix composition parameters were found to be correlated, i.e., w/c (I1) and cement amount (I3) (R = -0.7), cement mount (I3) and coarse aggregate (I5) (R = -0.7) and fine aggregate (I4) and coarse aggregate (I5) (R = -0.9). In addition, a strong correlation (R = 0.9) was found between age (I2) and cooling duration (I9) variables.

Nevertheless, despite the presence of correlations between a few input variables, all inputs were considered for the modeling stage to perform a complete model interpretation, which agrees with the study of (Ly et al., 2021).

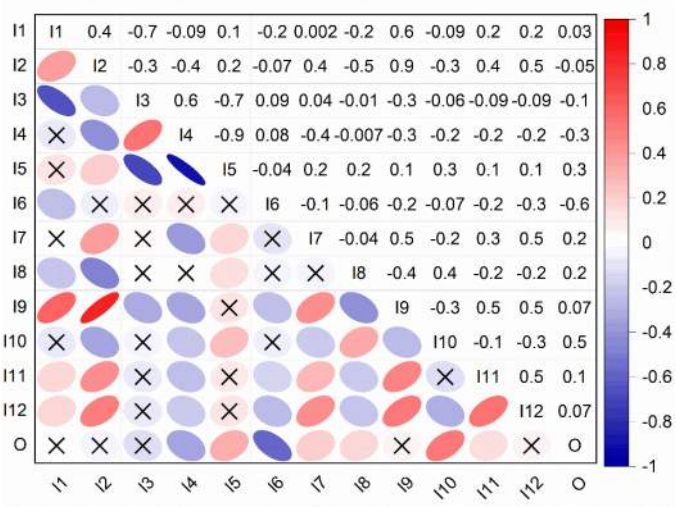

Figure 4.2. The correlation matrix of the input and output variables, symbol "x" depicts a statistically insignificant correlation (Rajczakowska et al. 2023a).

4.1.2. Modeling process

All calculations were performed in MATLAB software, version R2022b. Parts of the statistical analysis were done using OriginPro, version 2021. The prediction process is described below.

Step 1. Dataset division

The dataset containing 197 records was divided into two parts: for training and validation, 85% (167 records) and 15% for testing (30 records). The twelve input variables were: w/c, age of concrete, amount of cement, fine aggregate, coarse aggregate, peak loading temperature, duration of peak loading temperature, cooling regime, duration of cooling, curing regime, duration of curing, and specimen volume. The output was compressive strength recovery.

Step 2. Model optimization and performance assessment

To assess the models' accuracy, performance indices were calculated, i.e., the Mean Squared Error (MSE), Mean Absolute Error (MAE), coefficient of determination (R^2), Root Mean Squared Error (RMSE), and Normalized Root Mean Squared Error (NRMSE), according to the following equations:

$$MSE = \frac{\sum_{i=1}^{n}(t-y)^2}{n} \quad [-] \tag{4.2}$$

$$RMSE = \sqrt{\frac{\sum_{i=1}^{n}(t-y)^2}{n}} \quad [-] \tag{4.3}$$

$$MAE = \frac{\sum_{i=1}^{n}|t-y|}{n} \quad [-] \tag{4.4}$$

$$R^2 = 1 - \frac{\sum_{i=1}^{n}(t-y)^2}{\sum_{i=1}^{n}(t-\bar{t})^2} \quad [-] \tag{4.5}$$

$$NRMSE = \frac{RMSE}{\bar{t}} \cdot 100 \quad [\%] \tag{4.6}$$

where n is the number of data points, t is the measured (target) value for the i-th specimen, y is the predicted value from the model for the i-th specimen and $\bar{t}$ depicts the mean value from the measured data. The coefficient of determination (R^2), which can be equal between 0 and 1, showed how well the model fitted the data. The higher the value, the better the fit. Low values of the errors, i.e., MSE, MAE, RMSE, and NRMSE, indicated a high precision of the model.

Four ML approaches were analyzed, i.e., Support Vector Machines (SVM), regression trees (RT), an ensemble of regression trees (ET), and artificial neural networks (ANN). Background information regarding these algorithms is discussed in Chapter 2, Section 2.8 of this thesis. Training, validation, and testing were performed for 320 combinations of different hyperparameter sets (Table 4.3).

A k-fold cross-validation technique was applied (Saud et al. 2020), with k parameter equal to 5, to prevent overfitting and obtain a flexible model. In this method, the training and validation dataset (167 records) was divided randomly into five subsets, called the folds, from which one was used for validation and the other four – for training. The process was repeated k-times by shuffling the training and validation sets—each time the performance indices were calculated. Finally, the reported value of the performance was the average of all folds. A minimum value of the average MSE from cross-validation was considered the guiding parameter for the optimal model selection.

Table 4.3. Hyperparameters used to train the models (Rajczakowska et al. 2023a).

Algorithm	Support Vector Machines (SVM)	Regression trees (RT)	Ensemble of regression trees (ET)	Artificial neural networks (ANN)
Parameters	Kernel function (Gaussian, linear, cubic, quadratic) Kernel scale (1-15) Box constraint - constant Epsilon - constant	Minimum leaf size (1-15)	Boosted/Bagged Minimum leaf size (1-10) Number of learners (20-100) Learning rate (0.01-1)	Number of layers (1-3) Number of neurons in the layer (2-12) Activation function (ReLu, tansig, sigmoid)

Step 3. Robustness analysis

Additional robustness analysis was performed on the five models with the lowest validation MSE from Step 2. For this purpose, Monte Carlo simulations were applied to verify the models' sensitivity to training-testing dataset splits. The MCS *"uses random sampling and statistical modeling to estimate mathematical functions and mimic the operations of complex systems"* (Harrison, 2010). The principle of the method relies on the "law of large numbers," which states that the average of the large samples converges to the expected value μ when the number of samples n→∞. The Monte Carlo estimator can be computed as follows (van Dao et al., 2020):

$$C(N) = \frac{1}{\bar{X}} \frac{1}{N} \sum_{i=1}^{N} X_i \quad [-] \tag{4.7}$$

where $\bar{X}$ denotes the mean value of the variable X, and N is the number of Monte Carlo simulations (van Dao et al., 2020).

The following steps were performed to assess the robustness of the model:

- All data (197 records) were split randomly into 80% and 20% parts for training and testing, respectively. A random number generator implemented in MATLAB software was used.
- The models were then trained again on the randomly split datasets; 800 Monte Carlo simulations were performed per model (in total, 4000 simulations). Each time the MSE and R^2 were calculated for both training and testing.
- The statistical analysis was performed on the results of MSE and R^2 for each of the five models to assess the efficiency.

Step 4. Model interpretation

The goal of this study was to make the model's "black box" interpretable so that the mechanism of post-fire self-healing could be better understood. This was achieved by verifying how changes in each input variable impacted the corresponding changes for each output response when the other variables were fixed. Partial Dependency plots (PDPs) (Friedman, 2001) and individual conditional expectation (ICE) plots (Goldstein et al., 2015) were used for interpretation.

A PDP demonstrates a dependency of the average response on the particular input (Rajczakowska et al. 2023a). When strong dependencies between the predictors exist, the PDP does not give conclusive results. In this case, the ICE plots can provide supplementary information (Goldstein et al., 2015) by demonstrating the functional relation for single observation (Casalicchio et al., 2018). This way, the heterogeneity of the response can be studied. For instance, in the absence of relations between variables, the curves on the ICE plot lay on top of each other, whereas, in the opposite case, differences between single ICE curves will be present (Goldstein et al., 2015).

In this study, PDP and ICE plots were used for the causal interpretation of one of the models from Step 3. In addition, feature importance analysis was performed, and compressive strength recovery dependency on each input variable was investigated (Rajczakowska et al. 2023a).

4.1.3. Results and analysis

All ML algorithms performed better than linear regression in terms of errors, i.e., MSE, MAE, RMSE, R^2, and NRMSE (Table 4.4, Figure 4.3).

Table 4.4. Performance of the most accurate models for each ML approach (Rajczakowska et al. 2023a).

ML approach	Best model parameters	Dataset	MSE [-]	MAE [-]	R^2 [-]	RMSE [-]	NRMSE [%]
RT	Min. leaf size 2	Validation	0.0079 *	0.0651 *	0.826 *	0.0889 *	13.7 *
		Testing	0.0067	0.0667	0.892	0.0821	12.6
SVM	Cubic kernel, Kernel size 3	Validation	0.0078 *	0.0672 *	0.827 *	0.0886 *	13.6 *
		Testing	0.0092	0.0731	0.852	0.0960	14.8
ET	LSBoost algorithm, Min. Leaf size 3, Number of learners 40, Learning rate 0.5	Validation	0.0044 *	0.0448 *	0.903 *	0.0664 *	10.2 *
		Testing	0.0031	0.0424	0.950	0.0557	8.6
ANN	Layers 8:12:12, Activation function: sigmoid	Validation	0.0084 *	0.0617 *	0.815 *	0.0915 *	14.1 *
		Testing	0.0063	0.0598	0.899	0.0795	12.2
LR	-	Validation	0.0149 *	0.0914 *	0.672 *	0.1219 *	18.8 *
		Testing	0.0232	0.1119	0.628	0.1524	23.4

* The value is an average from 5-fold cross-validation

A regression tree (RT) model, with the lowest cross-validation MSE equal to 0.0079, was obtained for the minimum leaf size 2. Cubic kernel function with a kernel size of 3 produced the lowest validation MSE equal to 0.0092 for the SVM approach. ANN architecture with three hidden layers (8, 12, and 12 neurons) and sigmoid activation function achieved the cross-validation MSE of 0.0084. The ensemble of regression trees (ET) demonstrated the lowest MSE equal to 0.0044. The optimal hyperparameters for this model were the boosting algorithm LSBoost, minimum leaf size equal 3, the number of learners equal to 40, and 0.5 learning rate. It can be noticed that the ET model also achieved the lowest NRMSE for both validation and testing sets, equal to 10.2% and 8.6%, respectively. In comparison, linear regression yielded NRMSE equal to 18.8% and 23.4%, which was over two times higher than the ET (Rajczakowska et al. 2023a).

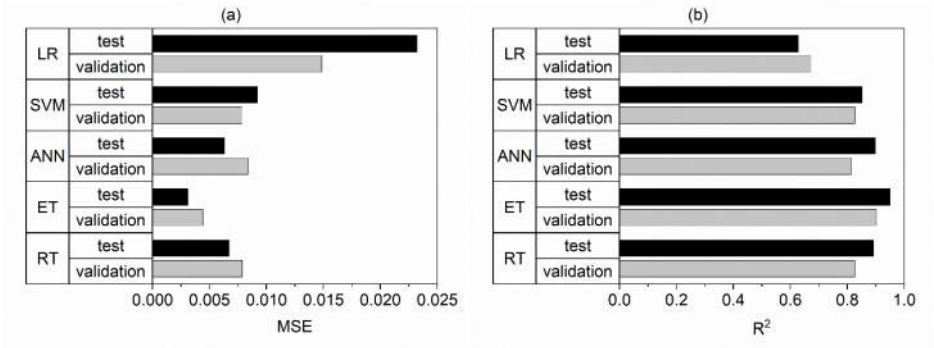

Figure 4.3. Comparison of the prediction accuracy for the best model within different ML approaches (RT, ET, ANN, and SVM) and linear regression (LR): (a) MSE for validation and testing; (b) R^2 for validation and testing (Rajczakowska et al. 2023a).

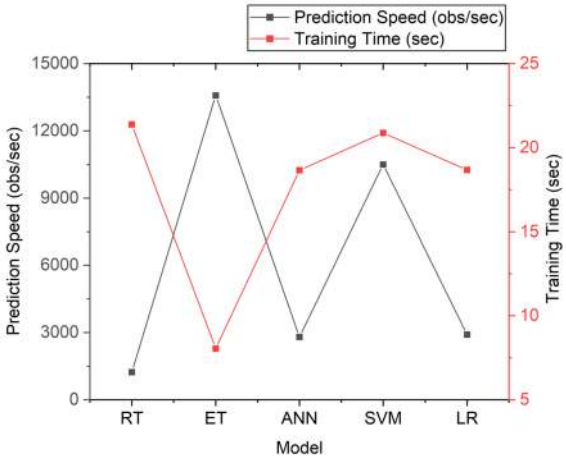

Figure 4.4. Comparison of the prediction speed and training time for best model within different ML approaches (RT, ET, ANN and SVM) and linear regression (LR) (Rajczakowska et al. 2023a).

In addition, the models' prediction speed and training time were compared (Figure 4.4). Training speed is essential since a fast calculation enables spending more resources on hyperparameter optimization (Wan et al. 2021). The slowest prediction speed, reaching around 3000 observations/second, characterized ANN and LR. The ET model was the fastest algorithm (14000 observations/second) with the shortest training time of approximately 7 seconds. On the other hand, the SVM model demonstrated a relatively fast prediction speed with around 10000 observations per second; however, the training of this algorithm took approximately 22 seconds. Reducing the dimensionality of data, i.e., applying Principal Component Analysis, could potentially improve the training speed of the algorithms (George and Vidyapeetham, 2012; Wan et al., 2021).

The ET approach with boosting algorithm demonstrated the lowest error indices, highest R2, and lowest training time. Furthermore, analysis of all the calculated combinations revealed that five models with the lowest cross-validated MSE belonged to the ensemble approach (Table 4.5) (Rajczakowska et al. 2023a).

Table 4.5. Five best performing models' performance (Rajczakowska et al. 2023a).

Model	Model parameters	Dataset	MSE [-]	MAE [-]	R^2 [-]	RMSE [-]	NRMSE [%]
ET1	LSBoost algorithm, Min. Leaf size 3, Number of learners 40, Learning rate 0.5	Validation	0.0044 *	0.0448 *	0.903 *	0.0664 *	10.2 *
		Testing	0.0031	0.0424	0.950	0.0557	8.6
ET2	LSBoost algorithm, Min. Leaf size 5, Number of learners 100, Learning rate 0.1	Validation	0.0044 *	0.0483 *	0.903 *	0.0662 *	10.2 *
		Testing	0.0048	0.0519	0.923	0.0692	10.6
ET3	LSBoost algorithm, Min. Leaf size 3, Number of learners 20, Learning rate 0.5	Validation	0.0044 *	0.0463 *	0.902 *	0.0666 *	10.2 *
		Testing	0.0043	0.0476	0.931	0.0657	10.1
ET4	LSBoost algorithm, Min. Leaf size 2, Number of learners 100, Learning rate 0.1	Validation	0.0045 *	0.0485 *	0.901 *	0.0669 *	10.3 *
		Testing	0.0045	0.0491	0.928	0.0669	10.3
ET5	LSBoost algorithm, Min. Leaf size 5, Number of learners 80, Learning rate 0.1	Validation	0.0045 *	0.0492 *	0.901 *	0.0671 *	10.3 *
		Testing	0.0053	0.0543	0.915	0.0728	11.2

* The value is an average from 5-fold cross-validation

The earlier ET models' prediction capacity (Table 4.5) was similar, with cross-validated MSE below 0.005 and R2 above 0.9. The model fit for ET1 for the validation and testing set is presented in Figure 4.5.

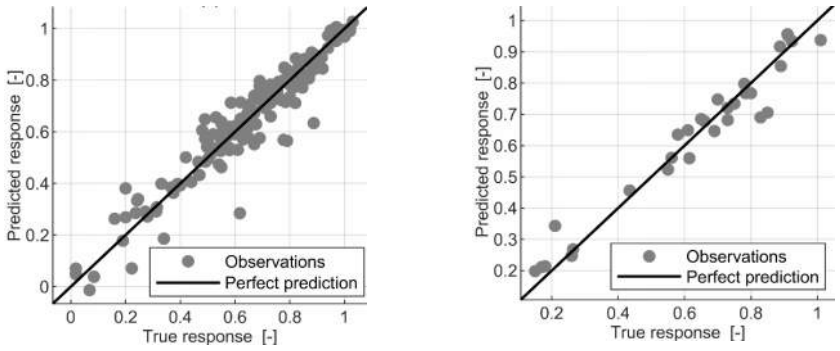

Figure 4.5. ET1 model fit for (a) training and validation, (b) testing dataset (modified from Rajczakowska et al. 2023a).

The hyperparameter effect on the model performance, i.e., cross-validated MSE, was also analyzed. The results suggested that for higher learning rates above 0.5, a smaller number of learners was acceptable (Figure 4.6b), e.g., 20 in model ET3. On the other hand, low learning rates below 0.1 required learners' numbers above 80 to achieve the same accuracy. In addition, the association between the number of learners and minimum leaf size was less pronounced, with the learners' number being the driving factor (Figure 4.6a) (Rajczakowska et al. 2023a).

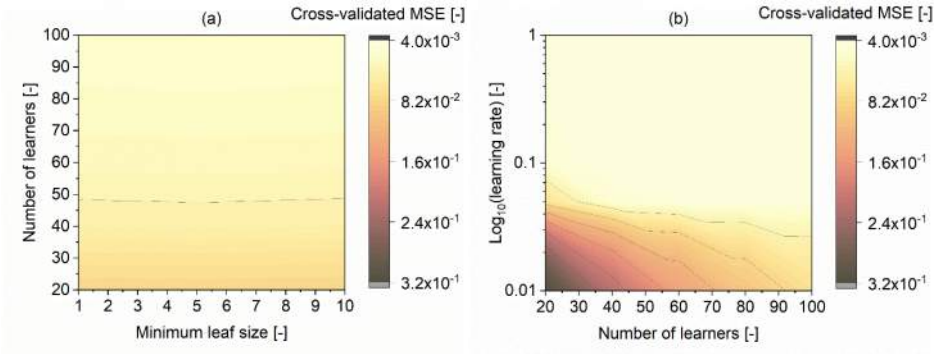

Figure 4.6. Hyperparameters effect on the ET model with LSBoost algorithm MSE for the training and validation dataset: (a) minimum leaf size vs. the number of learners, (b) a number of learners vs. log of the learning rate (Rajczakowska et al. 2023a).

Monte Carlo simulations of the effect of random training-testing dataset split on the model accuracy were performed for the five models with the best performance (Table 4.5). Changes in testing dataset MSE and R^2 are presented in Figure 4.7ac, whereas normal distributions are in Figure 4.7bd. It can be observed that 800 Monte Carlo realization is presumably sufficient to achieve convergence (Rajczakowska et al. 2023a).

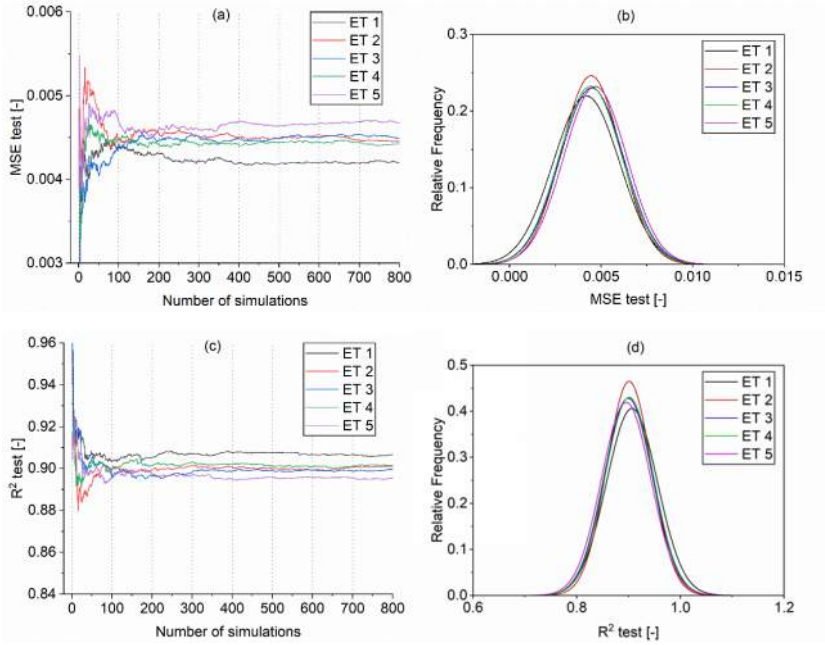

Figure 4.7. Results of the Monte Carlo simulations for models ET1 - ET5: (a) changes of MSE test, (b) normal distribution fitting of MSE, (c) changes of R^2 test, (d) normal distribution fitting of R^2 (Rajczakowska et al. 2023a).

Calculation of normalized convergence was performed for all the models according to Eq. (4.7). Examples of Normalized convergence curves for MSE and R^2 of the testing set for model ET1 are presented in Figure 4.8. Curves for other models are in Annex C, Figure C.2. The mean value from the 800 realizations and its 95% Confidence Interval (CI) bounds were marked in blue (Figure 4.8). The number of MCS realizations for the stability of testing MSE was compared for all the models (Table 4.6). Models ET1 and ET4 converged after approximately 350 realizations, models ET3 and ET5 after 500 realizations, and model ET2 after 700 realizations (Table 4.6) (Rajczakowska et al. 2023a).

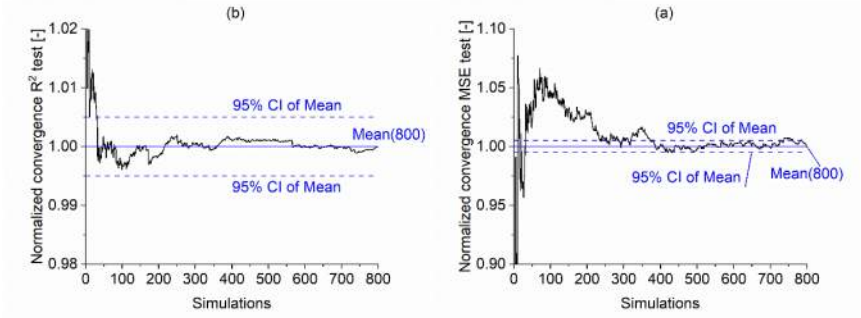

Figure 4.8. Exemplary Monte Carlo normalized convergence of MSE and R^2 for the testing set for model ET1 (modified from Rajczakowska et al. 2023a).

Finally, the statistical descriptors of the MSE and R^2 for the testing dataset are listed in Table 4.6. It can be observed that Model ET1 demonstrated the lowest mean value of MSE (MSE=0.0042) and the highest R^2 coefficient (R^2=0.907). At the same time, negligible differences in standard deviation were observed (Rajczakowska et al., 2023a).

Table 4.6. MCS performance summary for the testing dataset (Rajczakowska et al. 2023a).

Model	R^2 [-]				MSE [-]				Approximate no. of MCS realizations for MSE convergence [-]
	Min	Max	Mean	Std	Min	Max	Mean	Std	
ET1	0.437	0.979	0.907	0.049	0.0012	0.013	0.0042	0.0018	350
ET2	0.690	0.974	0.901	0.043	0.0010	0.012	0.0045	0.0016	700
ET3	0.537	0.977	0.900	0.047	0.0012	0.012	0.0045	0.0017	500
ET4	0.585	0.970	0.901	0.046	0.0016	0.015	0.0044	0.0017	350
ET5	0.512	0.972	0.895	0.048	0.0016	0.012	0.0047	0.0017	500

Model ET1 had the best prediction capacity based on the performance, speed, and robustness analysis. A causal interpretation of this model was performed using PDPs and ICE plots (Figure 4.9). In Figure 4.9, the thick red curve depicts the PDP, i.e., the average of all the individual grey curves. Dots represent the measured value of the specific variable.

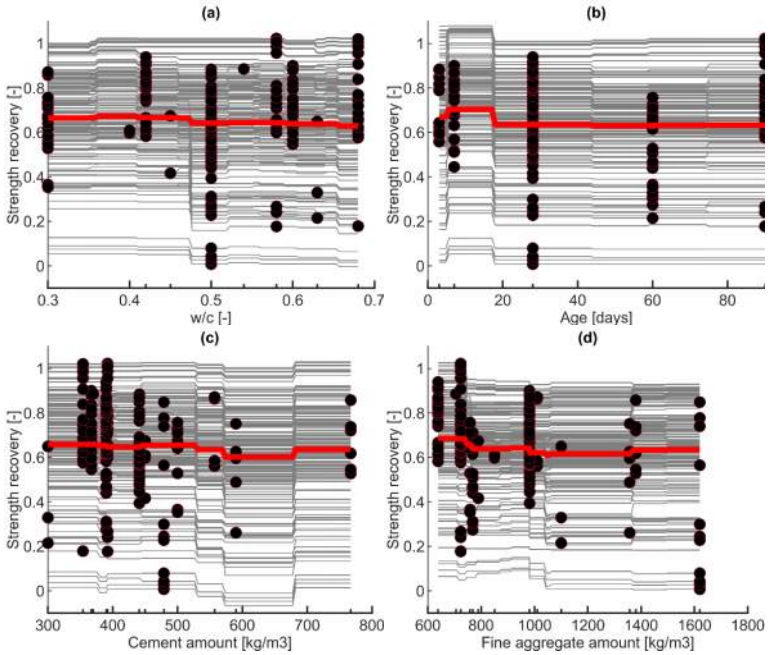

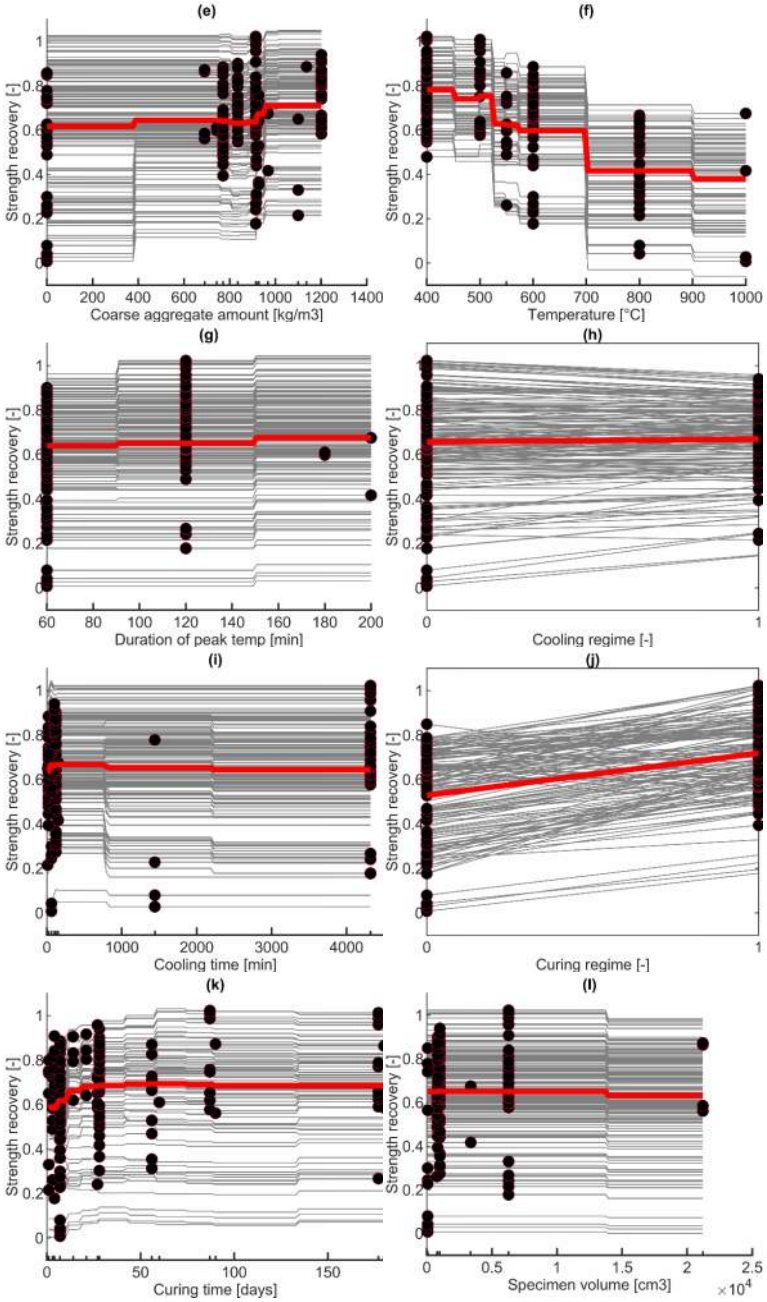

Figure 4.9. ICE plots for each input variable (PDP - thick red curve depicts the PDP; dot markers represent the measured value of the specific variable): (a) water-to-cement ratio (I1), (b) age (I2), (c) cement amount (I3), (d) fine aggregate (I4), (e) coarse aggregate (I5), (f) temperature (I6), (g) duration of peak temperature (I7), (h) cooling regime (I8), (i) cooling duration (I9), (j) curing regime (I10), (k) curing duration (I11), (l) specimen volume (I12) (Rajczakowska et al. 2023a).

As expected, the loading temperature variable is critical regarding the possibility of post-fire self-healing (Figure 4.9f) since it influences the amount and type of damage occurring in cementitious materials and causes chemical and physical changes in their microstructure (Rajczakowska et al. 2023a). For instance, calcium hydroxide decomposes at approximately 400–500°C while calcite and calcium silicate hydrate (C–S–H) at 700–900°C (Ming & Cao, 2020). Some of the reactions are reversible, e.g., rehydration of portlandite by reaction of calcium oxide with water in the presence of moisture. However, rapid rehydration of portlandite leads to expansion and, consequently, further loss of strength. This can possibly be associated with the noticeable CSR decline at around 500°C (Figures 4.9f, 4.10f). Another decrease in the strength recovery can be visible after approximately 700°C. It can be related to the increase in materials porosity and severe cracking. Self-healing of wider cracks is difficult without external stimulators (Reinhardt & Jooss, 2003). These results agree with previous experimental studies, e.g. (Poon et al., 2001).

The PDP suggests that the compressive strength recovery could be causally sensitive to the curing regime, with changes between approximately 0.5 to 0.75 (Figures 4.9j) (Rajczakowska et al. 2023a). This follows other studies on this topic where water curing (here marked as "1") led to significant durability and mechanical performance recovery (Akca & Özyurt, 2018; Henry et al., 2011; Lin et al., 2011), in contrast to the air curing (here marked as "0"). The studied model's limitation is dividing the curing regimes into two general groups. The curing effect could be more pronounced in the case of a more detailed analysis of environmental conditions, e.g., knowing the exact value of relative humidity and temperature. Currently, no such data have been systematically reported in the literature. The curing time PDP indicates that major changes occur within the first 50 days, with strength recovery values between 0.58 and 0.7. Later, there is a negligible CSR variation, below 2% (Rajczakowska et al. 2023a).

In contrast to the curing, the strength recovery is presumably causally insensitive to both the cooling regime (Figures 4.9h) and cooling time (Figures 4.9j), with CSR changes of approximately 2% and 4%, respectively (Rajczakowska et al. 2023a). The longer the cooling, the less significant the strength regain (Figures 4.9j). On the other hand, the ICE single observation curves do not follow the same pattern, i.e., some of the curves decrease and some increase, suggesting an interaction of the cooling regime variable with other inputs. Interestingly, analogical findings were reported in the literature. For example, water cooling had a deteriorating effect on strength recovery (Mendes et al., 2011), presumably due to the fast rehydration of portlandite, while in other cases, water cooling facilitated recovery, in contrast to air exposure (Karahan, 2011).

There are several variables with minor influence on the predicted self-healing strength recovery. Concrete's age changes (Figure 4.9b) caused only a small difference in the values of strength recovery, between approximately 0.63 and 0.71. The healing efficiency is slightly higher at an early age, presumably due to unhydrated cement particles, which can hydrate in the presence of moisture, increasing strength (Endait & Wagh, 2020). After 20 days, no observable changes were noted (Figures 4.9b). Looking at the PDP plots, the mix

properties related to the binder, such as w/c (Figures 4.9a) and cement amount (Figures 4.9c), exhibited a minor influence on the strength recovery, with only approximately 5% (0.05) change in relation to initial compressive strength (Rajczakowska et al. 2023a), which agrees with experimental results published by (L. Li et al., 2017; Lin et al., 2011). Nevertheless, comparing the ICE single observation curves, it can be noticed that there are differences in the shape of the curves for both variables, which can suggest the effect of another input interaction (Goldstein et al., 2015). A strong correlation (R = -0.7) between these predictors (Figure 4.2) could have altered the actual dependency. The specimen volume was insignificant according to the PDP (Figure 4.9l). If the effect of sample size is negligible, this study's conclusions could presumably be applied in the field on large-scale elements. Another modeling (Ly et al., 2021) and experimental research (Hamad, 2017; Zabihi & Eren, 2014) pointed out the secondary effects of specimen size on compressive strength. Regardless, this hypothesis still requires further verification in case of high-temperature damage recovery.

In opposition to the binder-related mix components, fine (Figure 4.9d) and coarse aggregates (Figure 4.9e) had a relatively significant influence on the strength recovery, with CSR changes between 0.61-0.69 and 0.62-0.72, respectively (Rajczakowska et al. 2023a).. The effect of fine aggregate is negative until the amount is around 1000 kg/m3 as opposed to coarse aggregate. A recent review paper (Li et al., 2020) compared post-fire healing for cement paste, mortar, and concrete. It was observed that concrete showed better healing efficiency than paste and mortar. The possible reason could be the formation of cracks resulting from different thermal expansion coefficients of aggregate and hydrated binder, which form an interconnected network probably having a higher capacity for the precipitation of self-healing products as well as facilitating the transport of the healing substances and moisture into the crack (L. Li et al., 2020; Schneider, 1988). Figure 4.10 shows a two-dimensional heatmap PDP for fine and coarse aggregate. Based on this relation, an optimal mix composition for high strength recovery can be suggested. It is visible that the highest value of CSR can be achieved for the fine aggregate amount of approximately 600 kg/m3 and coarse aggregate between 1000-1200 kg/m^3. Nevertheless, these variables' high correlation (R = -0.9) should be underlined (Figure 4.2 - upper). Similarly, the w/c ratio of approximately 0.34-0.4 and fine aggregate below 700 kg/m^3 could presumably warrant better healing than other mix parameters (Figure 4.2 - lower).

To visualize the significance of the impact of the variables on the modeled response, predictor importance analysis was computed (Figure 4.11). This method calculated the sum of changes in the node risk due to splits on every input. Subsequently, the sum was divided by the number of branch nodes. More information on the algorithm can be found in (The MathWorks, 2022). The analysis revealed that the loading temperature and curing were highly impactful, with the estimates approximately three times larger than the rest of the variables.

Further sensitivity analysis was conducted by re-training the model with different numbers of variables to compare the changes in the values of MSE. First, the model was trained and tested only with every single variable (Figure 4.12ab), and afterward, by

removing one variable per calculation (eleven variables included) (Figure 4.12cd). It is noticeable that, once more, temperature and curing have the most significant influence on the model error.

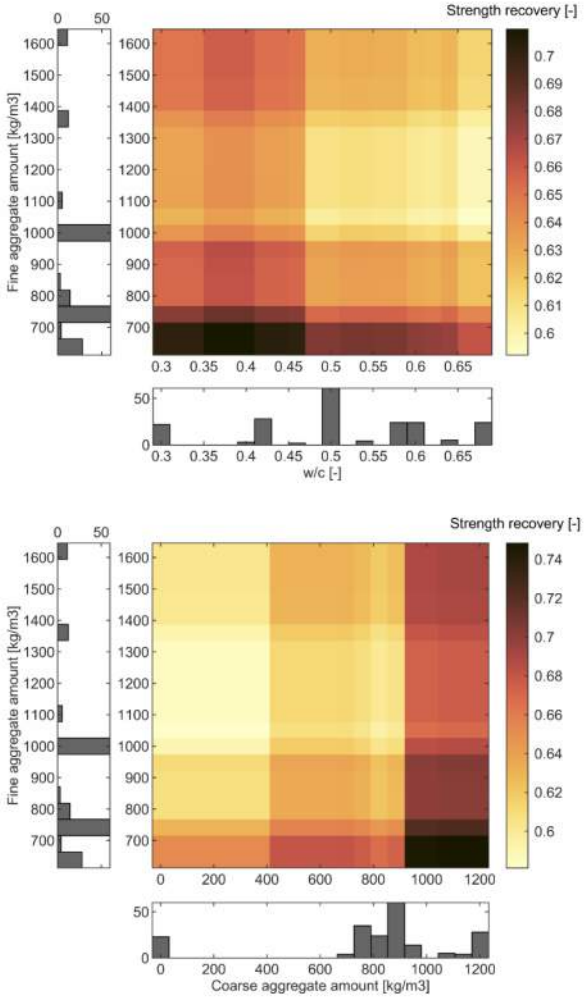

Figure 4.10. Heatmap PDP for the two variables; upper: coarse and fine aggregate vs. strength recovery (Rajczakowska et al. 2023a); lower: w/c and fine aggregate vs. strength recovery. Colors correspond to different values of strength recovery; color map from (Crameri, F. 2018; Crameri et al. 2020)

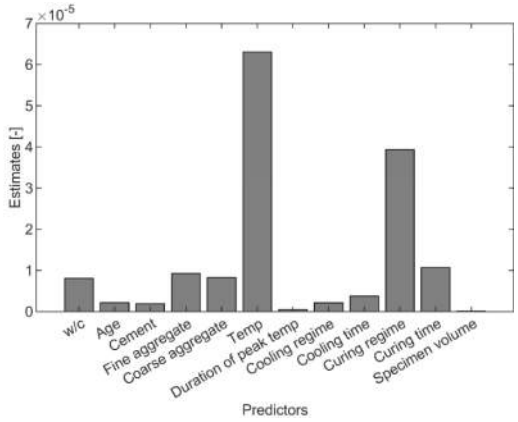

Figure 4.11. Feature importance estimates (Rajczakowska et al. 2023a).

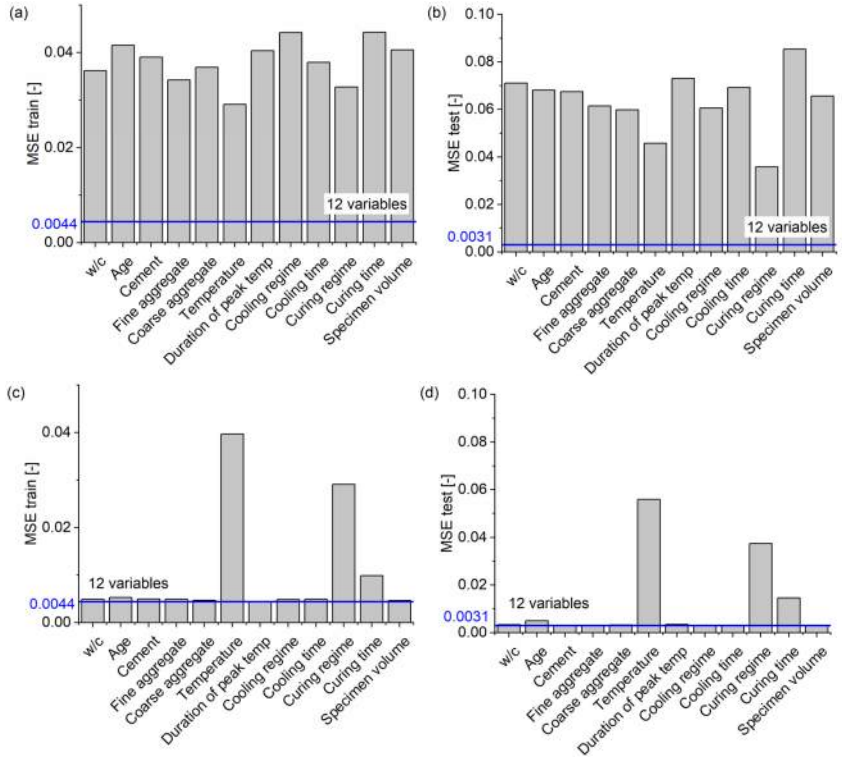

Figure 4.12. Performance of the model with a different number of variables: (a) trained only on one variable, MSE for the training set, (b) trained only on one variable, MSE for the testing set, (c) trained on 11 variables with one variable removed, MSE for the training set, (d) trained on 11 variables with one variable removed, MSE for the testing set (Rajczakowska et al. 2023a).

4.2. EXPERIMENTAL SETUP

Based on the model interpretation (Subchapter 4.1), experimental evaluation was performed to study the possibility of improving the self-healing process by applying novel environmental stimulators. First, selected treatments from Chapter 3 were applied. In addition, the cement paste was modified with a small dose of carbon nanomaterials, i.e., 0.1%wt binder of Multi-Wall Carbon Nanotubes (MWCNTs). MWCNTs positively affect cement hydration due to their high specific surface; they act as nucleation sites (Xiao et al., 2021). In addition, MWCNTs bridge the cracks and boost mechanical performance (Yao & Lu, 2021). These attributes could potentially promote the self-healing process.

The overview of the experimental setup is presented in Figure 4.13.

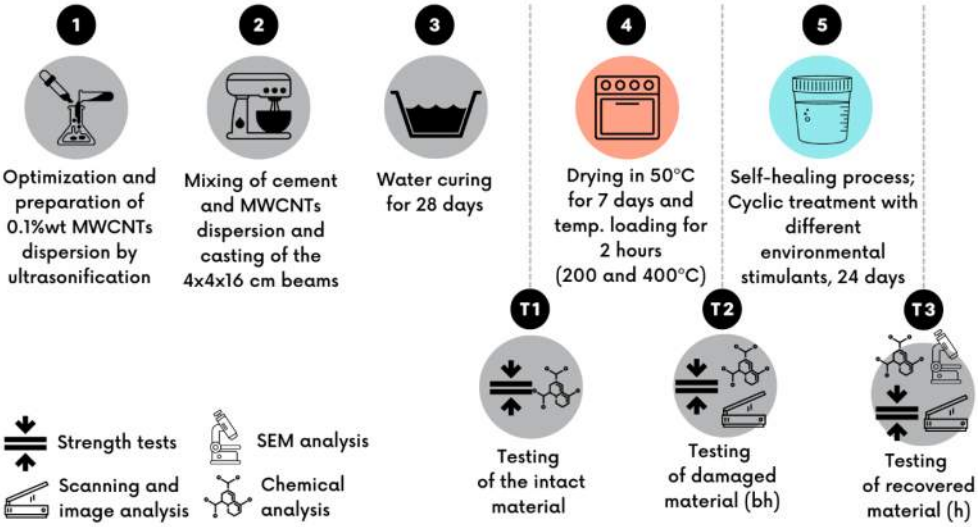

Figure 4.13. Overview of the experimental setup (Rajczakowska et al. 2023c).

4.2.1. Materials

Ordinary Portland cement (OPC) CEM I 42,5 N (Cementa Heidelbergcement Group, Stockholm, Sweden) was used to prepare cementitious materials (Table 4.7).

Table 4.7. Chemical composition of Portland cement (Rajczakowska et al. 2022).

Chemical compound	**CaO**	**SiO_2**	**Al_2O_3**	**Fe_2O_3**	**MgO**	**Na_2O**	**K_2O**	**SO_3**	**Cl**
Mean value [%]	63.3	21.2	3.4	4.1	2.2	0.18	0.56	2.7	<0.01

Two types of cement pastes were produced: with (CNT) and without (REF) multiwall-carbon nanotubes (MWCNTs). Industrial grade (92+%), untreated MWCNTs (Nanocyl SA, Sambreville, Belgium) were used with a diameter equal to 7-16 nm, and a length of 0.5-2.0 μm. The nanomaterials were added in the amount of 0.1%wt of cement. The overview of the experimental setup is presented in Figure 4.13.

First, the nanomaterials dispersion was prepared. MWCNTs were mixed with tap water and surfactant in the weight ratio of 1:2. Water-to-cement ratio was kept equal to 0.4. A commercially available polycarboxylate-based superplasticizer Sika ACE 30 (Sika, Baar, Switzerland) was chosen as a surfactant. Then, the ultra-sonification technique was applied to disperse the mixture using Hielscher sonicator UP200St (Hielscher Ultrasonics, Teltow, Germany) with an amplitude of 100% and 10 min sonification time (Figure 4.14a).

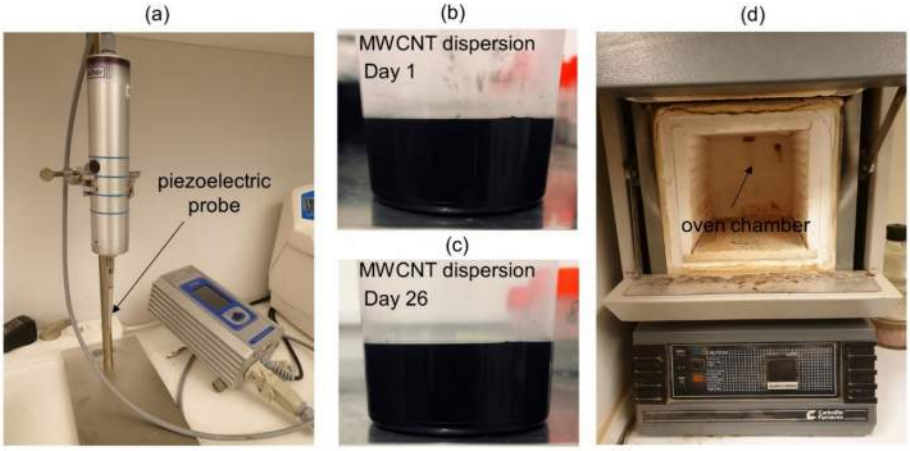

Figure 4.14. (a) ultrasonicator with the piezoelectric probe, MWCNT dispersion (b) 1 day after sonification, (c) 26 days after sonication, (d) oven (Rajczakowska et al. 2022).

All parameters, i.e., ultra-sonification constants and surfactant amount, were determined based on the trial-and-error approach. Preliminary testing indicated the stability of the dispersion controlled over 26 days (Figure 4.14bc). The final mix composition is presented in Table 4.8.

The dispersion was mixed with cement in a Hobart mixer for 3 min and cast into 40 x 40 x 160 mm steel molds. The specimens were removed from the molds after approximately 24 hours and cured under complete water immersion for 28 days.

Table 4.8. Parameter combinations (modified from Rajczakowska et al. 2023c).

Name	C (g)	W (-)	MWCNT (g)	SP (g)	Temp. (°C)	Conditions
REF 0	1000	0.4	0	0	No high temperature (only drying in 50°C)	Intact material, 28-day strength
CNT 0	1000	0.4	1	2	No high temperature (only drying in 50°C)	Intact material, 28-day strength

200 REF bh	1000	0.4	0	0	200	Before healing (no exposure applied)
200 REF W0	1000	0.4	0	0	200	Water cycle, 5 days wet, 1 day dry
200 REF W	1000	0.4	0	0	200	Water cycle, 3 days wet, 3 days dry
200 REF R	1000	0.4	0	0	200	Retarding admixture mixed with water cycle, 3 days wet, 3 days dry
200 REF L	1000	0.4	0	0	200	Lime water cycle 3 days wet, 3 days dry
400 REF bh	1000	0.4	0	0	400	Before healing (no exposure applied)
400 REF W0	1000	0.4	0	0	400	Water cycle, 5 days wet, 1 day dry
400 REF W	1000	0.4	0	0	400	Water cycle, 3 days wet, 3 days dry
400 REF R	1000	0.4	0	0	400	Retarding admixture mixed with water cycle, 3 days wet, 3 days dry
400 REF L	1000	0.4	0	0	400	Lime water cycle 3 days wet, 3 days dry
200 CNT bh	1000	0.4	1	2	200	Before healing (no exposure applied)
200 CNT W0	1000	0.4	1	2	200	Water cycle, 5 days wet, 1 day dry
200 CNT W	1000	0.4	1	2	200	Water cycle, 3 days wet, 3 days dry
200 CNT R	1000	0.4	1	2	200	Retarding admixture mixed with water cycle, 3 days wet, 3 days dry
200 CNT L	1000	0.4	1	2	200	Lime water cycle 3 days wet, 3 days dry
400 CNT bh	1000	0.4	1	2	400	Before healing (no exposure applied)
400 CNT W0	1000	0.4	1	2	400	Water cycle, 5 days wet, 1 day dry
400 CNT W	1000	0.4	1	2	400	Water cycle, 3 days wet, 3 days dry
400 CNT R	1000	0.4	1	2	400	Retarding admixture mixed with water cycle, 3 days wet, 3 days dry
400 CNT L	1000	0.4	1	2	400	Lime water cycle 3 days wet, 3 days dry

4.2.2. Thermal crack induction

The maximum loading temperatures were selected based on trial tests. As Chapter 2 (literature review) describes, cementitious materials undergo significant chemical and physical changes resulting from temperature loading. These changes get more severe with the increasing temperature. The analysis of the developed model (Section 4.1) also underlined the importance of exposure temperature on self-healing efficiency. Therefore, two temperatures were investigated in this study, 200°C and 400°C. This temperature range includes changes in C-S-H due to dehydration (starting from 20°C), and partial disintegration of Portlandite, which completely decomposes around 400-500°C (Szeląg,

2020). In addition, changes in cementitious materials after 200°C are rarely reported in the literature (Nalon et al. 2021); therefore, this study aimed to fill in this research gap. Unfortunately, higher temperatures lead to the extremely fragile microstructure of the specimens and could not be studied with the designed experimental setup.

After 28 days of curing, one of the surfaces of each sample was grinded with an oscillating grinder before being placed in the furnace to remove impurities and facilitate the observation of the cracking patterns after loading the sample. The procedure consisted of two steps. First, the specimens were dried at 50ºC for 7 days. After drying, the temperature loading was applied at 200ºC and 400ºC. The oven (Figure 4.14d) was preheated to the desired temperature before placing the specimens. The samples were exposed to high temperatures for 2 hours. Hot samples w quickly removed from the oven and cooled down by the natural temperature drop in room temperature at approximately 20°C.

4.2.3. Self-healing exposure

Upon cooling, the thermally cracked specimens were immersed in sealed containers with environmental stimulators (Table 4.8) to activate the healing process.

The choice of environmental exposures was performed based on the analysis from Chapter 3 (Table 3.4); however, only selected conditions were studied. Four treatments were applied: cyclic water immersion with cycle 5 days wet and 1 day dry (W0) and cycle 3 days wet and 3 days dry (W), as well as following the latter cycle, immersion in a 30%wt mixture of retarding admixture and water, and limewater (L). The same retarding admixture used as in the case of mechanical cracks (Chapter 3), i.e., SIKA Retarder, described as modified phosphates containing sodium metaphosphate (20%-30%), sodium gluconate $C_6H_{11}NaO_7$ (2%-5%), and water (70%-80%). The application of cyclic wetting conditions was aimed at mimicking more realistic field conditions. In comparison, a water cycle with a 5-day wetting phase was proposed to verify the effect of longer immersion on recovery. In total of 24 days of healing were assumed, i.e., four treatment cycles. A complete list of studied parameter combinations is presented in Table 4.8. Twenty-seven beams were prepared for each mix (in total fifty-four specimens), i.e., three beams to test the intact cement paste, six beams after temperature loading (three beams for each temperature, 200ºC, and 400ºC), and eighteen beams for the measurements after the healing process (three beams per exposure per temperature).

4.2.4. Self-healing efficiency measurements

Three-point bending test was performed to measure the flexural strength recovery using a universal loading machine with displacement control, type Wykeham Farrance, with a 50 kN loading cell combined with the QuantumX MX440B universal measuring amplifier (HBM, Darmstadt, Germany) (Figure 4.15c). Twelve beams were tested per mix: three intact samples, three after 200ºC and 400ºC temperature loading, and three after self-healing in each environmental stimulator. Two parameters described flexural strength

recovery, i.e., FSR0 (Eq. 4.8) and FSRt (Eq. 4.9), defined in the following equations (Rajczakowska et al. 2022):

$$FSR0 = \left(\frac{\sigma_{f,h}}{\sigma_{f,0}} - 1\right) \cdot 100\% \quad [\%] \tag{4.8}$$

$$FSRt = \left(\frac{\sigma_{f,h}}{\sigma_{f,bh}} - 1\right) \cdot 100\% \quad [\%] \tag{4.9}$$

where$\sigma_{f,0}$ is the flexural strength of the intact specimen at 28 days. $\sigma_{f,bh}$ and $\sigma_{f,h}$ are the flexural strengths before and after healing, respectively (Rajczakowska et al. 2022).

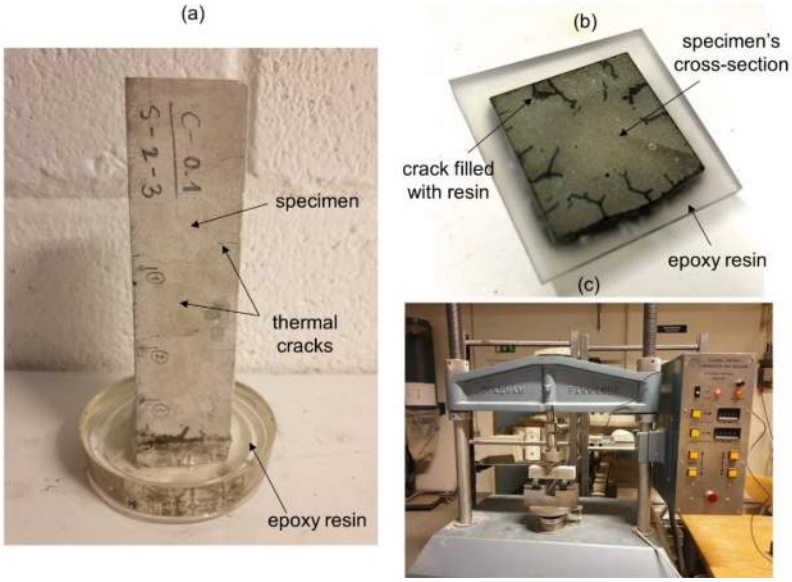

Figure 4.15. (a) preparation of the specimen cross-section for internal healing evaluation, (b) the specimen's cross-section embedded in resin, (c) a three-point bending setup (Rajczakowska et al. 2022).

Compressive strength recovery (CSR) was tested with the uniaxial compression machine, type Instron, model 1342 (Instron, Norwood, United States). Half-beams from the flexural strength measurement were used: five intact specimens, five samples after 200ºC and 400ºC temperature loading, and five samples after the healing process for each exposure. Two types of CSR parameters, i.e., CSR0 (Eq. 4.10) and CSRt (Eq. 4.11) were determined as follows (Rajczakowska et al. 2022):

$$CSR0 = \left(\frac{\sigma_{c,h}}{\sigma_{c,0}} - 1\right) \cdot 100\% \tag{4.10}$$

$$CSRt = \left(\frac{\sigma_{c,h}}{\sigma_{c,bh}} - 1\right) \cdot 100\% \tag{4.11}$$

where $\sigma_{c,0}$ is the compressive strength of the intact specimen at 28 days; $\sigma_{c,bh}$ and $\sigma_{c,h}$ are the compressive strengths before and after healing, respectively (Rajczakowska et al. 2022).

Cracking patterns on the specimen's surface caused by high-temperature loading was evaluated using an optical scanner Canon CanoScan LiDE 300 (Figure 4.16a). High-resolution 1200 dpi images with 1 pixel corresponding to approximately 20 μm were obtained for the surface of the sample before (Figure 4.16b) and after healing (Figure 4.16c). The cracking patterns were binarised (Figure 4.16cd) following the procedure of (Szelag, 2020) based on a machine learning image processing algorithm. A Trainable Weka Segmentation Fiji software plugin was used. Changes in the crack area before and after healing, i.e., the crack closure *SCC*, were calculated according to Eq. 4.12 below (Rajczakowska et al. 2022):

$$SCC = \left(1 - \frac{A_h}{A_{bh}}\right) \cdot 100\% \quad [\%] \tag{4.12}$$

where A_{bh} and A_h are the number of pixels associated with the crack area before and after the healing process, respectively (Rajczakowska et al., 2022).

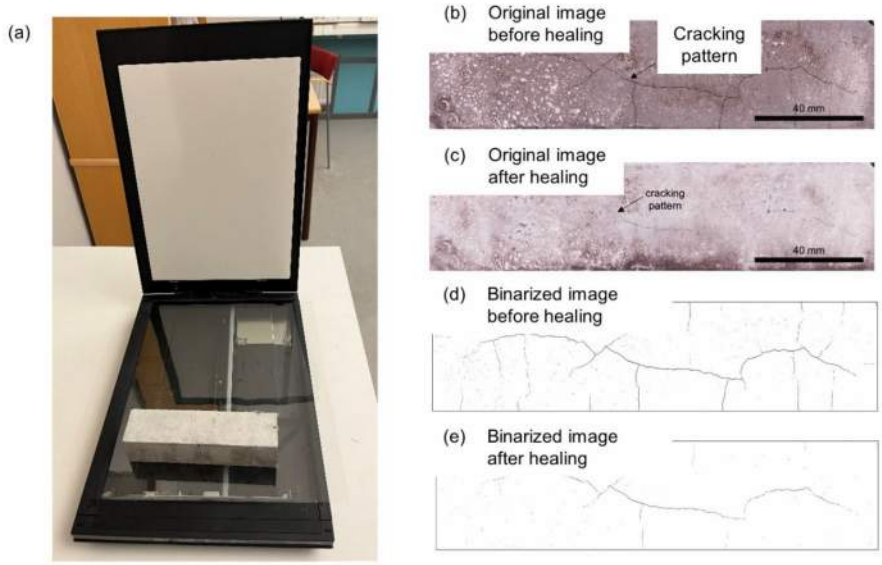

Figure 4.16. (a) scanner with one of the specimens, (b) scanned image of the cracking pattern after temperature exposure, and (c) after 24 days of water healing, the binarised image of the cracking pattern (d) after temperature exposure, (e) after 24 days of water healing (Rajczakowska et al. 2022).

The internal crack filling was studied using a digital optical microscope, type Dino-Lite Pro AM-413T. The end of the specimen was immersed in epoxy resin (Figure 4.15a) to glue the fragile cracked microstructure, and after hardening, a cross-section was prepared (Figure 4.15b). One cross-section per specimen was studied (Figure 4.17a). Afterward, the slice was cut into smaller parts which were once again impregnated and polished for SEM

analysis as described before. The filling of the cracks and the chemical composition of the healing material inside the cracks was verified using SEM with EDX (Figure 4.17b).

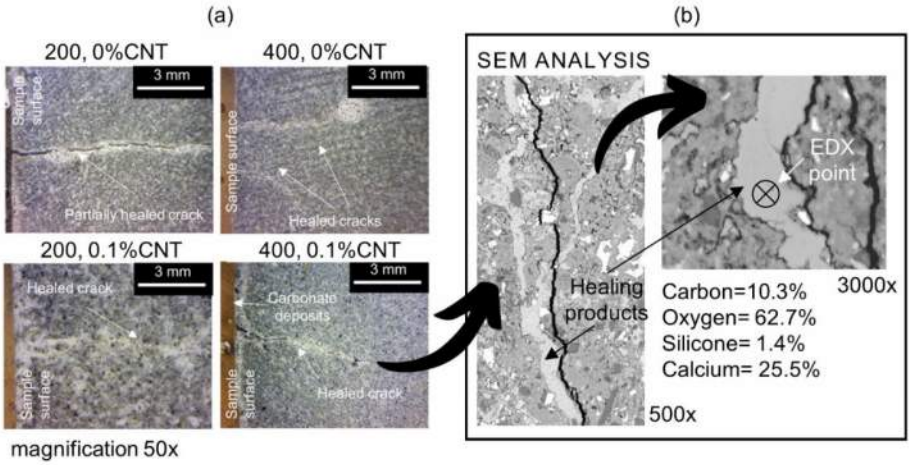

Figure 4.17. (a) Exemplary cross-section images, (b) exemplary SEM images and EDS analysis of the healing material inside the crack (Rajczakowska et al. 2022).

Microanalysis of the cement paste was performed using SEM Jeol JSM-IT100with a Bruker EDX. Small pieces of specimens were impregnated in epoxy resin and polished, using paraffin-based lamp oil as lubrication and cooling. Struers CitoVac and Labosystem (Struers, Ballerup, Denmark) were applied. Diamond sprays with decreasing particle sizes were used for polishing, i.e., 9 μm, 3 μm and 1 μm particle suspensions. To clean the surface from possible particle contamination, samples were rinsed in an isopropanol-filled ultrasonic bath. No coating was used for the SEM microanalysis. Details regarding this methodology are presented in Chapter 3.

Images were taken in backscatter electron (BE) mode at a low vacuum with the pressure set to 30 Pa, the accelerating voltage was 15 kV, and the working distance was 12±1 mm. Changes in volume fractions of Portlandite and unhydrated cement and porosity were calculated based on the thirty images captured at different locations with magnification 400x for each sample before and after self-healing. Image analysis was performed with the Fiji image processing package (Schindelin et al. 2012) with ImageJ2 software (Schindelin et al. 2015; Rueden et al. 2017). Segmentation of the pores was done using the overflow method (Wong et al. 2006). Grayscale histogram thresholding was used to determine the thresholds for the portlandite and unhydrated cement (Scrivener). The C–A–S–H inner (IP) and outer products (OP) composition was measured with EDX and calculated according to the procedure presented by (Rossen & Scrivener, 2017) to determine Ca/Si ratio variations before and after the self-healing process. Details regarding this methodology are presented in Chapter 3. The changes in microstructural parameters (Table 4.9) with relation to intact $X0$ and thermally damaged specimen Xt were calculated according to the following equations:

$$X0 = \left(\frac{X_h}{X_0} - 1\right) \cdot 100\% \ [\%] \tag{4.13}$$

$$Xt = \left(\frac{X_h}{X_{bh}} - 1\right) \cdot 100\% \ [\%] \tag{4.14}$$

where X_h, X_0, X_{bh} are the values of the microstructural parameters after healing, before the loading, and after temperature exposure, respectively.

Table 4.9. Microstructural parameters description.

Intact state	Damaged state	Parameter
Symbol	Symbol	[%]
OP0	OPt	Change in Si/Ca ratio of the outer product of C-S-H
IP0	IPt	Change in Si/Ca ratio of the inner product of C-S-H
P0	Pt	Porosity change
UC0	UCt	Unhydrated cement change
CH0	CHt	Portlandite change

4.3. RESULTS AND ANALYSIS

4.3.1. Effect of environmental conditions

The effect of the applied environmental conditions on self-healing strength recovery was studied. The results of compressive strength measurements after temperature loading (bh) and after healing treatments (W0, W, R, L) are presented in Figure 4.18 for loading temperatures of 200°C (Figure 4.18a) and 400°C (Figure 4.18b). In addition, the recovery of strength (CSRt) with relation to damaged specimens' strength is shown with a scatter plot (Figure 4.18ab). The intact specimens' strength at 28 days for mixed REF and CNT was measured at 58.45 ± 2.72 MPa and 57.18 ± 2.69 MPa.

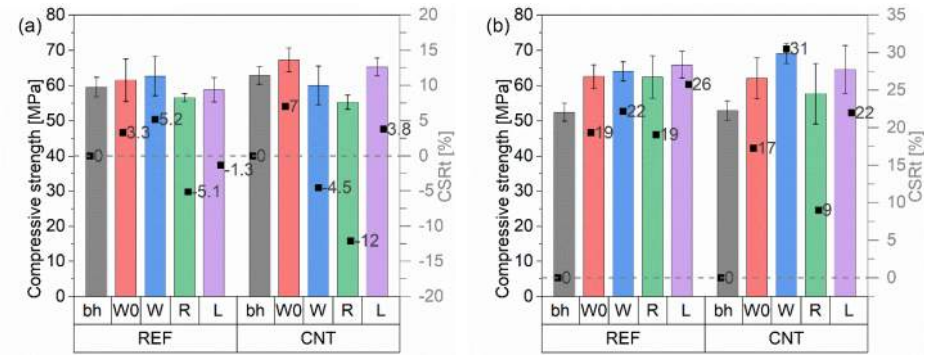

(a) (b)

Figure 4.18. Compressive strength results: (a) 200°C, (b) 400°C (Rajczakowska et al. 2023c).

Figure 4.19. Self-healing products on the fractured surface of selected specimens after compression test (modified from (Rajczakowska et al. 2023c).

It is visible that the differences between the compressive strength recovery of different exposures for 200°C are minimal. The lack of significant compressive strength recovery at 200°C is not surprising since it can be related to the fact that cementitious materials tend to exhibit higher strength after temperature exposure up to 250°C (Poon et al. 2001a). Exposure to lime water increased strength after healing for the CNT mix (Figure 4.18a, Table 4.10). An even more pronounced effect was noticed in the case of 400°C both for REF and CNT, with compressive strength reaching up to 65 MPa, which is approximately 15% higher than the intact strength and more than 20% higher than the temperature-damaged samples (Figure 4.18b, Table 4.10). Retarding admixture gave lower strength regain for both mixes. Strength recovery with respect to the damaged state can possibly be attributed to the porosity decrease and healing of the temperature cracks. Self-healing products were found at compression failure surfaces of 400°C (Figure 4.19).

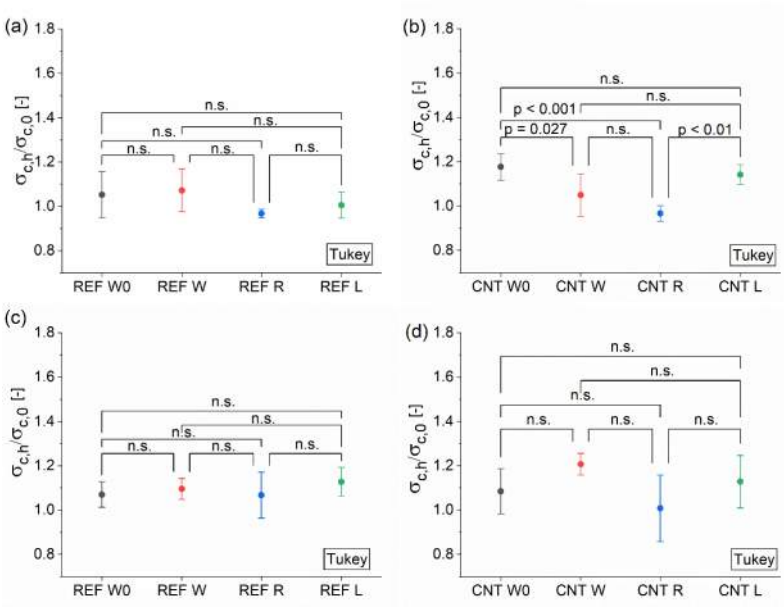

Figure 4.20. Compressive strength recovery concerning intact specimens (CSR0): (a) 200°C REF, (b) 200°C CNT; (a) 400°C REF, (b) 400°C CNT; (n.s. – not a significant difference) (Rajczakowska et al. 2023c).

The compressive strength recovery with respect to the intact specimen's strength was analyzed (Figure 4.20ab, Table 4.10). Interestingly all mixes, regardless of conditions, regained their initial strength with values of strength regain approximately equal to 1 or above. However, only in the CNT mix and 200°C temperature loading case (Figure 4.20b) was it observed that the retarding admixture exposure was significantly worse than the limewater cycle and the longer water immersion cycle (W0). In addition, a comparison between the water cycles indicated that more prolonged water exposure is more beneficial for CNT mix at 200°C (Figure 4.20b). No significant differences were observed between REF (Figure 4.20ac) and CNT mix at higher temperature loading (Figure 4.20d).

The results of flexural strength measurements after temperature loading (bh) and after healing treatments (W0, W, R, L) are presented in Figure 4.21 for loading temperatures of 200°C (Figure 4.21a) and 400°C (Figure 4.21b). In addition, the recovery of strength (CSRt) with relation to damaged specimens' strength is shown with a scatter plot (Figure 4.21ab). The measured flexural strength values of intact specimens for REF and CNT samples were equal to 3.33 ± 0.8 MPa and 3.78 ± 0.53 MPa, respectively.

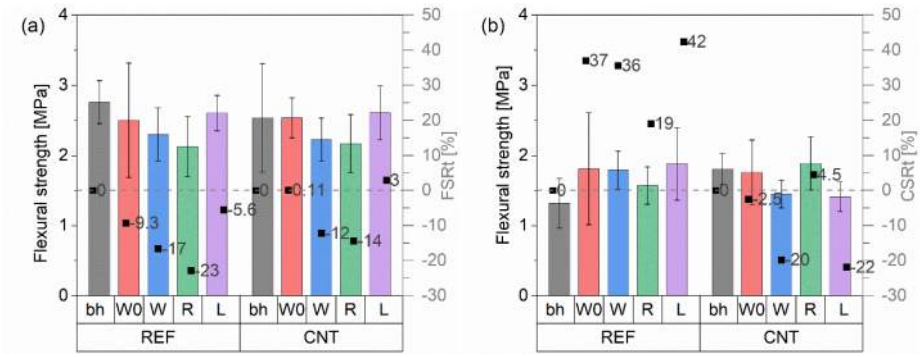

Figure 4.21. Flexural strength results: (a) 200°C, (b) 400°C (modified from (Rajczakowska et al. 2023c).

Subjecting cement paste to 400°C resulted in a significant loss of flexural strength, which did not recover to the intact specimen levels after self-healing for REF or CNT mixes (Table 4.9). In the case of the REF mix, a 20-42% (depending on exposure) increase with respect to the damaged state (FSRt) was noticed after healing the 400°C cracks (Figure 4.21, Table 4.10). For specimens with carbon nanomaterials, the flexural strength regained after curing was close to zero, or, in some cases, an additional 20% decrease in relation to the damaged state was observed. Nevertheless, flexural strength showed high variability of the results with large standard deviations for both 200 and 400°C (Figure 4.21ab); therefore, the results are not significant.

Literature studies on post-fire recovery of cementitious materials rarely report results on flexural strength, focusing primarily on compressive strength regain. Nevertheless, low flexural strength values were observed after the healing process (Vyšvařil et al. 2014), which agrees with this study. The large spread of the flexural strength results stems from

the high-temperature cracking patterns being randomly distributed and highly variable within the specimen population (Rajczakowska et al., 2022). In addition, the self-healing products formed on the walls of the cracks may not form a strong bond with the hydrated binder, resulting in the development of "weak" zones that are especially harmful in bending. Higher compressive strength but lower flexural strength could indicate that the samples become more brittle than intact cement paste. A similar effect was observed by (Vyšvařil et al. 2014). The strength recovery indexes' results for compressive and flexural strengths are summarized in Table. 4.10.

Table 4.10. Calculated strength recovery parameters (modified from (Rajczakowska et al. 2023c).

Specimen	Temp. [°C]	Case/exposure	CSR0 [-]	CSRt [-]	FSR0 [-]	FSRt [-]
REF	200	bh	1.9	0.0	1.2	0.0
		W0	5.2	3.3	-25.0	-9.3
		W	7.1	5.2	-15.7	-16.7
		R	-3.3	-5.1	-21.9	-22.8
		L	0.5	-1.3	-4.4	-5.6
CNT		bh	9.9	0.0	-7.1	0.0
		W0	17.6	7.9	-32.9	0.1
		W	4.9	-4.5	-18.4	-12.2
		R	-3.4	-12.1	-20.4	-14.4
		L	14.1	3.8	-4.3	3.6
REF	400	bh	-10.4	0.0	-50.9	0.0
		W0	6.9	19.3	-45.7	37.0
		W	9.5	22.2	-33.5	35.6
		R	6.7	19.1	-41.6	19.1
		L	12.7	25.8	-30.2	42.4
CNT		bh	-7.5	0.0	-32.9	0.0
		W0	8.4	17.3	-53.4	-2.5
		W	20.7	30.5	-46.2	-19.8
		R	0.8	9.9	-29.9	4.5
		L	12.8	22.0	-47.6	-21.8

Sealing cracks at the specimen surface was analyzed as a possible indirect indication of durability recovery. For all specimens, white precipitates were observed inside the cracks (Figure 4.22). In addition, initial visual observation suggested that narrow cracks were fully closed in most cases, whereas wider cracks, particularly visible for the higher temperature loading, were only partially filled with rehydrated phases (Figure 4.22b).

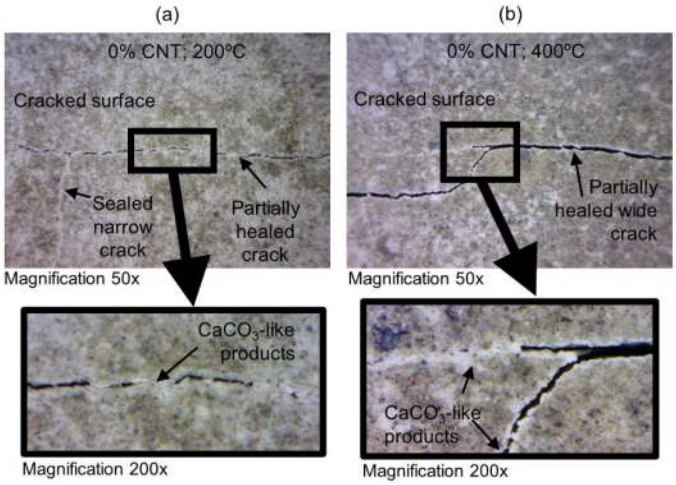

Figure 4.22. Example of optical microscope images of the crack surface after healing for mix REF after (a) 200ºC, (b) 400ºC temperature loading (Rajczakowska et al. 2022).

To make a quantitative comparison between applied environmental exposure, the surface crack closure parameter was calculated (Table 4.11). All exposures lead to partial healing of the cracks with an efficiency between approximately 30-60% for 200ºC temperature loading. The highest SCC index was obtained for limewater in the case of REF (SCC=55.1%) and CNT mixes (SCC=57.5%). More prolonged water exposure gave comparable (SCC=58.5%) crack sealing in the case of the CNT mix. In the case of 400ºC temperature loading, the crack closure results are significantly lower, with negative values for short water cycles. The highest efficiency was observed for the retarding admixture for both REF (SCC=17.7%) and CNT specimens (SCC=51.8%).

Table 4.11. Calculated surface crack closure (SCC) before and after healing based on the segmented cracking pattern images (modified from (Rajczakowska et al. 2023c).

Mix	Exposure	Temperature loading 200°C		Temperature loading 400°C	
		Mean [%]	Std [%]	Mean [%]	Std [%]
REF	W0	46.8	7.4	5.0	10.6
	W	47.3	6.8	-14.5	1.4
	R	38.0	25.3	17.7	12.0
	L	55.1	6.0	8.9	1.2
CNT	W0	58.5	6.7	15.7	1.4
	W	38.3	8.8	-15.7	11.5
	R	33.0	6.8	51.8	8.7
	L	57.5	10.2	12.8	1.0

In addition, the average (Figure 4.23ab) and maximum (Figure 4.23cd) crack widths before and after the healing process were calculated based on the obtained cracking patterns images. In the case of the average crack width, a weighted average from the local thickness distribution histogram was computed starting from the size of 2 pixels to avoid including noise.

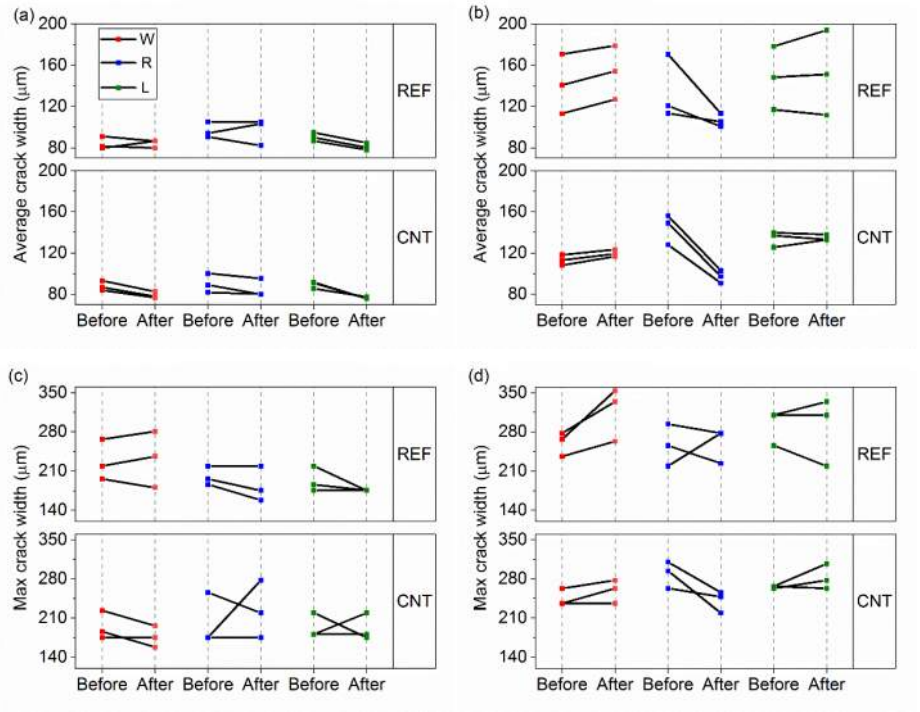

Figure 4.23. Crack width changes before and after self-healing in different exposures (red – W, blue – R, green – L): (a) average crack width at 200°C, (b) average crack width at 400°C, (c) max crack width at 200°C, (d) max crack width at 400°C (Rajczakowska et al. 2023c).

The average crack width of CNT decreased by approximately 10% with all the self-healing treatments at 200°C (Figure 4.23ab). Lime water resulted in the most efficient healing for CNT and REF, with approximately 14% and 11% crack reduction, respectively. For 400°C, the best results were obtained in retarding admixture exposure (R), with approximately 33% and 19% average crack width decrease for CNT and REF, respectively (Figure 23ab).

On the other hand, it is visible that there is a considerable variation between the specimens in each exposure concerning the maximum crack width changes (Figure 4.23cd). In the case of water exposure (W), there is even an increase in maximum crack widths,

which correlates with the negative values of SCC (Table 4.11). The short drying and wetting cycles may cause swelling and expansion due to rehydration and subsequent shrinkage of the hydrated cement material. At 200°C, changes in max width were negligible. At 400°C, the best combination was the CNT in the retarding admixture, achieving an average 16% (approx. 50 μm) narrower crack. None of the other cases lead to a maximum crack width decrease, which agrees with the values of SCC (Table 11).

It should be noted that the calculation of the maximum crack width has limitations as the parameter represents a local maximum which does not give sufficient information about healing. In addition, more complex descriptors of cracking patterns could be appropriate to describe the self-healing process. For instance, a local crack width distribution can be calculated according to the procedure described in Chapter 3 (Figure 4.24ab).

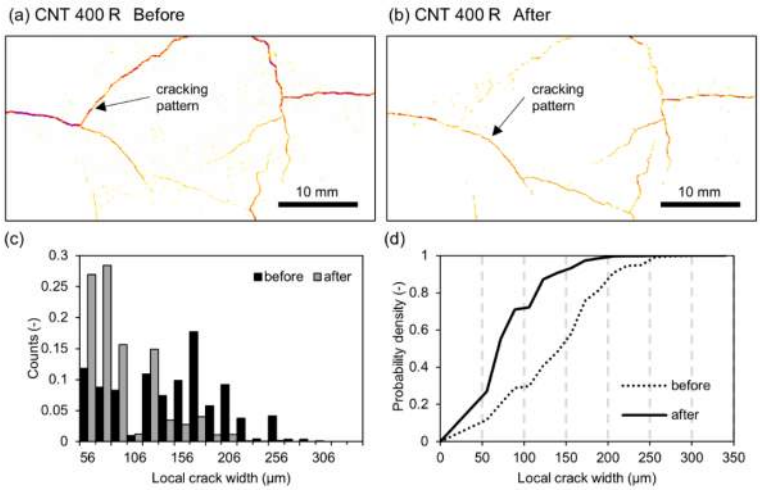

Figure 4.24. Changes of local crack width distribution for mix CNT subjected to 400°C and cured in retarding admixture: (a) fragment of the cracking pattern before healing, (b) after healing; (c) histogram of crack widths; (d) cumulative distribution function of crack widths.

An exemplary calculation has been performed for mix CNT subjected to 400°C and cured in retarding admixture before and after healing (Figure 4.24c). It suggested a bimodal distribution of crack widths (Figure 4.24) changes with the healing process, i.e., the number of narrow cracks below 100 μm increases whereas the number of wide cracks above 200 μm – decreases. The relation is also visible when the cumulative distribution functions are compared (Figure 4.24). Similar observations were made for all the mixes.

Analysis of the cross-sections of the sample with the optical microscope demonstrated the presence of the healing material inside the cracks of all specimens (Figure 4.25). White precipitates were visible deep inside the crack. In some cases, e.g., specimen 400 REF L,

there was a larger formation at the crack opening, but little self-healing phases formed inside the crack.

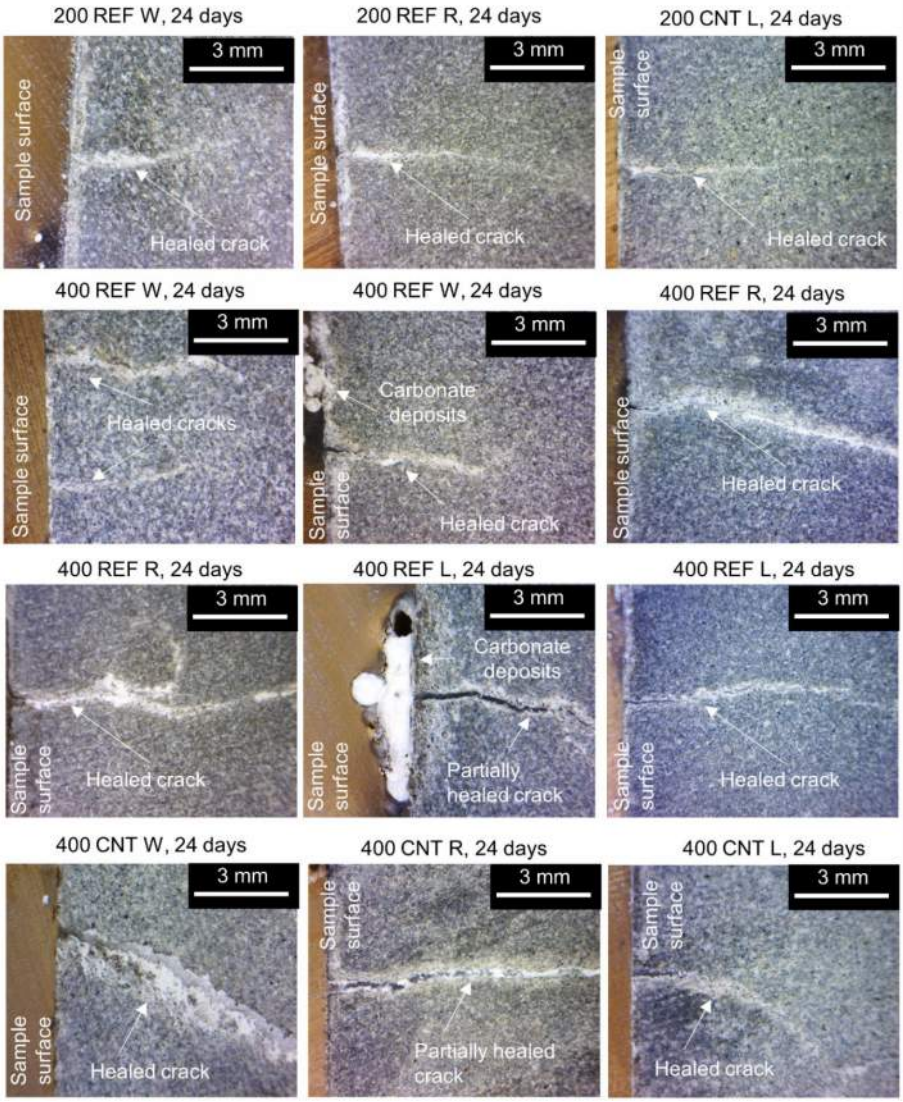

Figure 4.25. Optical images of the specimen's cross-section show cracks filled with healing products (Rajczakowska et al. 2023c).

In addition, SEM observations of the healing materials inside the crack were performed (Figures 4.26-4.29). The most pronounced internal crack closure, i.e., sealing the crack deep inside the specimen, was visible for specimens cured in retarding admixture solution

(Figure 4.26-4.29cd). This effect was consistent for both loading temperatures, regardless of the mix composition. Based on SEM analysis combined with EDX, several types of self-healing product morphology were observed with varied Si/Ca, Al/Ca, and P/Ca ratios and amount of sodium (Figure 4.30, Table 4.12). Irregular particles were detected inside the specimen and a homogenous filling mixture of presumably calcium phosphate with C—S—H (Table 4.12). Close to the surface (Figures 4.28c and 4.29c), a homogenous filling of possibly a mixture of calcium phosphate compounds with C—S—H with higher amounts of sodium was found.

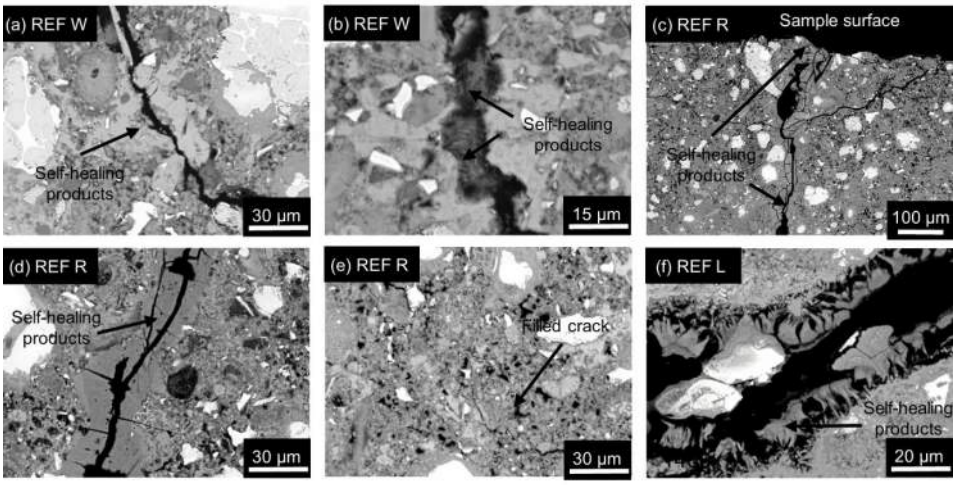

Figure 4.26. SEM images of self-healing products in the polished section of the 200°C cracks for REF specimens in different exposures (Rajczakowska et al. 2023c).

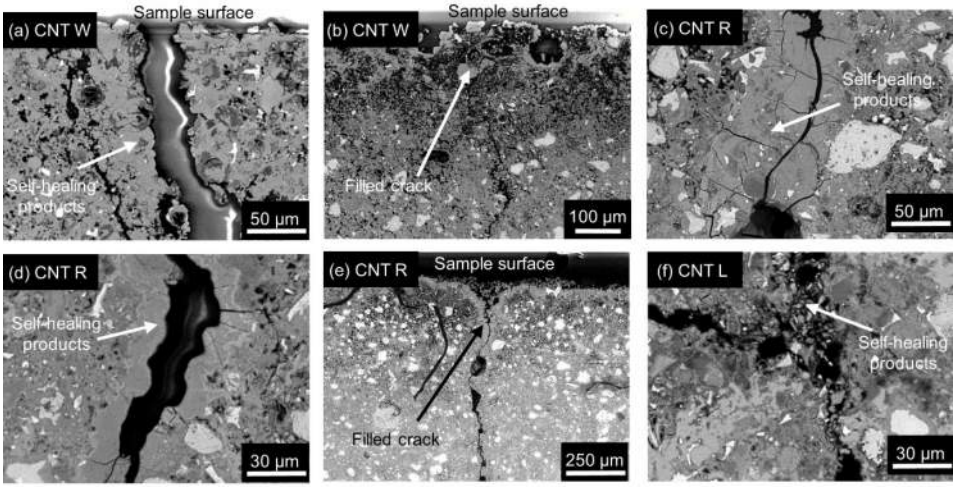

Figure 4.27. SEM images of self-healing products in the polished section of the 200°C cracks for 0.1% CNT specimens in different exposures (Rajczakowska et al. 2023c).

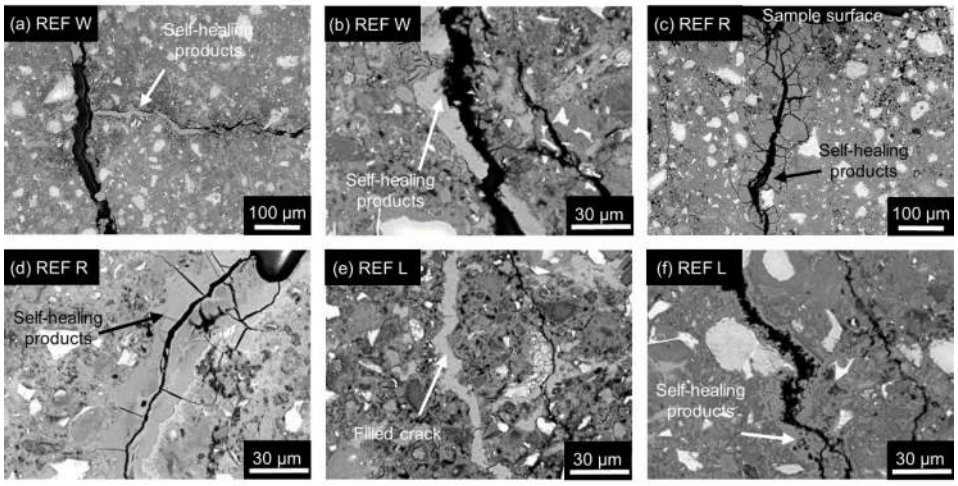

Figure 4.28. SEM images of self-healing products in the polished section of the 400°C cracks for REF specimens in different exposures (Rajczakowska et al. 2023c).

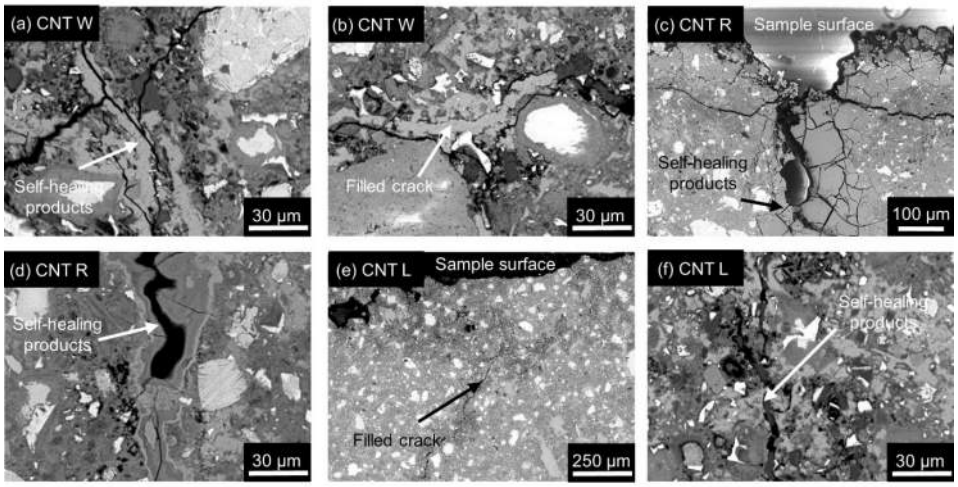

Figure 4.29. SEM images of self-healing products in the polished section of the 400°C cracks for 0.1% CNT specimens in different exposures (Rajczakowska et al. 2023c).

In the case of the water and lime water exposures, the self-healing phases presumably corresponded to the calcium carbonate layers at the surface and C-S-H mixed with calcium carbonate deeper inside the crack (Table 4.12). This agrees with earlier results obtained for mechanically cracked cementitious materials (Rajczakowska et al. 2019b). In addition, Ettringite presence was also speculated based on the sulfur detection, e.g., for 200 REF W (Table 4.12).

Table 4.12. Morphology and chemical composition of the healing products based on EDS analysis (Rajczakowska et al. 2023c).

Temp.	Paste type	Exposure	Morphology	Chemical composition
200°C	REF	W	- calcium carbonate mixed with C-S-H - ettringite needles	- Si/Ca=0.05±0.002, Al/Ca=0 - Si/Ca=0.13±0.02, Al/Ca=0.19±0.02, presence of Sulphur 2.14±0.3 %
	REF	R	- inside the specimen two types of products: * irregular particles * homogenous filling - mixture of calcium phosphate with C-S-H - close to the surface - homogenous filling - mixture of calcium phosphate with C-S-H	- inside the specimen: * Si/Ca=0.37±0.05, Al/Ca=0.03±0.02, presence of Sodium, Sulphur, Potassium * Si/Ca=0.10±0.03, Al/Ca=0.01±0.02, P/Ca=0.51±0.05, small amount of Sodium, Potassium - close to the surface - Si/Ca=0.08±0.02, Al/Ca=0, P/Ca=0.76±0.14, higher amount of Sodium 2.3±0.8 %,
	REF	L	- inside: possibly C-S-H mixed with calcium carbonate - close to the surface: calcium carbonate layers	- Si/Ca=0.25±0.02, Al/Ca=0, very small amounts of Sodium, Potassium - Si/Ca=0.07±0.02, Al/Ca=0, very small amounts of Potassium
	CNT	W	- calcium carbonate mixed with C-S-H	-Si/Ca=0.16±0.10, Al/Ca=0.02±0.03, very small amounts of Magnesium, Potassium
	CNT	R	- inside: homogenous filling - mixture of calcium phosphate with C-S-H - close to surface: homogenous filling - mixture of calcium phosphate with C-S-H	- inside - Si/Ca=0.10±0.01, Al/Ca=0.008±0.02, P/Ca=0.92±0.07, higher amount of Sodium 3.09±1.49 %, - outside - Si/Ca=0.53±0.45, Al/Ca=0.05±0.08, P/Ca=0.92±0.16, higher amount of Sodium 2.68±1.00 %,
	CNT	L	- healing products not visible on the cross-section	-
400°C	REF	W	- calcium carbonate mixed with C-S-H - ettringite needles	- Si/Ca=0.05±0.003, Al/Ca=0 - Si/Ca=0.10±0.006, Al/Ca=0.19±0.007, higher amount of Sulphur 2.64±0.6 %
	REF	R	- inside the specimen different types of products with mixture of porous and homogeneous filling (mixture of calcium phosphate with C-S-H) with varied Si/Ca, Al/Ca and P/Ca ratios and amount of Sodium: - close to the surface - homogenous filling - mixture of calcium phosphate with C-S-H with higher amounts of Sodium	-inside the specimen: * homogeneous type 1: Si/Ca=0.09±0.02, Al/Ca=0, P/Ca=0.45±0.04, Sodium 2.46±0.4 %, * homogeneous type 2: Si/Ca=0.21±0.03, Al/Ca=0.06±0.01, P/Ca=0.69±0.08, Sodium 5.04±0.9 %, * homogeneous type 3: Si/Ca=0.07±0.008, Al/Ca=0, P/Ca=0.48±0.07, Sodium 3.32±0.9 %, - close to the surface - Si/Ca=0.09±0.01, Al/Ca=0,

			P/Ca=0.97±0.06, higher amount of Sodium 6.7±0.8 %,
REF	L	- inside: calcium carbonate and possibly C-S-H mixed with calcium carbonate - close to the surface: calcium carbonate layers	- Si/Ca=0.06±0.005, Al/Ca=0 and Si/Ca=0.14±0.04, Al/Ca=0.01±0.02 with small amount of Magnesium and Potassium - Si/Ca=0.005±0.004, Al/Ca=0
CNT	W	- inside: calcium carbonate mixed with C-S-H - close to the surface: calcium carbonate layers	- Si/Ca=0.06±0.009, Al/Ca=0 - Si/Ca=0.04±0.01, Al/Ca=0
CNT	R	- inside: homogenous filling - mixture of calcium phosphate with C-S-H and calcium carbonate - close to surface: homogenous filling - mixture of calcium phosphate with C-S-H	- inside - Si/Ca=0.14±0.06, Al/Ca=0.02±0.02, P/Ca=0.37±0.14, higher amount of Sodium 2.37±1.14 %, - outside - Si/Ca=0.86±1.10, Al/Ca=0.03±0.08, P/Ca=0.97±0.25, higher amount of Sodium 3.62±2.95 %,
CNT	L	- calcium carbonate mixed with C-S-H	- Si/Ca=0.05±0.004, Al/Ca=0

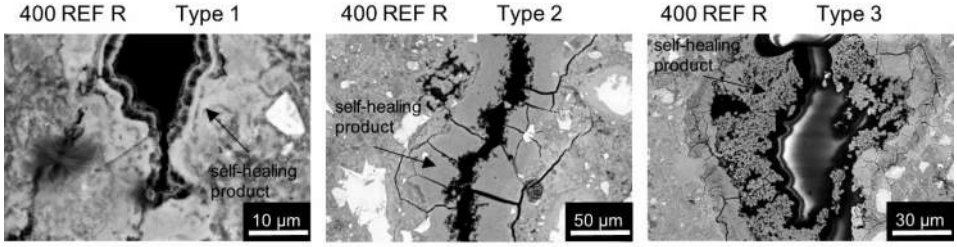

Figure 4.30. Different types of self-healing products (Table 4.12) in 400 REF R specimen (Rajczakowska et al. 2023c).

4.3.2. Effect of loading temperature

The relation between the maximum loading temperature and self-healing efficiency was evaluated based on the obtained results of the strength recovery (CSR0, CSRt, FSR0, FSRt) and surface crack closure (SCC). Two distinct groups of points are visible regarding the relation between CSR0, SCC, and FSR0 and CSRt, SCC, and FSRt, which suggests the influence of the loading temperature on the healing process (Figure 4.31). This relation was observed earlier in this Chapter, and it is in agreement with other studies (e.g., Poon et al., 2001).

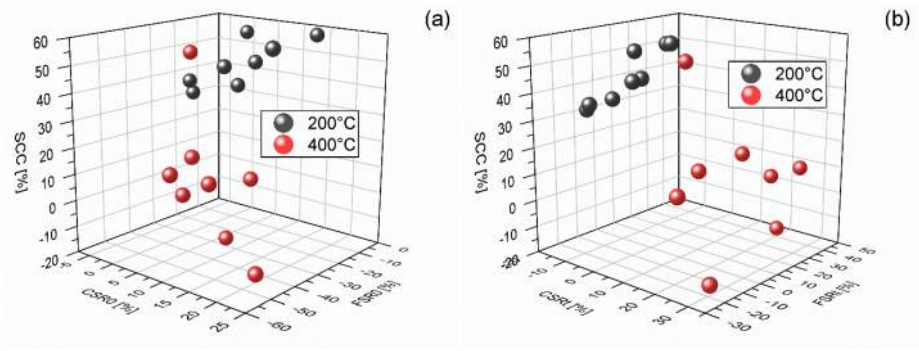

Figure 4.31. 3D scatter plot of: (a) SCC vs FSR0 and CSR0, (b) SCC vs FSRt and CSRt (Rajczakowska et al. 2023c).

In addition, a correlation analysis between temperature and self-healing efficiency parameters was performed using the point-biserial and Pearson correlation coefficients (Figure 4.32).

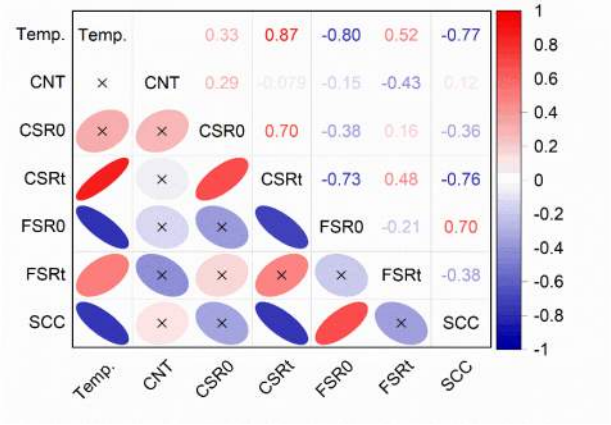

Figure 4.32. Correlation coefficients for different pairs of variables ("x" marks statistically non-significant correlations); significant level of 95% (Rajczakowska et al. 2023c).

Temperature demonstrated a high positive correlation with the CSRt with R=0.87 and a moderate positive correlation with the FSRt with R=0.52 (Figure 4.32). Both of those parameters describe strength regains in relation to the damaged specimens. The results suggest that the more damaged the material's structure, the more efficient the self-healing process, i.e., the more strength is recovered. It can be related to the wider cracks, which have more space to form self-healing phases. Another reason could be the more porous and

cracked hydrated cement matrix, which facilitates the transport of ions and healing material into the cracks, leading to better healing.

In contrast, the FSR0, i.e., flexural strength regain with respect to the performance of the intact specimens, showed a high negative correlation with loading temperature (Figure 4.32). Since the loss in flexural strength was only 1-7% after 200°C but 30-50% after 400°C, the damage which occurred in the specimens was challenging to heal at higher temperatures, i.e., the cracks were too wide, which could justify the negative correlation. No statistically significant correlation was observed for the CSR0, which agrees with the literature and ML model analysis (Figure 4.9f). The first significant drop in CS0 would be expected in the temperature above 400°C due to the decomposition of Portlandite.

The surface crack closure (SCC) also demonstrated negative relation to the temperature. As mentioned before, the increasing width of the cracks for higher temperature loading was presumably more difficult to close fully.

In addition, Figure 4.32 indicates that there are a few correlations between the self-healing efficiency parameters. For instance, flexural strength recovery FSR0 positively correlates with the surface crack closure SCC (Figure 4.32). It is visible that this relation is presumably associated with the temperature loading (Figure 4.33a) since two "clusters" points can be observed, corresponding to 200ºC (brown color) and 400ºC (green color). The crack sealing was significantly higher for lower temperatures, and the flexural strength loss was less pronounced. In contrast, a negative correlation was found between surface crack closure SCC and compressive strength recovery CSRt, i.e., with respect to the damaged state. Once again, two clusters of points are visible, linked to the loading temperature (Figure 4.33b). The samples gained relatively more compressive strength after healing from 400ºC temperature damage, yet the surface crack closure was very low in this case. It suggests that the mechanism of strength regain is presumably governed by another phenomenon, e.g., internal crack healing or chemical changes in the binder matrix, e.g., rehydration of phases.

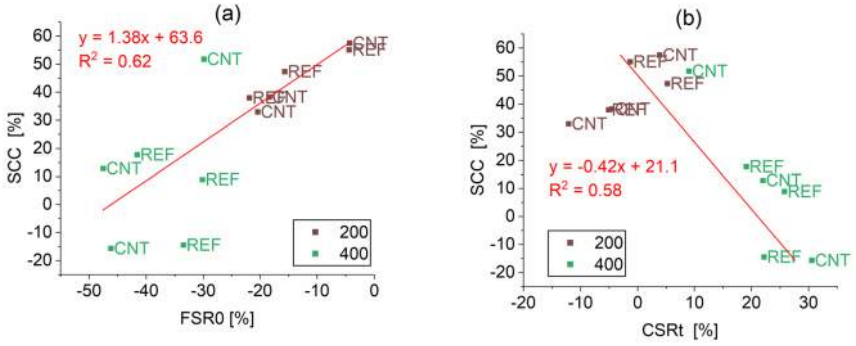

Figure 4.33. Relation between self-healing parameters: (a) SCC and FSR0, (b) SCC and CSRt (Rajczakowska et al. 2023c).

4.3.3. Effect of nanomaterials

A small dosage of carbon nanomaterials, i.e., 0.1wt% of MWCNTs, was added to the cement paste as a possible "booster" of the self-healing process. However, the correlation results (Figure 4.32) show no statistically significant correlations between MWCNTs and self-healing efficiency parameters. Nevertheless, differences were analyzed between the REF mix and CNT for each applied exposure group (Figures 4.34 and 4.35).

It can be noticed that for more prolonged water exposure (W0), the MWCNTs generally have a positive influence both on compressive strength recovery (Figures 4.34ab) and surface crack closure (Figures 4.35ab). However, the effect is not visible for the shorter water cycle (W). It could be related to the fact that these materials act as nucleation sites and potentially promote further hydration; therefore, they need extended time of re-curing in water.

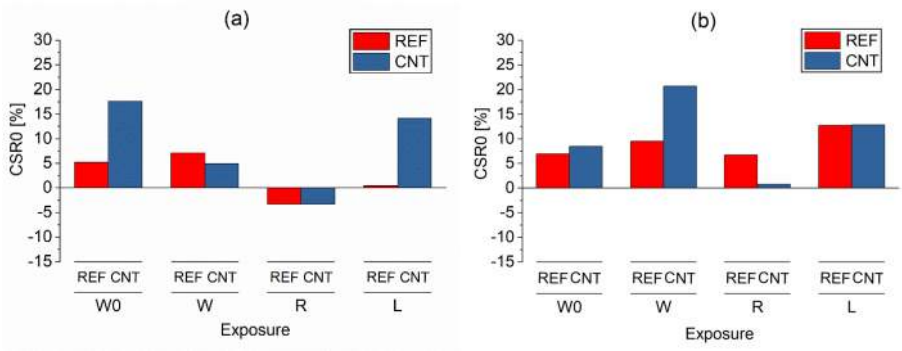

Figure 4.34. CNT vs CSR0: (a) 200°C, (b) 400°C (Rajczakowska et al. 2023c).

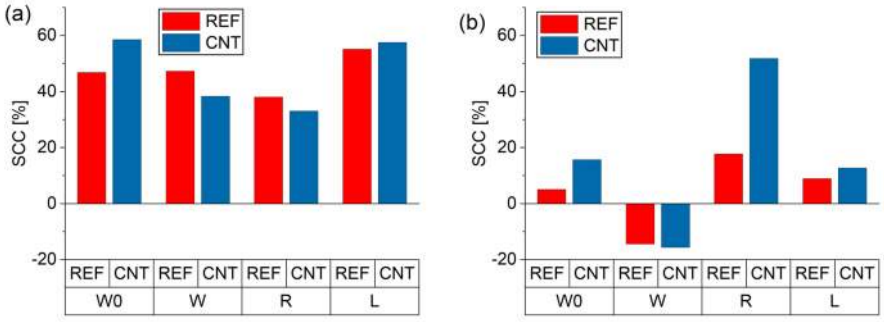

Figure 4.35. CNT vs SCC: (a) 200°C, (b) 400°C (Rajczakowska et al. 2023c).

For 400ºC loading, there is a positive effect of MWCNTs on the SCC in the case of retarding admixture (R); however, it is not visible after 200ºC loading (Figure 4.35). This can be an outcome of several factors. Firstly, the carbon nanomaterials might be bridging the microcracks and creating the nucleation sites on the crack planes inside the material,

facilitating the formation of the healing phases. In the case of retarding admixture, there is not only calcium carbonate and C-S-H forming in the cracks but also other compounds (Table 4.12), which possibly enables crack closure. The effect might be more pronounced for higher temperatures due to more cracks and pores forming an interconnected network to transport the calcium ions and healing activator into the crack.

The differences in the behavior of mixes REF and CNT are not pronounced. Nevertheless, only one dosage of MWCNTs was used. Therefore, observation of self-healing cementitious materials with varying content of nanomaterials could be beneficial.

4.3.4. Effect of microstructural changes

Chemical and physical transformations of the cement paste due to the healing process were studied based on changes in Si/Ca ratio for the inner and outer product of the C-S-H gel (Figures 4.36 and 4.37), porosity (Figure 4.39), unhydrated cement (Figure 4.40), and Portlandite (Figure 4.41) changes.

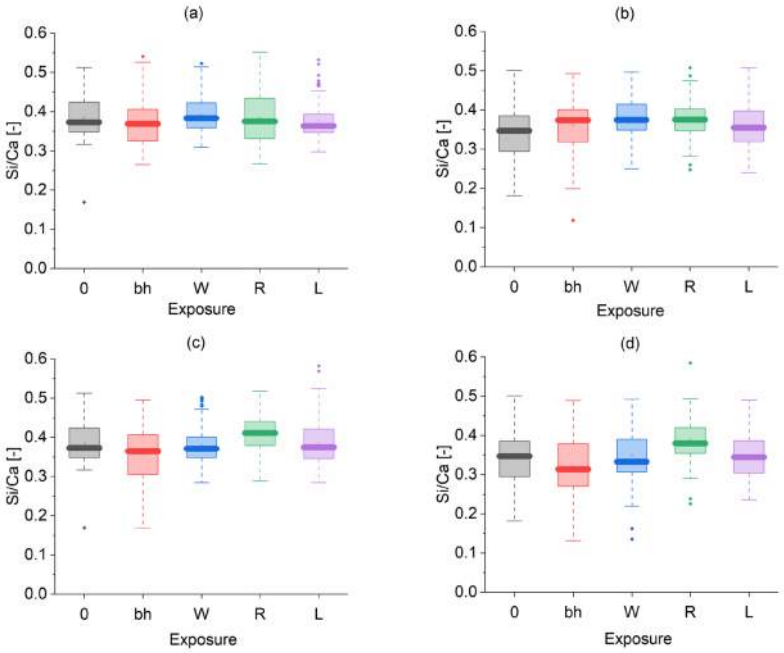

Figure 4.36. Box charts of measured Si/Ca ratios for C-S-H for REF mix: (a) IP 200°C, (b) OP 200°C, (c) IP 400°C, (d) OP 400°C (Rajczakowska et al. 2023c).

The differences in Si/Ca ratios for IP and OP measured for different exposures are between 10-20%, both in the case of REF (Figure 4.36) and CNT mixes (Figure 4.37). Considering the variation of measurements, they can be considered negligible. It indicates that possibly no major chemical changes occur in the C-S-H structure until 400 ºC, which is consistent with the literature (e.g., Jia et al. 2019).

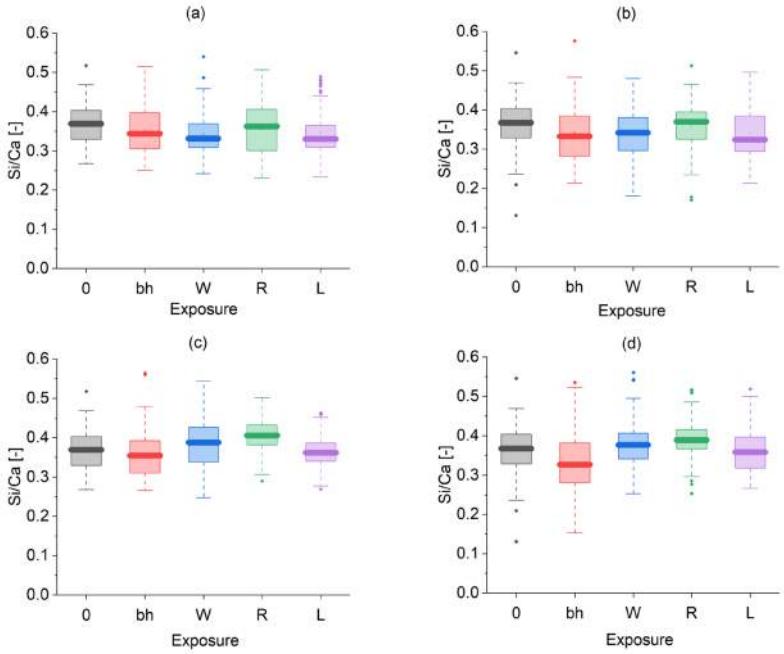

Figure 4.37. Box charts of measured Si/Ca ratios for C-S-H for CNT mix: (a) IP 200°C, (b) OP 200°C, (c) IP 400°C, (d) OP 400°C (Rajczakowska et al. 2023c).

Nevertheless, it should be noted that the obtained values of the Si/Ca are relatively low. The increase of Ca/Si (so decrease of Si/Ca) in IP and OP was observed for the OPC paste, e.g., 0.48 for 400ºC (Jia et al. 2019). However, in this study, values of approximately 0.4±0.05 were measured also for the control specimens, dried at 50 ºC. The carbonation of the specimens during preparation or inhomogeneities within the cement paste beams can be the cause. It might also be related to the SEM measurement setup since lack of applied coating results in higher current and low vacuum mode necessary to get an appropriate signal and avoid charging, thus possibly leading to intermixing of several phases, C-S-H, CH, AFt (Jia et al. 2019, Rossen and Scrivener, 2017).

The volume fractions of Portlandite and unhydrated cement were calculated using thirty SEM BSE images. Figure 4.38 presents an example of SEM cross-sections of 0.1%CNT, i.e., intact (control) samples, after 200ºC and 400ºC temperature loading (before healing) and after healing in water.

Based on the visual observations, it can be speculated that the temperature loading caused an increase in porosity (Figure 4.38). Dehydration and shrinking of the hydrated phases presumably cause these changes, e.g., the free and absorbed water is lost at 105ºC (Rajczakowska et al. 2022, Ma et al. 2015, Feldman et al. 1971), dehydration and decomposition of the main phases start, i.e., AFt/AFm phases at 105 ºC, C-S-H at 200ºC and portlandite at 350ºC (Ming et al. 2020, Ma et al. 2015). At 400ºC, there is an increased

formation of microcracks and coarsening of porosity due to, e.g., evaporation of capillary water (Ma et al. 2015), which is visible in Figure 4.37. However, after healing, the hydrated binder matrix looks similar to the control (Figure 4.38)

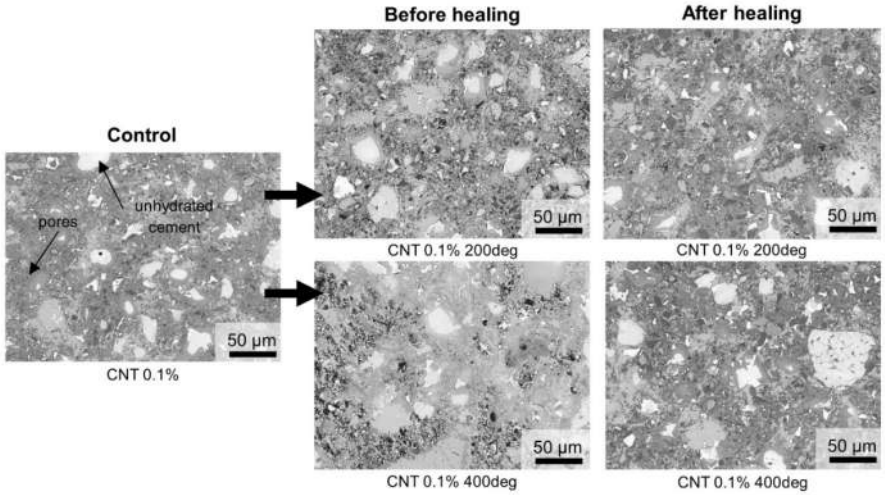

Figure 4.38. Microstructure changes for 0.1%CNT (Rajczakowska et al. 2022).

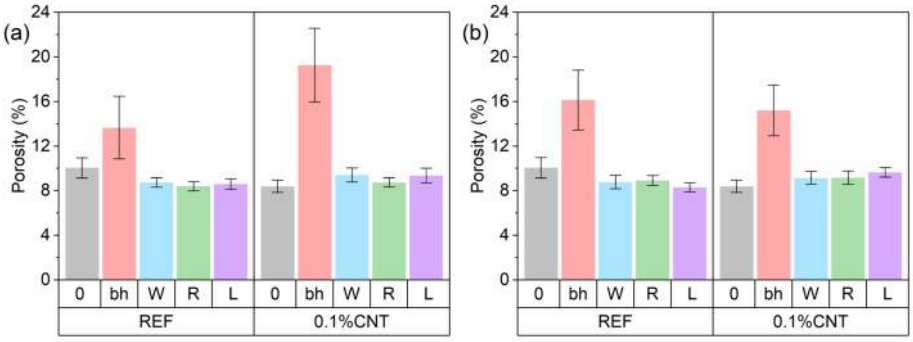

Figure 4.39. Porosity results: (a) 200°C, (b) 400°C (Rajczakowska et al. 2023c).

Further hydration of unhydrated cement grains in thermally cracked cement paste could lead to performance recovery. However, obtained results suggest that the amount of unhydrated cement does not change significantly, oscillating around 12% before and after the temperature exposure and after the self-healing process (Figure 4.40ab).

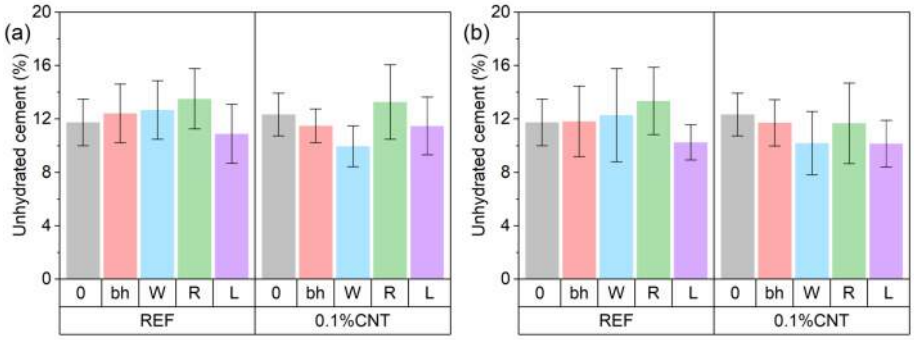

Figure 4.40. Unhydrated cement results: (a) 200°C, (b) 400°C (Rajczakowska et al. 2023c).

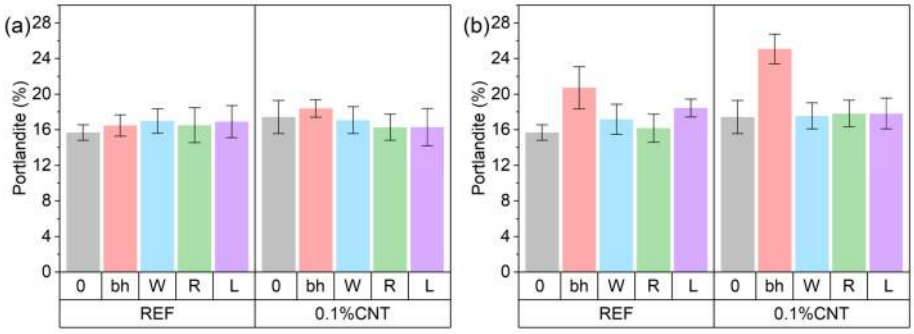

Figure 4.41. Portlandite fraction: (a) 200°C, (b) 400°C (Rajczakowska et al. 2023c).

This observation was confirmed with the calculation of porosity (Figure 4.39). The initial porosity (0) for both mixes was approximately 10%. After temperature exposure, the porosity increased to 14-18% (bh). However, it decreased again after healing, reaching the level of the intact specimen (Figure 4.39). The effect was visible for all exposure conditions. Presumably, the rehydrated phases formed in the pores, filling the matrix.

The fraction of Portlandite phases did not change for 200°C temperature exposure (Figure 4.41a). In contrast, 10-30% changes were observed after 400°C temperature loading. Other studies observed that the amount of Portlandite and C-S-H does not change significantly until the temperature reaches 400°C (Zhang et al. 2013). Nevertheless, it was also noted that the hydration products shrink below 400°C (Dias et al. 1990, Zhang et al. 2013). Since the C-S-H phases start decomposing earlier than Portlandite, the relative amount of Portlandite may be presumably higher at 400°C, as observed in this study.

In addition, the correlation analysis between the microstructural parameter changes (Table 4.9) and self-healing efficiency was performed to verify the relations (Figure 4.42).

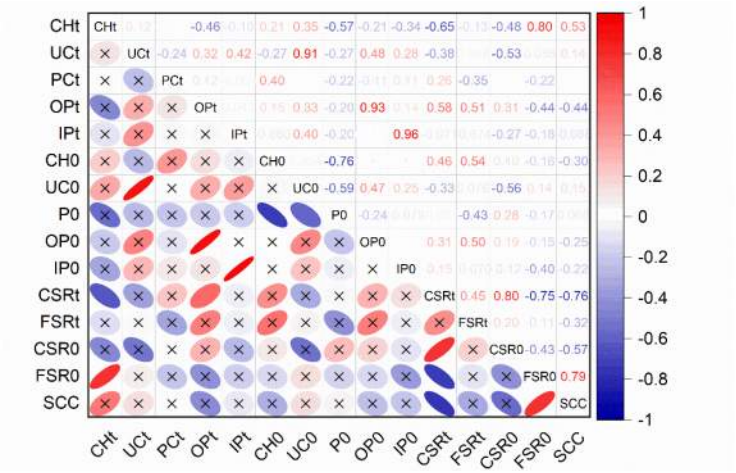

Figure 4.42. Pearson correlation coefficient for the microstructural parameters (x – non-significant correlations) (Rajczakowska et al. 2023c).

It is visible that most of the correlations are statistically insignificant due to a limited number of observations (Figure 4.42). Nevertheless, the Portlandite change concerning the damaged state (CHt) was found to be negatively correlated with the CSRt. As shown in Figure 4.43a, this relation is strictly related to the temperature loading. As mentioned before, the increased amount of Portlandite after 400ºC exposure can be related to the decomposition and shrinkage of other phases, e.g., C-S-H and AFt/AFm, leading to a relatively higher fraction of CH in the binder matrix. More CH and higher porosity presumably contribute to lower compressive strength of thermally damaged specimens. Therefore, a more significant change in CH after healing results in a higher strength increase concerning the damaged state (CSRt).

On the other hand, the FSR0 is positively correlated with the CHt (Figure 4.42). This relation is also directly connected to the loading temperature (Figure 4.43b). In this case, the healing was minimal, with a large spread of the results; therefore, it is impossible to speculate on this relationship's physical causes.

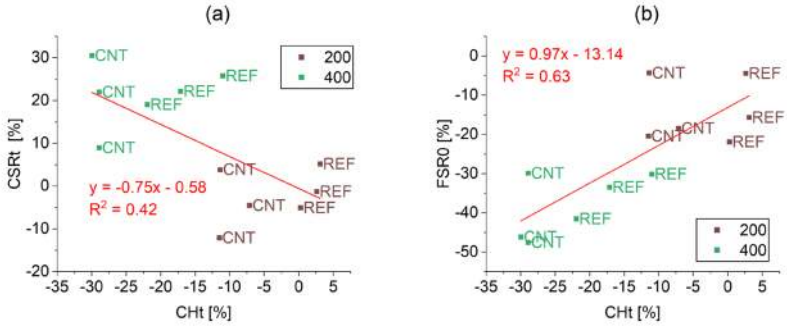

Figure 4.43. Relation between (a) CHt and CSRt, (b) CHt and FSR0 (Rajczakowska et al. 2023c).

4.4. SUMMARY

In Chapter 4, the self-healing of thermally cracked cementitious materials was studied using computational and experimental methods.

The following main conclusions were established based on Chapter 4:

- ML methods enabled the construction of the strength recovery model of thermally damaged concrete with accuracy twice as good as linear regression.
- Ensemble of regression trees with boosting algorithm obtained the lowest error and training time.
- Performed sensitivity analysis and interpretation of the model with the PDPs and ICE plots pointed out the importance of the loading temperature and curing treatment on the self-healing efficiency. According to the model, the binder-related mix components had a secondary role in the process; however, the model did not consider SCMs.
- Using substances other than water did not significantly improve the self-healing efficiency of thermally cracked cement paste.
- For 400ºC loading, there was a positive effect of MWCNTs on the SCC in the case of retarding admixture, which was not visible in the case of 200ºC loading.
- For more prolonged water exposure, the MWCNTs positively affected the compressive strength recovery; the effect was not observed for the shorter water cycle; presumably, an extended time of re-curing in water is needed for these materials to “boost” the hydration process.
- In general, self-healing was more pronounced for 400ºC damage, possibly due to more cracks and pores forming an interconnected network transporting the calcium ions and environmental stimulator into the crack.
- Self-healing products were observed inside the cracks for all exposures, both at the crack mouth and deeper inside the crack. Calcite dominated in the case of water and limewater, whereas a mixture of C-S-H, calcite, and calcium-phosphate compounds for retarding admixture exposure.
- The amount of unhydrated cement did not change during the self-healing process; however, the porosity decreased significantly compared to the damaged state. Presumably, the rehydrated phases formed in the pores, filling the matrix.

5

Discussion and outlook

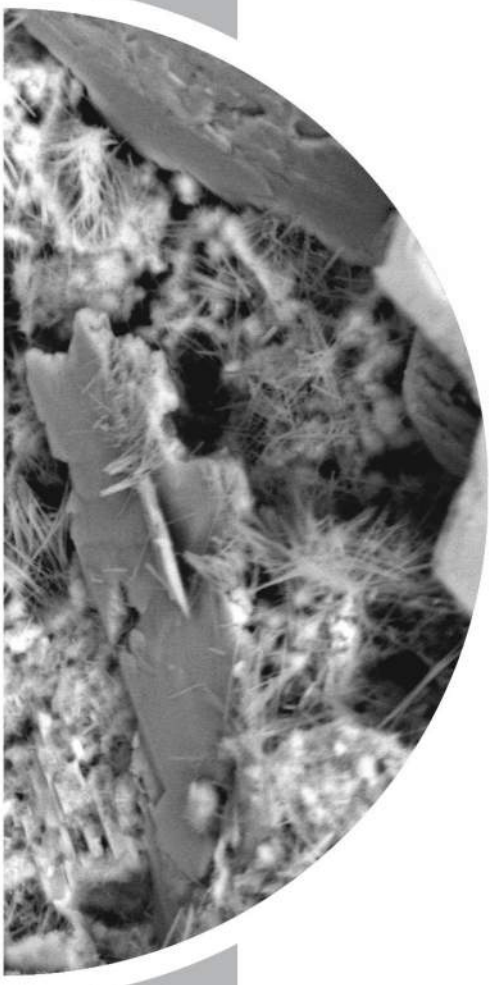

"If Isaac Newton had never said to himself 'I don't know', the apples in his little orchard might have dropped to the ground like hailstones and at best he would have stooped to pick them up and gobble them with gusto."

Wisława Szymborska
1996 Literature
Nobel Prize winner

5. DISCUSSION AND OUTLOOK

5.1. AUTOGENOUS SELF-HEALING MECHANISM

This research consisted of several stages to deepen the understanding of the autogenous self-healing mechanism (Chapter 1, Figure 1.1). During initial studies (Chapter 3.1), an "extreme" mix composition was chosen, i.e., UHPC, to confirm that the amount of available unhydrated cement drives self-healing. The results suggested that this dependency is not as strong as predicted. Furthermore, lower crack closure was observed for the UHPC mix than in mortars with lower cement amount and higher water-to-cement ratio (Rajczakowska 2019, Rajczakowska et al. 2019b). The conclusions from this investigation led to the formulation of the proposed self-healing mechanism (Figure 5.1).

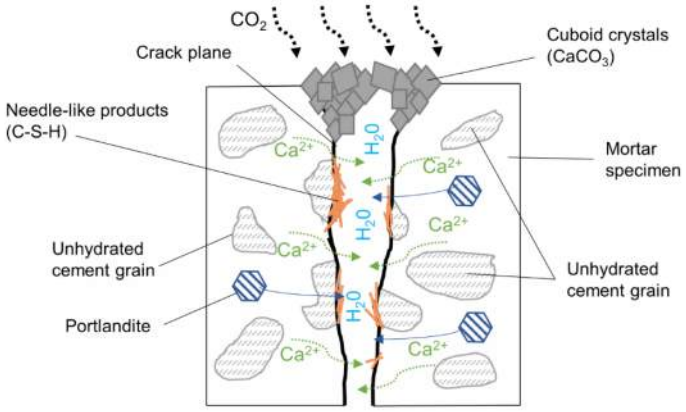

Figure 5.1. Observed self-healing patterns in initial studies (Rajczakowska et al., 2019b).

Different self-healing processes dominated inside the crack and at the crack mouth. White cuboid crystals, identified as calcium carbonate, were observed at the crack mouth, supporting the sealing of the crack. This process could presumably lead to durability recovery by blocking the movement of aggressive substances into the crack. On the other hand, a mix of various hydrated phases, including C-S-H, $CaCO_3$, and Ettringite, were examined deeper inside the cracks of the specimens with higher flexural strength recovery (mix A1 and U1). These findings were in agreement with the previous studies, e.g., (Granger et al., 2007ab).

The two types of observed autogenous self-healing behavior can be linked to the generally accepted mechanisms, i.e., calcium precipitation and ongoing hydration (e.g., De Rooij et al. 2013).

Calcite precipitation is driven by the diffusion-dissolution-precipitation processes connected to the leaching of calcium from the Portlandite and C-S-H due to water exposure.

First, calcium ions are transported by diffusion because of the difference in concentration between the tap water and the pore solution of the hydrated binder (Adenot and Buil, 1992). The ions react inside the crack with the carbonate ions originating from the atmospheric CO_2 dissolved in water. In this study, the calcite crystals were found in large quantities adjacent to the crack opening, which can be related to a locally favorable environment. Presumably, close to the surface, carbonate and calcium ions concentrations are optimal for the chemical reactions (precipitation) to occur (Sisomphon et al., 2012). The water remaining inside the sealed crack (Figure 5.1) has a higher ion concentration which facilitates the growth of other self-healing phases, such as C-S-H, Portlandite, and ettringite (Huang et al., 2013).

In addition, in the initial studies, the dependency of the self-healing process on the material's age was observed. Aged UHPC specimens (U12) obtained substantially smaller crack closure than the 1-day-old sample (U1). Furthermore, the early-age specimen was characterized by the higher interconnected porosity suggesting that the pore network is a critical factor for the auto-repair process. The formation of self-healing products inside the crack is governed by the availability of ions, i.e., calcium, transported from the hydrated phases. Thus, dense hydrated cement binder with low porosity, e.g., like in UHPC, may prevent or slow down this process.

The self-healing features affecting the mechanism were identified based on the initial study results. First, the amount of unhydrated cement particles resulting from a high amount of binder and the low water-to-cement ratio does not seem to assure an efficient recovery of the material properties. At the same time, adding fly ash led to the successful sealing of the crack with calcite. However, it did not achieve corresponding strength regain, possibly due to hindering the formation of C-S-H inside the crack. This observation pointed out a potential strong dependency of the healing efficiency on the presence of SCMs. Based on the performed results analysis of the preliminary study, the following hypotheses were addressed in the follow-up research:

- **Hypothesis 1:** The impermeable hydration product shell, quickly formed on the surface of freshly exposed unhydrated cement, prevents the ongoing hydration process inside the crack.
- **Hypothesis 2:** The dense binder matrix with low interconnected porosity related to, e.g., the low water-to-binder ratio leads to insufficient calcium and silicone ion concentration inside the crack.
- **Hypothesis 3:** The supplementary cementitious materials, e.g., fly ash, support the crack sealing due to calcite precipitation.

5.1.1. Hypothesis 1 – environmental exposure

Hypothesis 1 was addressed by testing various environmental conditions, i.e., healing exposures, which could enhance self-healing by increasing the ion concentration inside the crack and controlling the hydration rate (Chapter 3.2.1). Four groups of potentially stimulating substances were investigated: various water immersion regimes, temperature

effect, the hydration rate-modifying admixtures, and mixtures of water with other ions/particles. Scientific justification of exposure conditions selection was specified in Table 3.5, Chapter 3 of this thesis. It is important to note that similar crack opening width was maintained in all the specimens, considering the influence of the crack width on the healing efficiency. The results of the experiments are outlined in Table 5.1.

Table 5.1. Summary of the results of various environmental conditions, Chapter 3.2 (Rajczakowska et al., 2019c).

Exposure	Abbreviation	External self-healing	Internal self-healing
Deionized water mixed with Accelerator in proportions 3:1 (immersion)	EXP 1	Minimal crack closure; Several calcite crystals of various shapes	Almost no healing; Several microns thick calcite layer under the surface, inside – few thicker deposits of calcite mixed with CSH (Si/Ca=0.19)
Deionized water mixed with Retarder in proportions 3:1 (immersion)	EXP 2	The crack almost wholly healed; calcium phosphate compounds on the surface with some amount of sodium originating from the self-healing mixture	Very high internal crack closure; Calcium phosphate compounds as well as CSH; Si/Ca and Ca/P increasing with crack depth
Saturated lime water immersion	EXP 3	Very good external self-healing: a dense layer of calcite crystals present at the surface	Almost no internal self-healing; few self-healing products with an average Si/Ca of 0.3
Coca-Cola immersion	EXP 4	Efficient external crack closure; calcium phosphate compounds with Ca/P ranging from 1.5 to 2.5	Self-healing products visible inside with CSH-like precipitates with Si/Ca of around 0.3-0.4; some calcium phosphate products present
Deionized water immersion	EXP 5	Minimal external healing, ettringite and calcite crystals filling the crack	Ettringite is visible close to the surface; no internal self-healing
Deionized water immersion with cyclic evaporation (72 h cycle)	EXP 6	Some crack closure; large calcite crystals covering the crack	A layer of calcite inside of the sample closure to the surface, few self-healing products in deeper parts of the crack
Dry/wet (deionized water) cycles 24 h/24 h	EXP 7	Almost no external self-healing with a small calcite crystal layer at the surface	No internal self-healing except for few healing products deposited on the PVA fibers' surface
Deionized water immersion up to 1 mm height of the sample	EXP 8	Minimal external healing, ettringite present; no noticeable differences between exposure 8 and 9	Ettringite is visible close to the surface; no internal self-healing
Deionized water immersion up to 5 mm height of the sample	EXP 9		
Water immersion temperature cycle 24 h/ 20°C and 24 h/ 40°C	EXP 10	Minimal external healing, calcite crystals filling the crack	Hardly any internal healing, with only single calcite crystals

Water immersion temperature cycle 24 h/ 20°C and 24 h/ 5°C	EXP 11	Efficient external crack closing; calcite crystals inside the crack as well as a thick layer of ettringite	
Deionized immersion with micro-silica particles 1.25%w	EXP 12	Very high external self-healing with densified calcite structure filling the crack	Agglomerates of micro-silica particles inside the crack without self-healing products.

The results of the experiment pointed out several patterns. First, the environmental conditions based on water exposure (EXP 5-9, Table 5.1) demonstrated limited crack closure and strength recovery. Temperature affected the phases forming in the crack, with a large amount of ettringite visible for mortar exposed to water at 5°C (EXP 11, Table 5.1). It can be speculated that the self-healing process can be enhanced by longer exposure time and mix composition optimization.

Two environmental conditions were found to facilitate the self-healing process, i.e., adding micro silica particles into the water (EXP 12, Table 5.1) and mixing water with retarding admixture (EXP 2, Table 5.1). In addition, the following mechanisms supporting these outcomes can be hypothesized.

In the case of micro-silica-based exposure (EXP 12), the particles possibly sedimented from the water mixture into the crack and acted as nucleation sites for the growth of self-healing phases (Figure 5.2). A similar phenomenon was observed when PVA fibers were present. In hydrating cement, the silica fume particles were observed to accelerate C-S-H formation by seeding (Roberts 1989, Cheung et al. 2011); therefore, they might presumably speed the formation of C-S-H inside the crack as well. Since the C-S-H is the load-bearing phase, presumably responsible for the strength recovery after the healing process, it could explain this exposure's relatively high flexural strength recovery. On the other hand, since agglomerated particles were observed deeper inside the crack, the sedimentation process might have led to the blockage of the cracks, resulting in improved strength.

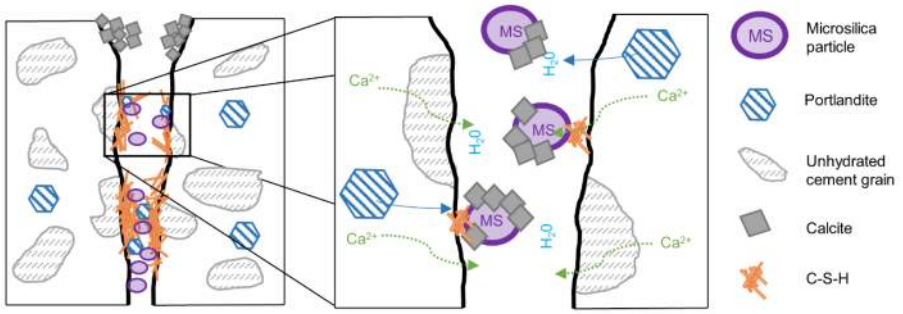

Figure 5.2. Possible self-healing mechanism for samples exposed to the micro-silica-water mixture.

On the other hand, the retarding admixture exposure may act according to two processes (Figure 5.3). It should be mentioned that since the exact chemical composition of the commercial retarding admixture is complex (Chapter 3.1), the hypothesized processes are only a possible theory.

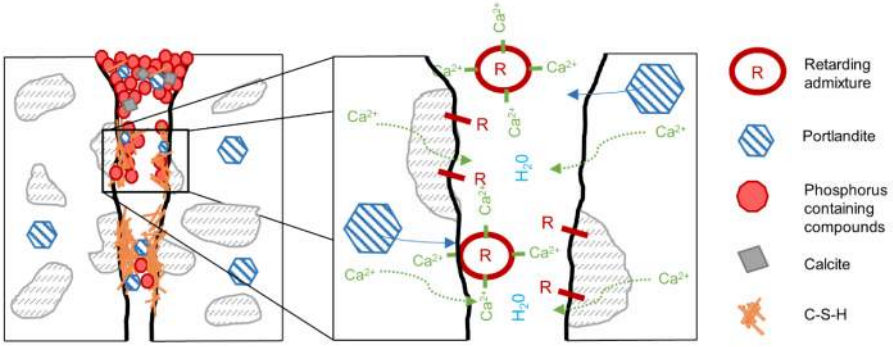

Figure 5.3. Possible self-healing mechanism for samples exposed to Retarder mixed with water (modified from Rajczakowska et al., 2019c).

First, the formation of a dense hydration shell on the unhydrated cement grains exposed by a crack is prevented by a typical retarding action, possibly due to the adsorption of the phosphate/phosphonate ions on the surface of unhydrated cement grains (Figure 5.3). As a result, the growth of the self-healing phases, i.e., C-S-H, Portlandite, and Ettringite, is delayed, allowing the ions to release into the crack. Analysis with SEM and EDX revealed the increasing amount of the C-S-H with the distance from the sample's surface (Chapter 3.2), suggesting a higher concentration of calcium and silicate ions deeper inside the crack, reinforcing this hypothesis. It should be noted that this treatment was only done on freshly formed cracks. Old cracks which were in contact with moisture have not been studied.

Second, a parallel activity of this particular retarding admixture may be associated with the direct reaction between the phosphate/phosphonate ions from the retarder and calcium ions in the mixture inside the crack (Figure 5.3). Precipitation of homogenous compounds with relatively high amounts of calcium and phosphorus was observed during SEM and EDX analysis (Chapter 3.2), facilitating nearly complete crack closure. Analogical reactivity was detected in the wastewater treatment research, where calcium released from the C-S-H reacted with the phosphate anions (Maeda et al., 2018; Karageorgiou et al., 2007; Naus et al., 2007; Guan et al., 2013). Formed compounds, e.g., HAP, were found to be more stable and less soluble than calcium hydroxide (Naus et al. 2007); however, they exhibit low flexural strength. This characteristic could explain a minimal regain of strength in this self-healing exposure (Chapter 3.1).

5.1.2. Hypothesis 2 and 3 – mix composition

To address Hypotheses 2 and 3 (Chapter 5.1), the effect of the microstructure of different mortar mix compositions on the self-healing efficiency was studied. Furthermore, mortars with 50% cement replacement by limestone in connection with SCMs (Chapter 3.1, Table 3.2) were analyzed since one of the project objectives was to focus on environmentally friendly materials. Limestone is a locally available, relatively cheap material, commonly used as a filler with up to 15%wt cement to improve concrete properties. However, due to the predicted depletion of the SCMs sources, such as fly ash or slag, limestone appears to be a prime candidate for decreasing concrete carbon footprints. Aside from the climate impact and accessibility, the following supportive arguments for the material choice were considered, associated with Hypotheses 2 and 3:

- Above 15%wt of cement replacement with limestone leads to higher open porosity and permeability (Courard and Michel, 2014), partially due to the dilution effect (Bentz, 2006), which could presumably facilitate the transfer of ions into the crack.
- For early-age cracks, it can be beneficial that limestone accelerates the hydration of cement, leading to the production of larger quantities of Portlandite at an early age. In addition, since Portlandite appears to be the primary source of calcium ions, a more considerable amount of $Ca(OH)_2$ could potentially enable more calcium to leach into the crack. The positive correlation between the addition of $CaCO_3$ and the formation of new calcite due to calcium hydroxide leaching was observed in earlier studies (Catinaud et al., 2000).
- The combined application of limestone and SCMs forces significant changes in the phase assemblage and microstructure of the hydrated binder, which can have positive and negative consequences for the healing process. For example, more Portlandite at an early age facilitates the pozzolanic reaction due to hydration acceleration. However, a resulting consumption of the Portlandite may cause a decreased concentration of ions inside the crack. On the other hand, a lower amount of Portlandite suggests less calcium in the pore solution, which, under water exposure, may lead to a higher diffusion rate of calcium from the hydrated binder due to a higher concentration gradient. In addition, the increased pozzolanic reaction may produce a dense binder matrix, hindering the transfer of ions into the crack.

In addition, similarly to initial studies, "extreme" mix compositions were chosen (Table 3.7). The primary goal was to obtain detectable differences in the pore network, phase assemblage, and pore solutions. The effect of these features was measured concerning the self-healing efficiency (Chapter 3.2.2).

Considering the calcium leaching process, cyclic water exposure was selected, with water exchange between the cycles. The purpose was to impose higher ion concentration gradients and potentially increase the ion transfer into the crack. In previous studies, the calcium leaching caused corrosion by renewed water was studied in relation to the radioactive waste disposal facilities; however, the rate of the reactions was slow (Adenot and Buil, 1992).

The study's results demonstrated significant self-healing behavior differences between cementitious materials, possibly connected to their transport properties dependent on the assemblage of solid phases, pore structure, and pore solution composition (Sui et al. 2019). In addition, hypothetical mechanisms of self-healing were analyzed with respect to the presence of SCMs.

The ongoing hydration was possibly the process for the self-healing of slag binders due to the availability of unreacted material (Lothenbach et al. 2011). Slag demonstrates similarities with the OPC, i.e., it has high hydration activity and CaO content which supports ongoing hydration. In this study, mixes containing slag exhibited efficient recovery, which can possibly be attributed to the synergistic effect of limestone. Limestone content between 20 and 50% wt. boosts slag performance (Proske, et al. 2018)

Relatively high strength and durability recovery were observed for silica fume mixes; however, the surface crack closure was less pronounced (Chapter 3.2). It can be associated with the changes in the C-S-H and $Ca(OH)_2$ phases. Portlandite was observed to grow between the grains and hydration shell, as well as the changes in pore solution are observable with age. At early ages, there is more calcium in the pore solution, while later, silicone takes over (Rossen et al. 2015). The SEM measurements uncovered higher porosity, which may facilitate the transfer of the ions into the crack. EDX analysis indicated a higher Si/Ca ratio of the IP C-S-H, potentially suggesting that C-S-H phases inside the crack contributed to the strength recovery, while limited calcite precipitated at the crack mouth.

The application of low calcium fly ash had several implications on the self-healing process due to its slow reaction rate and high activation energy. The synergistic effect of limestone can be hypothesized for lower amounts of fly ash (mix FA12.5) since it accelerates the reaction and is found to lower the apparent activation energy (Bentz, 2014). However, it did not seem to be valid for mix FA50 with a large amount of fly ash, possibly due to a slower reaction rate (Lottenbach et al. 2011). The early age of cracking, i.e., 7 days, could also affect the chemical reactions and self-healing process. The depletion of CH phase due to the pozzolanic activity accelerates after 7 days (Lottenbach et al. 2011), which could lead to an insufficient amount of Portlandite to supply calcium ions into the crack. Furthermore, the unhydrated fly ash particles presumably could not be activated by the water solution in the crack (Luo et al. 2021), implying a lack of an ongoing hydration process.

The consumption of Portlandite during pozzolanic reaction may presumably be the reason for a relatively low crack closure for all the mixes, with a maximum of 60% for slag and 40% for silica fume mixes. This agrees with other studies (Maddalena et al., 2021). The negative effect on self-healing may be attributed to several developments. First, additional C-S-H was formed, densifying the hydrated binder matrix, possibly hindering the ions' transfer to the crack. Even though the Portlandite was speculated as the main supplier of calcium ions inside the crack, in this study, the amount of CH did not positively correlate with the recovery efficiency. Again, the early cracking age of the materials can be behind this observation. Finally, each of the SCMs consumed CH in pozzolanic activity

at a different speed, leading to inconclusive results concerning the effect of Portlandite on the self-healing process.

Furthermore, the pore solution composition, i.e., the ion concentration and pH, can be hypothesized as one of the significant variables. The reaction of binders with a high amount of slag and fly ash presumably slowed down inside the crack due to decreased calcium concentration in the pore solution (Vollpracht et al. 2016). A more extended water immersion period could potentially facilitate the diffusion-dissolution-precipitation processes within the crack, leading to increased pH in the crack and enhancing the reactivity of the SCMs. The dissociation of the carbonic acid inside the crack, crucial in the calcite precipitation process, was also found to depend on the pore solution's pH (Yildirim et al. 2015).

The porosity results with connection to the sorptivity coefficient gave information on the presumable pore network features, which could affect the self-healing. Although fly ash mixes showed low porosity values, the high sorptivity coefficient value for undamaged FA12.5 specimens suggested a possibly high amount of open capillary pores (Durdziński, 2016). Therefore, efficient self-healing of this material could be explained by the interconnected porous network facilitating ion transport. This effect was not visible in the performance of the FA50 mix, which had low porosity and sorptivity values. Silica fume mixes exhibited higher porosity than slag and fly ash, possibly due to a high replacement ratio. It agrees with other studies, where over 8 wt % of silica fume produced increased porosity (Zelic et al., 2000). Despite a large number of pores, lower permeability was observed, which can suggest limited network connectivity (Zelic et al., 2000), possibly causing a low crack closure in the case of the SF50 mix. In other studies, smaller capillary porosity of the silica fume binders was noticed due to homogenous OP C-A-S-H (Rossen et al. 2015).

5.2. MECHANICAL VS THERMAL LOADING

As mentioned before, the main physicochemical processes contributing to the autogenous self-healing of cementitious materials are diffusion, dissolution, and precipitation related to calcium leaching and ongoing hydration. Each of those processes is present in the self-healing of mechanically and thermally cracked cementitious materials. However, the initial conditions, i.e., the state of the hydrated binder, are different, which affects the recovery process, involving, as before, the three components: phase assemblage, pore solution, and pore structure.

For mechanically induced cracks, two cases can be differentiated: matured (above 28 days) and early age. In the former case, the hydrated binder matrix is stable, i.e., the hydration process has (mostly) finished, the hydrated phases are formed, and porosity is established. In the latter case, depending on the binder composition, the hydration process is ongoing, with the volume fraction of major phases changing, e.g., due to pozzolanic reaction as in the case of SCM-rich binder investigated in this research (Chapter 3). These reactions increase concrete's durability and mechanical performance; however, they do not

directly contribute to self-healing. Consequently, the primary self-healing feature is the closure of the mechanically induced crack.

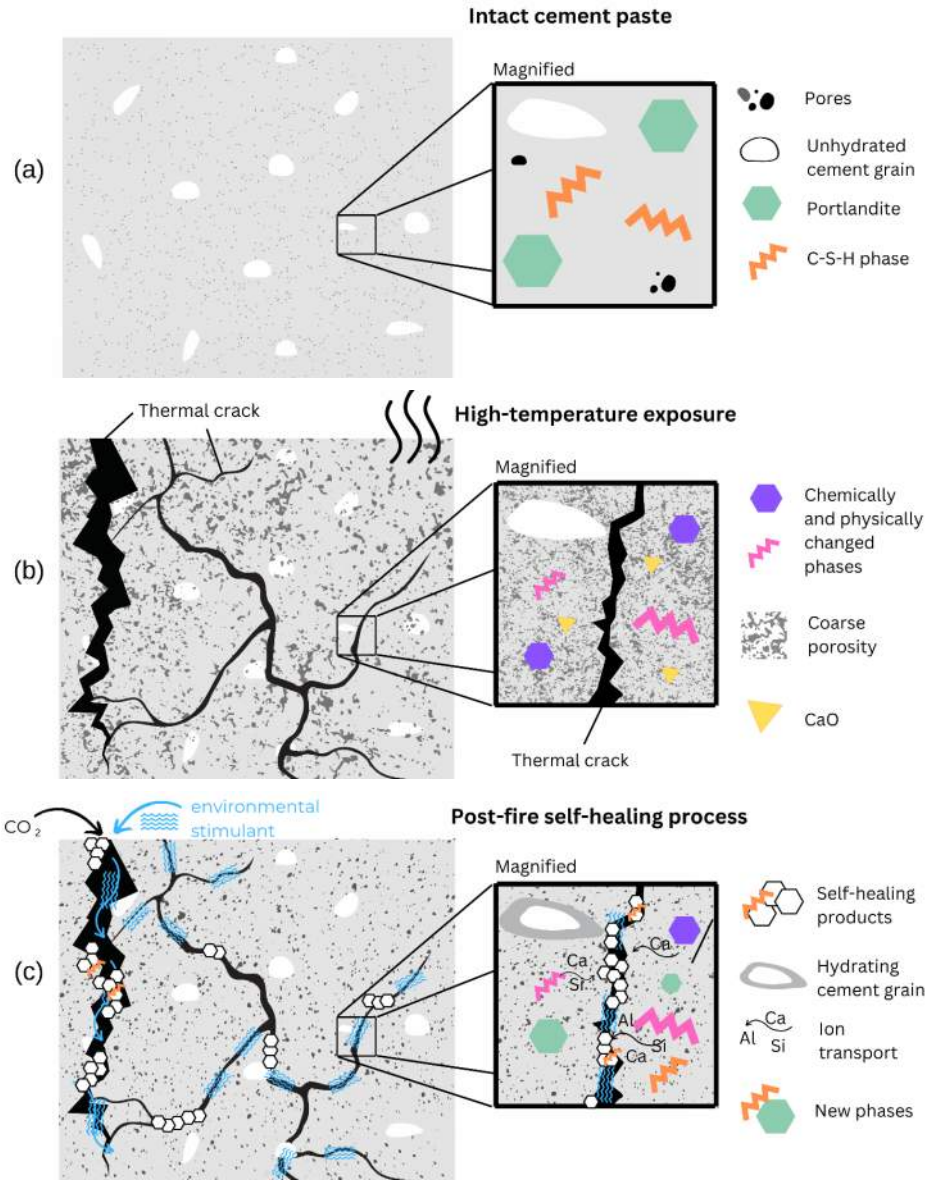

Figure 5.4. Self-healing mechanism of high-temperature damaged cement paste (Rajczakowska et al. 2023c).

In contrast, the thermally damaged hydrated binder is in an unstable state with reference to the intact material (Figure 5.4). High temperature leads to chemically and physically changed phases, e.g., dehydration, decomposition of C-S-H, Ettringite, and Portlandite which decomposes to calcium oxide. In addition, the coarsening of porosity occurs, and cracks form a network due to material weakening in the whole volume. Applying environmental stimulators, e.g., water exposure after the cooling of the concrete, can lead to partial reversing of these changes due to the autogenous self-healing process. In this case, the recovery process involves two components, i.e., the closure of the formed cracks, as in the mechanical loading case, and the thermally damaged binder rehydration. Both of those processes support the recovery of mechanical performance and durability. However, the extent of their contribution depends on the temperature of exposure and the type of healing treatment.

Similarities can be observed in both types of damage, i.e., mechanical and high temperature. The interconnected pore/microcrack network seems to be a significant factor in enhancing the self-healing process by facilitating the transfer of ions from the hydrated phases into the solution inside the crack. The ML model suggested that the presence of aggregates in the case of high-temperature exposure leads to a better recovery, possibly due to the formation of more cracks caused by different thermal expansion coefficients. On the other hand, the dense impermeable matrix was probably the cause of UHPC's lower healing efficiency in the case of mechanically cracked mortar.

5.3. STIMULATED SELF-HEALING?

One of the objectives of this research (Chapter 1.1) was to search for a potential novel stimulator of the autogenous self-healing process.

In the case of mechanically cracked cementitious materials, two major groups were analyzed, i.e., related to healing exposure conditions (Chapter 3.2.1) and binder composition, with a focus on the environmentally friendly solution (Chapter 3.2.2). Comparison of different mix compositions under cyclic water exposure revealed a better self-healing efficiency of the SCMs-limestone binders than pure OPC or OPC/limestone binder (Rajczakowska et al. 2023b). The synergistic effect between the limestone and the mineral additions could possibly be the explanation (Mounanga et al. 2011, Siad et al. 2015). Limestone particles presumably act as nucleation sites and increase the reactivity of cement. Consequently, the pozzolanic reaction is activated at an early age because of increased calcium hydroxide production (Mounanga et al. 2011). Cementitious materials with 50%wt of cement replaced with limestone and slag demonstrated the most successful self-healing properties, i.e., crack closure, compressive strength recovery, and water absorption (Figure 5.5).

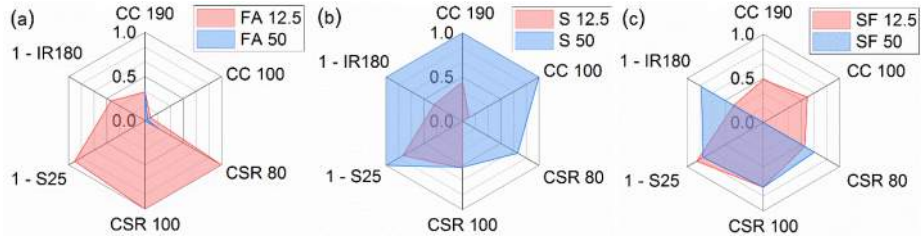

Figure 5.5. Radar plots showing a comparison among selected mixes: (a) FA 12.5 and FA 50, (b) S 12.5 and S 50, (c) SF 12.5 and SF 50. Data are normalized by the maximum and minimum values of each parameter. (Rajczakowska et al. 2023b)

Considering self-healing environmental exposure conditions, a few treatments showed potentially improved self-healing than water (Figure 5.6). Continuous water immersion was more effective for pure OPC mix (REF, Figure 5.6a), whereas cyclic water exposure for the mixes with 20% slag (Figure 5.6a) and fly ash (Figure 5.6b). Self-healing treatments with water solutions with the addition of retarding admixture (R) and micro-silica particles (M) were the most efficient concerning the crack closure. Limited strength recovery was obtained in all cases, with the highest score, approximately 60%, for micro-silica solution in the case of REF mix (Figure 5.6a). More details on the mechanism can be found in sections 3.2 and 5.1. In addition, durability studies, as well as a more detailed analysis of the effect of retarding admixture treatment on the intact material properties, should be performed in the potential follow-up stage.

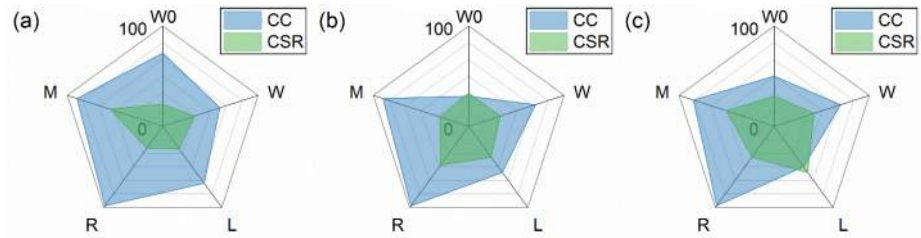

Figure 5.6. Radar plots showing a comparison among selected exposures for mixes: (a) REF, (b) 20% fly ash, (c) 20% slag. (W0 – continuous water immersion, W – water cycle, L – lime water, R – retarding admixture with water, M – micro silica with water) (prepared based on papers (Rajczakowska et al. 2019c, Rajczakowska et al. 2020)

In the case of thermally cracked cementitious materials, the potential of environmental stimulators and MWCNTs was studied based on the surface crack closure and compressive and flexural strength regain. Here, obtained self-healing indexes are combined for both mixes of REF and CNT for 200°C and 400°C to assess a general high-temperature recovery capacity (Figure 5.7). By evaluating the relative size of the area corresponding to each exposure on the radar plot, it can be seen that lime water (L, purple color) seems to have the highest efficiency when both temperatures are considered. It could be associated with

the higher concentration of calcium or increased pH of the crack solution; however, further studies should be conducted to confirm this observation.

Water exposure with an extended wetting phase (W0, red color) was more efficient in the case of the CNT mix than REF. Retarding admixture demonstrated the lowest self-healing efficiency, based on the radar plot area (green color, R) for both mixes. Since, in the case of thermally damaged cement paste, the recovery includes crack closure and rehydration processes of the damaged binder, the admixture possibly delayed the reactions, resulting in reduced performance, especially considering flexural and compressive strength.

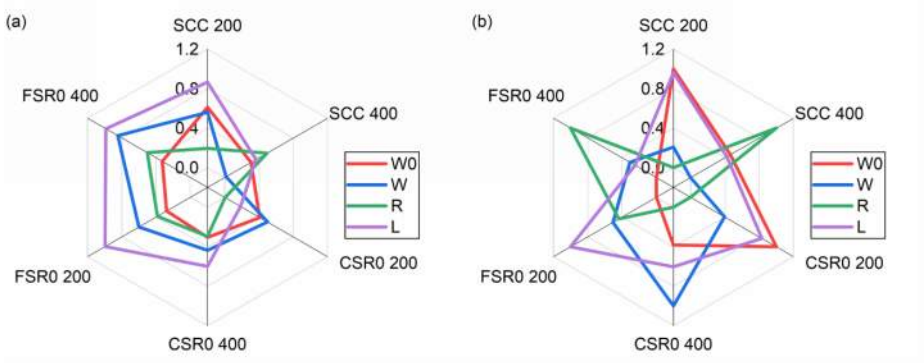

Figure 5.7. Figure 18. Radar plots of the self-healing performance for different combinations: (a) mix REF, (b) mix CNT. Data are normalized by the maximum and minimum values of each parameter. (Rajczakowska et al. 2023c).

5.4. MODELING AND REALITY

> "Essentially, all models are wrong, but some are useful."
> George E. P. Box, British statistician

In Section 4.1, the machine learning model was built to predict the compressive strength recovery of thermally cracked cementitious materials. The performed investigation was "simply" a regression analysis accomplished using more sophisticated tools, i.e., artificial intelligence, to reach a better fit than, e.g., using linear regression. ML modeling gives results as good as the quality of the data used for prediction. Nevertheless, in this case, the model's primary purpose was to uncover the underlying relations between the input variables and the predicted response. The causal analysis gave information on the contributions of each feature to the possibility of achieving an efficient strength recovery. In other words, with the guidance of the constructed model, the critical inputs can be selected which optimization/further studies can help improve the healing performance of thermally induced cracks in the cementitious materials.

To verify the model's performance, the measurement results for the recovery of compressive strength after high-temperature damage from Section 4.2 are here compared

with the ML model's prediction. Due to the input's assumptions (Section 4.1.1), it was impossible to model each of the exposures used, but all exposures were considered water input. At the same time, the CNT amount was omitted since the model did not include this variable. Considering these limitations, it was expected that the prediction might not be accurate. On the other hand, since the influence of CNTs and other types of exposures was small (Section 4.2), a reasonable error was anticipated. Therefore, three datasets were constructed, i.e., considering all measured data, only water exposures for mix REF and CNT, and finally, only REF mix healed in water. The calculation of NRMSE (Figure 5.8a) suggested that the model worked well, with the lowest NRMSE = 5.79 % for the case of only REF mix and water. This relation is evident since the model was trained only on the data incorporating water-related re-curing treatments.

As discussed in Section 4.1.1, the database used for the model training did not consider records that included cement replacement with SCMs. Several studies dealt with the effect of SCMs on the recovery of mechanical performance; In Table 5.2, the research on high-temperature damage recovery, including SCMs, is listed with the types of SCMs considered. It is visible that a variety of SCMs was used, e.g., slag, fly ash, and metakaolin; therefore, the database would have many missing inputs. Nevertheless, the data from these studies (Table 5.2) are used here as input for the developed model to verify how well the prediction generalizes if the SCMs are considered. In addition, the total binder amount replaced the "Cement amount" variable (Section 4.1.1 for comparison).

Table 5.2. Database with SCMs used for additional model testing.

Reference	SCMs used	Number of records
Akca and Özyurt 2018a	Slag, fly ash F-type	4
Hamad and MohamadAli 2021	Limestone	3
Li et al. 2017	fly ash F-type	6
Mendes et al. 2010	Slag	10
Ming et al. 2020	Fly ash	3
Poon and Azhar, 2003	Slag, fly ash, silica fume	72
Poon et al. 2001	Slag, fly ash, silica fume, metakaolin	144
Yaragal et al. 2015	Slag	28

The scatter plot indicated that the model must be updated to incorporate the SCM input variable since most points lay far from the "perfect prediction" line (Figure 5.8b). In addition, the model's error is high, with NRMSE above 45% (Figure 5.8a). The results (Figure 5.8a) imply that the effect of cement replacement on compressive strength recovery after high-temperature exposure is significant and should be further studied.

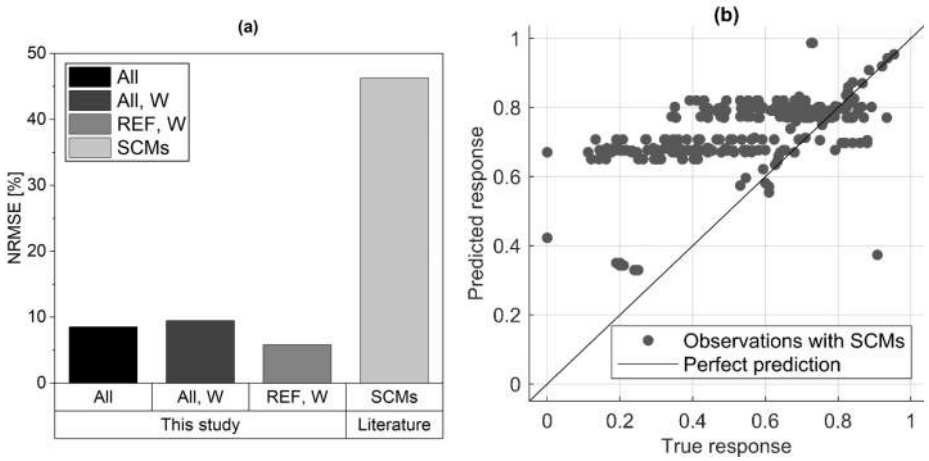

Figure 5.8. Additional model testing: (a) NRMSE results for the prediction of CSR based on the measured data in this study and database with SCMs, (b) scatter plot of measured data versus predicted response for the database with SCMs (Table 5.2).

5.5. LARGE-SCALE APPLICATIONS – OUTLOOK

This research focused solely on the laboratory-scale experiments of self-healing cementitious materials. Consequently, mortar and paste behavior was studied, i.e., the presence of coarse aggregates was excluded from the scope (Section 1.6). Nevertheless, the potential for the large-scale application of the analyzed self-healing stimulators should be considered.

The applied exposure conditions which yielded successful self-healing efficiency, e.g., the retarding admixture solution, should be further studied concerning the durability and their effect on other concrete properties. In addition, since these stimulators require external application in the crack area, a simple technology with a field application capacity should be developed for different types of concrete elements, such as horizontal slabs or vertical columns. This technology could involve periodic spraying on the concrete surface (Figure 5.9ac) or continuous dosing, e.g., in the form of saturated wraps (Figure 5.9bd).

Furthermore, the mix composition stimulators, i.e., the PVA fibers, SCMs, limestone, or multiwall carbon nanotubes, would require further mix optimization. In the case of MWCNTs, other up-scaling impediments should be acknowledged. For example, optimal dispersion of nanomaterials is a significant difficulty. The ultrasonication with the addition of surfactant, which was applied in the laboratory testing, is only a viable solution for preparing small amounts of dispersion. On the other hand, lately, other methods have been proven to perform equally well, such as mechanical mixing with a large amount of superplasticizer (D'Alessandro et al. 2016) or adding silica fume to the concrete mix (Tamimi et al. 2016). Considering the cost of MWCNTs, current production of industrial-grade material reaches around US$30 per kilogram (Su et al. 2022), which, in the case of a dosage of 0.1%wt of cement, would lead to approximately US$12 higher price of 1 m^3 of

ordinary concrete (Rajczakowska et al. 2022). However, since the improvement of the self-healing recovery performance was limited, additional studies should be performed to rationalize the large-scale effort and complexity.

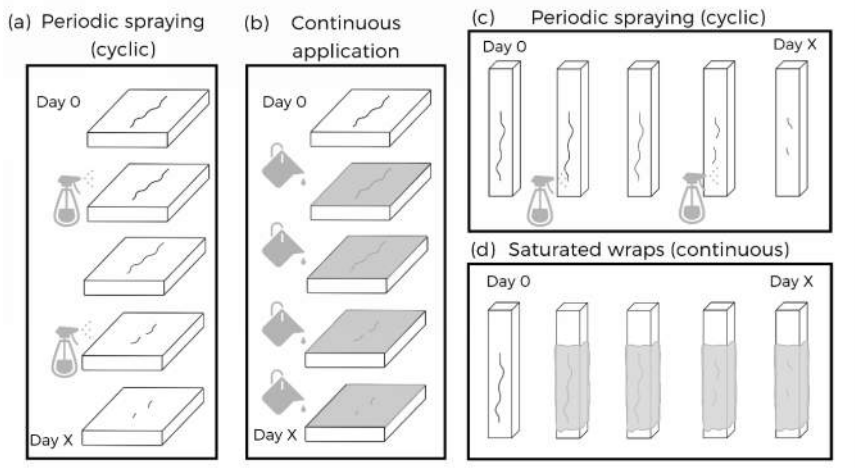

Figure 5.9. A proposed simple exposure stimulator application technology for horizontal concrete elements (a) periodic spraying, (b) continuous application; and for vertical concrete elements: (c) periodic spraying, (b) continuous application, e.g., saturated wraps.

The initial large-scale testing stage of the project started in the Autumn of 2021. In the preliminary phase, three concrete slabs with dimensions 0.3 x 1 x 1.2 m and three walls with dimensions 0.2 x 1 x 1.8 m were cast on site (Figure 5.10). The first round of results is planned for the end of 2023.

Figure 5.10. Overview of the large-scale testing site, Luleå, Sweden, October 2021 (photo credit: Trung Hieu Nguyen).

5.6. THE TRIPLE BOTTOM LINE

> "It often happens that I wake up at night and begin to think about a serious problem and decide I must tell the Pope about it. Then I wake up completely and remember that I am the Pope…"
>
> Pope John XXIII

In the past decades, the industry, including the construction sector, realized that climate issues are more than just a grandiloquent fantasy of environmentalists, and the responsibility for taking action is in their hands (Elkington, 1994). With new EU policies and increasing prices of CO_2 emissions, the environment also became a pressing financial issue. Sustainable development was described in the World Commission on Environment and Development's 1987 report (1987) as: "*Development that meets the needs of the present without compromising the ability of future generations to meet their needs.*" However, this general statement does not give straightforward instructions on how the companies should implement sustainable actions. In the early 90s, the triple bottom line concept was introduced as a guideline for measuring a company's sustainability-related performance considering three areas, i.e., economic, social, and environmental (Elkington & Rowlands, 1999; Alhaddi, 2015). This definition includes three dimensions, the so-called 3Ps: Profit, People, and Planet (Alhaddi, 2015).

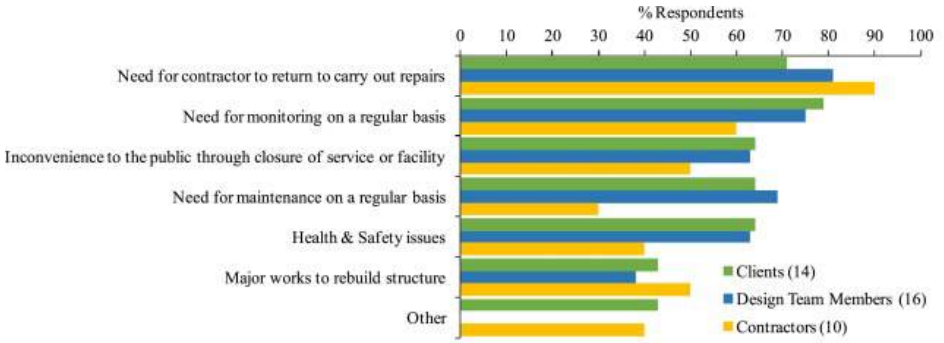

Other includes: Litigation or the implications of litigation. Having to pay for work if they are out of their guarantee phase. Delay to progress on the live construction site. Reputational issues. Real risk or danger to the public due to failure. Most issues appear within a minimum of 10 to 12 years, long after the 3 year original contract has expired. Financial constraints.

Figure 5.11. The consequences of problems with concrete. (Gardner et al., 2018).[14]

About 50% of the EU budget (Cailleux & Pollet, 2009; Gardner et al., 2018) is spent repairing, maintaining, and replacing concrete structures. The results of a market research survey conducted in the UK (Gardner et al. 2018) suggested that contractors and clients face multiple problems with concrete structures. (Figure 5.11). These include actions involving additional routine costs, such as the need for regular monitoring and maintenance, affecting the construction companies' profit. In addition, there are societal

[14] Reproduced from (Gardner et al., 2018) with permission from Elsevier, Creative Commons CC-BY

disturbances pointed out by over 60% of survey respondents, such as public inconvenience due to the closure of the road or facility and health and safety issues (the "People" dimension). Finally, in many cases, the repair involves restoring a large part of the structures (Figure 5.11). Considering the high CO2 emissions of the cement production process, using more material to rebuild concrete elements contributes to environmental issues (the "Planet" dimension).

Cementitious materials with improved autogenous self-healing capacity have the potential to provide a solution to concrete damage problems. First, intrinsic auto-repair does not require external components potentially incompatible with concrete properties, as discussed in Chapter 2 of this thesis. In addition, the increased price of ingredients/treatments potentially boosting the self-healing process, such as polymer fibers, SCMs, or nanomaterials, can be justified by the improved durability and increased service life of the structures. Similarly, applying stimulating external treatments, such as cyclic spraying of water, would not be problematic compared to traditional time-consuming and costly repairs.

In addition, the enhanced self-healing properties of blended mortars with high cement replacement show further advantages concerning the environmental impact. Here, an elementary analysis of the sustainability of this solution is presented. Binder sustainability was evaluated from the perspective of embodied energy and carbon footprint. Embodied energy is defined as the total energy consumption related to material manufacturing. The carbon footprint depicts the total carbon dioxide emissions connected to material production. The values for each binder constituent used in this study were adopted from the literature (Table 5.3).

It should be noted that the addition of the polymer fibers, despite their high environmental impact, was not taken into account in the analysis since they were added to all the mixes; therefore, there is no difference between them. Furthermore, a small dosage, below 2v%, of PP fibers was found to have an impact smaller than cement, reaching 9–68% (Van den Heede et al. 2018). For this reason, only the binder was considered a critical factor.

Table 5.3. Embodied energy and CO_2 emissions for different binder materials.

Parameter	Embodied energy (MJ/kg)	CO_2 (kg/ton)	References
Cement CEM I	5.5	900	(Zhu et al., 2020)
Limestone	0.124	515	(Gettu et al. 2019; Jamieson et al. 2015)
Fly ash	0.05	0	(Jamieson et al. 2015)
Blast furnace slag	1.33	0.07	(Jones et al. 2011)
Silica fume	0.16	0.02	(Zanoletti et al. 2018)

For each binder composition (Section 3.1, Table 3.3), the total CO_2 emissions and embodied energy were calculated as a relative value to the reference mix (% of the REF mix) based on pure ordinary Portland cement. Since fly ash, blast furnace slag, and silica

fume are considered waste materials, their associated CO_2 emissions are very low (Table 5.3). Despite limestone's relatively high carbon footprint, the results indicate (Figure 5.12a) that all mixes have a decreased carbon footprint by 20 to 50% compared to the REF mix. The effect is even more pronounced for the relative embodied energy values (Figure 5.12a).

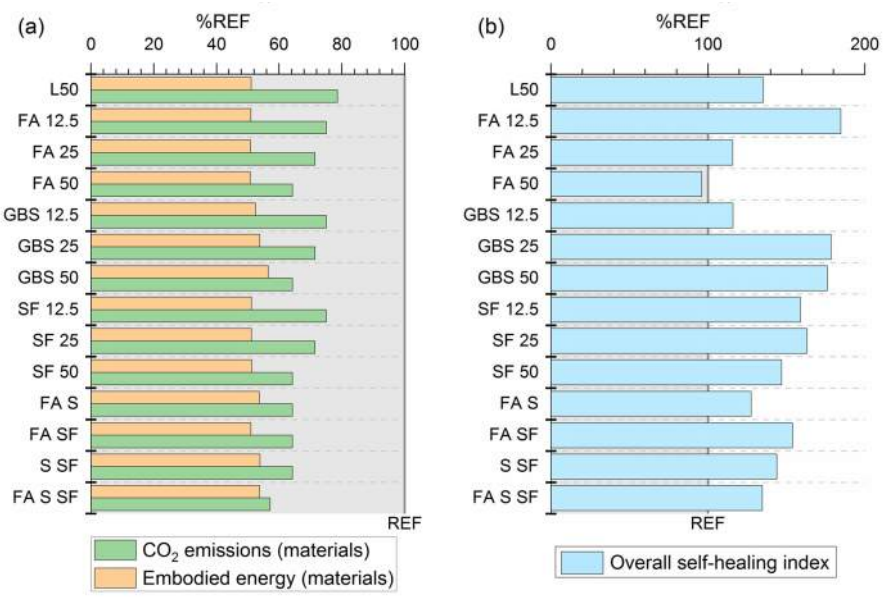

Figure 5.12. (a) Embodied energy and CO_2 emissions in % of the values for reference mix %REF (100%OPC), (b) Self-healing efficiency (based on average CC and CSR) in % of the values for reference mix %REF (100%OPC).

Regarding material-related sustainability, an overall self-healing index was determined. Self-healing contributes indirectly to a decrease in Recurrent Embodied Energy (REE) by extending the service life of structures and limiting the maintenance and repair works. The overall self-healing index was calculated considering the average values of CSR and CC. Similarly, the results (Figure 5.12b) are relative to the reference mix (% of mix REF). It is visible that low-carbon multicomponent binders demonstrate higher self-healing efficiency than OPC mix (REF) in dry/wet cyclic exposure applied in this study. For limestone blended with higher amounts of slag (25 and 50%) and limestone mixed with a moderate amount of fly ash (12.5%), the self-healing performance was improved approximately by two times compared to the pure OPC (100%OPC). Enhanced self-healing was also achieved for some quaternary blends, including limestone, fly ash, and silica fume. Extended service life connected to better self-healing properties combined with low carbon emissions and embodied energy suggests that future research on multicomponent cementitious binders should further explore possible improvements in this area.

6

Conclusions

"Nothing is innocent, and nothing is insignificant, it's all a big endless puzzle."

Olga Tokarczuk
2018 Literature
Nobel Prize winner

6. CONCLUSIONS

6.1. CONCLUSIONS

The following major conclusions can be drawn from the research summarized in this doctoral thesis:

- Self-healing of thermally damaged cement paste involves sealing cracks and chemical-physical changes of the hydrated binder, which facilitate the recovery of mechanical performance. In contrast, in the case of mechanical damage, self-healing occurs in the cracks, leading to durability enhancement and strength regains.
- For mechanically and thermally damaged cementitious materials, the mechanism of crack self-healing is presumably based on the diffusion-dissolution-precipitation processes.
- Interconnected pore/microcrack network is likely to be a significant feature regulating the transfer of ions into cracks, enabling the self-healing process to develop for mechanically and thermally cracked cementitious materials. Therefore, cementitious materials with dense binder matrix and low permeability tend to have a lower self-healing efficiency.
- For mechanically cracked material, mix composition parameters and environmental exposure play a significant role in self-healing. Nevertheless, a large amount of unhydrated cement particles does not guarantee successful self-healing. On the other hand, the maximum loading temperature, type of environmental exposure (re-curing regime), and amounts of fine and coarse aggregates are identified as pivotal concerning the compressive strength recovery of thermally damaged cementitious materials. For OPC-based materials (without SCMs), mix composition parameters, e.g., amount of cement and water-to-cement ratio, are presumably less critical.
- Water is necessary for the self-healing process, both in the case of mechanically and thermally cracked cementitious materials. However, the water exposure showed limited efficiency for the mechanically induced cracks. Therefore, applying externally certain environmental stimulators, i.e., water mixed with different ions/particles, may lead to more extensive healing. For instance, mixing water with retarding admixture based on sodium metaphosphate enhances crack closure at the crack mouth and deep inside the crack. The mechanism presumably involves two processes, i.e., preventing the growth of hydration shell on the unhydrated cement surface and precipitation of self-healing phases containing phosphorus and calcium. Nevertheless, this exposure does not facilitate strength recovery. In addition, water mixed with micro-silica facilitated crack closure at the crack mouth and flexural strength recovery. The self-healing products presumably grow on the particles sedimenting inside the crack, which act as nucleation sites, similar to PVA fibers.

On the other hand, for thermally damaged cracks, the improvement of self-healing performance was minimal with reference to water exposure. It can be speculated that since the rehydration processes play an essential role in the recovery of the mechanical performance, water is a sufficient exposure for the changes to occur.

- A pattern was observed concerning the spatial distribution of the healing phases and its possible implications for mechanically and thermally damaged cementitious materials. White cuboid crystals, i.e., calcium carbonate, grow at the crack mouth and close to the sample surface. This calcite layer governs the crack conditions, e.g., enabling higher ion concentration. However, it does not support mechanical performance recovery. On the other hand, C-S-H and ettringite forming deeper inside the crack can presumably be linked to the strength recovery due to self-healing.

6.2. ADDRESSING RESEARCH QUESTIONS

RQ1: *What is a more reliable self-healing approach for concrete considering the efficiency, impact on fresh and hardened properties, cost, safety, and full-scale applications?*

(Paper I)

The performed literature studies, Paper I (Rajczakowska et al. 2019a), and comparison of effects related to different self-healing approaches on the fresh and hardened concrete properties suggested that autogenous self-healing is more reliable than autonomous methods. Furthermore, since autogenous self-healing does not require external components, e.g., microcapsules, it is also less expensive, relatively simple, and safer, thus more suitable for up-scaling. However, it should be noted that the literature review was performed at the beginning of the research project, in 2018-2019, and newer findings might be available.

RQ2: *How do the mix composition and age affect the efficiency of the autogenous self-healing process of mechanically induced cracks?*

(Papers II and IV)

Mix composition is one of the crucial factors for the self-healing of mechanically cracked cementitious materials. Considering the ongoing hydration mechanism, it can be expected that increasing the cement and/or decreasing the w/c ratio, leading to more unhydrated material, should enhance the self-healing properties. However, this study suggested that this is not a governing parameter of the healing process. It appears that a dense impermeable binder matrix, e.g., for mixes with a low w/c ratio, hinders the transport of ions into the crack, decreasing the growth of healing phases. Similarly, the recovery process probably weakens with the material's age, which can be linked to the densification of the hydrated binder matrix and decreasing the amount of unhydrated cement.

Furthermore, the study indicated that limestone and SCMs presumably enhance self-healing. It depends on the phase assemblage, pore structure, composition of the pore solution, and effects of several other mechanisms that can be associated with the recovery process.

RQ3: *What are the driving factors of the self-healing of thermally induced cracks?*

(Paper V)

Maximum loading temperature and re-curing regime (healing treatment) were found to be the critical factors controlling the compressive strength recovery of the thermally induced cracks. In addition, the presence of fine and coarse aggregates might significantly affect self-healing. They could possibly contribute to forming the interconnected pore network driven by different thermal expansion coefficients of aggregates and hydrated binder.

RQ4: *What is the effect of environmental exposure on the self-healing of mechanically and thermally cracked cementitious materials?*

(Papers III, V, and VII)

The presence of moisture inside the crack is required for the self-healing process.

However, for mechanically induced cracks, water alone does not induce successful healing of wider cracks (above 200 μm). Applying other substances, such as water mixed with different ions/particles, improves the recovery efficiency. For example, mixing water with retarding admixture based on sodium metaphosphate enhances crack closure at the crack mouth and deep inside the crack. The mechanism presumably involves two processes, i.e., preventing the growth of hydration shell on the unhydrated cement surface and precipitation of self-healing phases containing phosphorus and calcium. It should be noted that the theory is primarily valid for freshly exposed cracks. Old cracks which were in contact with moisture were not considered. Nevertheless, this exposure does not facilitate strength recovery. In addition, water mixed with micro-silica facilitated crack closure at the crack mouth and some flexural strength recovery. The self-healing products presumably grow on the particles sedimenting inside the crack, which act as nucleation sites, similar to PVA fibers.

In contrast, for thermally damaged cracks, applying other types of treatments, e.g., water mixed with retarding admixture does not warrant significantly improved self-healing compared to water exposure, even though the cracks were filled with self-healing products. It could suggest that the rehydration processes of damaged binder, which require water for chemical reaction, play a principal role in the performance recovery.

RQ5: *Which geometrical parameters of the crack impact the self-healing of mechanically induced cracks?*

(Paper IV)

Fractal dimension (FD) and maximum crack width (crack opening) presumably control the transport properties recovery of the mechanically damaged specimens, i.e., for wider and complex cracks, less efficient healing is probable. On the other hand, the complexity of the crack, characterized by FD, was not correlated with crack closure. Nevertheless, since the measured range of the crack geometry parameters was relatively narrow, more extreme cases should be analyzed, preferably keeping the other self-healing variables constant, to confirm this hypothesis.

RQ6: *What are the differences in self-healing mechanisms of mechanically and thermally induced cracks?*

(Papers II-VIII)

For mechanically damaged cementitious materials, the self-healing processes take place predominantly inside the cracks. Crack sealing leads to durability and strength regaining. Processes occurring in the hydrated binder during the healing period in water exposure, e.g., continuous hydration at an early age and the pozzolanic reactions of SCMs, affect the material's performance; however, they presumably do not directly contribute to the recovery of damage. Nevertheless, changes in phase assemblage/porosity resulting from these processes influence self-healing efficiency.

On the other hand, self-healing of thermally damaged cement paste involves both sealing the cracks and chemical reactions/physical processes happening in the damaged hydrated binder, e.g., filling the pores with healing products and rehydration of the phases. Rehydration processes seemed to be primarily crucial for the recovery of compressive strength.

REFERENCES

A. Karperien, FracLac for ImageJ. http://rsb.info.nih.gov/ij/plugins/fraclac/FLHe lp/Introduction.htm, 1999-2013

Adenot, F., & Buil, M. (1992). Modelling of the corrosion of the cement paste by deionized water. Cement and Concrete research, 22(2-3), 489-496.

Agrawal, A., & Choudhary, A. (2016). Perspective: Materials informatics and big data: Realization of the "fourth paradigm" of science in materials science. Apl Materials, 4(5), 053208.

Ahn, E., Kim, H., Park, B., & Shin, M. (2021). Long-term autogenous healing and re-healing performance in concrete: Evaluation using air-coupled surface-wave method. Construction and Building Materials, 307, 124939.

Ahn, T. H., & Kishi, T. (2010). Crack self-healing behavior of cementitious composites incorporating various mineral admixtures. Journal of Advanced Concrete Technology, 8(2), 171-186.

Akca, A. H., & Özyurt, N. (2018). Effects of re-curing on residual mechanical properties of concrete after high temperature exposure. Construction and Building Materials, 159, 540–552.

Akhavan, A., & Rajabipour, F. (2012). Quantifying the effects of crack width, tortuosity, and roughness on water permeability of cracked mortars. Cement and Concrete Research, 42(2), 313-320.

Alghamri, R., Kanellopoulos, A., & Al-Tabbaa, A. (2016). Impregnation and encapsulation of lightweight aggregates for self-healing concrete. Construction and Building Materials, 124, 910-921.

Alhaddi, H. (2015). Triple bottom line and sustainability: A literature review. Business and Management Studies, 1(2), 6-10.

Alhamad, A., Yehia, S., Lublóy, É., & Elchalakani, M. (2022). Performance of Different Concrete Types Exposed to Elevated Temperatures: A Review. Materials, 15(14), 5032.

Aliko-Benítez, A., Doblaré, M., & Sanz-Herrera, J. A. (2015). Chemical-diffusive modeling of the self-healing behavior in concrete. International Journal of Solids and Structures, 69, 392-402.

Alyousif, A., Lachemi, M., Yildirim, G., & Şahmaran, M. (2015). Effect of self-healing on the different transport properties of cementitious composites. Journal of Advanced Concrete Technology, 13(3), 112-123.

Amos Esteves, I. C., Ongaratto Trentin, P., & Medeiros-Junior, R. A. (2021). Effect of Fly Ash Contents in Autogenous Self-Healing of Conventional Concretes Analyzed Using Different Test Tools. Journal of Materials in Civil Engineering, 33(7), 04021157.

Arganda-Carreras, I., Fernández-González, R., Muñoz-Barrutia, A., & Ortiz-De-Solorzano, C. (2010). 3D reconstruction of histological sections: Application to mammary gland tissue. Microscopy research and technique, 73(11), 1019-1029.

Asteris, P. G., Skentou, A. D., Bardhan, A., Samui, P., & Pilakoutas, K. (2021). Predicting concrete compressive strength using hybrid ensembling of surrogate machine learning models. Cement and Concrete Research, 145, 106449.

ASTM C1585-20 – Standard Test Method for Measurement of Rate of Absorption of Water by Hydraulic-Cement Concretes

Bagga, M., Hamley-Bennett, C., Alex, A., Freeman, B. L., Justo-Reinoso, I., Mihai, I. C., ... & Ofiţeru, I. D. (2022). Advancements in bacteria based self-healing concrete and the promise of modelling. Construction and Building Materials, 358, 129412.

Beglarigale, A., Eyice, D., Tutkun, B., & Yazıcı, H. (2021). Evaluation of enhanced autogenous self-healing ability of UHPC mixtures. Construction and Building Materials, 280, 122524.

Bello, M. A., & Gonzalez, A. G. (1996). Determination of phosphate in cola beverages using nonsuppressed ion chromatography: an experiment introducing ion chromatography for quantitative analysis. Journal of chemical education, 73(12), 1174.

Bénard, P., Coumes, C. C. D., Garrault, S., Nonat, A., & Courtois, S. (2008). Dimensional stability under wet curing of mortars containing high amounts of nitrates and phosphates. Cement and Concrete Research, 38(10), 1181-1189.

Bénard, P., Garrault, S., Nonat, A., & Cau-Dit-Coumes, C. (2005). Hydration process and rheological properties of cement pastes modified by orthophosphate addition. Journal of the European Ceramic Society, 25(11), 1877-1883.

Bentz, D. P. (2006). Modeling the influence of limestone filler on cement hydration using CEMHYD3D. Cement and Concrete Composites, 28(2), 124-129.

Bentz, D. P. (2014). Activation energies of high-volume fly ash ternary blends: Hydration and setting. Cement and Concrete Composites, 53, 214-223.

Blaiszik, B. J., Kramer, S. L., Olugebefola, S. C., Moore, J. S., Sottos, N. R., & White, S. R. (2010). Self-healing polymers and composites. Annual review of materials research, 40(1), 179-211.

EN 12504-4 (2004). Testing concrete. Determination of ultrasonic pulse velocity.

Burger, E. B., & Starbird, M. (2004). The heart of mathematics: An invitation to effective thinking. Springer Science & Business Media.

Cailleux, E., & Pollet, V. (2009, June). Investigations on the development of self-healing properties in protective coatings for concrete and repair mortars. In Proceedings of the 2nd international conference on self-healing materials, Chicago, IL, USA (Vol. 28, p. 1).

Casalicchio, G., Molnar, C., & Bischl, B. (2018). Visualizing the feature importance for black box models. Joint European Conference on Machine Learning and Knowledge Discovery in Databases, 655–670.

Castellote, M., Alonso, C., Andrade, C., Turrillas, X., & Campo, J. (2004). Composition and microstructural changes of cement pastes upon heating, as studied by neutron diffraction. Cement and Concrete Research, 34(9), 1633–1644.

Catinaud, S., Beaudoin, J. J., & Marchand, J. (2000). Influence of limestone addition on calcium leaching mechanisms in cement-based materials. Cement and Concrete Research, 30(12), 1961-1968.

CEMBUREAU, T. (2022). World Statistical Review 1996-2022 Cement Production. Trade, Consumption Data.

Chen, G., Tang, W., Chen, S., Wang, S., & Cui, H. (2022). Prediction of self-healing of engineered cementitious composite using machine learning approaches. Applied Sciences, 12(7), 3605.

Chen, H., Qian, C., & Huang, H. (2016). Self-healing cementitious materials based on bacteria and nutrients immobilized respectively. Construction and Building Materials, 126, 297-303.

Chen, J., & Ye, G. (2019). A Lattice Boltzmann single component model for simulation of the autogenous self-healing caused by further hydration in cementitious material at mesoscale. Cement and Concrete Research, 123, 105782.

Cheung, J., Jeknavorian, A., Roberts, L., & Silva, D. (2011). Impact of admixtures on the hydration kinetics of Portland cement. Cement and concrete research, 41(12), 1289-1309.

Choi, H., Choi, H., Inoue, M., & Sengoku, R. (2017). Control of the polymorphism of calcium carbonate produced by self-healing in the cracked part of cementitious materials. Applied Sciences, 7(6), 546.

Choi, H., Inoue, M., Kwon, S., Choi, H., & Lim, M. (2016). Effective crack control of concrete by self-healing of cementitious composites using synthetic fiber. Materials, 9(4), 248.

Choi, J. W., Lee, M. J., Oh, S. H., & Kim, K. M. (2019). Changes in the physical properties and color stability of aesthetic restorative materials caused by various beverages. Dental materials journal, 38(1), 33-40.

Chou, J. S., Tsai, C. F., Pham, A. D., & Lu, Y. H. (2014). Machine learning in concrete strength simulations: Multi-nation data analytics. Construction and Building materials, 73, 771-780.

Courard, L., & Michel, F. (2014). Limestone fillers cement based composites: Effects of blast furnace slags on fresh and hardened properties. Construction and Building Materials, 51, 439-445.

Crameri, F. (2018). Scientific colour maps. Zenodo, 10.

Crameri, F., Shephard, G. E., & Heron, P. J. (2020). The misuse of colour in science communication. Nature communications, 11(1), 1-10.

Cuenca, E., & Ferrara, L. (2017). Self-healing capacity of fiber reinforced cementitious composites. State of the art and perspectives. KSCE Journal of Civil Engineering, 1-13.

Cuenca, E., Lo Monte, F., Moro, M., Schiona, A., & Ferrara, L. (2021). Effects of autogenous and stimulated self-healing on durability and mechanical performance of UHPFRC: Validation of tailored test method through multi-performance healing-induced recovery indices. Sustainability, 13(20), 11386.

D'Alessandro, A., Rallini, M., Ubertini, F., Materazzi, A. L., & Kenny, J. M. (2016). Investigations on scalable fabrication procedures for self-sensing carbon nanotube cement-matrix composites for SHM applications. Cement and Concrete Composites, 65, 200-213.

Danner, T., Hjorth Jakobsen, U., & Geiker, M. R. (2019). Mineralogical sequence of self-healing products in cracked marine concrete. Minerals, 9(5), 284.

Darquennes, A., Olivier, K., Benboudjema, F., & Gagné, R. (2016). Self-healing at early-age, a way to improve the chloride resistance of blast-furnace slag cementitious materials. Construction and Building Materials, 113, 1017-1028.

De Belie, N., Gruyaert, E., Al-Tabbaa, A., Antonaci, P., Baera, C., Bajare, D., ... & Jonkers, H. M. (2018). A review of self-healing concrete for damage management of structures. Advanced materials interfaces, 5(17), 1800074.

De Muynck, W., Cox, K., De Belie, N., & Verstraete, W. (2008). Bacterial carbonate precipitation as an alternative surface treatment for concrete. Construction and Building Materials, 22(5), 875-885.

De Rooij, M., Van Tittelboom, K., De Belie, N., & Schlangen, E. (Eds.). (2013). Self-healing phenomena in cement-Based materials: state-of-the-art report of RILEM technical committee 221-SHC: self-Healing phenomena in cement-Based materials (Vol. 11). Springer Science & Business Media.

de Souza Oliveira, A., Gomes, O. D. F. M., Ferrara, L., Fairbairn, E. D. M. R., & Toledo Filho, R. D. (2021). An overview of a twofold effect of crystalline admixtures in cement-based materials: from permeability-reducers to self-healing stimulators. Journal of Building Engineering, 41, 102400.

Di Luzio, G., & Cusatis, G. (2013). Solidification–microprestress–microplane (SMM) theory for concrete at early age: Theory, validation and application. International Journal of Solids and Structures, 50(6), 957-975.

Di Luzio, G., Ferrara, L., & Krelani, V. (2018). Numerical modeling of mechanical regain due to self-healing in cement based composites. Cement and Concrete Composites, 86, 190-205.

di Summa, D., Tenório Filho, J. R., Snoeck, D., Van den Heede, P., Van Vlierberghe, S., Ferrara, L., & De Belie, N. (2022). Environmental and economic sustainability of crack mitigation in reinforced concrete with SuperAbsorbent polymers (SAPs). Journal of Cleaner Production, 358, 131998.

Dias, W. P. S., Khoury, G. A., & Sullivan, P. J. E. (1990). Shrinkage of hardened cement paste at temperatures up to 670 C (1238 F). Materials Journal, 87(3), 204-209

Durdziński, P. T. (2016). Hydration of multi-component cements containing cement clinker, slag, calcareous fly ash and limestone (No. THESIS). EPFL.

E. B. Burger and M. P. Starbird, The Heart of Mathematics: an Invitation to Effective Thinking, New York: Springer-Verlag, 2005, p. 546.

Edvardsen, C. (1999). Water permeability and autogenous healing of cracks in concrete. In Innovation in concrete structures: Design and construction (pp. 473-487). Thomas Telford Publishing.

Edvardsen, C. (1999). Water permeability and autogenous healing of cracks in concrete. ACI Materials Journal-American Concrete Institute, 96(4), 448-454.

Elkhadiri, I., Palacios, M., & Puertas, F. (2009). Effect of curing temperature on cement hydration. Ceram Silik, 53(2), 65-75.

Elkington, J., & Rowlands, I. H. (1994). Cannibals with forks: The triple bottom line of 21st century business. Alternatives Journal, 25(4), 42.

EN 1015-11-2019 Methods of test for mortar for masonry Part 11: Determination of flexural and compressive strength of hardened mortar

EN 12504-4:2004 Testing concrete - Determination of ultrasonic pulse velocity

Endait, M., & Wagh, S. (2020). Effect of elevated temperature on mechanical properties of early-age concrete. Innovative Infrastructure Solutions, 5(1), 1–8.

Environment, U. N., Scrivener, K. L., John, V. M., & Gartner, E. M. (2018). Eco-efficient cements: Potential economically viable solutions for a low-CO2 cement-based materials industry. Cement and Concrete Research, 114, 2-26.

Escalante-Garcia, J. I., & Sharp, J. H. (1998). Effect of temperature on the hydration of the main clinker phases in portland cements: Part I, neat cements. Cement and Concrete Research, 28(9), 1245-1257.

Feldman, R. F., & Ramachandran, V. S. (1971). Differentiation of interlayer and adsorbed water in hydrated Portland cement by thermal analysis. Cement and Concrete Research, 1(6), 607-620.

Feng, D. C., Liu, Z. T., Wang, X. D., Chen, Y., Chang, J. Q., Wei, D. F., & Jiang, Z. M. (2020). Machine learning-based compressive strength prediction for concrete: An adaptive boosting approach. Construction and Building Materials, 230, 117000.

Feng, J., Su, Y., & Qian, C. (2019). Coupled effect of PP fiber, PVA fiber and bacteria on self-healing efficiency of early-age cracks in concrete. Construction and Building Materials, 228, 116810.

Ferguson, J. B., Schultz, B. F., & Rohatgi, P. K. (2014). Self-healing metals and metal matrix composites. Jom, 66(6), 866-871.

Ferrara, L. (2019). High performance fibre reinforced cementitious composites: Six memos for the XXI century societal and economical challenges of civil engineering. Case Studies in Construction Materials, 10, e00219.

Ferrara, L., Krelani, V., & Carsana, M. (2014). A “fracture testing” based approach to assess crack healing of concrete with and without crystalline admixtures. Construction and Building Materials, 68, 535-551.

Ferrara, L., Krelani, V., & Moretti, F. (2016). On the use of crystalline admixtures in cement based construction materials: from porosity reducers to promoters of self healing. Smart materials and structures, 25(8), 084002.

Ferrara, L., Krelani, V., & Moretti, F. (2016). Autogenous healing on the recovery of mechanical performance of High Performance Fibre Reinforced Cementitious Composites (HPFRCCs): Part 2–Correlation between healing of mechanical performance and crack sealing. Cement and Concrete Composites, 73, 299-315.

Ferrara, L., Krelani, V., Moretti, F., Flores, M. R., & Ros, P. S. (2017). Effects of autogenous healing on the recovery of mechanical performance of High Performance Fibre Reinforced Cementitious Composites (HPFRCCs): Part 1. Cement and Concrete Composites, 83, 76-100.

Foroutan-pour, K., Dutilleul, P., & Smith, D. L. (1999). Advances in the implementation of the box-counting method of fractal dimension estimation. Applied mathematics and computation, 105(2-3), 195-210.

Friedman, J. H. (2001). Greedy function approximation: a gradient boosting machine. Annals of Statistics, 1189–1232.

Gagné, R., & Argouges, M. (2012). A study of the natural self-healing of mortars using air-flow measurements. Materials and structures, 45(11), 1625-1638.

Gardner, D., Lark, R., Jefferson, T., & Davies, R. (2018). A survey on problems encountered in current concrete construction and the potential benefits of self-healing cementitious materials. Case studies in construction materials, 8, 238-247.

George, A., & Vidyapeetham, A. (2012). Anomaly detection based on machine learning: dimensionality reduction using PCA and classification using SVM. International Journal of Computer Applications, 47(21), 5-8.

Georget, F., Wilson, W., & Scrivener, K. L. (2021). edxia: Microstructure characterisation from quantified SEM-EDS hypermaps. Cement and Concrete Research, 141, 106327.

Gettu, R., Patel, A., Rathi, V., Prakasan, S., Basavaraj, A. S., Palaniappan, S., & Maity, S. (2019). Influence of supplementary cementitious materials on the sustainability parameters of cements and concretes in the Indian context. Materials and Structures, 52(1), 1-11.

Goldstein, A., Kapelner, A., Bleich, J., & Pitkin, E. (2015). Peeking inside the black box: Visualizing statistical learning with plots of individual conditional expectation. Journal of Computational and Graphical Statistics, 24(1), 44–65.

Gollapudi, U. K., Knutson, C. L., Bang, S. S., & Islam, M. R. (1995). A new method for controlling leaching through permeable channels. Chemosphere, 30(4), 695-705.

Gonzalez, M. A., & Irassar, E. F. (1997). Ettringite formation in low C3A Portland cement exposed to sodium sulfate solution. Cement and Concrete Research, 27(7), 1061-1071.

Gopalan, M. K. (1993). Nucleation and pozzolanic factors in strength development of class fly ash concrete. Materials Journal, 90(2), 117-121.

Granger, S., Loukili, A., Pijaudier-Cabot, G., & Chanvillard, G. (2007). Experimental characterization of the self-healing of cracks in an ultra high performance cementitious material: Mechanical tests and acoustic emission analysis. Cement and Concrete Research, 37(4), 519-527.

Granger, S., Loukili, A., Pijaudier-Cabot, G., & Chanvillard, G. (2005, August). Mechanical characterization of the self-healing effect of cracks in Ultra High Performance Concrete (UHPC). In Proceedings Third International Conference on Construction Materials, Performance, Innovations and Structural Implications, ConMat (Vol. 5, pp. 22-24).

Gray, R. J. (1984). Autogenous healing of fibre/matrix interfacial bond in fibre-reinforced mortar. Cement and Concrete Research, 14(3), 315-317.

Greil, P. (2020). Self-Healing Engineering Ceramics with Oxidation-Induced Crack Repair. Advanced Engineering Materials, 22(9), 1901121.

Guan, W., Ji, F., Chen, Q., Yan, P., & Zhang, Q. (2013). Preparation and phosphorus recovery performance of porous calcium–silicate–hydrate. Ceramics International, 39(2), 1385-1391.

Gupta, S., Al-Obaidi, S., & Ferrara, L. (2021). Meta-analysis and machine learning models to optimize the efficiency of self-healing capacity of cementitious material. Materials, 14(16), 4437.

Gupta, S., Kua, H. W., & Dai Pang, S. (2018). Healing cement mortar by immobilization of bacteria in biochar: An integrated approach of self-healing and carbon sequestration. Cement and Concrete Composites, 86, 238-254.

Hager, M. D., Greil, P., Leyens, C., van der Zwaag, S., & Schubert, U. S. (2010). Self-healing materials. Advanced Materials, 22(47), 5424-5430.

Hamad, A. G., & MohamadAli, A. A. (2021). Effects of air post curing on recovery of bond strength and elastic modulus of fire-damaged self compacted concrete. Materials Today: Proceedings, 42, 1908-1914.

Hamad, A. J. (2017). Size and shape effect of specimen on the compressive strength of HPLWFC reinforced with glass fibres. Journal of King Saud University-Engineering Sciences, 29(4), 373–380.

Han, N. X., & Xing, F. (2016). A Comprehensive Review of the Study and Development of Microcapsule Based Self-Resilience Systems for Concrete Structures at Shenzhen University. Materials, 10(1), 2.

Harrison, R. L. (2010, January). Introduction to monte carlo simulation. In AIP conference proceedings (Vol. 1204, No. 1, pp. 17-21). American Institute of Physics.

He, H., Guo, Z., Stroeven, P., & Stroeven, M. (2009). Numerical assessment of concrete's self-healing potential for promoting durability. International Journal of Modelling, Identification and Control, 7(2), 142-147.

He, H., Guo, Z., Stroeven, P., Stroeven, M., & Sluys, L. J. (2007). Self-healing capacity of concrete-computer simulation study of unhydrated cement structure. Image Analysis & Stereology, 26(3), 137-143.

Hearn, N. (1998). Self-sealing, autogenous healing and continued hydration: What is the difference?. Materials and Structures, 31(8), 563-567.

Hearn, N., & Morley, C. T. (1997). Self-sealing property of concrete – experimental evidence. Materials and structures, 30(7), 404-411.

Henry, M., Ahn, T.-H., Kato, Y., & Kishi, T. (2008). Evaluation of re-curing for the recovery of high-strength mortar exposed to fire. Proceedings of the Japan Concrete Institute, 30(1), 435–440.

Henry, M., Suzuki, M., & Kato, Y. (2011). Behavior of Fire-Damaged Mortar under Variable Re-curing Conditions. ACI Materials Journal, 108(3).

Herbert, E. N., & Li, V. C. (2013). Self-healing of microcracks in engineered cementitious composites (ECC) under a natural environment. Materials, 6(7), 2831-2845.

Herbert, E. N., & Li, V. C. (2012). Self-healing of engineered cementitious composites in the natural environment. In High Performance Fiber Reinforced Cement Composites 6 (pp. 155-162). Springer, Dordrecht.

Hildebrand, T., & Rüegsegger, P. (1997). A new method for the model-independent assessment of thickness in three-dimensional images. Journal of microscopy, 185(1), 67-75.

Hilloulin, B., Grondin, F., Matallah, M., & Loukili, A. (2014). Modelling of autogenous healing in ultra high performance concrete. Cement and Concrete Research, 61, 64-70.

Hilloulin, B., Hilloulin, D., Grondin, F., Loukili, A., & De Belie, N. (2016). Mechanical regains due to self-healing in cementitious materials: Experimental measurements and micro-mechanical model. Cement and Concrete Research, 80, 21-32.

Hilloulin, B., Van Tittelboom, K., Gruyaert, E., De Belie, N., & Loukili, A. (2015). Design of polymeric capsules for self-healing concrete. Cement and Concrete Composites, 55, 298-307.

Homma, D., Mihashi, H., & Nishiwaki, T. (2009). Self-healing capability of fibre reinforced cementitious composites. Journal of Advanced Concrete Technology, 7(2), 217-228.

Horiguchi, T., & Suhaendi, S. L. (2010). Recovery Behavior of Hybrid Fiber Reinforced High Strength Concrete After Fire Exposure (Vol. 1, Issue 4).

Hou, S., Li, K., Wu, Z., Li, F., & Shi, C. (2022). Quantitative evaluation on self-healing capacity of cracked concrete by water permeability test–A review. Cement and Concrete Composites, 127, 104404.

Huang, H., & Ye, G. (2012). Simulation of self-healing by further hydration in cementitious materials. Cement and Concrete Composites, 34(4), 460-467.

Huang, H., & Ye, G. (2015). Self-healing of cracks in cement paste affected by additional Ca2 ions in the healing agent. Journal of Intelligent Material Systems and Structures, 26(3), 309-320.

Huang, H., Ye, G., & Damidot, D. (2013). Characterization and quantification of self-healing behaviors of microcracks due to further hydration in cement paste. Cement and Concrete Research, 52, 71-81.

Huang, H., Ye, G., & Damidot, D. (2014). Effect of blast furnace slag on self-healing of microcracks in cementitious materials. Cement and concrete research, 60, 68-82.

Huang, H., Ye, G., & van Breugel, K. (2010). Numerical simulation on moisture transport in cracked cement-based materials in view of self-healing of crack. Journal of Wuhan University of Technology-Mater. Sci. Ed., 25(6), 1077-1081.

Huang, X., Wasouf, M., Sresakoolchai, J., & Kaewunruen, S. (2021). Prediction of healing performance of autogenous healing concrete using machine learning. Materials, 14(15), 4068.

Huang, Z., Song, Z., Zhang, Y., Donkor, S., Jiang, L., & Chu, H. (2022). A state-of-the-art review of self-healing stimuli-responsive microcapsules in cementitious materials. Journal of Industrial and Engineering Chemistry.

Hung, C. C., & Su, Y. F. (2016). Medium-term self-healing evaluation of engineered cementitious composites with varying amounts of fly ash and exposure durations. Construction and Building Materials, 118, 194-203.

Hung, C. C., Su, Y. F., & Su, Y. M. (2018). Mechanical properties and self-healing evaluation of strain-hardening cementitious composites with high volumes of hybrid pozzolan materials. Composites Part B: Engineering, 133, 15-25.

IEA, WBCSD, Cement Technology Road-map 2009 Carbon Emissions Reductions up to 2050, OECD/IEA:; WBCSD, Paris:; Conches-Geneva, Switzerland (2009)

Imbabi, M. S., Carrigan, C., & McKenna, S. (2012). Trends and developments in green cement and concrete technology. International Journal of Sustainable Built Environment, 1(2), 194-216.

Islam, S., & Bhat, G. (2021). Progress and challenges in self-healing composite materials. Materials Advances, 2(6), 1896-1926.

Iwama, K., & Maekawa, K. (2022). Modeling of carbonation, de-carbonation and re-carbonation processes of structural concrete subjected to high temperature heating. Cement and Concrete Composites, 129, 104493.

Jamei, E., & Vrcelj, Z. (2021). Biomimicry and the built environment, learning from nature's solutions. Applied Sciences, 11(16), 7514.

Jamieson, E., McLellan, B., Van Riessen, A., & Nikraz, H. (2015). Comparison of embodied energies of Ordinary Portland Cement with Bayer-derived geopolymer products. Journal of Cleaner Production, 99, 112-118.

Jensen, O. M., & Hansen, P. F. (2001). Water-entrained cement-based materials: I. Principles and theoretical background. Cement and concrete research, 31(4), 647-654.

Jia, Z., Chen, C., Shi, J., Zhang, Y., Sun, Z., & Zhang, P. (2019). The microstructural change of CSH at elevated temperature in Portland cement/GGBFS blended system. Cement and Concrete Research, 123, 105773.

Jiang, Z., Li, W., & Yuan, Z. (2015). Influence of mineral additives and environmental conditions on the self-healing capabilities of cementitious materials. Cement and Concrete Composites, 57, 116-127.

Jiang, Z., Li, W., Yuan, Z., & Yang, Z. (2014). Self-healing of cracks in concrete with various crystalline mineral additives in underground environment. Journal of Wuhan University of Technology-Mater.Sci.Ed., 29(5), 938-944.

Joa, B. W., Ali Sikandar, M., Baloch, Z., & Asad Khan, R. M. (2015). Effect of incorporation of self healing admixture (SHA) on physical and mechanical properties of mortars. J. Ceram. Process. Res, 16, s138-s143.

Joint, A.C.I. Code Requirements for Determining Fire Resistance of Concrete and Masonry Construction Assemblies (ACI 216.1-07, TMS-216-07): An ACI/TMS Standard.; American Concrete Institute, 2007.

Jones, R., McCarthy, M., & Newlands, M. (2011, May). Fly ash route to low embodied CO2 and implications for concrete construction. In World of Coal Ash Conference, Denver, Colorado, USA.

Jonkers, H. M. (2007). Self-healing concrete: a biological approach. In Self-Healing Materials (pp. 195-204). Springer Netherlands.

Jonkers, H. M. (2007). Self-healing concrete: a biological approach. In Self-Healing Materials (pp. 195-204). Springer Netherlands

Jonkers, H. M. (2011). Bacteria-based self-healing concrete. Heron, 56(1/2), 1-12.

Jonkers, H. M., & Schlangen, E. (2007). Self-healing of cracked concrete: a bacterial approach. Proceedings of FRACOS6: fracture mechanics of concrete and concrete structures. Catania, Italy, 1821-1826.

Jonkers, H. M., & Schlangen, E. (2007, April). Crack repair by concrete-immobilized bacteria. In Proceedings of the first international conference on self healing materials (Vol. 18, p. 20).

Jonkers, H. M., Thijssen, A., Muyzer, G., Copuroglu, O., & Schlangen, E. (2010). Application of bacteria as self-healing agent for the development of sustainable concrete. Ecological engineering, 36(2), 230-235.

Kalina, L., Bílek, V., Novotný, R., Mončeková, M., Másilko, J., & Koplík, J. (2016). Effect of Na3PO4 on the hydration process of alkali-activated blast furnace slag. Materials, 9(5), 395.

Kan, L. L., & Shi, H. S. (2012). Investigation of self-healing behavior of Engineered Cementitious Composites (ECC) materials. Construction and Building Materials, 29, 348-356.

Kan, L. L., Shi, H. S., Sakulich, A. R., & Li, V. C. (2010). Self-Healing Characterization of Engineered Cementitious Composite Materials. ACI Materials Journal, 107(6).

Kan, L., & Shi, H. (2012). Investigation of self-healing behavior of engineered cementitious composites (ECC) materials. Construction and Building Materials, 29, 348-356.

Kanellopoulos, A., Qureshi, T. S., & Al-Tabbaa, A. (2015). Glass encapsulated minerals for self-healing in cement based composites. Construction and Building Materials, 98, 780-791.

Karageorgiou, K., Paschalis, M., & Anastassakis, G. N. (2007). Removal of phosphate species from solution by adsorption onto calcite used as natural adsorbent. Journal of Hazardous Materials, 139(3), 447-452.

Karahan, O. (2011). Residual compressive strength of fire-damaged mortar after post-fire-air-curing. Fire and Materials, 35(8), 561-567.

Karimpour, M., Belusko, M., Xing, K., & Bruno, F. (2014). Minimising the life cycle energy of buildings: Review and analysis. Building and environment, 73, 106-114.

Keskin, S. B., Keskin, O. K., Anil, O., Şahmaran, M., Alyousif, A., Lachemi, M., ... & Ashour, A. F. (2016). Self-healing capability of large-scale engineered cementitious composites beams. Composites Part B: Engineering, 101, 1-13.

Kim, D. J., Kang, S. H., & Ahn, T. H. (2014). Mechanical characterization of high-performance steel-fiber reinforced cement composites with self-healing effect. Materials, 7(1), 508-526.

Kirov, G. K., Vesselinov, I., & Cherneva, Z. (1972). Conditions of formation of calcite crystals of tabular and acute rhombohedral habits. Kristall Und Technik, 7(5), 497-509.

Kjellsen, K. O., Detwiler, R. J., & Gjørv, O. E. (1991). Development of microstructures in plain cement pastes hydrated at different temperatures. Cement and Concrete Research, 21(1), 179-189.

L.R.Roberts, Microsilica in Concrete, in: I.J.Skalny(Ed.), Materials Science of Concrete, American Ceramic Society, Westerville, 1989, pp.197–222.

Lee, T. C., Kashyap, R. L., & Chu, C. N. (1994). Building skeleton models via 3-D medial surface axis thinning algorithms. CVGIP: Graphical Models and Image Processing, 56(6), 462-478.

Li, C. H., & Zuo, J. L. (2020). Self-healing polymers based on coordination bonds. Advanced Materials, 32(27), 1903762.

Li, L., Jia, P., Dong, J., Shi, L., Zhang, G., & Wang, Q. (2017). Effects of cement dosage and cooling regimes on the compressive strength of concrete after post-fire-curing from 800 C. Construction and Building Materials, 142, 208-220.

Li, L., Shi, L., Wang, Q., Liu, Y., Dong, J., Zhang, H., & Zhang, G. (2020). A review on the recovery of fire-damaged concrete with post-fire-curing. Construction and Building Materials, 237, 117564.

Li, V., C. (1998). (1998). Engineered Cementitious Composites (ECC) – tailored composites through micromechanical modelling. Micromechanical, T. C. T.

Li, Z., Yoon, J., Zhang, R., Rajabipour, F., Srubar III, W. V., Dabo, I., & Radlińska, A. (2022). Machine learning in concrete science: applications, challenges, and best practices. npj Computational Materials, 8(1), 1-17.

Lin, Y., Hsiao, C., Yang, H., & Lin, Y. F. (2011). The effect of post-fire-curing on strength–velocity relationship for nondestructive assessment of fire-damaged concrete strength. Fire Safety Journal, 46(4), 178-185.

Liu, H., Zhang, Q., Gu, C., Su, H., & Li, V. (2017). Self-healing of microcracks in Engineered Cementitious Composites under sulfate and chloride environment. Construction and Building Materials, 153, 948-956.

Liu, Z., Jiao, W., Sha, A., Gao, J., Han, Z., & Xu, W. (2017). Portland cement hydration behavior at low temperatures: Views from calculation and experimental study. Advances in Materials Science and Engineering, 2017

Lothenbach, B., Le Saout, G., Gallucci, E., & Scrivener, K. (2008). Influence of limestone on the hydration of Portland cements. Cement and Concrete Research, 38(6), 848-860.

Lothenbach, B., Scrivener, K., & Hooton, R. D. (2011). Supplementary cementitious materials. Cement and concrete research, 41(12), 1244-1256.

Luo, M., Jing, K., Bai, J., Ding, Z., Yang, D., Huang, H., & Gong, Y. (2021). Effects of curing conditions and supplementary cementitious materials on autogenous self-healing of early age cracks in cement mortar. Crystals, 11(7), 752.

Lv, L., Schlangen, E., Yang, Z., & Xing, F. (2016). Micromechanical Properties of a New Polymeric Microcapsule for Self-Healing Cementitious Materials. Materials, 9(12), 1025.

Lv, L., Yang, Z., Chen, G., Zhu, G., Han, N., Schlangen, E., & Xing, F. (2016). Synthesis and characterization of a new polymeric microcapsule and feasibility investigation in self-healing cementitious materials. Construction and Building Materials, 105, 487-495.

Lv, Z., & Chen, H. (2012). Modeling self-healing efficiency on cracks due to unhydrated cement nuclei in cementitious materials: splitting crack mode. Science and Engineering of Composite Materials, 19(1), 1-7.

Lv, Z., & Chen, H. (2013). Self-healing efficiency of unhydrated cement nuclei for dome-like crack mode in cementitious materials. Materials and structures, 46(11), 1881-1892.

Ly, H.-B., Nguyen, T.-A., & Tran, V. Q. (2021). Development of deep neural network model to predict the compressive strength of rubber concrete. Construction and Building Materials, 301, 124081.

Ma, H., Herbert, E., Ohno, M., & Li, V. C. (2019). Scale-linking model of self-healing and stiffness recovery in Engineered Cementitious Composites (ECC). Cement and Concrete Composites, 95, 1-9.

Ma, H., Qian, S., & Zhang, Z. (2014). Effect of self-healing on water permeability and mechanical property of medium-early-strength engineered cementitious composites. Construction and Building Materials, 68, 92-101.

Ma, Q., Guo, R., Zhao, Z., Lin, Z., & He, K. (2015). Mechanical properties of concrete at high temperature—A review. Construction and Building Materials, 93, 371-383.

Maddalena, R., Taha, H., & Gardner, D. (2021). Self-healing potential of supplementary cementitious materials in cement mortars: Sorptivity and pore structure. Developments in the Built Environment, 6, 100044.

Maeda, H., Yokota, S., & Kasuga, T. (2018). Structural changes in calcium silicate hydrate gel and resulting improvement in phosphate species removal properties after mechanochemical treatment. Royal Society Open Science, 5(12), 181403.

Maes, M., Snoeck, D., & de Belie, N. (2016). Chloride penetration in cracked mortar and the influence of autogenous crack healing. Construction and Building Materials, 115, 114–124.

Malinskii, Y. M., Prokopenko, V. V., Ivanova, N. A., & Kargin, V. A. (1970). Investigation of self-healing of cracks in polymers. Polymer Mechanics, 6(2), 240-244.

Matschei, T., & Glasser, F. P. (2010). Temperature dependence, 0 to 40 C, of the mineralogy of portland cement paste in the presence of calcium carbonate. Cement and Concrete Research, 40(5), 763-777.

Medjigbodo, S., Bendimerad, A. Z., Rozière, E., & Loukili, A. (2018). How do recycled concrete aggregates modify the shrinkage and self-healing properties?. Cement and Concrete Composites, 86, 72-86.

Mehdipour, I., Zoughi, R., & Khayat, K. H. (2018). Feasibility of using near-field microwave reflectometry for monitoring autogenous crack healing in cementitious materials. Cement and Concrete Composites, 85, 161-173.

Mekmene, O., Quillard, S., Rouillon, T., Bouler, J., Piot, M., & Gaucheron, F. (2009). Effects of pH and ca/P molar ratio on the quantity and crystalline structure of calcium phosphates obtained from aqueous solutions. Dairy Science & Technology, 89(3-4), 301-316.

Mendes, A., Sanjayan, J. G., & Collins, F. (2011). Effects of slag and cooling method on the progressive deterioration of concrete after exposure to elevated temperatures as in a fire event. Materials and Structures, 44(3), 709–718.

Ming, X., & Cao, M. (2020). Development of eco-efficient cementitious composites with high fire resistance and self-healing abilities-a review. In Resources, Conservation and Recycling (Vol. 162). Elsevier B.V.

Ming, X., Cao, M., Lv, X., Yin, H., Li, L., & Liu, Z. (2020). Effects of high temperature and post-fire-curing on compressive strength and microstructure of calcium carbonate whisker-fly ash-cement system. Construction and Building Materials, 244, 118333.

Moreira, T. N. D. C., Krelani, V., Ferreira, S. R., Ferrara, L., & Toledo Filho, R. D. (2022). Self-healing of slag-cement ultra-high performance steel fiber reinforced concrete (UHPFRC) containing sisal fibers as healing conveyor. Journal of Building Engineering, 104638.

Mostavi, E., Asadi, S., Hassan, M. M., & Alansari, M. (2015). Evaluation of self-healing mechanisms in concrete with double-walled sodium silicate microcapsules. Journal of Materials in Civil Engineering, 27(12), 04015035.

Mounanga, P., Khokhar, M. I. A., El Hachem, R., & Loukili, A. (2011). Improvement of the early-age reactivity of fly ash and blast furnace slag cementitious systems using limestone filler. Materials and structures, 44(2), 437-453.

Munhoz, G. S., Dobrovolski, M. E. G., Pereira, E., & Medeiros-Junior, R. A. (2021). Effect of improved autogenous mortar self-healing in the alkali-aggregate reaction. Cement and Concrete Composites, 117, 103905.

Na, S. H., Hama, Y., Taniguchi, M., Katsura, O., Sagawa, T., Zakaria, M. (2012). "Experimental Investigation on Reaction Rate and Self-Healing Ability in Fly Ash Blended Cement Mixtures." Journal of Advanced Concrete Technology, 10(7), 240-253.

Nalon, G. H., Ribeiro, J. C. L., de Araújo, E. N. D., Pedroti, L. G., de Carvalho, J. M. F., Santos, R. F., & de Oliveira, D. S. (2021). Residual mechanical properties of mortars containing carbon nanomaterials exposed to high temperatures. Construction and Building Materials, 275, 122123.

Namnoum, C. Y., Hilloulin, B., Grondin, F., & Loukili, A. (2021). Determination of the origin of the strength regain after self-healing of binary and ternary cementitious materials including slag and metakaolin. Journal of Building Engineering, 41, 102739.

Naseri, H., Jahanbakhsh, H., Hosseini, P., & Nejad, F. M. (2020). Designing sustainable concrete mixture by developing a new machine learning technique. Journal of cleaner production, 258, 120578.

Naus, D. J., Mattus, C. H., & Dole, L. R. (2007). No title. Assessment of Potential Phosphate Ion-Cementitious Materials Interactions,

Neto, J. A. D. F., Sombra, T. N., Haach, V. G., & Corrêa, M. R. S. (2022). Effects of post-fire curing on the residual mechanical behavior of cement-lime masonry mortars. Construction and Building Materials, 327, 126613.

Nishiwaki, T., Kwon, S., Homma, D., Yamada, M., Mihashi, H. (2014). "Self-Healing Capability of Fiber-Reinforced Cementitious Composites for Recovery of Watertightness and Mechanical Properties." Materials, 7(3), 2141-2154.

Nishiwaki, T., Sasaki, H., & Sukmin, K. (2015). Experimental study on self-healing effect of FRCC with PVA fibers and additives. J. Ceram. Process. Res, 16(1), 89-94.

Nodehi, M., Ozbakkaloglu, T., & Gholampour, A. (2022). A systematic review of bacteria-based self-healing concrete: Biomineralization, mechanical, and durability properties. Journal of Building Engineering, 49, 104038.

Olivier, K., A. Darquennes, F. Benboudjema, and R. Gagné. 2016. “Early age self-healing of cementitious materials containing ground granulated blast-furnace slag under water curing.” J. Adv. Concr. Technol. 14 (11): 717–727.

Olson, G. B. (1997). Computational design of hierarchically structured materials. Science, 277(5330), 1237-1242.

Orial, G., Vieweger, T., & Loubiere, J. F. (2002). Les mortiers biologiques: une solution pour la conservation de la sculpture monumentale en pierre. Art Biology and Conservation, Metropolitan Museum New York.

Özbay, E., Šahmaran, M., Lachemi, M., & Yücel, H. E. (2013). Self-Healing of Microcracks in High-Volume Fly-Ash-Incorporated Engineered Cementitious Composites. ACI Materials Journal, 110(1).

Özbay, E., Sahmaran, M., Yücel, H. E., Erdem, T. K., Lachemi, M., & Li, V. C. (2013). Effect of sustained flexural loading on self-healing of engineered cementitious composites. Journal of Advanced Concrete Technology, 11(5), 167-179.

Palin, D., Wiktor, V., & Jonkers, H. M. (2015). Autogenous healing of marine exposed concrete: Characterization and quantification through visual crack closure. Cement and Concrete Research, 73, 17-24.

Paruelo, J., & Tomasel, F. (1997). Prediction of functional characteristics of ecosystems: a comparison of artificial neural networks and regression models. Ecological Modelling, 98(2–3), 173–186.

Poon, C.-S., & Azhar, S. (2003). Deterioration and Recovery of Metakaolin Blended Concrete Subjected to High Tempera-ture. In Fire Technology (Vol. 39).

Poon, C.-S., Azhar, S., Anson, M., & Wong, Y.-L. (2001). Strength and durability recovery of fire-damaged concrete after post-fire-curing. Cement and Concrete Research, 31(9), 1307–1318.

Proske, T., Rezvani, M., Palm, S., Müller, C., & Graubner, C. A. (2018). Concretes made of efficient multi-composite cements with slag and limestone. Cement and Concrete Composites, 89, 107-119.

Qian, S. Z., Zhou, J., & Schlangen, E. (2010). Influence of curing condition and precracking time on the self-healing behavior of engineered cementitious composites. Cement and Concrete Composites, 32(9), 686-693.

Qian, S., Zhou, J., De Rooij, M. R., Schlangen, E., Ye, G., & Van Breugel, K. (2009). Self-healing behavior of strain hardening cementitious composites incorporating local waste materials. Cement and Concrete Composites, 31(9), 613-621.

Qiu, J., Tan, H. S., & Yang, E. H. (2016). Coupled effects of crack width, slag content, and conditioning alkalinity on autogenous healing of engineered cementitious composites. Cement and Concrete Composites, 73, 203-212.

Qureshi, T. S., Kanellopoulos, A., & Al-Tabbaa, A. (2016). Encapsulation of expansive powder minerals within a concentric glass capsule system for self-healing concrete. Construction and Building Materials, 121, 629-643.

Qureshi, T. S., & Al-Tabbaa, A. (2016). Self-healing of drying shrinkage cracks in cement-based materials incorporating reactive MgO. Smart Materials and Structures, 25(8), 084004.

Rajczakowska, M. (2019). Self-healing concrete (Licentiate dissertation, Luleå tekniska universitet).

Rajczakowska, M., Habermehl-Cwirzen, K., Hedlund, H., & Cwirzen, A. (2019a). Autogenous Self-Healing: A Better Solution for Concrete. Journal of Materials in Civil Engineering, 31(9), 03119001.

Rajczakowska, M., Habermehl-Cwirzen, K., Hedlund, H., & Cwirzen, A. (2019c). The effect of exposure on the autogenous self-healing of ordinary Portland cement mortars. Materials, 12(23), 3926.

Rajczakowska, M., Habermehl-Cwirzen, K., Law, D., Gunasekara, C., Hedlund, H., & Cwirzen, A. (2020). Improved self-healing of mortars with partial cement replacement. In 74th RILEM Annual Week and 40th Cement and Concrete Science Conference, 31 August-4 September 2020. Hosted online by The University of Sheffield.

Rajczakowska, M., Nilsson, L., Habermehl-Cwirzen, K., Hedlund, H., & Cwirzen, A. (2019b). Does a High Amount of Unhydrated Portland Cement Ensure an Effective Autogenous Self-Healing of Mortar?. Materials, 12(20), 3298.

Rajczakowska, M., Szeląg, M. Habermehl-Cwirzen, K., Hedlund, H., & Cwirzen, A. (2023a). Interpretable machine learning for prediction of concrete post-fire self-healing (Under review)

Rajczakowska, M., Szeląg, M. Habermehl-Cwirzen, K., Hedlund, H., & Cwirzen, A. (2023c). Autogenous self-healing of thermally damaged cement paste with carbon nanomaterials subjected to different environmental stimulators (Submitted)

Rajczakowska, M., Szeląg, M., Habermehl-Cwirzen, K., Hedlund, H., & Cwirzen, A. (2022) Is Cement Paste Modified with Carbon Nanomaterials Capable of Self-Repair after a Fire?. Nordic Concrete Research, 67(2), 79-97.

Rajczakowska, M., Tole, I. Habermehl-Cwirzen, K., Hedlund, H., & Cwirzen, A. (2023b). Autogenous self-healing of low embodied energy cementitious materials: effect of multi-component binder and crack geometry (Under review)

Ramadan Suleiman, A., & Nehdi, M. L. (2017). Modeling self-healing of concrete using hybrid genetic algorithm–artificial neural network. Materials, 10(2), 135.

Ramakrishnan, V., Panchalan, R. K., Bang, S. S., & Khokhlova, A. (2013, May). 4843-Improvement of concrete durability by bacterial mineral precipitation. In ICF11, Italy 2005.

Reinhardt, H. W., & Jooss, M. (2003). Permeability and self-healing of cracked concrete as a function of temperature and crack width. Cement and concrete research, 33(7), 981-985.

Roig-Flores, M., Moscato, S., Serna, P., & Ferrara, L. (2015). Self-healing capability of concrete with crystalline admixtures in different environments. Construction and Building Materials, 86, 1-11.

Roig-Flores, M., Pirritano, F., Serna, P., & Ferrara, L. (2016). Effect of crystalline admixtures on the self-healing capability of early-age concrete studied by means of permeability and crack closing tests. Construction and Building Materials, 114, 447-457.

Rossen, J. E., & Scrivener, K. L. (2017). Optimization of SEM-EDS to determine the C–A–S–H composition in matured cement paste samples. Materials Characterization, 123, 294-306.

Rossen, J. E., Lothenbach, B., & Scrivener, K. L. (2015). Composition of C–S–H in pastes with increasing levels of silica fume addition. Cement and Concrete Research, 75, 14-22.

Roy, R., Rossi, E., Silfwerbrand, J., & Jonkers, H. (2020). Encapsulation techniques and test methods of evaluating the bacteria-based self-healing efficiency of concrete: a literature review. Nordic Concrete Research, 62(1), 63-85.

Rueden, C. T., Schindelin, J., Hiner, M. C., DeZonia, B. E., Walter, A. E., Arena, E. T., & Eliceiri, K. W. (2017). ImageJ2: ImageJ for the next generation of scientific image data. BMC bioinformatics, 18(1), 1-26.

Ryou, J. S., Ha, S. W., Ahn, T. H., Bang, S. Y., & Shim, K. B. (2016). Effects of air-cooled blast furnace slag fine aggregate in mortar with self-healing capability exposed to sulfuric acid attack. JOURNAL OF CERAMIC PROCESSING RESEARCH, 16(Special 1).

Sage, A. J., Liu, Y., & Sato, J. (2022). From Black Box to Shining Spotlight: Using Random Forest Prediction Intervals to Illuminate the Impact of Assumptions in Linear Regression. The American Statistician, 1–16.

Şahmaran, M., Keskin, S. B., Ozerkan, G., Yaman, I. O. (2008). "Self-Healing of Mechanically-Loaded Self Consolidating Concretes with High Volumes of Fly Ash." Cement and Concrete Composites, 30(10), 872-879.

Sahmaran, M., Yildirim, G., & Erdem, T. K. (2013). Self-healing capability of cementitious composites incorporating different supplementary cementitious materials. Cement and Concrete Composites, 35(1), 89-101.

Saito, T., & Toriwaki, J. I. (1994). New algorithms for euclidean distance transformation of an n-dimensional digitized picture with applications. Pattern recognition, 27(11), 1551-1565.

Salet, T. A. M., & Wolfs, R. J. M. (2016). Potentials and challenges in 3D concrete printing. In 2nd International Conference on Progress in Additive Manufacturing (Pro-Am 2016), May 16-19 2016, Singapore (pp. 8-13). Research Publishing.

San Wu, Y., van Vliet, L. J., Frijlink, H. W., & van der Voort Maarschalk, K. (2006). The determination of relative path length as a measure for tortuosity in compacts using image analysis. European journal of pharmaceutical sciences, 28(5), 433-440.

Sanjuan, M. A., Andrade, C., & Bentur, A. (1997). Effect of crack control in mortars containing polypropylene fibers on the corrosion of steel in a cementitious matrix. ACI Materials Journal, 94(2), 134-141.

Saud, S., Jamil, B., Upadhyay, Y., & Irshad, K. (2020). Performance improvement of empirical models for estimation of global solar radiation in India: A k-fold cross-validation approach. Sustainable Energy Technologies and Assessments, 40, 100768.

Schindelin, J., Arganda-Carreras, I., Frise, E., Kaynig, V., Longair, M., Pietzsch, T., ... & Cardona, A. (2012). Fiji: an open-source platform for biological-image analysis. Nature methods, 9(7), 676-682.

Schindelin, J., Rueden, C. T., Hiner, M. C., & Eliceiri, K. W. (2015). The ImageJ ecosystem: An open platform for biomedical image analysis. Molecular reproduction and development, 82(7-8), 518-529.

Schlangen, E., Heide, N. T., & Breugel, K. V. (2006). Crack healing of early age cracks in concrete. In Measuring, monitoring and modeling concrete properties (pp. 273-284). Springer, Dordrecht.

Schneider, C. A., Rasband, W. S., & Eliceiri, K. W. (2012). NIH image to ImageJ: 25 years of image analysis. Nature Methods, 9(7), 671.

Scrivener, K. L. & Kirkpatrick, R. J. Innovation in use and research on cementitious material. Cem. Concr. Res. 38, 128–136 (2008).

Scrivener, K. L. (2004). Backscattered electron imaging of cementitious microstructures: understanding and quantification. Cement and concrete Composites, 26(8), 935-945.

Scrivener, K. L., John, V. M., & Gartner, E. M. (2018). Eco-efficient cements: Potential economically viable solutions for a low-CO2 cement-based materials industry. Cement and Concrete Research, 114, 2-26.

Sherir, M. A., Hossain, K. M., & Lachemi, M. (2016). Self-healing and expansion characteristics of cementitious composites with high volume fly ash and MgO-type expansive agent. Construction and Building Materials, 127, 80-92.

Sherir, M. A., Hossain, K. M., & Lachemi, M. (2017). The influence of MgO-type expansive agent incorporated in self-healing system of Engineered cementitious Composites. Construction and Building Materials, 149, 164-185.

Sherir, M. A., Hossain, K. M., & Lachemi, M. (2017). Development and recovery of mechanical properties of self-healing cementitious composites with MgO expansive agent. Construction and Building Materials, 148, 789-810.

Shumuye, E. D., Li, W., Liu, J., Wang, Z., Yu, J., & Wu, H. (2022). Self-healing recovery and micro-structural properties of slag/fly-ash based engineered cementitious composites under chloride environment and tidal exposure. Cement and Concrete Composites, 134, 104789.

Siad, H., Alyousif, A., Keskin, O. K., Keskin, S. B., Lachemi, M., Sahmaran, M., & Hossain, K. M. A. (2015). Influence of limestone powder on mechanical, physical and self-healing behavior of Engineered Cementitious Composites. Construction and Building Materials, 99, 1-10.

Siad, H., Lachemi, M., Sahmaran, M., & Hossain, K. M. A. (2017). Mechanical, physical, and self-healing behaviors of engineered cementitious composites with glass powder. Journal of Materials in Civil Engineering, 29(6), 04017016.

Sisomphon, K., Copuroglu, O., & Fraaij, A. (2011). Application of encapsulated lightweight aggregate impregnated with sodium monofluorophosphate as a self-healing agent in blast furnace slag mortar. Heron, 56(1/2), 13-32.

Sisomphon, K., Copuroglu, O., & Koenders, E. A. B. (2012). Self-healing of surface cracks in mortars with expansive additive and crystalline additive. Cement and Concrete Composites, 34(4), 566-574.

Sisomphon, K., Copuroglu, O., & Koenders, E. A. B. (2013). Effect of exposure conditions on self healing behavior of strain hardening cementitious composites incorporating various cementitious materials. Construction and Building Materials, 42, 217-224.

Snellings, R., Chwast, J., Cizer, Ö., De Belie, N., Dhandapani, Y., Durdzinski, P., ... & Lothenbach, B. (2018). RILEM TC-238 SCM recommendation on hydration stoppage by solvent exchange for the study of hydrate assemblages. Materials and Structures, 51(6), 1-4.

Snoeck, D. Self-healing and microstructure of cementitious materials with microfibres and superabsorbent polymers. Doctoral dissertation. Ghent University. 2015.

Snoeck, D., & De Belie, N. (2012). Mechanical and self-healing properties of cementitious composites reinforced with flax and cottonised flax, and compared with polyvinyl alcohol fibres. Biosystems Engineering, 111(4), 325-335.

Snoeck, D., & De Belie, N. (2016). Repeated autogenous healing in strain-hardening cementitious composites by using superabsorbent polymers. Journal of Materials in Civil Engineering, 28(1), 04015086-1.

Snoeck, D., Van Tittelboom, K., Steuperaert, S., Dubruel, P., & De Belie, N. (2014). Self-healing cementitious materials by the combination of microfibres and superabsorbent polymers. Journal of Intelligent Material Systems and Structures, 25(1), 13-24.

Song, Z., Xu, N., Yu, L., & Guo, M. Z. (2022). Influence of ultrasonic triggering parameters on recovery performance of microcapsule-mediated self-healing cement mortar. Journal of Building Engineering, 62, 105413.

Eurocode 2: Design of Concrete Structures-Part 1.2 General Rules-Structural Fire Design 2004.

Strieth-Kalthoff, F., Sandfort, F., Segler, M. H. S., & Glorius, F. (2020). Machine learning the ropes: principles, applications and directions in synthetic chemistry. Chemical Society Reviews, 49(17), 6154–6168.

Su, X., Wang, R., Li, X., Araby, S., Kuan, H. C., Naeem, M., & Ma, J. (2022). A comparative study of polymer nanocomposites containing multi-walled carbon nanotubes and graphene nanoplatelets. Nano Materials Science, 4(3), 185-204.

Sui, S., Georget, F., Maraghechi, H., Sun, W., & Scrivener, K. (2019). Towards a generic approach to durability: Factors affecting chloride transport in binary and ternary cementitious materials. Cement and Concrete Research, 124, 105783.

Suleiman, A. R., & Nehdi, M. L. (2018). Effect of environmental exposure on autogenous self-healing of cracked cement-based materials. Cement and Concrete Research, 111, 197-208.

Suleiman, A. R., & Nehdi, M. L. (2021). Effect of autogenous crack self-healing on mechanical strength recovery of cement mortar under various environmental exposure. Scientific Reports, 11(1), 1–14.

Sun, C., Yarmohammadi, A., Isfahani, R. B., Nejad, M. G., Toghraie, D., Fard, E. K., ... & Khandan, A. (2021). Self-healing polymers using electrosprayed microcapsules containing oil: molecular dynamics simulation and experimental studies. Journal of Molecular Liquids, 325, 115182.

Suresh, N., Rao, V., & Akshay, B. S. (2022). Evaluation of mechanical properties and post-fire cured strength recovery of recycled aggregate concrete. Journal of Structural Fire Engineering, 13(4), 491–505.

Suryanto, B., Buckman, J. O., Thompson, P., Bolbol, M., & McCarter, W. J. (2016). Monitoring micro-crack healing in an engineered cementitious composite using the environmental scanning electron microscope. Materials Characterization, 119, 175-185..

Szeląg, M. (2020). Fractal characterization of thermal cracking patterns and fracture zone in low-alkali cement matrix modified with microsilica. Cement and Concrete Composites, 114, 103732.

Tamimi, A., Hassan, N. M., Fattah, K., & Talachi, A. (2016). Performance of cementitious materials produced by incorporating surface treated multiwall carbon nanotubes and silica fume. Construction and Building Materials, 114, 934-945.

Tan, H., Zou, F., Liu, M., Ma, B., Guo, Y., & Jian, S. (2017). Effect of the adsorbing behavior of phosphate retarders on hydration of cement paste. Journal of Materials in Civil Engineering, 29(9), 04017088.

Tan, N. P. B., Keung, L. H., Choi, W. H., Lam, W. C., & Leung, H. N. (2016). Silica-based self-healing microcapsules for self-repair in concrete. Journal of Applied Polymer Science, 133(12).

Tang, S. W., Yao, Y., Andrade, C., & Li, Z. J. (2015). Recent durability studies on concrete structure. Cement and Concrete Research, 78, 143-154.

Tavangarian, F., & Li, G. (2015). Bio-inspired crack self-healing of SiC/spinel nanocomposite. Ceramics International, 41(2), 2828-2835.

Termkhajornkit, P., Nawa, T., Yamashiro, Y., & Saito, T. (2009). Self-healing ability of fly ash–cement systems. Cement and concrete composites, 31(3), 195-203.

The MathWorks, Inc. (2022). Deep Learning Toolbox: User's Guide (r2022b).

Tian, Y., Bao, J., Guo, W., Zhang, P., Cui, Y., & Zhao, T. (2022). Autogenous self-healing of cracked concrete exposed to the marine tidal zone. Construction and Building Materials, 357, 129336.

Tomczak, K., & Jakubowski, J. (2018). The effects of age, cement content, and healing time on the self-healing ability of high-strength concrete. Construction and Building Materials, 187, 149-159.

Toutanji, H., Delatte, N., Aggoun, S., Duval, R., & Danson, A. (2004). Effect of supplementary cementitious materials on the compressive strength and durability of short-term cured concrete. Cement and concrete research, 34(2), 311-319.

Tziviloglou, E., Wiktor, V., Jonkers, H. M., & Schlangen, E. (2016). Bacteria-based self-healing concrete to increase liquid tightness of cracks. Construction and Building Materials, 122, 118-125.

Van Belleghem, B., Van den Heede, P., Van Tittelboom, K., & De Belie, N. (2017). Quantification of the service life extension and environmental benefit of chloride exposed self-healing concrete. Materials, 10(1), 5.

Van Damme, H. Concrete material science: Past, present, and future innovations. Cem. Concr. Res. 112, 5–24 (2018).

van Dao, D., Adeli, H., Ly, H. B., Le, L. M., Le, V. M., Le, T. T., & Pham, B. T. (2020). A sensitivity and robustness analysis of GPR and ANN for high-performance concrete compressive strength prediction using a monte carlo simulation. Sustainability (Switzerland), 12(3).

Van den Heede, P., Mignon, A., Habert, G., & De Belie, N. (2018). Cradle-to-gate life cycle assessment of self-healing engineered cementitious composite with in-house developed (semi-) synthetic superabsorbent polymers. Cement and Concrete Composites, 94, 166-180.

Van Tittelboom, K., & De Belie, N. (2013). Self-healing in cementitious materials—A review. Materials, 6(6), 2182-2217.

Van Tittelboom, K., De Belie, N., De Muynck, W., & Verstraete, W. (2010). Use of bacteria to repair cracks in concrete. Cement and Concrete Research, 40(1), 157-166.

Van Tittelboom, K., De Belie, N., Van Loo, D., & Jacobs, P. (2011). Self-healing efficiency of cementitious materials containing tubular capsules filled with healing agent. Cement and Concrete Composites, 33(4), 497-505.

Van Tittelboom, K., Gruyaert, E., Rahier, H., & De Belie, N. (2012). Influence of mix composition on the extent of autogenous crack healing by continued hydration or calcium carbonate formation. Construction and Building Materials, 37, 349-359.

Vapnik, V. (1999). The nature of statistical learning theory. Springer science & business media.

Vapnik, V. N. (1999). An overview of statistical learning theory. IEEE Transactions on Neural Networks, 10(5), 988–999.

Vollpracht, A., Lothenbach, B., Snellings, R., & Haufe, J. (2016). The pore solution of blended cements: a review. Materials and Structures, 49(8), 3341-3367.

Vyšvařil, M., Bayer, P., Chromá, M., & Rovnaníková, P. (2014). Physico-mechanical and microstructural properties of rehydrated blended cement pastes. Construction and Building Materials, 54, 413-420.

Wan, Z., Xu, Y., & Šavija, B. (2021). On the use of machine learning models for prediction of compressive strength of concrete: influence of dimensionality reduction on the model performance. Materials, 14(4), 713.

Wang, X., Sun, P., Han, N., & Xing, F. (2017). Experimental Study on Mechanical Properties and Porosity of Organic Microcapsules Based Self-Healing Cementitious Composite. Materials, 10(1), 20.

WCED, S. W. S. (1987). World commission on environment and development. Our common future, 17(1), 1-91.

White, S. R., Sottos, N. R., Geubelle, P. H., Moore, J. S., Kessler, M., Sriram, S. R., ... & Viswanathan, S. (2001). Autonomic healing of polymer composites. Nature, 409(6822), 794.

Wolfs, R., & Salet, T. (2016). Potentials and challenges in 3D concrete printing. In Proc., 2nd Int. Conf. on Progress in Additive Manufacturing (pp. 8-13).

Wong, H. S., Head, M. K., & Buenfeld, N. R. (2006). Pore segmentation of cement-based materials from backscattered electron images. Cement and Concrete Research, 36(6), 1083-1090.

Wu, M., Johannesson, B., & Geiker, M. (2012). A review: Self-healing in cementitious materials and engineered cementitious composite as a self-healing material. Construction and Building Materials, 28(1), 571-583.

Xiao, J., Han, N., Li, Y., Zhang, Z., & Shah, S. P. (2021). Review of recent developments in cement composites reinforced with fibers and nanomaterials. Frontiers of Structural and Civil Engineering, 15(1), 1-19.

Xu, L., Wang, P., & Zhang, G. (2012). Formation of ettringite in portland cement/calcium aluminate cement/calcium sulfate ternary system hydrates at lower temperatures. Construction and Building Materials, 31, 347-352.

Yang, L., Liu, S., Tsoka, S., & Papageorgiou, L. G. (2017). A regression tree approach using mathematical programming. Expert Systems with Applications, 78, 347–357.

Yang, Y. Z., Lepech, M. D., & Li, V. C. (2005). Self-healing of ECC under cyclic wetting and drying.

Yang, Y., Ding, X., & Urban, M. W. (2015). Chemical and physical aspects of self-healing materials. Progress in Polymer Science, 49, 34-59.

Yang, Y., Lepech, M. D., Yang, E., & Li, V. C. (2009). Autogenous healing of engineered cementitious composites under wet–dry cycles. Cement and Concrete Research, 39(5), 382-390.

Yang, Y., Yang, E., & Li, V. C. (2011). Autogenous healing of engineered cementitious composites at early age. Cement and Concrete Research, 41(2), 176-183.

Yang, Z., Hollar, J., He, X., & Shi, X. (2011). A self-healing cementitious composite using oil core/silica gel shell microcapsules. Cement and Concrete Composites, 33(4), 506-512.

Yao, Y., & Lu, H. (2021). Mechanical properties and failure mechanism of carbon nanotube concrete at high temperatures. Construction and Building Materials, 297, 123782.

Yao, Y., Wang, Z., & Wang, L. (2012). Durability of concrete under combined mechanical load and environmental actions: A review. Journal of Sustainable Cement-Based Materials, 1(1–2), 2–15.

Yaragal, S. C., Kittur, M. M., & Narayan, K. S. B. (2015). Recuring Studies on Concretes Subjected to Elevated Temperatures and Suddenly Cooled by Water Quenching (Vol. 6, Issue 1).

Yaragal, S., Kittur, M., & Narayan, K. (2015). Recuring studies on concretes subjected to elevated temperatures and suddenly cooled by water quenching. Journal of Structural Fire Engineering.

Yildirim, G., Sahmaran, M., & Ahmed, H. U. (2015). Influence of hydrated lime addition on the self-healing capability of high-volume fly ash incorporated cementitious composites. Journal of Materials in Civil Engineering, 27(6), 04014187.

Young, B. A., Hall, A., Pilon, L., Gupta, P., & Sant, G. (2019). Can the compressive strength of concrete be estimated from knowledge of the mixture proportions?: New insights from statistical analysis and machine learning methods. Cement and Concrete Research, 115, 379-388.

Yu, J. H., Chen, W., Yu, M. X., Hua, Y. E. (2010). "The Microstructure of Self-Healed PVA ECC Under Wet and Dry Cycles." Materials Research, 13(2), 225-231.

Zabihi, N., & Eren, Ö. (2014). Compressive strength conversion factors of concrete as affected by specimen shape and size. Research Journal of Applied Sciences, Engineering and Technology, 7(20), 4251–4257.

Zanoletti, A., Vassura, I., Venturini, E., Monai, M., Montini, T., Federici, S., ... & Bontempi, E. (2018). A new porous hybrid material derived from silica fume and alginate for sustainable pollutants reduction. Frontiers in chemistry, 6, 60.

Zelić, J., Krstulović, R., Tkalčec, E., & Krolo, P. (2000). The properties of Portland cement-limestone-silica fume mortars. Cement and Concrete Research, 30(1), 145-152.

Zhang, L., Catalan, L. J., Balec, R. J., Larsen, A. C., Esmaeili, H. H., & Kinrade, S. D. (2010). Effects of saccharide set retarders on the hydration of ordinary Portland cement and pure tricalcium silicate. Journal of the American ceramic society, 93(1), 279-287.

Zhang, Q., Ye, G., & Koenders, E. (2013). Investigation of the structure of heated Portland cement paste by using various techniques. Construction and Building Materials, 38, 1040-1050.

Zhang, W., Zheng, Q., Ashour, A., & Han, B. (2020). Self-healing cement concrete composites for resilient infrastructures: A review. Composites Part B: Engineering, 189, 107892.

Zhang, Z., & Zhang, Q. (2017). Self-healing ability of Engineered Cementitious Composites (ECC) under different exposure environments. Construction and Building Materials, 156, 142-151.

Zhang, Z., Qian, S., & Ma, H. (2014). Investigating mechanical properties and self-healing behavior of micro-cracked ECC with different volume of fly ash. Construction and Building Materials, 52, 17-23.

Zhong, W., & Yao, W. (2008). Influence of damage degree on self-healing of concrete. Construction and building materials, 22(6), 1137-1142.

Zhou, C., Li, K., & Pang, X. (2012). Geometry of crack network and its impact on transport properties of concrete. Cement and concrete research, 42(9), 1261-1272.

Zhou, Y., Elchalakani, M., Du, P., Sun, C., Zhang, Z., & Wang, H. (2023). Sunlight to heal mortar cracks: Photocatalytic self-healing mortar. Cement and Concrete Composites, 135, 104816.

Zhu, H., Zhang, D., Wang, T., Wu, H., & Li, V. C. (2020). Mechanical and self-healing behavior of low carbon engineered cementitious composites reinforced with PP-fibers. Construction and Building Materials, 259, 119805.

Zhu, Y., Yang, Y., & Yao, Y. (2012). Autogenous self-healing of engineered cementitious composites under freeze–thaw cycles. Construction and Building Materials, 34, 522-530.

Zhu, Y., Zhang, Z. C., Yao, Y., Guan, X. M., & Yang, Y. Z. (2016). Analysis of crack microstructure, self-healing products, and degree of self-healing in engineered cementitious composites. Journal of Materials in Civil Engineering, 28(6), 04016017.

ANNEXES

A) Supplementary experimental results

B) Modeling data

C) Supplementary modeling results

ANNEX A – Supplementary experimental results

Table A1. Results of compressive strength measurements (Rajczakowska et al. 2023b).

Mix	Compressive strength, undamaged S_{un} (MPa)		Compressive strength, 80%damage, after healing S_{80} (MPa)		Compressive strength, 100% damage, after healing S_{100} (MPa)	
	Mean value	Standard deviation	Mean value	Standard deviation	Mean value	Standard deviation
REF	71.7	4.5	83.1	4.2	38.5	11.5
LM50	22.3	4.2	29.4	7.8	18.8	5.0
FA12.5	19.8	0.6	38.1	3.5	28.8	5.3
FA25	24.6	7.2	29.6	4.2	21.0	5.5
FA50	29.4	1.7	32.1	1.4	16.7	5.9
S12.5	22.9	2.5	21.7	11.3	23.8	5.2
S25	29.8	3.5	44.6	10.6	33.1	1.7
S50	36.0	3.1	59.6	3.5	37.1	13.4
SF12.5	25.2	1.2	37.3	14.1	30.6	7.2
SF25	32.3	4.0	48.8	2.1	37.5	2.0
SF50	35.6	13.3	60.3	31.1	37.5	1.0
FA S	31.5	5.5	28.5	12.7	27.9	11.0
FA SF	23.8	7.0	33.4	4.9	27.3	2.5
S SF	40.0	2.6	48.1	19.1	35.4	2.5
FA S SF	4.2	7.2	36.9	4.9	27.3	5.5

Table A2. Cumulative water absorption at 25 min (I25) and after 180 min/end of the experiment (I180) and calculated sorption coefficient S25 (during first 25 min) (Rajczakowska et al. 2023b).

Mix	Healed (h) / Undamaged (un)	I_{25} (mm)		I_{180} (mm)		S_{25} (-)	
		Mean	Standard deviation	Mean	Standard deviation	Value	Standard error
REF	h	1.28	0.05	2.99	0.12	0.261	0.008
	un	0.36	0.09	0.96	0.18	0.069	0.008
LM50	h	1.76	0.55	6.09	2.66	0.352	0.015
	un	0.66	0.06	1.37	0.06	0.138	0.031
FA12.5	h	2.08	0.05	6.59	0.16	0.431	0.024
	un	1.02	0.36	3.28	1.51	0.192	0.012
FA50	h	2.66	0.08	6.30	0.16	0.568	0.018
	un	0.31	0.08	0.96	0.18	0.047	0.000
S12.5	h	1.61	0.24	4.82	0.59	0.294	0.021
	un	0.36	0.05	1.17	0.23	0.078	0.016
S50	h	1.04	0.05	2.58	0.21	0.132	0.054
	un	0.63	0.00	1.80	0.21	0.094	0.001
SF12.5	h	1.67	0.39	5.00	0.79	0.359	0.017
	un	0.55	0.08	1.43	0.05	0.131	0.024
SF50	h	0.91	0.05	2.27	0.08	0.127	0.009
	un	0.29	0.05	0.63	0.08	0.035	0.025

Table A3. Calculated IP C–A–S–H composition (Si/Ca ratio) and porosity values (Rajczakowska et al. 2023b).

Sample	IP C–A–S–H composition				Porosity		
	n (-)	μ (-)	σ (-)	Si/Ca (-)	n (-)	μ_p (%)	σ_p (%)
REF	100	0.41	0.048	0.51	31	8.90	0.57
LM50	100	0.44	0.048	0.54	29	3.53	0.83
FA12.5	100	0.46	0.045	0.55	30	3.09	0.83
FA50	100	0.52	0.044	0.60	30	3.47	0.90
S12.5	100	0.44	0.040	0.52	30	3.77	0.95
S50	100	0.47	0.049	0.56	30	6.58	0.94
SF12.5	100	0.48	0.040	0.56	30	3.02	1.07
SF50	100	0.58	0.049	0.68	30	14.77	2.33
FA S SF	100	0.61	0.052	0.72	30	14.27	2.45

ANNEX B – Modeling database

Table B.1. Database records (I1 – water-to-cement ratio; I2 – age; I3 – cement amount; I4 – fine aggregate amount; I5 – coarse aggregate amount; I6 – temperature; I7 – duration of peak temperature; I8 – cooling regime; I9 – cooling duration; I10 – curing regime; I11 – curing duration; I12 – specimen volume; O – response variable, compressive strength recovery).

References	I1 (-)	I2 (days)	I3 (kg/m^3)	I4 (kg/m^3)	I5 (kg/m^3)	I6 (ºC)	I7 (min)	I8 (-)	I9 (min)	I10 (-)	I11 (days)	I12 (cm^3)	O (-)
Karahan 2011	0.5	28	478.8	1620	0	1000	60	0	60	0	7	64	0.02
Karahan 2011	0.5	28	478.8	1620	0	1000	60	0	1440	0	7	64	0.02
Karahan 2011	0.5	28	478.8	1620	0	800	60	0	60	0	7	64	0.07
Karahan 2011	0.5	28	478.8	1620	0	800	60	0	1440	0	7	64	0.08
Lin et al. 2011	0.68	90	354	723	914	600	120	0	4320	0	87	6283	0.15
Lin et al. 2011	0.68	90	354	723	914	600	120	0	4320	0	4	6283	0.16
Lin et al. 2011	0.68	90	354	723	914	600	120	0	4320	0	177	6283	0.17
Lin et al. 2011	0.68	90	354	723	914	600	120	0	4320	0	27	6283	0.18
Lin et al. 2011	0.58	90	392	723	914	600	120	0	4320	0	4	6283	0.19
Lin et al. 2011	0.58	90	392	723	914	600	120	0	4320	0	27	6283	0.20
Mendes et al. 2010	0.63	60	300	1100	1100	800	60	1	10	0	1	6283	0.20
Mendes et al. 2010	0.63	60	300	1100	1100	800	60	0	120	0	7	6283	0.21
Karahan 2011	0.5	28	478.8	1620	0	800	60	1	60	0	7	64	0.22
Karahan 2011	0.5	28	478.8	1620	0	600	60	0	60	0	7	64	0.24
Karahan 2011	0.5	28	478.8	1620	0	600	60	0	1440	0	7	64	0.24
Henry et al. 2011	0.5	28	590	1357	0	550	120	0	60	0	3	785	0.25
Lin et al. 2011	0.58	90	392	723	914	600	120	0	4320	0	87	6283	0.26
Henry et al. 2011	0.5	28	590	1357	0	550	120	0	60	0	28	785	0.26
Poon and Azhar 2003	0.5	60	390	768	917	800	60	0	120	0	7	1000	0.27

Lin et al. 2011	0.58	90	392	723	914	600	120	0	4320	0	177	6283	0.28
Poon and Azhar 2003	0.5	60	390	768	917	800	60	0	120	0	28	1000	0.31
Poon and Azhar 2003	0.5	60	390	768	917	800	60	0	120	0	56	1000	0.31
Poon and Azhar 2003	0.3	60	500	758	927	800	60	0	120	0	7	1000	0.33
Mendes et al. 2010	0.63	60	300	1100	1100	800	60	0	120	0	1	6283	0.34
Poon and Azhar 2003	0.3	60	500	758	927	800	60	0	120	0	28	1000	0.37
Poon and Azhar 2003	0.3	60	500	758	927	800	60	0	120	0	56	1000	0.37
Endait and Wagh 2020	0.5	28	441	981.3	771.02	800	60	1	20	1	7	833	0.39
Akca and Özyurt 2018a	0.45	28	450	789	968	1000	200	0	150	0	28	3375	0.40
Endait and Wagh 2020	0.5	28	441	981.3	771.02	800	60	0	120	1	7	833	0.42
Poon and Azhar 2003	0.5	60	390	768	917	800	60	0	120	1	7	1000	0.43
Poon and Azhar 2003	0.5	60	390	768	917	600	60	0	120	0	7	1000	0.44
Poon and Azhar 2003	0.5	60	390	768	917	600	60	0	120	0	28	1000	0.47
Endait and Wagh 2020	0.5	7	441	981.3	771.02	800	60	1	20	1	7	833	0.47
Endait and Wagh 2020	0.5	28	441	981.3	771.02	400	60	1	20	1	7	833	0.48
Endait and Wagh 2020	0.6	28	367	980.77	835.47	400	60	1	20	1	7	833	0.49
Henry et al. 2011	0.5	28	590	1357	0	550	120	1	60	1	3	785	0.49
Poon and Azhar 2003	0.5	60	390	768	917	600	60	0	120	0	56	1000	0.49
Poon and Azhar 2003	0.5	60	390	768	917	800	60	0	120	1	28	1000	0.50
Endait and Wagh 2020	0.5	28	441	981.3	771.02	800	60	1	20	1	28	833	0.50
Endait and Wagh 2020	0.5	28	441	981.3	771.02	600	60	1	20	1	7	833	0.50
Endait and Wagh 2020	0.5	7	441	981.3	771.02	800	60	1	20	1	28	833	0.51
Henry et al. 2011	0.3	28	767	1380	0	550	120	0	60	0	3	785	0.52
Endait and Wagh 2020	0.5	7	441	981.3	771.02	800	60	0	120	1	7	833	0.52
Poon and Azhar 2003	0.3	60	500	758	927	800	60	0	120	1	56	1000	0.52
Endait and Wagh 2020	0.5	3	441	981.3	771.02	400	60	1	20	1	7	833	0.53

Poon and Azhar 2003	0.3	60	500	758	927	800	60	0	120	1	7	1000	0.54
Poon and Azhar 2003	0.5	60	390	768	917	800	60	0	120	1	56	1000	0.55
Endait and Wagh 2020	0.5	28	441	981.3	771.02	800	60	0	120	1	28	833	0.55
Endait and Wagh 2020	0.6	28	367	980.77	835.47	400	60	0	120	1	7	833	0.55
Endait and Wagh 2020	0.5	7	441	981.3	771.02	600	60	1	20	1	7	833	0.55
Endait and Wagh 2020	0.5	3	441	981.3	771.02	600	60	1	20	1	7	833	0.55
Horiguchi and Suhaendi 2010	0.3	28	557	1010	690	400	120	0	120	0	90	21206	0.55
Lin et al. 2011	0.68	90	354	723	914	500	120	0	4320	0	27	6283	0.55
Endait and Wagh 2020	0.5	7	441	981.3	771.02	800	60	0	120	1	28	833	0.56
Yaragal et al. 2015	0.42	28	390	638.04	1201.59	800	120	1	100	1	1	1000	0.56
Yaragal et al. 2015	0.42	28	390	638.04	1201.59	800	120	1	100	1	3	1000	0.58
Henry et al. 2011	0.3	28	767	1380	0	550	120	0	60	0	28	785	0.58
Endait and Wagh 2020	0.5	28	441	981.3	771.02	600	60	0	120	1	7	833	0.58
Endait and Wagh 2020	0.5	7	441	981.3	771.02	600	60	0	120	1	7	833	0.58
Endait and Wagh 2020	0.5	3	441	981.3	771.02	600	60	0	120	1	7	833	0.58
Horiguchi and Suhaendi 2010	0.3	28	557	1010	690	400	120	0	120	0	180	21206	0.58
Henry et al. 2011	0.5	28	590	1357	0	550	120	1	60	1	28	785	0.58
Lin et al. 2011	0.68	90	354	723	914	500	120	0	4320	0	4	6283	0.59
Lin et al. 2011	0.68	90	354	723	914	500	120	0	4320	0	87	6283	0.59
Lin et al. 2011	0.68	90	354	723	914	500	120	0	4320	0	177	6283	0.59
Endait and Wagh 2020	0.6	3	367	980.77	835.47	600	60	1	20	1	7	833	0.60
Hamad and MohamadAli 2021	0.4	28	450	850	743	600	180	0	120	0	7	6283	0.60
Endait and Wagh 2020	0.5	28	441	981.3	771.02	400	60	0	120	1	7	833	0.61
Hamad and MohamadAli 2021	0.4	28	450	850	743	600	180	0	120	0	30	6283	0.61

Hamad and MohamadAli 2021	0.4	28	450	850	743	600	180	0	120	0	60	6283	0.61
Lin et al. 2011	0.58	90	392	723	914	500	120	0	4320	0	27	6283	0.61
Poon and Azhar 2003	0.3	60	500	758	927	800	60	0	120	1	28	1000	0.61
Yaragal et al. 2015	0.42	28	390	638.04	1201.59	800	120	1	100	1	7	1000	0.62
Karahan 2011	0.5	28	478.8	1620	0	600	60	1	60	0	7	64	0.62
Endait and Wagh 2020	0.5	7	441	981.3	771.02	400	60	0	120	1	7	833	0.62
Endait and Wagh 2020	0.5	3	441	981.3	771.02	400	60	0	120	1	7	833	0.62
Endait and Wagh 2020	0.6	3	367	980.77	835.47	400	60	1	20	1	7	833	0.62
Lin et al. 2011	0.58	90	392	723	914	500	120	0	4320	0	87	6283	0.62
Lin et al. 2011	0.58	90	392	723	914	600	120	0	4320	1	4	6283	0.62
Poon and Azhar 2003	0.5	60	390	768	917	600	60	0	120	1	7	1000	0.62
Yaragal et al. 2015	0.42	28	390	638.04	1201.59	800	120	1	100	1	14	1000	0.62
Henry and Kato 2008 Henry et al. 2011	0.3	28	767	1380	0	550	120	1	60	1	3	785	0.63
Lin et al. 2011	0.58	90	392	723	914	500	120	0	4320	0	4	6283	0.63
Lin et al. 2011	0.68	90	354	723	914	600	120	0	4320	1	177	6283	0.63
Lin et al. 2011	0.58	90	392	723	914	500	120	0	4320	0	177	6283	0.64
Henry et al. 2011	0.5	28	590	1357	0	550	120	0	60	1	3	785	0.64
Yaragal et al. 2015	0.42	28	390	638.04	1201.59	800	120	1	100	1	56	1000	0.65
Poon and Azhar 2003	0.3	60	500	758	927	600	60	0	120	0	7	1000	0.65
Endait and Wagh 2020	0.6	3	367	980.77	835.47	400	60	0	120	1	7	833	0.65
Endait and Wagh 2020	0.6	3	367	980.77	835.47	600	60	0	120	1	7	833	0.65
Lin et al. 2011	0.58	90	392	723	914	600	120	0	4320	1	27	6283	0.65
Lin et al. 2011	0.68	90	354	723	914	600	120	0	4320	1	87	6283	0.65
Lin et al. 2011	0.58	90	392	723	914	600	120	0	4320	1	177	6283	0.65
Mendes et al. 2010	0.63	60	300	1100	1100	400	60	1	10	0	1	6283	0.65

Yaragal et al. 2015	0.42	28	390	638.04	1201.59	800	120	1	100	1	28	1000	0.65
Yaragal et al. 2015	0.42	28	390	638.04	1201.59	800	120	1	100	1	21	1000	0.65
Poon and Azhar 2003	0.5	60	390	768	917	600	60	0	120	1	28	1000	0.65
Lin et al. 2011	0.68	90	354	723	914	600	120	0	4320	1	4	6283	0.66
Lin et al. 2011	0.58	90	392	723	914	600	120	0	4320	1	87	6283	0.66
Endait and Wagh 2020	0.6	28	367	980.77	835.47	600	60	0	120	1	28	833	0.67
Endait and Wagh 2020	0.5	28	441	981.3	771.02	600	60	1	20	1	28	833	0.67
Endait and Wagh 2020	0.5	7	441	981.3	771.02	400	60	1	20	1	7	833	0.67
Poon and Azhar 2003	0.3	60	500	758	927	600	60	0	120	0	28	1000	0.67
Poon and Azhar 2003	0.3	60	500	758	927	600	60	0	120	0	56	1000	0.68
Endait and Wagh 2020	0.6	28	367	980.77	835.47	600	60	0	120	1	7	833	0.68
Akca and Özyurt 2018a	0.45	28	450	789	968	1000	200	0	150	1	28	3375	0.69
Endait and Wagh 2020	0.6	7	367	980.77	835.47	600	60	1	20	1	7	833	0.69
Lin et al. 2011	0.68	90	354	723	914	600	120	0	4320	1	27	6283	0.69
Poon and Azhar 2003	0.3	60	500	758	927	600	60	0	120	1	56	1000	0.69
Poon and Azhar 2003	0.5	60	390	768	917	600	60	0	120	1	56	1000	0.70
Endait and Wagh 2020	0.6	3	367	980.77	835.47	600	60	1	20	1	28	833	0.70
Endait and Wagh 2020	0.6	28	367	980.77	835.47	600	60	1	20	1	28	833	0.71
Endait and Wagh 2020	0.5	7	441	981.3	771.02	600	60	1	20	1	28	833	0.71
Lin et al. 2011	0.58	90	392	723	914	400	120	0	4320	0	4	6283	0.71
Poon and Azhar 2003	0.3	60	500	758	927	600	60	0	120	1	7	1000	0.71
Henry and Kato 2008 Henry et al. 2011	0.3	28	767	1380	0	550	120	0	60	1	3	785	0.71
Lin et al. 2011	0.68	90	354	723	914	400	120	0	4320	0	4	6283	0.72
Endait and Wagh 2020	0.5	28	441	981.3	771.02	400	60	1	20	1	28	833	0.73
Endait and Wagh 2020	0.6	28	367	980.77	835.47	400	60	1	20	1	28	833	0.73
Endait and Wagh 2020	0.5	28	441	981.3	771.02	600	60	0	120	1	28	833	0.73

Endait and Wagh 2020	0.6	7	367	980.77	835.47	400	60	1	20	1	7	833	0.73
Lin et al. 2011	0.58	90	392	723	914	400	120	0	4320	0	27	6283	0.73
Lin et al. 2011	0.58	90	392	723	914	400	120	0	4320	0	87	6283	0.73
Henry and Kato 2008 Henry et al. 2011	0.3	28	767	1380	0	550	120	1	60	1	28	785	0.73
Lin et al. 2011	0.68	90	354	723	914	400	120	0	4320	0	87	6283	0.74
Yaragal et al. 2015	0.42	28	390	638.04	1201.59	600	120	1	100	1	1	1000	0.74
Endait and Wagh 2020	0.5	7	441	981.3	771.02	600	60	0	120	1	28	833	0.75
Endait and Wagh 2020	0.6	7	367	980.77	835.47	400	60	0	120	1	7	833	0.75
Lin et al. 2011	0.68	90	354	723	914	400	120	0	4320	0	27	6283	0.75
Yaragal et al. 2015	0.42	28	390	638.04	1201.59	500	120	1	100	1	1	1000	0.75
Henry et al. 2011	0.5	28	590	1357	0	550	120	0	60	1	28	785	0.75
Endait and Wagh 2020	0.6	28	367	980.77	835.47	400	60	0	120	1	28	833	0.76
Karahan 2011	0.5	28	478.8	1620	0	400	60	0	1440	0	7	64	0.76
Yaragal et al. 2015	0.42	28	390	638.04	1201.59	600	120	1	100	1	3	1000	0.77
Lin et al. 2011	0.68	90	354	723	914	400	120	0	4320	0	177	6283	0.77
Karahan 2011	0.5	28	478.8	1620	0	400	60	0	60	0	7	64	0.78
Yaragal et al. 2015	0.42	28	390	638.04	1201.59	600	120	1	100	1	7	1000	0.78
Endait and Wagh 2020	0.5	28	441	981.3	771.02	400	60	0	120	1	28	833	0.78
Endait and Wagh 2020	0.6	3	367	980.77	835.47	600	60	0	120	1	28	833	0.78
Lin et al. 2011	0.58	90	392	723	914	400	120	0	4320	1	4	6283	0.78
Yaragal et al. 2015	0.42	28	390	638.04	1201.59	500	120	1	100	1	3	1000	0.78
Poon and Azhar 2003	0.3	60	500	758	927	600	60	0	120	1	28	1000	0.78
Endait and Wagh 2020	0.5	7	441	981.3	771.02	400	60	1	20	1	28	833	0.79
Endait and Wagh 2020	0.6	28	367	980.77	835.47	600	60	1	20	1	7	833	0.79
Yaragal et al. 2015	0.42	28	390	638.04	1201.59	400	120	1	100	1	1	1000	0.79
Yaragal et al. 2015	0.42	28	390	638.04	1201.59	600	120	1	100	1	14	1000	0.80

Endait and Wagh 2020	0.6	7	367	980.77	835.47	600	60	1	20	1	28	833	0.80
Lin et al. 2011	0.58	90	392	723	914	400	120	0	4320	0	177	6283	0.80
Endait and Wagh 2020	0.5	3	441	981.3	771.02	600	60	1	20	1	28	833	0.81
Yaragal et al. 2015	0.42	28	390	638.04	1201.59	500	120	1	100	1	7	1000	0.81
Yaragal et al. 2015	0.42	28	390	638.04	1201.59	600	120	1	100	1	21	1000	0.82
Endait and Wagh 2020	0.6	3	367	980.77	835.47	400	60	1	20	1	28	833	0.82
Endait and Wagh 2020	0.6	7	367	980.77	835.47	600	60	0	120	1	7	833	0.82
Yaragal et al. 2015	0.42	28	390	638.04	1201.59	400	120	1	100	1	3	1000	0.82
Karahan 2011	0.5	28	478.8	1620	0	400	60	1	60	0	7	64	0.82
Yaragal et al. 2015	0.42	28	390	638.04	1201.59	500	120	1	100	1	14	1000	0.82
Yaragal et al. 2015	0.42	28	390	638.04	1201.59	600	120	1	100	1	28	1000	0.83
Suresh et al. 2022	0.54	28	370	705	1136.5	700	120	0	120	1	7	1000	0.83
Endait and Wagh 2020	0.6	7	367	980.77	835.47	400	60	1	20	1	28	833	0.83
Lin et al. 2011	0.68	90	354	723	914	400	120	0	4320	1	4	6283	0.83
Yaragal et al. 2015	0.42	28	390	638.04	1201.59	500	120	1	100	1	21	1000	0.83
Yaragal et al. 2015	0.42	28	390	638.04	1201.59	600	120	1	100	1	56	1000	0.85
Henry and Kato 2008 Henry et al. 2011	0.3	28	767	1380	0	550	120	0	60	1	28	785	0.85
Endait and Wagh 2020	0.6	7	367	980.77	835.47	600	60	0	120	1	28	833	0.85
Mendes et al. 2010	0.63	60	300	1100	1100	400	60	0	120	0	1	6283	0.85
Yaragal et al. 2015	0.42	28	390	638.04	1201.59	500	120	1	100	1	28	1000	0.85
Endait and Wagh 2020	0.5	3	441	981.3	771.02	600	60	0	120	1	28	833	0.86
Horiguchi and Suhaendi 2010	0.3	28	557	1010	690	400	120	1	120	1	180	21206	0.87
Yaragal et al. 2015	0.42	28	390	638.04	1201.59	500	120	1	100	1	56	1000	0.87
Endait and Wagh 2020	0.6	7	367	980.77	835.47	400	60	0	120	1	28	833	0.88
Endait and Wagh 2020	0.6	3	367	980.77	835.47	400	60	0	120	1	28	833	0.88

Endait and Wagh 2020	0.5	3	441	981.3	771.02	400	60	1	20	1	28	833	0.88
Horiguchi and Suhaendi 2010	0.3	28	557	1010	690	400	120	1	120	1	90	21206	0.88
Suresh et al. 2022	0.54	28	370	705	1136.5	500	120	0	120	1	7	1000	0.89
Suresh et al. 2022	0.54	28	370	705	1136.5	600	120	0	120	1	7	1000	0.89
Lin et al. 2011	0.58	90	392	723	914	500	120	0	4320	1	4	6283	0.89
Yaragal et al. 2015	0.42	28	390	638.04	1201.59	400	120	1	100	1	7	1000	0.89
Yaragal et al. 2015	0.42	28	390	638.04	1201.59	400	120	1	100	1	14	1000	0.90
Endait and Wagh 2020	0.5	7	441	981.3	771.02	400	60	0	120	1	28	833	0.90
Lin et al. 2011	0.58	90	392	723	914	400	120	0	4320	1	27	6283	0.91
Yaragal et al. 2015	0.42	28	390	638.04	1201.59	400	120	1	100	1	56	1000	0.91
Yaragal et al. 2015	0.42	28	390	638.04	1201.59	400	120	1	100	1	21	1000	0.92
Lin et al. 2011	0.68	90	354	723	914	500	120	0	4320	1	4	6283	0.92
Suresh et al. 2022	0.54	28	370	705	1136.5	400	120	0	120	1	7	1000	0.92
Lin et al. 2011	0.68	90	354	723	914	500	120	0	4320	1	177	6283	0.94
Yaragal et al. 2015	0.42	28	390	638.04	1201.59	400	120	1	100	1	28	1000	0.94
Lin et al. 2011	0.68	90	354	723	914	400	120	0	4320	1	27	6283	0.95
Lin et al. 2011	0.68	90	354	723	914	500	120	0	4320	1	27	6283	0.97
Lin et al. 2011	0.58	90	392	723	914	500	120	0	4320	1	177	6283	0.97
Lin et al. 2011	0.58	90	392	723	914	500	120	0	4320	1	27	6283	0.98
Lin et al. 2011	0.68	90	354	723	914	400	120	0	4320	1	177	6283	1.00
Lin et al. 2011	0.68	90	354	723	914	500	120	0	4320	1	87	6283	1.00
Endait and Wagh 2020	0.5	3	441	981.3	771.02	400	60	0	120	1	28	833	1.01
Lin et al. 2011	0.58	90	392	723	914	400	120	0	4320	1	87	6283	1.02
Lin et al. 2011	0.58	90	392	723	914	400	120	0	4320	1	177	6283	1.02
Lin et al. 2011	0.58	90	392	723	914	500	120	0	4320	1	87	6283	1.02
Lin et al. 2011	0.68	90	354	723	914	400	120	0	4320	1	87	6283	1.03

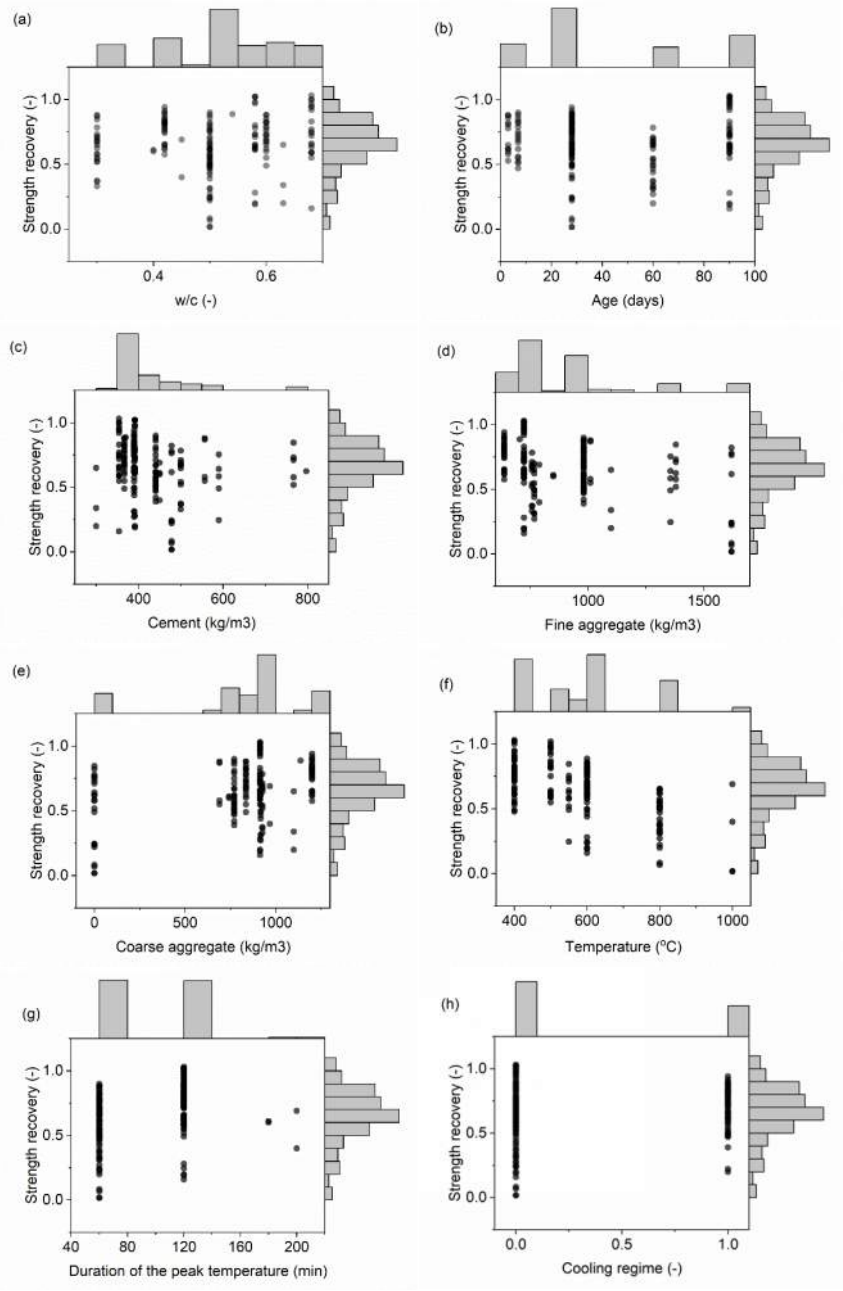
(a)
Strength recovery (-)
1.0
0.5
0.0
0.4
0.6
w/c (-)
(b)
Strength recovery (-)
1.0
0.5
0.0
0
20
40
60
80
100
Age (days)
(c)
Strength recovery (-)
1.0
0.5
0.0
400
600
800
Cement (kg/m3)
(d)
Strength recovery (-)
1.0
0.5
0.0
1000
1500
Fine aggregate (kg/m3)
(e)
Strength recovery (-)
1.0
0.5
0.0
0
500
1000
Coarse aggregate (kg/m3)
(f)
Strength recovery (-)
1.0
0.5
0.0
400
600
800
1000
Temperature (°C)
(g)
Strength recovery (-)
1.0
0.5
0.0
40
80
120
160
200
Duration of the peak temperature (min)
(h)
Strength recovery (-)
1.0
0.5
0.0
0.0
0.5
1.0
Cooling regime (-)

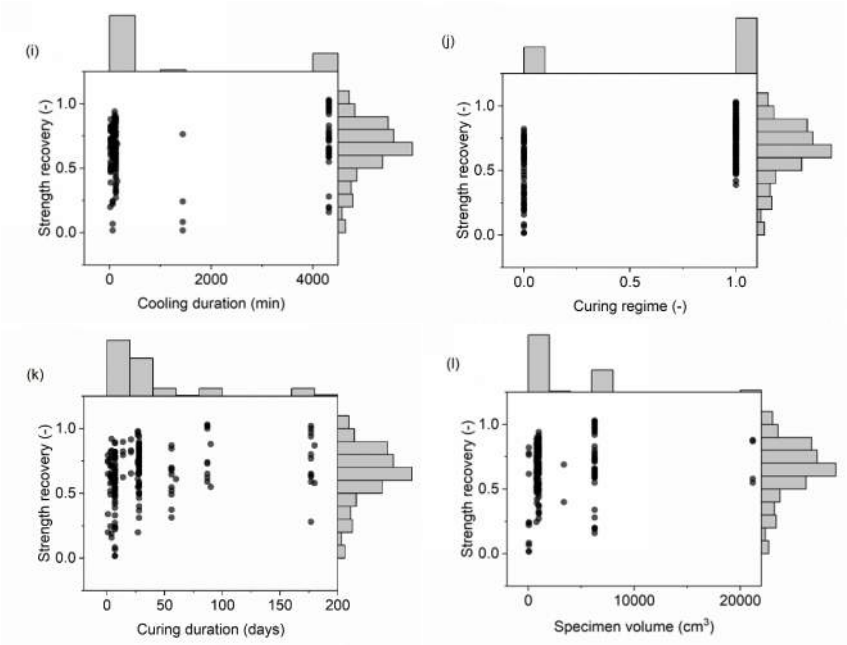

Figure B.1. Relation between the input and output variables including histograms: (a) water-to-cement ratio (I1), (b) age (I2), (c) cement amount (I3), (d) fine aggregate (I4), (e) coarse aggregate (I5), (f) temperature (I6), (g) duration of peak temperature (I7), (h) cooling regime (I8), (i) cooling duration (I9), (j) curing regime (I10), (k) curing duration (I11), (l) specimen volume (I12) (Rajczakowska et al. 2023a)

ANNEX C – Supplementary modeling results

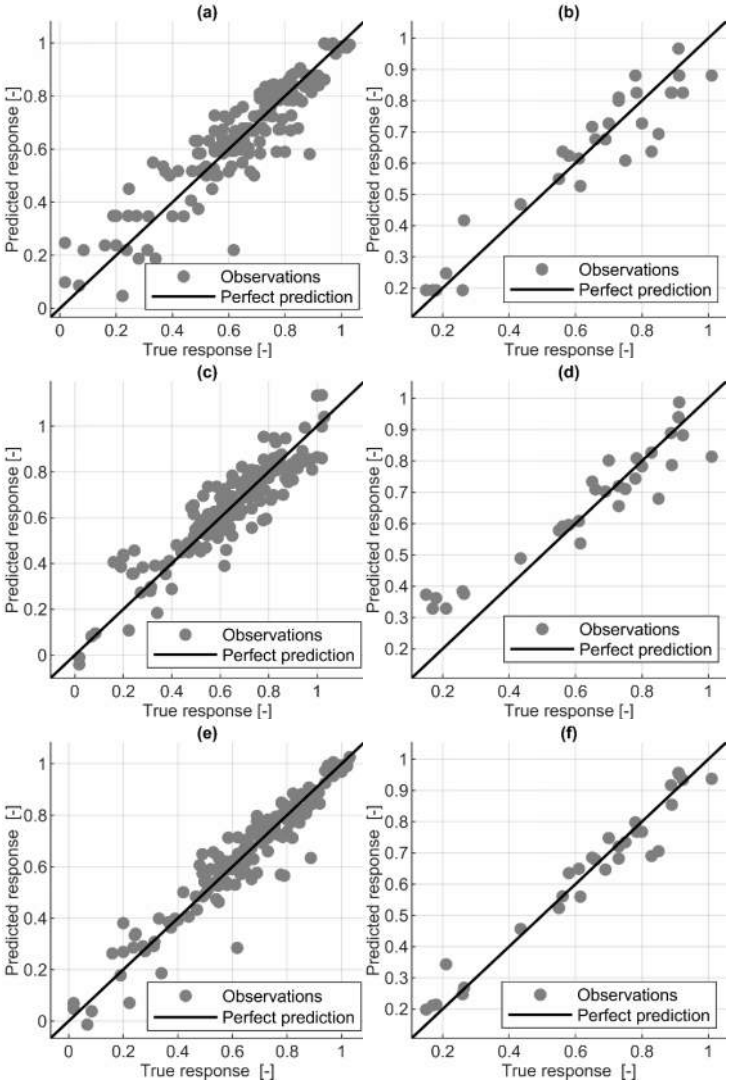

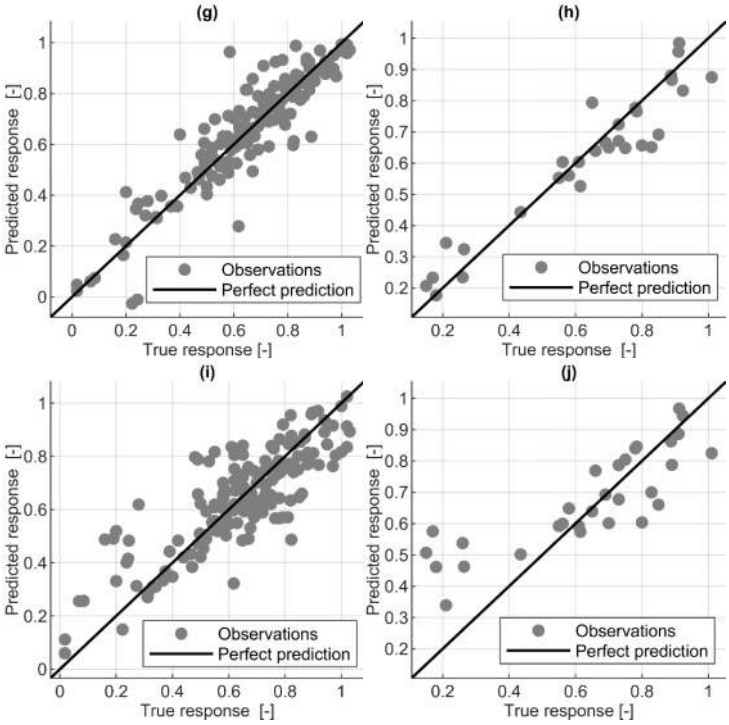

Figure C.1. Comparison of the prediction accuracy for best model within different ML approaches and LR: training and validation (a) RT, (c) SVM, (e) ET, (g) ANN, (i) LR; testing: (b) RT, (d) SVM, (f) ET, (h) ANN, (j) RT (Rajczakowska et al. 2023a).

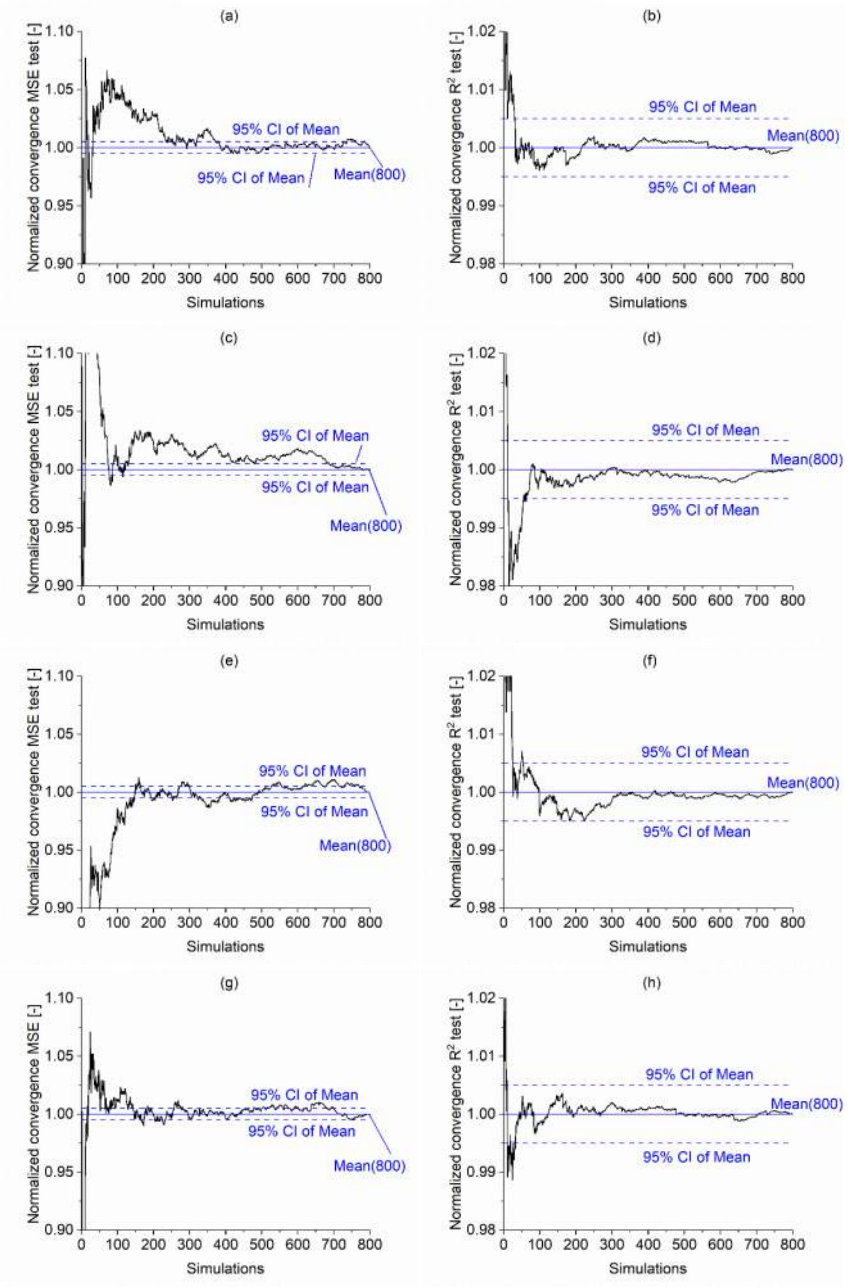
(a)
Normalized convergence MSE test [-]
95% CI of Mean
95% CI of Mean
Mean(800)
Simulations
(b)
Normalized convergence R² test [-]
95% CI of Mean
Mean(800)
95% CI of Mean
Simulations
(c)
Normalized convergence MSE test [-]
95% CI of Mean
95% CI of Mean
Mean(800)
Simulations
(d)
Normalized convergence R² test [-]
95% CI of Mean
Mean(800)
95% CI of Mean
Simulations
(e)
Normalized convergence MSE test [-]
95% CI of Mean
95% CI of Mean
Mean(800)
Simulations
(f)
Normalized convergence R² test [-]
95% CI of Mean
Mean(800)
95% CI of Mean
Simulations
(g)
Normalized convergence MSE [-]
95% CI of Mean
95% CI of Mean
Mean(800)
Simulations
(h)
Normalized convergence R² test [-]
95% CI of Mean
Mean(800)
95% CI of Mean
Simulations

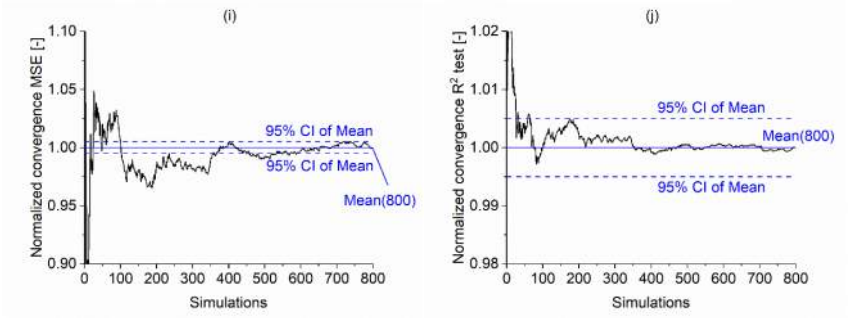

Figure C.2. Comparison of the Monte Carlo normalized convergence of testing set MSE and R2 for selected models: (a) (b) ET1, (c) (d) ET2, (e) (f) ET3, (g) (h) ET4, (i) (j) ET5. (Rajczakowska et al. 2023a).

Department of Civil, Environmental and Natural Resources Engineering
Division of Structural and Fire Engineering

ISSN 1402-1544
ISBN 978-91-8048-227-1
ISBN 978-91-8048-228-8

Luleå University of Technology 2023

Print: Lenanders Grafiska, 463157

LULEÅ
UNIVERSITY
OF TECHNOLOGY